Structure of disordered materials: from geological fluids to network glasses

submitted by

Annalisa Polidori

for the degree of Doctor of Philosophy

of the

University of Bath

Department of Physics

March 14, 2017

COPYRIGHT

Signature of Author .... Annalisa Polidori

Annalisa Polidori

Contents

Acknowledgements

Tell me and I will forget,
teach me and I may remember,
involve me and I will understand.

Looking over the past few years, I have a great desire to express my deepest gratitude to those I have encountered along this journey.

Firstly, I would like to express my gratitude to my advisor Phil Salmon. Thanks for having involved me in this fascinating and challenging research activity. During these years I had the chance of learning from the passion, dedication and seriousness you put at stake in your research. I am grateful for your guidance, especially during the experiments and the thesis writing.

I would like to offer my thanks to my supervisor at the Institut Laue Langevin, Henry Fischer. Through your experienced guidance in the world of neutron science and the work we made together, I have particularly enjoyed my time at the ILL. You gave me freedom, responsibility and trust for planning and developing our projects. Thanks for helping me to identify my drawbacks, attitudes and strengths.

I would like to offer special thanks to Anita Zeidler. Without your expertise and passion, part of this project could have not been realised. Your help, guidance and friendship were absolutely fundamental for me.

I am pleased to express my gratitude to Burkhard Annighöfer. Thanks for all the work you have thrown yourself into during our collaboration. Your positive and effective attitude towards finding solutions has often encouraged me. Learning with you has helped me to enjoy more our work.

I would like to extend my thanks to Stefan Klotz, for his guidance during the high-pressure experiments and the useful discussions we had.

Many thanks also to:
H. Bone, P. Reddish, S. Dodd and P. Sykes from the University of Bath; A. Hannon and C. Bull from ISIS; M.C. Bellissent-Funel, L. Hennet and J. Darpentigny from the LLB; Claude Payre, James Maurice and Eddy Lelievre-Berna from the SANE service of the ILL, for your kind help during the high-pressure experiments, and to Alain Bertoni for your technical work on D4c. I feel grateful to the ILL directors, Helmut Shober and William Stirling, for taking a sincere interest in the work I have been doing.

I express all my gratitude to the University of Bath and the Institut Laue Langevin in Grenoble for funding this PhD project. The chance of living in the UK and in France has given the opportunity of a life-changing experience, a path of human and scientific growth.

I would like to acknowledge all the colleagues I met during these years, in particular Ruth Rowlands, Kiron Pizzey, Greg Moody and Michela Buscemi from the University of Bath, as well as Hasti, Rose and all the friends who always welcomed me during my visits in Bath. Thanks to the colleagues I met at the ILL, especially those with whom I have shared the office, for the care we had towards each other.

Con profonda gratitudine vorrei ringraziare tutti gli amici vicini e lontani che mi hanno fatto compagnia in questi anni. A coloro che mi hanno fatto sentire a casa in paesi stranieri, così come a coloro che mi ricordano che non c'è vera distanza quando si guarda la vita insieme: semplicemente grazie per esserci e per volermi bene.

Un grazie particolare alle persone con cui ho condiviso di più il cammino di questi ultimi tempi: a Lucia, per la tua quotidiana ed allo stesso tempo eccezionale compagnia a casa, a Caterina F. per la tua umanità viva e leale, a Daniela perchè ci sei sempre e comunque, a Caterina M. per la tua gioia contagiosa. A Gualtiero, Maria Rosa, Stefano e Lorenzo: grazie per la vostra accoglienza e per i passi fatti insieme in questi anni. A Paolo, grazie per la tua compagnia unica e libera che mi spinge sempre a guardare più in là, oltre la mia misura.

Alla mia famiglia, a mia mamma Donatella, mio papà Abramo e mio fratello Alessandro, porto di approdo sicuro in ogni circostanza della vita: grazie per il vostro amore incondizionato e la forza d'animo che mi infondete sempre. Questi anni e questo lavoro di tesi sono il frutto di tante gioie e fatiche condivise, e per questo li dedico a voi.

List of publications

Published articles:

- E. Guarini, U. Bafile, F. Barocchi, A. De Francesco, E. Farhi, F. Formisano, A. Laloni, A. Orecchini, A. Polidori, M. Puglini, and F. Sacchetti. Dynamics of liquid Au from neutron Brillouin scattering and ab initio simulations: Analogies in the behavior of metallic and insulating liquid. *Phys. Rev. B* **88** 104201, 2013
- A. Zeidler, K. Wezka, R. F. Rowlands, D. A. J. Whittaker, P. S. Salmon, A. Polidori, J. W. E. Drewitt, S. Klotz, H. E. Fischer, M. C. Wilding, C. L. Bull, M. G. Tucker and M. Wilson. High-Pressure Transformation of SiO_2 from a Tetrahedral to an Octahedral Network: A Joint Approach Using Neutron Diffraction and Molecular Dynamics. *Phys. Rev. Lett.*, **113** 135501, 2014

List of acronyms

AS	Aluminosilicates
AXD	Anomalous X-ray Diffraction
CCS	Carbon Capture and Storage
CFS	Cation Field Strength
CON	Chemically Ordered Network
EPSR	Empirical Potential Structural Refinement
ERO	Extended Range Order
EXAFS	Extended X-ray Absorption Fine Structure
FPMD	First Principle Molecular Dynamics
FSDP	First Sharp Diffraction Peak
ILL	Institut Laue Langevin
IP	Intermediate Phase
IRO	Intermediate Range Order
MAS-NMR	Magic Angle Spinning-Nuclear Magnetic Resonance
MD	Molecular Dynamics
NMR	Nuclear Magnetic Resonance
ND	Neutron Diffraction
NDIS	Neutron Diffraction with Isotopic Substitution
PE	Paris-Edinburgh
PP	Principal Peak
R	Rare Earth
RAS	Rare-Earth Aluminosilicates
RCN	Random Covalent Network
RMC	Reverse Monte Carlo
TMWD	Total Minus Weighted

Abstract

The method of neutron diffraction with isotopic or isomorphic substitution (NDIS) was employed to investigate the atomic-scale structure of several disordered multi-component materials, thus reducing the complexity of correlations associated with a single diffraction pattern.

The solvation of the Cl^- ion in a 5 molal solution of NaCl in D_2O was investigated at temperatures and pressures up to 150 °C and 33.8 kbar, respectively, thus extending the state conditions for studying the structure of this geological fluid. Changes to the structure with increasing temperature at 0.1 kbar may be attributed to a reduction in the dielectric permittivity, and the structural variation with increasing pressure at 150 °C reflects changes in the structure of water to a more simple-fluid like phase.

NDIS with Se-isotopes was used to help untangle the composition-dependent structure of As-Se glasses. The results for $As_{0.30}Se_{0.70}$ and $As_{0.35}Se_{0.65}$ favour the formation of a chemically ordered over a chemically disordered network, while the results for $As_{0.40}Se_{0.60}$ reveal broken chemical order through the appearance of homopolar bonds. The work shows a need to improve previous structural models that were produced by using both the reverse Monte Carlo and first-principles molecular-dynamics methods.

Rare-earth clustering in the aluminosilicate glass $(R_2O_3)_{0.2}(Al_2O_3)_{0.2}(SiO_2)_{0.6}$ was investigated via NDIS, using Nd and Pr as an isomorphic pair. The results indicate a network structure based on SiO_4 tetrahedra along with AlO_4 and AlO_5 units in the approximate ratio of 4:1. Each rare-earth (R) ion has, on average, 7.3(2) nearest-neighbour oxygen atoms at a distance of $\bar{r}_{\mathrm{RO}} = 2.43(2)$ Å, and the R-R nearest neighbour distance is 3.9(4) Å. The results are discussed by reference to the structure of a rare-earth glass of the same composition, but where Nd/Pr is replaced by a smaller rare-earth ion pair such as Dy or Ho.

1. Introduction

Disordered materials such as liquids and glasses are ubiquitous in nature and in our daily lives, where examples range from geologically relevant systems to optical fibres and phase-change memory alloys [1–4]. These materials have in common a disordered atomic structure which lacks the long-range order typical of crystals, where a unit cell is repeated periodically to form a highly ordered lattice. However, decades of studies have shown that some kind of order does exist within disordered materials on short (≤ 5 Å), intermediate (up to ≈ 20 Å) and extended (> 20 Å) length scales [5–9].

A disordered material is often formed from local structural motifs, such as cation-centred pyramids or tetrahedra, that link to form a network structure. The topology of this network will depend on the chemical nature of the motifs, on their relative abundance, on the addition of modifying atoms, and on the pressure and temperature [10–13]. Because different network topologies give rise to different material properties, knowledge of this structure is a matter of great interest for both fundamental and applied research. In fact, the development of realistic microscopic models for these systems may lead to an ability to predict, control and fine-tune the related physical properties, following the principles of rational design [4, 10, 14].

In order to guide in the development of realistic microscopic models, detailed experimental information on the atomic-scale structure and dynamics is fundamental. However, unravelling the structural features of multi-component systems is quite challenging, because topological and chemical disorder lead to complexity. X-ray and neutron diffraction provide tools for helping to unravel this complexity, and provide information at the pair-correlation function level (two-body correlations).

Site-specific experimental probes include neutron diffraction with isotopic or isomorphic substitution (NDIS), Anomalous X-ray diffraction (AXD) and spectroscopic techniques such as extended X-ray absorption fine structure (EXAFS), X-ray absorption near edge structure (XANES) and nuclear magnetic resonance (NMR) [15–19]. A complete description of a disordered material often emerges through a combination of the results obtained by using several different methods. However, spectroscopic techniques often require some *a priori* structural information to interpret the data, while

AXD is best exploited to probe systems having atoms with an atomic number $Z > 30$ and requires an ability to accurately calculate the real and imaginary parts of the dispersion terms [20].

In the present work, NDIS has been employed to investigate the structure of three different disordered systems. Having a neutral charge, neutrons can easily penetrate a material and investigate its structure by interacting strongly with nuclei. Here, the scattering power is found to vary not only between elements, but also between isotopes of the same atomic species. When the difference in the scattering power of two isotopes offers a good contrast, ND with isotope substitution can be employed. By using this method, which was for the first time employed by Enderby and co-workers in the Sixties [15], diffraction patterns of isotopically labelled samples can be combined via simple mathematical relations to access the pair-correlation functions and related quantities, such as the coordination numbers and bond distances. An alternative way of obtaining a neutron-scattering-length contrast is by using the method of isomorphic substitution, where samples that have an identical structure are made by using different chemical species. The substituted chemical species have to be chosen such that they are chemically isomorphic, *i.e.* they have similar structural chemistry and ionic radii. ND with isotopic or isomorphic substitution therefore represents an extremely powerful tool for reducing the complexity of correlations associated with a single diffraction pattern for a multi-component system, and for obtaining site-specific experimental information on the structure of liquids and glasses. Signatures of intermediate and extended range order manifest themselves by peaks in the measured diffraction patterns. The appearance of a so-called first sharp diffraction peak at a scattering vector $Q_{\mathrm{FSDP}} \approx 1 - 1.5$ Å^{-1} is associated with intermediate range order (IRO), while the so-called principal peak at $Q_{\mathrm{PP}} \approx 2.0 - 2.7$ Å^{-1} is associated with extended range order (ERO). The underlying periodicities associated with these peaks are given by $2\pi/Q_{\mathrm{FSDP}}$ or $2\pi/Q_{\mathrm{PP}}$, with a correlation length of $2\pi/\Delta Q_{\mathrm{FSDP}}$ or $2\pi/\Delta Q_{\mathrm{PP}}$, that depends on the full-width at half-maximum of the FSDP or PP [9].

In this work, some examples are shown of how the experimental information on the structure of disordered systems can provide a severe test for the validity of Reverse Monte Carlo (RMC) modelled data and molecular-dynamics simulations. In fact, structure refinement methods such as RMC [21] and Empirical Potential Structure Refinement (EPSR) [22] are often used to provide models that are in agreement with the experimental information. This is achieved by constructing three-dimensional models in which atoms are moved until configurations are produced that are in agreement with measured diffraction patterns and other applied constraints such as the measured number density, distance of closest approach between the centres of two atoms, and characteristics of the local structural motifs. Once a model is constructed that is in agreement with experimental data, additional information related to three and four-body correlations, such as bond-angles and torsion-motions distributions, can be inferred. However, such information needs to be treated carefully, since the original experimental data are provided only at the two-body correlation level. MD simulations are also often employed to model the structural and dynamical properties of liquids and network glass-forming materials. Any MD method aims at solving, via iterative numerical schemes, the equations of motion that describe the physical evolution of a system. However, finding the right ingredients for describing an analytical potential that models correctly the interactions is not trivial. Also, there is often a trade-off between an accurate description of the chemical bonds and the number of atoms that can be dealt with on a realistic computational time scale [4].

Thesis outline

The content of the thesis is organised as follow:

- Chapter 2 - The essential theory of neutron scattering is presented and the Faber-Ziman formalism used for multi-component disordered materials is introduced. The methods of isotopic and isomorphic substitution are also explained, and the formalism of first-order difference functions is introduced.

- Chapter 3 - The D4c and GEM diffractometers used to perform the ND experiments are presented, and the procedures for correcting and analysing the data are explained.

- Chapter 4 - The structure of a 5 molal solution of NaCl in water is investigated via the Cl-isotope substitution method over a wide range of state conditions, spanning pressures between 100 bar and 33.8 kbar, and temperatures between 50 °C and 150 °C. The experiments were performed using a Ti-Zr pressure-cell at pressures up to 1 kbar and a Paris-Edinburgh press at higher pressures [23].

- Chapter 5 - The method of ND with Se-isotope substitution is used to investigate the structure of the chalcogenide glasses As_xSe_{1-x} with $x = 0.30$, $x = 0.35$ and $x = 0.40$. The results are compared to those obtained from recent RMC and first-principles MD simulations [24–26].

- Chapter 6 - The structure of the rare-earth aluminosilicate glass $(R_2O_3)_{0.2}(Al_2O_3)_{0.2}(SiO_2)_{0.6}$ was investigated via ND with isomorphic substitution using the large rare-earth elements Nd and Pr as an isomorphic pair. The results are compared to those obtained via the same experimental method for the structure of a rare-earth aluminosilicate glass having an identical composition, where the isomorphic pair were the small rare-earth elements Dy and Ho [27].

- Chapter 7 - Overall conclusions for the work presented in this thesis are drawn and a future perspective is given.

I declare that this thesis is my own work and has not been submitted in any form for another degree or diploma at any university or other institute of tertiary education. Information derived from the published or unpublished work of others has been acknowledged in the text and a list of references is given.

2. Theory

2.1 Neutron diffraction

In 1932, James Chadwick discovered the neutron, one of the fundamental building blocks for the atomic nucleus [28]. Within the next ten years, Fermi found that slow neutrons are more easily captured by nuclei than fast ones (1934) [29], nuclear fission was discovered (1938) [30], and the first nuclear reactor was built (1942) [31]. In the nineteen fifties, Shull and Brockhouse began the development of neutron scattering techniques: neutron diffraction and inelastic scattering are now established techniques that play a major role in the investigation of condensed matter.

Having a neutral charge, neutrons can easily penetrate a material and probe its structure by interacting strongly with nuclei. Neutrons have a non-zero magnetic moment that leads to magnetic scattering through interactions with the magnetic dipole moment of the atomic electrons. The energy E, mass m_n and wavelength λ of a neutron are related via

$$E = \frac{h^2}{2m_n\lambda^2} = \frac{\hbar^2 k^2}{2m_n} \tag{2.1}$$

where $h = 6.626 \cdot 10^{34}$ J s is Planck's constant and $\hbar = \frac{h}{2\pi}$, $m_n = 1.67 \cdot 10^{-27}$ kg. The neutron wavevector can be expressed in terms of the associated wavelength as:

$$k = \frac{2\pi}{\lambda}, \tag{2.2}$$

such that

$$p = \hbar k \tag{2.3}$$

is the neutron momentum. If the neutron energy is in units of meV and the wavelength is in units of Å, then

$$\lambda(\text{Å}) = 9.04[E(\text{meV})]^{-1/2} \tag{2.4}$$

and it is straight-forward to calculate that neutrons with energies of the order of ten to a hundred meV have wavelengths on an interatomic scale. A scattering event between an incident unpolarised neutron and a nucleus in a non-magnetised sample can occur only via the strong force. Such interactions can be modelled as point-like in the form of the Fermi pseudo-potential [29, 32]

$$V(\mathbf{r}) = \frac{2\pi\hbar^2}{m_n} b\delta(\mathbf{r}), \tag{2.5}$$

where $\mathbf{r}$ is the position of the neutron relative to the nucleus, and b is the bound scattering length, which is a measure of the scattering power of each nucleus and is in general spin-dependent [33]. In a diffraction experiment, neutrons with an incident flux Φ are either transmitted or scattered once they reach the sample. Neutrons having an initial wavevector $\mathbf{k}_i$ and energy E_i are scattered to give a final wavevector $\mathbf{k}_f$ and final energy E_f in a direction $(2\theta,\phi)$, as shown in Figure 2-1, where the geometry of a neutron-scattering event is illustrated.

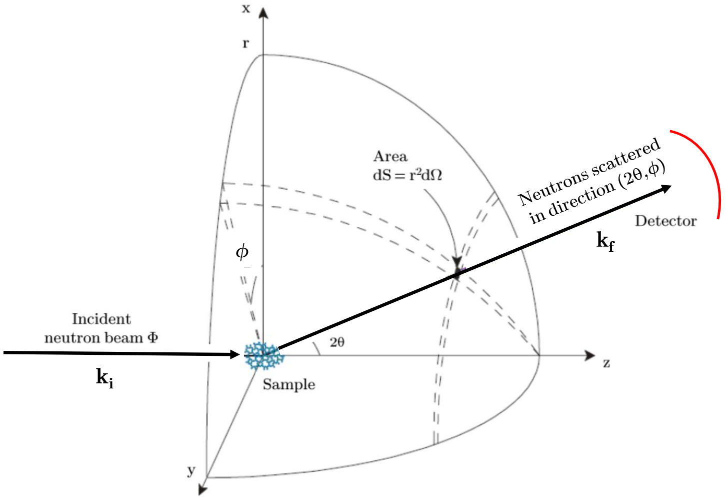

Figure 2-1: Schematic for a neutron-scattering experiment. A neutron in the incident beam of flux Φ, having initial wavevector $\mathbf{k}_i$, is scattered to give a final wavevector $\mathbf{k}_f$ in the direction $(2\theta,\phi)$ [34].

The scattering wavevector, or momentum transfer, is defined as

$$\mathbf{Q} = \mathbf{k}_i - \mathbf{k}_f \tag{2.6}$$

and, according to the scattering triangle illustrated in Figure 2-2, its modulus can be expressed as

$$Q^2 = {k_i}^2 + {k_f}^2 - 2k_ik_f\cos(2\theta). \tag{2.7}$$

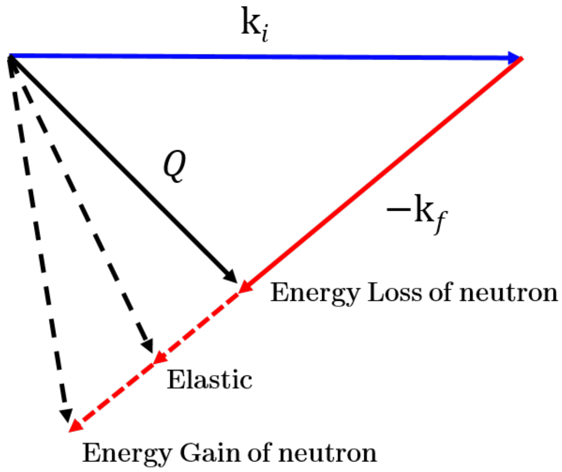

Figure 2-2: The scattering triangle that defines the momentum transfer.

The energy that a neutron loses to the sample during a scattering event is defined as

$$\Delta E = E_i - E_f = \hbar\omega. \tag{2.8}$$

If $\Delta E \neq 0$, the scattering event is inelastic and $k_i \neq k_f$. When the scattering event is elastic, *i.e.* $\Delta E = 0$ and $k_i = k_f$, or in the "static approximation", when $k_i \approx k_f$, Eq. (2.7) can be re-written, using Eq. (2.2), in the form

$$Q = \frac{4\pi}{\lambda}\sin\theta. \tag{2.9}$$

The static approximation requires that the incident neutron energy is much larger than the energy exchanged with the sample, $E_i >> \hbar\omega$, such that the change in the magnitude of the momentum of a neutron following a scattering event is negligible. If the system has a maximum thermal energy $\hbar\omega_{\max}$, then the minimum characteristic time for the atomic motion is $\tau_{\min} \sim {\omega_{\max}}^{-1}$, which corresponds to the period of the atomic vibrations in a solid or to the atomic-scale relaxation time in a liquid. Therefore, in terms of timescales, the static approximation is satisfied when $\tau_{\text{snapshot}} << \tau_{\min}$, where $\tau_{\text{snapshot}} \sim {\omega_{\min}}^{-1}$ is the characteristic time for a neutron to travel one interatomic distance ($\approx \lambda_i$ for a diffraction experiment). This condition implies that the structure of the sample is relatively static when the neutron probes it, and hence that a scattering event results in a "snapshot" of the system. Atomic motions typically occur with $\tau_{\min} \approx 10^{-13} - 10^{-12}$ s, while for neutrons having an incident energy in the range of tens or a few hundred of meV, $10^{-15} \leqslant \tau_{\text{snapshot}} \leqslant 10^{-13}$ s. Hence, the static approximation is not completely valid in neutron diffraction and dynamical effects have to be considered.

The differential scattering cross section, which is the quantity measured in a neutron-diffraction experiment, can be defined as [20]

$$\frac{\mathrm{d}\sigma}{\mathrm{d}\Omega} = \frac{\text{number of neutrons scattered into solid angle } \mathrm{d}\Omega \text{ per second}}{\Phi \mathrm{d}\Omega}. \tag{2.10}$$

By taking into account that in a real sample each scattering centre has a certain position and scattering length, Eq.(2.10) can be expressed as

$$\frac{d\sigma}{d\Omega}(\mathbf{Q}) = \overline{\left\langle \left| \sum_{i=1}^{N} b_i e^{i\mathbf{Q}\cdot\mathbf{r}_i} \right|^2 \right\rangle} = \left\langle \sum_{i,j}^{N} \overline{b_i b_j^*} e^{i\mathbf{Q}\cdot\mathbf{r}_{ij}} \right\rangle, \tag{2.11}$$

where the vector $\mathbf{r}_{ij} = \mathbf{r}_i - \mathbf{r}_j$ denotes the relative position of the scattering centres i and j. The asterisk in b_j^* represents a complex conjugate, as b_i can have both a real and an imaginary part. The latter is associated to absorption events and has to be taken into account if the incident neutron energy is close to an absorption resonance of an isotope. The triangular brackets in Eq.(2.11) denote a thermal average of the atomic positions that, during the time of an experiment, undergo thermal displacement. Let's assume that there is no correlation between (1) nuclear spin-state and site, (2) nuclear spin themselves, (3) isotopic mass and site. Under these assumptions, the horizontal bars in Eq.(2.11) represent an average over an ensemble of samples having the same structure and isotopic composition, where the scattering lengths for each member of the ensemble are randomly and differently distributed [20]. In this case, the term $\overline{b_i b_j^*}$ can be rewritten as [32]

$$\overline{b_i b_j^*} = \overline{b^2} \quad \text{if} \quad \mathrm{i} = \mathrm{j} \tag{2.12}$$

$$\overline{b_i b_j^*} = \bar{b}^2 \quad \text{if} \quad \mathrm{i} \neq \mathrm{j} \tag{2.13}$$

and Eq.(2.11) can be expressed as

$$\frac{d\sigma}{d\Omega}(\mathbf{Q}) = N\overline{b^2} + \bar{b}^2 \left\langle \sum_{i,j\neq i}^{N} e^{i\mathbf{Q}\cdot\mathbf{r}_{ij}} \right\rangle \tag{2.14}$$

$$= \left[\frac{d\sigma}{d\Omega}(\mathbf{Q})\right]^{\text{self}} + \left[\frac{d\sigma}{d\Omega}(\mathbf{Q})\right]^{\text{distinct}} \tag{2.15}$$

where the self term describes the scattering coming from the same site ($i = j$), while the distinct term is associated with scattering from different sites ($i \neq j$).
By adding and subtracting $\bar{b}^2$ between the terms in Eq. (2.14), it follows that

$$\begin{aligned}\frac{d\sigma}{d\Omega}(\mathbf{Q}) &= N(\overline{b^2} - \bar{b}^2) + \bar{b}^2 \left\langle \sum_{i,j}^{N} e^{i\mathbf{Q}\cdot\mathbf{r}_{ij}} \right\rangle \\ &= N b_{\text{inc}}^2 + b_{\text{coh}}^2 \left\langle \sum_{i,j}^{N} e^{i\mathbf{Q}\cdot\mathbf{r}_{ij}} \right\rangle \\ &= \left[\frac{d\sigma}{d\Omega}(\mathbf{Q})\right]^{\text{inc}} + \left[\frac{d\sigma}{d\Omega}(\mathbf{Q})\right]^{\text{coh}} . \end{aligned} \tag{2.16}$$

The incoherent scattering term of Eq.(2.16) describes the variation of the scattering lengths about their mean value and contains no structural information. The associated scattering length is called incoherent and it is defined by $b_{\text{inc}}^2 \equiv \overline{b^2} - \bar{b}^2$. The coherent scattering term in Eq.(2.16) contains instead information about the relative positions of the scattering centres, and the coherent scattering length is defined by $b_{\text{coh}} \equiv \bar{b}$. For a polyatomic system having N_S atoms of n different chemical species α, it is convenient to generalise Eq. (2.15) and expressed the differential scattering cross section per atom as:

$$\frac{1}{N_S}\left[\frac{\mathrm{d}\sigma}{\mathrm{d}\Omega}(Q)\right] = \frac{1}{N_S}\left[\frac{\mathrm{d}\sigma}{\mathrm{d}\Omega}(Q)\right]^{\text{self}} + \frac{1}{N_S}\left[\frac{\mathrm{d}\sigma}{\mathrm{d}\Omega}(Q)\right]^{\text{distinct}} , \tag{2.17}$$

where

$$\frac{1}{N_S}\left[\frac{\mathrm{d}\sigma}{\mathrm{d}\Omega}(Q)\right]^{\text{self}} = \sum_{\alpha}^{n} c_\alpha (b_{\text{coh},\alpha}^2 + b_{\text{inc},\alpha}^2)[1 + P_\alpha(Q)]. \tag{2.18}$$

and

$$\frac{1}{N_S}\left[\frac{\mathrm{d}\sigma}{\mathrm{d}\Omega}(Q)\right]^{\text{distinct}} = F(Q) + P_{\text{distinct}}(Q), \tag{2.19}$$

The self term describes the isotropic diffraction from individual atomic sites α, where $P_\alpha(Q)$ is the associated inelastic scattering term for chemical species α. The total structure factor $F(Q)$ is built from the diffraction pattern collected from pairs of different atomic sites and contains the desired structural information. $P_{\text{distinct}}(Q)$ is an inelastic-scattering term associated with distinct scattering. The inelasticity terms results from the breakdown of the static approximation due to the recoil of nuclei in their interaction with incident neutrons, and are therefore more severe in the presence of light nuclei such as hydrogen and deuterium.

2.1.1 Nuclear and Magnetic Differential Scattering Cross Section

The neutron has a finite magnetic dipole moment, $\gamma_n = -1.913\ \mu_N$, where $\mu_N = 5.051 \cdot 10^{-27}$ J T^{-1} is the nuclear magneton. Hence, if a material has a magnetic dipole moment, a magnetic interaction can occur between neutrons and atoms of the material, during a scattering event. In this case, the total differential scattering cross section, containing contributions from both nuclear and magnetic interactions, can be defined as

$$\left[\frac{\mathrm{d}\sigma}{\mathrm{d}\Omega}(Q)\right]_{\text{total}} = \left[\frac{\mathrm{d}\sigma}{\mathrm{d}\Omega}(Q)\right]_{\text{nuclear}} + \left[\frac{\mathrm{d}\sigma}{\mathrm{d}\Omega}(Q)\right]_{\text{magnetic}}. \tag{2.20}$$

In a diffraction experiment, the desired structural information is contained only in the nuclear component of Eq. (2.20), and corrections to subtract the magnetic component are therefore required. For paramagnetic ions, the magnetic scattering can be quantified using the free-ion approximation [35, 36] such that

$$\left[\frac{\mathrm{d}\sigma}{\mathrm{d}\Omega}(Q)\right]_{\text{magnetic}} = c_{\mathrm{p}}(\gamma_n r_e)^2 \frac{1}{6} J(J+1) g_J^2 \mathscr{F}^2(Q), \tag{2.21}$$

where c_{p} is the atomic fraction of the paramagnetic ion in the sample, J is the total angular-momentum quantum number, g_J is the Landé splitting factor [37], r_e is the classical radius of an electron and $(\gamma_n r_e)^2 = 0.2906$ barn. The magnetic form factor $\mathscr{F}(Q)$ is given by

$$\begin{aligned}\mathscr{F}^2(Q) \;=\;& \langle j_0(Q)\rangle^2 + C_{02}\langle j_0(Q)\rangle\langle j_2(Q)\rangle + C_{22}\langle j_2(Q)\rangle^2 + C_{24}\langle j_2(Q)\rangle\langle j_4(Q)\rangle \\ &+ C_{44}\langle j_4(Q)\rangle^2 + C_{46}\langle j_4(Q)\rangle\langle j_6(Q)\rangle + C_{66}\langle j_6(Q)\rangle^2,\end{aligned} \tag{2.22}$$

where the radial integrals $\langle j_i(Q)\rangle$ ($i = 0, 2, 4$ and 6) are given by [38] and the coefficients C_{ij} ($i = 0, 2, 4$ or 6 and $j = 2, 4$ or 6) are given by [35].

2.2 Faber-Ziman formalism

According to the Faber-Ziman formalism [39], the total structure factor for a multi-component system having n different chemical species can be expressed in terms of $n(n+1)/2$ partial structure factors $S_{\alpha\beta}(Q)$ such that

$$F(Q) = \sum_{\alpha,\beta}^{n} c_\alpha c_\beta b_\alpha b_\beta [S_{\alpha\beta}(Q) - 1], \tag{2.23}$$

where c_α and c_β are the atomic fractions, b_α and b_β the coherent scattering lengths for chemical species α and β, respectively. The total pair-distribution function $G(r)$ is the Fourier transform of $F(Q)$ and contains the desired real-space information

$$G(r) = \frac{1}{2\pi^2 \rho r} \int\limits_0^\infty Q F(Q) \sin(Qr) dQ \tag{2.24}$$

$$= \sum_{\alpha,\beta}^{n} c_\alpha c_\beta b_\alpha b_\beta \left[g_{\alpha\beta}(r) - 1 \right], \tag{2.25}$$

where ρ is the atomic number density of the sample. The partial pair-distribution function $g_{\alpha\beta}(r)$ in Eq. (2.25) provides a measure of the probability of finding an atom of chemical species β at a radial distance r from a central atom of chemical species α. The coordination number $\bar{n}_\alpha^\beta$ is obtained from the expression

$$\bar{n}_\alpha^\beta = 4\pi \rho c_\beta \int_{r_1}^{r_2} g_{\alpha\beta}(r) r^2 dr, \tag{2.26}$$

and represents the average number of atoms of chemical species β contained within a spherical shell of radii r_1 and r_2 centred on an atom of chemical species α. If the peak in $g_{\alpha\beta}(r)$ is not symmetrical, it can be helpful to define a weighted peak position by

$$\bar{r}_{\alpha\beta} = \frac{\int\limits_{r_1}^{r_2} r g_{\alpha\beta}(r) dr}{\int\limits_{r_1}^{r_2} g_{\alpha\beta}(r) dr}. \tag{2.27}$$

Below the distance of closest approach between two atoms, $G(r)$ is given by the low-r limit

$$G(r \to 0) = G(0) = -\sum_{\alpha,\beta}^{n} c_\alpha c_\beta b_\alpha b_\beta \tag{2.28}$$

and the sum rule [15]

$$\int_0^\infty F(Q)Q^2 dQ = 2\pi^2 \rho G(0) \tag{2.29}$$

can be derived from Eq. (2.24) by taking the limit as $r \to 0$.

The partial structure factors and partial pair-distribution functions are related via the Fourier transform pair:

$$S_{\alpha\beta}(Q) - 1 = \frac{4\pi\rho}{Q} \int_0^\infty r[g_{\alpha\beta}(r) - 1]\sin(Qr)dr \tag{2.30}$$

$$g_{\alpha\beta}(r) - 1 = \frac{1}{2\pi^2 r\rho} \int_0^\infty Q[S_{\alpha\beta}(Q) - 1]\sin(Qr)dQ. \tag{2.31}$$

In general, a total pair-distribution function will contain multiple overlapping peaks corresponding to different partial pair-distribution functions. These peaks can be fitted, in order to find parameters such as the coordination number and peak position, by taking into account the finite Q-range that can be accessed by a diffractometer. The density correlation function can be defined as

$$D_{\text{exp}}(r) = \frac{2}{\pi} \int_0^\infty Q \frac{F(Q)}{\left|G(0)\right|} \sin(Qr) M(Q)\, \mathrm{d}Q, \tag{2.32}$$

where the normalisation by $\left|G(0)\right|$ ensures that the weighting factors for the $g_{\alpha\beta}(r)$ functions sum to unity, and the modification function $M(Q)$, defined by the step-function

$$M(Q) = \begin{cases} 1 & \text{if } Q \leq Q_{\text{max}} \\ 0 & \text{if } Q > Q_{\text{max}}, \end{cases} \tag{2.33}$$

takes into account the maximum Q-value, Q_{max}, that can be accessed by a diffractometer. In some cases, a Lorch modification function [40] can be used instead of a step function, in order to reduce Fourier transform artefacts that affect the real space function:

$$L(Q) = \begin{cases} \frac{\sin(\frac{\pi Q}{Q_{\text{max}}})}{(\frac{\pi Q}{Q_{\text{max}}})} & \text{if } Q \leq Q_{\text{max}} \\ 0 & \text{if } Q > Q_{\text{max}}. \end{cases} \tag{2.34}$$

Equation (2.32) can be rewritten as [41]

$$\begin{aligned} D_{\mathrm{exp}}(r) &= 4\pi\rho r \frac{G(r)}{\left|G(0)\right|} \otimes P(r) \\ &= 4\pi\rho \sum_{\alpha=1}^{n} \sum_{\beta=1}^{n} \frac{c_\alpha c_\beta b_\alpha b_\beta}{\left|G(0)\right|} r g_{\alpha\beta}(r) \otimes P(r) - 4\pi\rho r, \end{aligned} \tag{2.35}$$

where the symbol $\otimes$ denotes the 1-D convolution operator and $P(r)$ is the Fourier transform of the modification function $M(Q)$, which in the case of the step function (Eq. (2.33)) is given by

$$\begin{aligned} P(r) &= \frac{1}{\pi} \int_0^{Q_{\mathrm{max}}} \cos(Qr)\,\mathrm{d}Q \\ &= \frac{Q_{\mathrm{max}}}{\pi} \mathrm{sinc}(Q_{\mathrm{max}} r). \end{aligned} \tag{2.36}$$

A real-space peak in $r g_{\alpha\beta}(r)$, labelled by i, can be represented by a Gaussian function centred at $r_{\alpha\beta}(i)$, of width $\sigma_{\alpha\beta}(i)$ and area that gives a coordination number $\overline{n}_\alpha^\beta(i)$. Then, the function

$$\begin{aligned} D_{\mathrm{fit}}\left(r; r_{\alpha\beta}, \overline{n}_\alpha^\beta, \sigma_{\alpha\beta}\right) = \sum_i \Bigg(& w_{\alpha\beta}(i) \frac{\overline{n}_\alpha^\beta(i)}{c_\beta(i) r_{\alpha\beta}(i)} \frac{1}{\sqrt{2\pi}\sigma_{\alpha\beta}(i)} \times \\ & \exp\left\{ \frac{-\left[r - r_{\alpha\beta}(i)\right]^2}{2\left[\sigma_{\alpha\beta}(i)\right]^2} \right\} \otimes P(r) \Bigg) - 4\pi\rho r, \end{aligned} \tag{2.37}$$

where $w_{\alpha\beta} = 2c_\alpha c_\beta b_\alpha b_\beta / \left|G(0)\right|$ for $\alpha \neq \beta$ and $w_{\alpha\beta} = c_\alpha^2 b_\alpha^2 / \left|G(0)\right|$ for $\alpha = \beta$, can be fitted to $D_{\mathrm{exp}}(r)$ by minimising the goodness of the parameter fit R_χ, defined as [42]

$$R_\chi\left(r_{\alpha\beta}, \overline{n}_\alpha^\beta, \sigma_{\alpha\beta}\right) = \sqrt{\frac{\sum_i \left[D_{\mathrm{exp}}(r_i) - D_{\mathrm{fit}}(r_i)\right]^2}{\sum_i D_{\mathrm{exp}}^2(r_i)}}. \tag{2.38}$$

Hence, the peak positions and coordination numbers can be obtained for each set of pair-correlation functions.

2.3 Neutron Diffraction with Isotopic or Isomorphic Substitution

The neutron scattering length b is a measure of the scattering power of each nucleus. This quantity is found to vary not only between elements, but also between isotopes of the same atomic species. Fig. 2-3 shows how the coherent component of the neutron scattering length b varies with the atomic weight. An exploitation of this variation of the coherent neutron scattering length for a given chemical species enables the application of the neutron diffraction with isotope substitution (NDIS) method, where diffraction patterns are measured for samples that are identical in every respect except for the isotopic composition of one or more of their elements. An alternative way of obtaining a neutron-scattering-length contrast is by using the isomorphic substitution method, where samples having an identical structure are made by using different chemical species. The substituted chemical species have to be chosen such that they are chemically isomorphic, for instance by having the same number of valence electrons and a similar size.

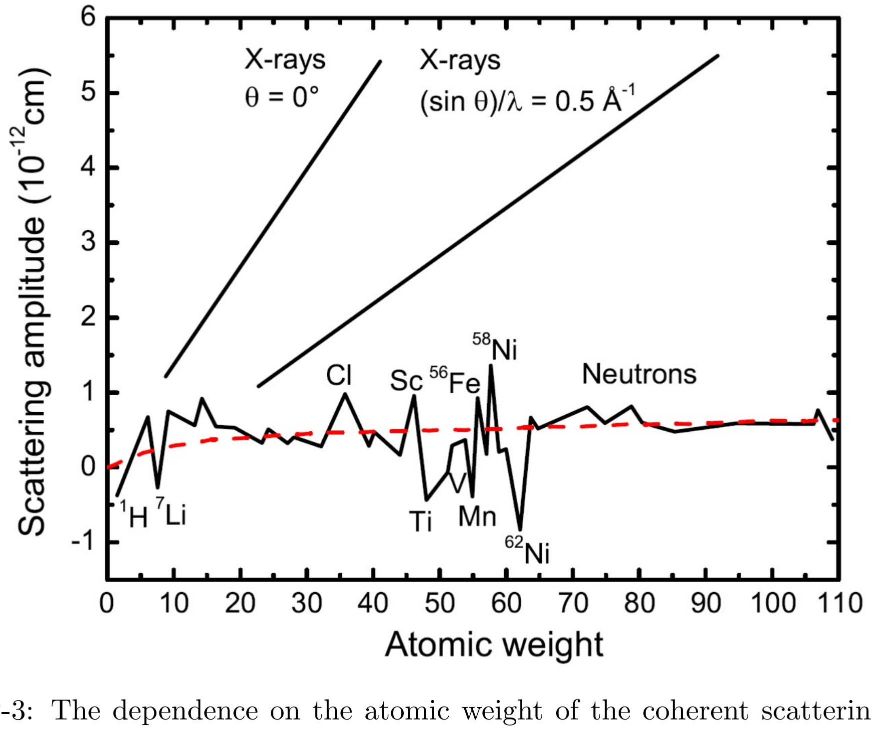

Figure 2-3: The dependence on the atomic weight of the coherent scattering lengths for neutrons and X-rays (reproduced from references [43, 44]). The X-ray scattering amplitude depends on $Q \propto \sin(\theta)/\lambda$, and scales with the atomic number. Neutrons do not show such a dependence and the scattering amplitude varies in an irregular manner. The red dashed line indicates the potential scattering for neutrons.

2.4 Difference functions

The structure of a sample containing n different chemical species is described by $m = (n+1)n/2$ different partial structure factors. Let's consider the simple case of a binary system ($n = 2$) for which $m = 3$ total structure factors $F_1(Q)$, $F_2(Q)$ and $F_3(Q)$ are measured. In matrix notation

$$\begin{pmatrix} F_1(Q) \\ F_2(Q) \\ F_3(Q) \end{pmatrix} = \begin{pmatrix} c_\alpha^2 b_{\alpha,1}^2 & c_\beta^2 b_{\beta,1}^2 & 2c_\alpha c_\beta b_{\alpha,1} b_{\beta,1} \\ c_\alpha^2 b_{\alpha,2}^2 & c_\beta^2 b_{\beta,2}^2 & 2c_\alpha c_\beta b_{\alpha,2} b_{\beta,2} \\ c_\alpha^2 b_{\alpha,3}^2 & c_\beta^2 b_{\beta,3}^2 & 2c_\alpha c_\beta b_{\alpha,3} b_{\beta,3} \end{pmatrix} \cdot \begin{pmatrix} S_{\alpha\alpha}(Q) - 1 \\ S_{\beta\beta}(Q) - 1 \\ S_{\alpha\beta}(Q) - 1 \end{pmatrix}, \tag{2.39}$$

which, by introducing the column vectors $\mathbf{F}(Q)$ and $\mathbf{S}(Q)$, and the scattering matrix $\mathbf{A}$, can be re-written as

$$\mathbf{F}(Q) = \mathbf{A} \cdot \mathbf{S}(Q). \tag{2.40}$$

The full set of partial structure factors can then be obtained from the equation

$$\mathbf{S}(Q) = \mathbf{A}^{-1} \cdot \mathbf{F}(Q), \tag{2.41}$$

where $\mathbf{A}^{-1}$ is the inverse of $\mathbf{A}$.

In many cases, and especially for multicomponent systems with $n > 2$ chemical species, it is not feasible to measure the full set of partial structure factors. Site-specific information can be accessed, however, by forming difference functions, where the complexity of pair-correlation functions associated with a single $F(Q)$ is reduced by eliminating, in turn, different partial structure factors. For instance, let's consider a two-component system where

$$\begin{aligned} F_1(Q) = {} & c_\alpha^2 b_\alpha^2 \left[S_{\alpha\alpha}(Q) - 1\right] + c_\beta^2 b_{\beta,1}^2 \left[S_{\beta\beta}(Q) - 1\right] + \\ & 2c_\alpha b_\alpha c_\beta b_{\beta,1} \left[S_{\alpha\beta}(Q) - 1\right] \end{aligned} \tag{2.42}$$

and

$$\begin{aligned} F_2(Q) = {} & c_\alpha^2 b_\alpha^2 \left[S_{\alpha\alpha}(Q) - 1\right] + c_\beta^2 b_{\beta,2}^2 \left[S_{\beta\beta}(Q) - 1\right] + \\ & 2c_\alpha b_\alpha c_\beta b_{\beta,2} \left[S_{\alpha\beta}(Q) - 1\right] \end{aligned} \tag{2.43}$$

are the total structure factors measured for two samples that are identical in every respect except for the isotopic composition of chemical specie β. Then, the difference function

$$\begin{aligned}\Delta F_\beta(Q) &= F_2(Q) - F_1(Q) \\ &= c_\beta^2 \left(b_{\beta,2}^2 - b_{\beta,1}^2\right) \left[S_{\beta\beta}(Q) - 1\right] + 2c_\alpha c_\beta b_\alpha \left(b_{\beta,2} - b_{\beta,1}\right) \left[S_{\alpha\beta}(Q) - 1\right] \end{aligned} \tag{2.44}$$

removes $S_{\alpha\alpha}(Q)$, whereas the weighted difference function

$$\begin{aligned}\Delta F_\alpha(Q) &= F_1(Q) - \frac{b_{\beta,1}^2}{b_{\beta,2}^2} F_2(Q) \\ &= c_\alpha^2 b_\alpha^2 \left(1 - \frac{b_{\beta,1}^2}{b_{\beta,2}^2}\right) \left[S_{\alpha\alpha}(Q) - 1\right] + 2c_\alpha c_\beta b_\alpha \left(b_{\beta,1} - \frac{b_{\beta,1}^2}{b_{\beta,2}}\right) \left[S_{\alpha\beta}(Q) - 1\right] \end{aligned} \tag{2.45}$$

removes $S_{\beta\beta}(Q)$. Similarly, the weighted difference function

$$\begin{aligned}\Delta F_X(Q) &= \frac{b_{\beta,1}}{b_{\beta,2}} F_2(Q) - F_1(Q) \\ &= c_\alpha^2 b_\alpha^2 \left(\frac{b_{\beta,1}}{b_{\beta,2}} - 1\right) \left[S_{\alpha\alpha}(Q) - 1\right] + c_\beta^2 \left(b_{\beta,2} b_{\beta,1} - b_{\beta 1}^2\right) \left[S_{\beta\beta}(Q) - 1\right] \end{aligned} \tag{2.46}$$

removes $S_{\alpha\beta}(Q)$. The Fourier transform of a difference function provides the corresponding real-space information, *e.g.*

$$\begin{aligned}\Delta G_X(r) &= \frac{1}{2\pi^2 r\rho} \int\limits_0^\infty \Delta F_X(Q) \sin(Qr) Q dQ \\ &= \frac{b_{\beta,1}}{b_{\beta,2}} G_2(r) - G_1(r) \\ &= c_\alpha^2 b_\alpha^2 \left(\frac{b_{\beta,1}}{b_{\beta,2}} - 1\right) g_{\alpha\alpha}(r) + c_\beta^2 \left(b_{\beta,2} b_{\beta,1} - b_{\beta,1}^2\right) g_{\beta\beta}(r) + \Delta G_X(0), \end{aligned} \tag{2.47}$$

where the low-r limit is given by

$$\Delta G_X(0) = \frac{b_{\beta,1}}{b_{\beta,2}} G_2(0) - G_1(0) \quad = -c_\alpha^2 b_\alpha^2 \left(\frac{b_{\beta,1}}{b_{\beta,2}} - 1\right) - c_\beta^2 \left(b_{\beta,2} b_{\beta,1} - b_{\beta,1}^2\right). \tag{2.48}$$

3. Instrumentation and data analysis

Neutron diffraction can be performed using both continuous neutron sources, as at the nuclear reactor of the Institut Laue Langevin (ILL) in Grenoble (France), and pulsed neutron sources, as at ISIS (Rutherford Appleton Laboratory, Didcot, UK). In the present chapter, a description is given of the neutron sources and of the instrumentation employed for this thesis work. Also, the method used for the data treatment is outlined.

3.1 The ILL reactor neutron source

At the research High Flux Reactor (HFR) of the ILL the fission of ^{235}U nuclei is exploited to produce a continuous neutron beam, via the nuclear reactions

$$ {}^{235}_{92}\mathrm{U} + {}^{1}n \rightarrow {}^{91}_{36}\mathrm{Kr}^{*} + {}^{145}_{56}\mathrm{Ba}^{*} + \mathrm{Energy} \tag{3.1} $$

$$ {}^{91}_{36}\mathrm{Kr}^{*} + {}^{145}_{56}\mathrm{Ba}^{*} \rightarrow {}^{90}_{36}\mathrm{Kr} + {}^{144}_{56}\mathrm{Ba} + 2n + \gamma, {}^{91}_{36}\mathrm{Kr}^{*} + {}^{145}_{56}\mathrm{Ba}^{*} \rightarrow {}^{90}_{36}\mathrm{Kr} + {}^{144}_{56}\mathrm{Ba} + 2n + \gamma, \tag{3.2} $$

where an asterisk labels an unstable nucleus. The emitted neutrons n are also used to self-sustain the chain reaction. As shown in Figure 3-1, the fuel element is placed in the reactor core, where it is surrounded by heavy water (D_2O) that acts as a moderator medium [45]. The highly energetic neutrons ($E \approx 1$ MeV) produced from the fission events are slowed down via inelastic collisions with the water molecules. The geometry is optimised such that the resultant neutron spectrum, described by a Maxwell-Boltzmann distribution, has a peak in intensity at an energy of 25 meV. The integrated flux of thermal neutrons (1.5×10^{15} neutrons cm^2) is maximum at a distance from the core centre of approximately 40 cm: here, cold or hot sources are placed, as well as the noses of beam tubes for the extraction of neutrons, as shown in Figure 3-1. Two D_2

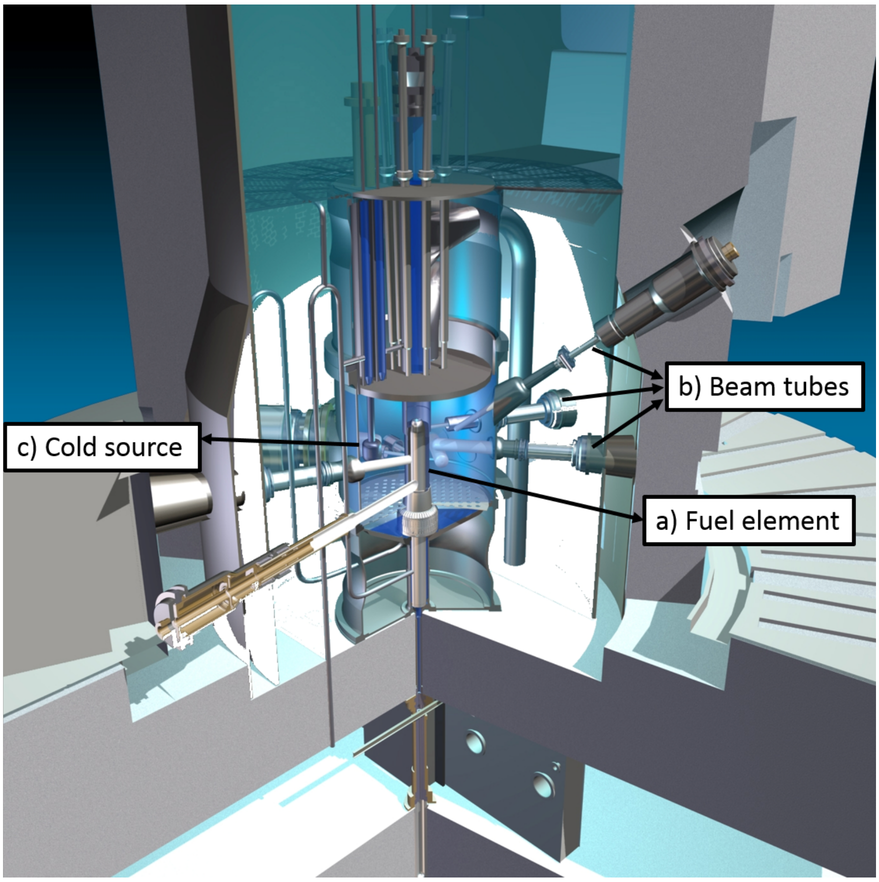

Figure 3-1: A 3D image of the reactor core at the ILL (Courtesy of the ILL), where some of the main components are shown. The fuel element (a) is surrounded by D_2O to moderate the highly energetic neutrons produced by nuclear fission. Some of the noses of the beam tubes (b) are pointing towards the region of maximum flux, in order to extract and convey neutrons to the instruments. One of the cold sources is also visible (c).

cold sources at 25 K are used to provide slow neutrons with low energies and therefore higher wavelengths. Also, a block of graphite, that is heated to 2400 K via γ-radiation emitted from the core, allows for the production of high-energy neutrons, called hot neutrons, to provide a spectrum of more energetic neutrons with shorter wavelengths.

3.1.1 The D4c diffractometer

The two-axis diffractometer D4c at the ILL is one of the instruments that receives neutrons from the hot source [46]. The schematic layout in Figure 3-2 shows the typical path followed by a neutron beam in a two-axis neutron diffractometer. The neutrons extracted from the moderator are collimated and guided towards a monochromator, where a specific wavelength is selected via Bragg scattering. After impinging on the sample, neutrons are scattered and detected over a wide scattering angle 2θ range. The D4c layout is shown in Figure 3-3. The available monochromators allow for both vertical and horizontal focusing. Depending on their take-off angles, the monochromators can provide three possible wavelengths: $\lambda = 0.7$ Å via the Cu (220) reflection, $\lambda = 0.5$ Å via the Cu (220) reflection, and $\lambda = 0.35$ Å via the Cu (331) reflection. A Rh or Ir filter is used to suppress $\lambda/2$ contamination for incident wavelengths of $\lambda = 0.5$ Å or $\lambda = 0.7$ Å, respectively. A high-transmission monitor, located between the monochromator and the beam-slits at the entrance to the belljar, is used to measure the incident-beam intensity so that it can be normalised. The sample is mounted in an evacuated cylindrical belljar (outer diameter = 46 cm, height = 55 cm) that has a thin aluminium window facing the detectors. Vertical and horizontal slits allow the incident beam to be defined at the sample position, giving a maximum illuminated height of 5 cm in the vertical direction, and width of 2 cm in the horizontal direction. The instrument is equipped with nine 1D position-sensitive microstrip detectors pressurized with ^{3}He-gas to 15 bar for efficient detection of short-wavelength neutrons. Each detector has 64 cells and covers a scattering-angle range $2\theta = 8°$. There is a gap of $2\theta = 7°$ between the detectors, so that more than one detector position is required to collect a complete diffraction pattern. Usually, scans of 6 detector positions are used in order to reach the same counting statistics at different angles. The final 2θ range for a diffraction pattern is $1.5° \leq 2\theta \leq 140°$. The maximum available Q-range depends on the selected incident wavelength, so that $0.5\ \text{Å}^{-1} \leq Q \leq 33\ \text{Å}^{-1}$ for $\lambda = 0.35$ Å, $0.3\ \text{Å}^{-1} \leq Q \leq 23\ \text{Å}^{-1}$ for $\lambda = 0.5$ Å and $0.2\ \text{Å}^{-1} \leq Q \leq 17\ \text{Å}^{-1}$ for $\lambda = 0.7$ Å.

3.2 The ISIS spallation neutron source

A schematic of the ISIS spallation neutron source is shown in Fig. 3-4. Initially, H^- ions are produced and then accelerated in the LINAC. As they enter the synchrotron, the ions are stripped of their electrons by a tin foil, leaving bare protons that are accelerated to a high energy of ≈ 800 MeV. The proton beam is then fired at a Tantalum target, and the violent process of spallation occurs. The interaction between a proton and a target nucleus results in the emission of neutrons and the production of light nuclear fragments, so that each proton produces about 15 neutrons. Protons are fired into the target with a pulse repetition rate of 50 Hz, and hence the resulting neutron flux is also pulsed. Before their use in a scattering experiment, the neutrons are slowed down by a moderator in order to give a suitable wavelength distribution, as shown in Fig. 3-5. The data collection at ISIS is based upon the principle of time-of-flight neutron scattering. This technique consists of measuring the time of flight t taken for a neutron to travel a total flight path L from the moderator to the detector, via the sample, as

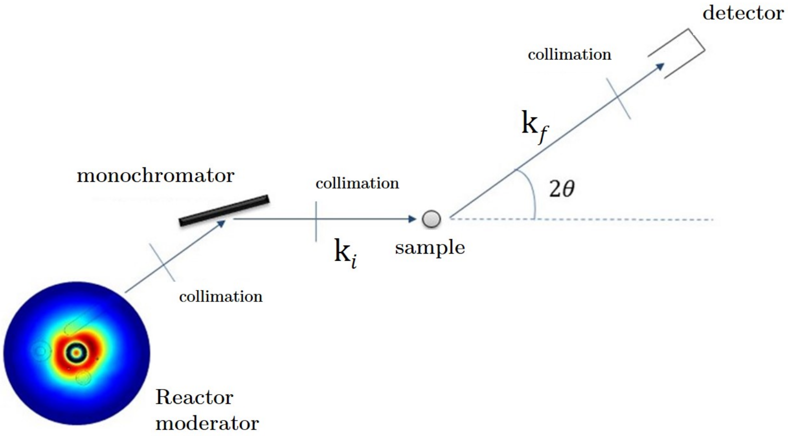

Figure 3-2: Schematic of a typical diffraction experiment at a continuous neutron source.

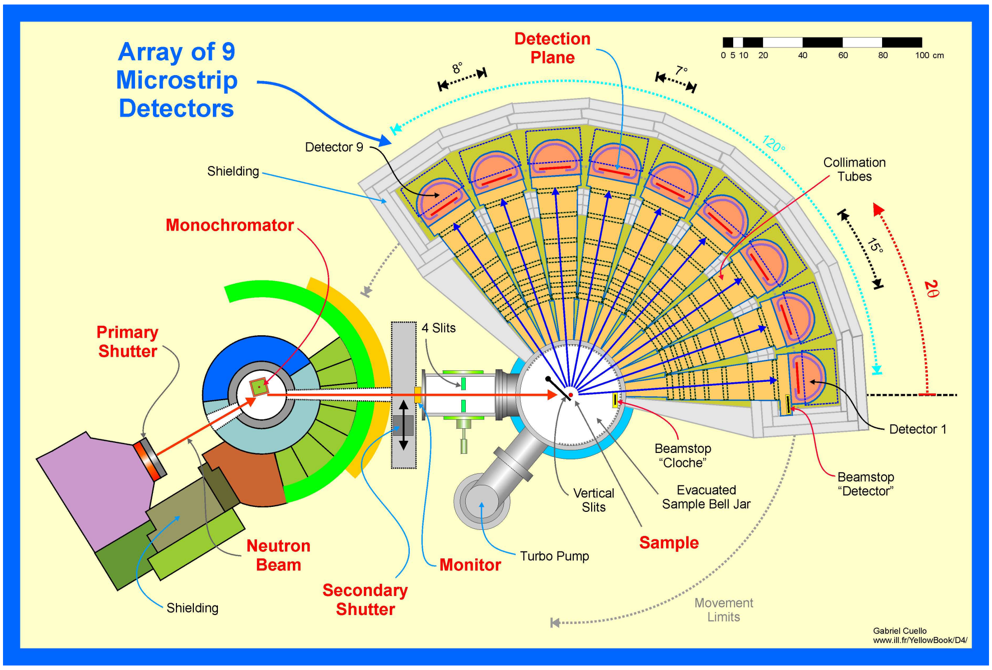

Figure 3-3: Top view schematic of D4c [46].

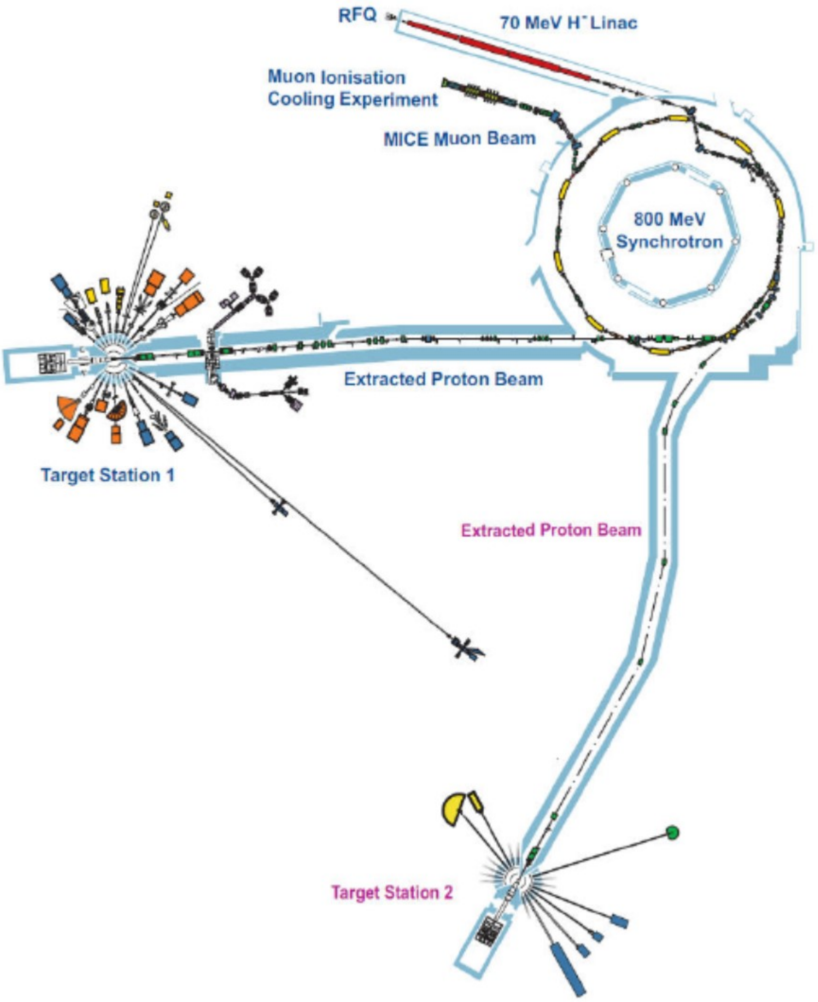

Figure 3-4: Schematic of the ISIS accelerator-based neutron source at the RAL [34].

shown in Figure 3-6. The de Broglie relation gives a neutron wavelength, $\lambda = h/m_n v$, where m_n is the neutron mass, and the neutron speed v can be expressed in terms of the moderator-sample distance L_i and the sample-detector distance L_f as

$$v = \frac{L_i + L_f}{t}. \tag{3.3}$$

It follows that Eq. (2.9) can be rewritten as

$$Q = \frac{4\pi m}{ht}(L_i + L_f)\sin\theta. \tag{3.4}$$

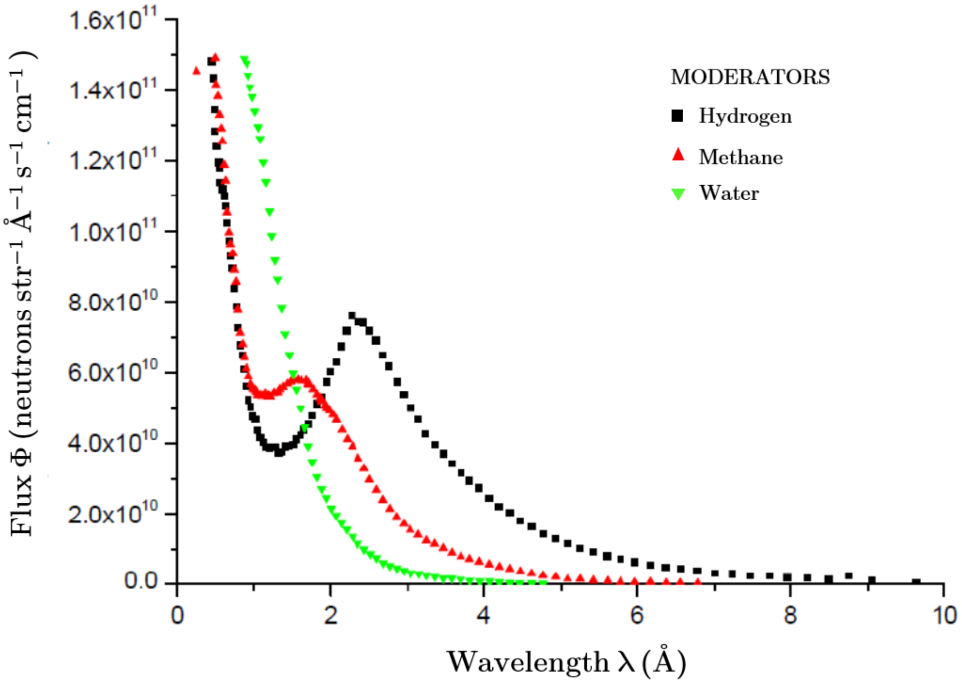

Figure 3-5: Wavelength distribution of the three moderators used at ISIS, which are hydrogen, methane or water based [48].

3.2.1 The GEM diffractometer at ISIS

The General Materials diffractometer, GEM, located at ISIS Target Station 1, is dedicated to both amorphous materials and powder crystallography [47]. GEM receives neutrons after they have been slowed down by a liquid methane moderator. The primary flight path L_i is 17 m, while the secondary flight path varies depending on the scattering angle. A long flight path leads to high-Q resolution in reciprocal space. The large GEM $Q_{\text{max}} = 55$ Å^{-1} is helpful for obtaining well-defined peaks in real space. The sample tank, in which the candle stick holding the sample is inserted, is evacuated during the experiment to a pressure below 1 mbar in order to minimise background due to scattering from air. The detector array, shown in Fig. 3-7, is divided into 8 detector banks, giving a total detector area of 7.270 m^2, and a wide range of scattering angles from 1.2° to 171.4°.

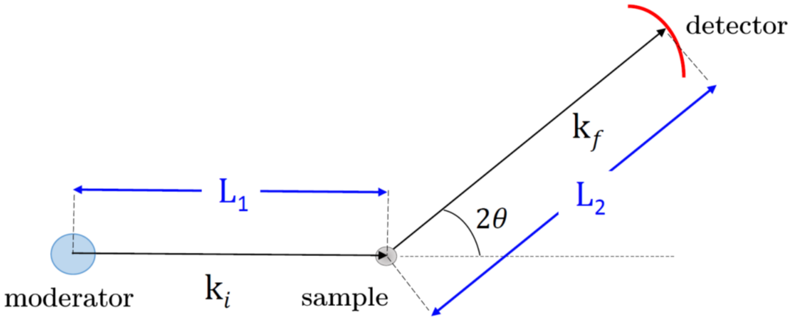

Figure 3-6: Schematic of a typical time-of-flight diffraction experiment using a spallation neutron source.

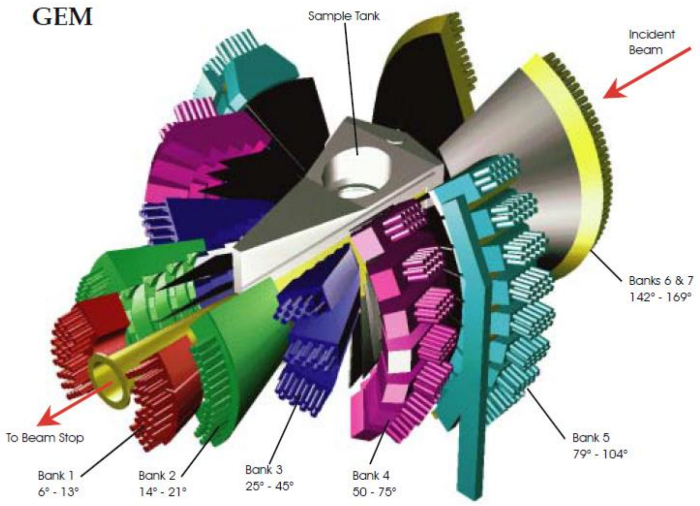

Figure 3-7: Schematic layout of the detector banks of the GEM detector array. All of the detectors are constructed using ZnS(Ag)/^{6}Li scintillators [34].

3.3 Neutron-diffraction data analysis

The theory outlined in Chapter 2 refers to the small sample limit, where an incident neutron undergoes a single scattering event when impinging on the sample. In a real experiment, it is necessary to take into account the facts that absorption and scattering events lead to an attenuation of the incident and scattered neutron beams, and that neutrons can be multiply scattered. Also, for most diffraction experiments, the sample is held in a container. Therefore, in order to correct the data to obtain the sample scattering cross-section of Eq. (2.10), some complementary measurements and calculations are required. In this section, a description of the data treatment is given. The formalism used is valid for a neutron-diffraction experiment performed with a monochromatic incident neutron beam. For pulsed sources, where the incident beam has neutrons with different wavelengths, it is necessary to take into account that, at each scattering angle 2θ, neutrons of all the available energies can be detected. This feature also implies that each detector bank will require a different wavelength-dependent correction for inelasticity effects.

3.3.1 Attenuation and multiple scattering corrections

In the case of a sample having cylindrical geometry, the attenuation coefficient $A_{i,j}(\theta)$ can be calculated using the method of Paalman and Pings [49]. The attenuation coefficient $A_{i,j}(\theta)$ refers to events in which a neutron scattered in medium i is attenuated in medium j. The multiple-scattering cross-section can be calculated by using the quasi-isotropic approximation [50]. For instance, for the simple case of a bare sample S, the multiple scattering cross section $M_{\mathrm{S}}(\theta)$ is given by

$$M_{\mathrm{S}}(\theta) = N_{\mathrm{S}} A_{\mathrm{S,S}}(\theta) \frac{\sigma_{\mathrm{S}}}{4\pi} \Delta_{\mathrm{S}}(\theta) \left[1 + P_{\mathrm{S}}(\theta)\right] , \tag{3.5}$$

where $\sigma_{\mathrm{S}} = 4\pi \left(b_{\mathrm{S}}^2 + b_{\mathrm{S,inc}}^2 \right)$ is the total scattering cross-section of the sample, Δ_{S} is the ratio of multiple scattering to single scattering, and $P_{\mathrm{S}}(\theta)$ is an inelasticity correction.

3.3.2 Background and container corrections

Let's consider a diffraction experiment in which the scattered intensity, normalised to the incident flux, is measured for the sample S in its container C, $I_{\mathrm{SC}}^{\mathrm{E}}(\theta)$, for the empty container, $I_{\mathrm{C}}^{\mathrm{E}}(\theta)$, and for the background B when no sample or container is present $I_{\mathrm{B}}^{\mathrm{E}}(\theta)$. The background-corrected intensity is then given by

$$I_{\mathrm{SC}}^{\mathrm{E}'}(\theta) = I_{\mathrm{SC}}^{\mathrm{E}}(\theta) - I_{\mathrm{B}}^{\mathrm{E}}(\theta) = A_{\mathrm{S,SC}}(\theta) I_{\mathrm{S}}(\theta) + A_{\mathrm{C,SC}}(\theta) I_{\mathrm{C}}(\theta) + a(\theta) M_{\mathrm{SC}}(\theta). \tag{3.6}$$

Similarly, the background-corrected intensity for the empty container is given by

$$I_{\mathrm{C}}^{\mathrm{E}'}(\theta) = I_{\mathrm{C}}^{\mathrm{E}}(\theta) - I_{\mathrm{B}}^{\mathrm{E}}(\theta) = A_{\mathrm{C,C}}(\theta) I_{\mathrm{C}}(\theta) + a(\theta) M_{\mathrm{C}}(\theta). \tag{3.7}$$

In these equations, $I_{\mathrm{SC}}^{\mathrm{E}'}(\theta)$ and $I_{\mathrm{C}}^{\mathrm{E}'}(\theta)$ are expressed in terms of:

- the sample intensity $I_{\mathrm{S}}(\theta)$ as calculated in the small-sample limit, and the attenuation factor for the sample in the presence of the sample and its container $A_{\mathrm{S,SC}}(\theta)$;
- the container intensity $I_C(\theta)$ as calculated in the small-sample limit, and the attenuation factor for the container in the presence of the sample and its container $A_{\mathrm{C,SC}}(\theta)$;
- a calibration factor $a(\theta)$ that converts a cross-section to an intensity;
- the multiple-scattering cross-section for the sample-container system $M_{\mathrm{SC}}(\theta)$;
- the attenuation coefficient for the empty container $A_{\mathrm{C,C}}(\theta)$;
- the multiple-scattering cross-section for the empty container $M_{\mathrm{C}}(\theta)$.

If N_{S} is the number of sample scattering centres illuminated by the neutron beam, the single-scattered intensity for the sample can be written as

$$I_{\mathrm{S}} = a(\theta) N_{\mathrm{S}} \left.\frac{d\sigma}{d\Omega}\right|_{\mathrm{S}}(\theta) \tag{3.8}$$

and, likewise, the single-scattered intensity for the empty container can be written as

$$I_{\mathrm{C}} = a(\theta) N_{\mathrm{C}} \left.\frac{d\sigma}{d\Omega}\right|_{\mathrm{C}}(\theta). \tag{3.9}$$

By combining Eqs. (3.6) - (3.8), the differential scattering cross section can be written as

$$\left.\frac{d\sigma}{d\Omega}\right|_{\mathrm{S}} = \frac{1}{N_{\mathrm{S}} A_{\mathrm{S,SC}}} \left[\left(\frac{I_{\mathrm{SC}}^{\mathrm{E}'}(\theta)}{a(\theta)} - M_{\mathrm{SC}}(\theta) \right) - \frac{A_{\mathrm{C,SC}}}{A_{\mathrm{C,C}}} \left(\frac{I_{\mathrm{C}}^{\mathrm{E}'}(\theta)}{a(\theta)} - M_{\mathrm{C}}(\theta) \right) \right]. \tag{3.10}$$

3.3.3 Vanadium normalisation

The scattered intensities can be placed on an absolute cross-section scale by using the inchoerent scattering from vanadium for which $\sigma_{\mathrm{coh}} = 0.01838(12)$ barn and $\sigma_{\mathrm{incoh}} = 5.08(6)$ barn. Therefore, the diffraction pattern for a piece of vanadium is always measured in a neutron-diffraction experiment. The measured intensity for vanadium, normalised to the incident flux and corrected for background scattering, is given by

$$I_{\mathrm{V}}^{\mathrm{E}'}(\theta) = A_{\mathrm{V,V}}(\theta) I_{\mathrm{V}}(\theta) + a(\theta) M_{\mathrm{V}}(\theta), \tag{3.11}$$

where the single scattered intensity for vanadium is given by

$$I_{\mathrm{V}}(\theta) = a(\theta) N_{\mathrm{V}} \frac{d\sigma}{d\Omega}(\theta)\bigg|_{\mathrm{V}} = a(\theta) N_{\mathrm{V}} \frac{\sigma_{\mathrm{V}}}{4\pi}(1 + P_{\mathrm{V}}(\theta)) \tag{3.12}$$

and the multiple-scattering cross-section can be expressed as

$$M_{\mathrm{V}}(\theta) = N_{\mathrm{V}} A_{\mathrm{V,V}}(\theta) \frac{\sigma_{\mathrm{V}}}{4\pi} \Delta_{\mathrm{V}}(\theta)(1 + P_{\mathrm{V}}(\theta)). \tag{3.13}$$

In Equations (3.12) and (3.13), N_V is the number of vanadium scattering centres in the neutron beam, $A_{\mathrm{V,V}}(\theta)$ is the attenuation coefficient, $\sigma_{\mathrm{V}} = 4\pi b_{\mathrm{inc}}^2$ is the incoherent scattering cross section, $P_V(\theta)$ is the correction term for inelasticity effects, and $\Delta_{\mathrm{V}}(\theta)$ is the fraction of neutrons undergoing multiple scattering. On combining these equations, the measured experimental intensity for vanadium can be rewritten as

$$I_{\mathrm{V}}^{\mathrm{E}'}(\theta) = a(\theta) A_{\mathrm{V,V}}(\theta) N_{\mathrm{V}} \left[\frac{\sigma_{\mathrm{V}}}{4\pi}(1 + P_{\mathrm{V}}(\theta))\right] [1 + \Delta_{\mathrm{V}}(\theta)], \tag{3.14}$$

such that the calibration coefficient is given by

$$a(\theta) = \frac{I_{\mathrm{V}}^{\mathrm{E}'}(\theta)}{A_{\mathrm{V,V}}(\theta) N_{\mathrm{V}} \left[\frac{\sigma_{\mathrm{V}}}{4\pi}(1 + P_{\mathrm{V}}(\theta))\right] [1 + \Delta_{\mathrm{V}}(\theta)]}. \tag{3.15}$$

3.3.4 Data analysis flow-chart

The flow-chart in Figure 3-8 outlines the general data-analysis procedure that is followed to treat the data obtained from a diffraction experiment on D4c or GEM, where the isotopic or isomorphic substitution method may be employed. For example, when the total pair distribution function $G(r)$ is obtained by Fourier transforming $F(Q)$, some low-r oscillations are introduced that should oscillate around the $G(r \to 0)$ limit. However, these oscillations are artefacts that are introduced by the Fourier transform procedure, and do not have physical meaning. Therefore, the back Fourier transform of $G(r)$, obtained by setting the low-r oscillations to the $G(r \to 0)$ limit, should agree with the measured $F(Q)$. A large discrepancy between these two functions may imply *e.g.* an incorrect background subtraction or data normalisation.

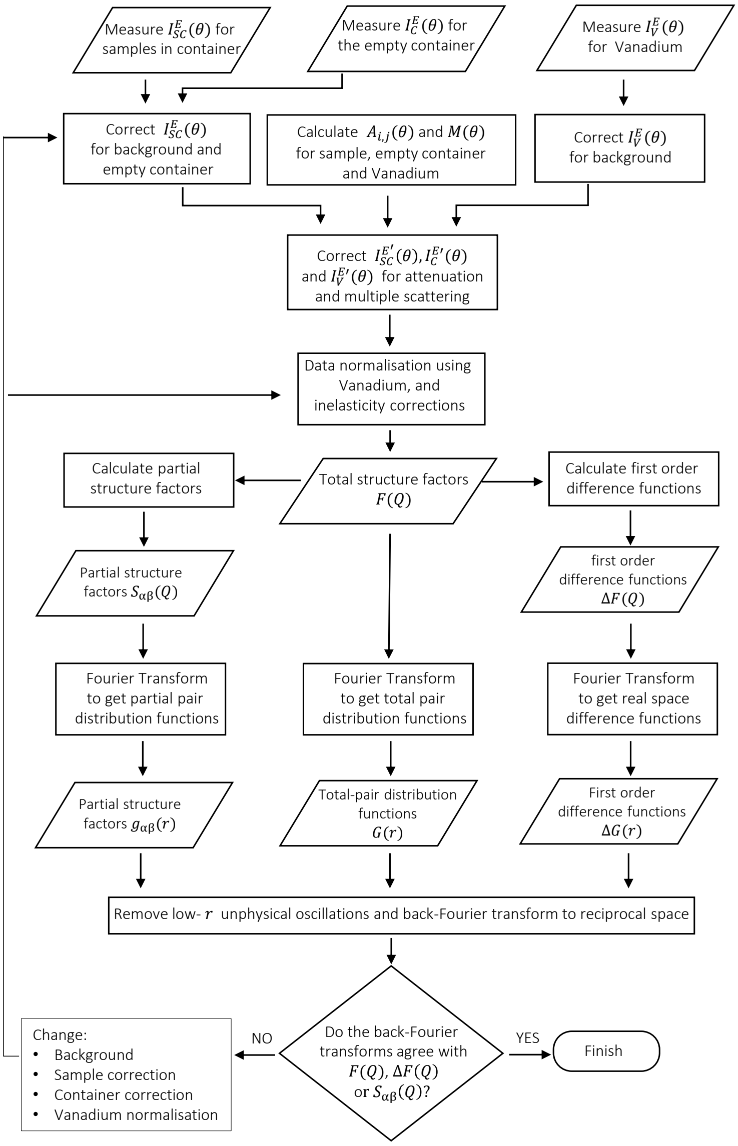

Figure 3-8: Data-analysis flow-chart for measurements from a diffraction experiment.

4. Structure of an aqueous solution of NaCl under high pressure and temperature conditions

4.1 Introduction

Sodium chloride in water is one of the most common fluids in many different settings, ranging from cellular biological processes [51], to environmental industrial applications in Carbon Capture and Storage (CCS) [14]. Known also as brine, this fluid plays a fundamental role in geological settings where the state conditions for a wide range of fluid compositions can vary over a broad range of temperatures and pressures. On the sea floor, for instance, the salinity, temperature and pressure conditions can be such that ice-like clathrate hydrate structures occur when sufficient methane is produced by organic matter on degradation. This typically happens on the continental margins, where temperatures do not exceed 20 °C at pressures of a few hundred bar [52–54]. On the other hand, relevant hydrothermal conditions for the formation of ore deposits can also be encountered in the ocean, where sea-water can even reach temperatures and pressures above the critical point of water, 407 °C and 298 bar [55]. Pressures between 15 and 25 kbar, at temperatures up to 770 °C, are found in the subduction zones, where the salinity of aqueous fluids can reach high values up to 20 wt% NaCl, corresponding to a 5 molal aqueous solution of NaCl [1]. Halite-bearing fluid inclusions in hydrothermal ore-forming systems can even reach salinity values between 40 and 70 wt% NaCl [56, 57].

The quantitative modelling of such processes represents a real challenge for geochemists. One of the reasons is the paucity of experimental data over an extended range of concentrations, temperatures and pressures. Another is the lack of a molecular-scale understanding of fundamental phenomena such as the ion speciation in aqueous solutions. The thermodynamic parameters used in geochemical models are therefore usually estimated via empirical correlations [58], and extrapolated to hydrothermal conditions using the Hegelson-Kirkham-Flowers equation of state [59], which originates from the dielectric continuum theory of Born [60]. This theory is based on the primary assumption that the dielectric permittivity of the solvent near to ions is the same as that in bulk solution, an over-simplification that can affect the calculation of relevant geochemical parameters. It is therefore of fundamental importance to provide the scientific community with experimental information at the microscopic level that can guide in the development of models at the atomic scale [61].

In this direction, different experimental techniques can be used and combined with molecular-dynamics simulations. Spectroscopic techniques, such as Raman and infrared spectroscopy, provide insight into the nature and energy of bonds, but do not provide information on the geometry of the hydration shell [62]. Experimental methods, such as NDIS [63, 64] and Extended X-Ray Absorption Fine Structure spectroscopy (EXAFS) [65, 66], are the main site-specific techniques for providing structural information on the ion-speciation in aqueous solutions, and its pressure and temperature dependence. With respect to X-rays, neutrons are more sensitive to light nuclei such as hydrogen. Also, neither the Na or Cl K-edges are accessible via EXAFS, and NDIS is therefore a more appropriate technique for investigating the structures of water and aqueous solutions of NaCl.

Over the last few years, the advancement in high-pressure and high-temperature experimental setups has provided unprecedented insight into the molecular-scale structure of solutions, even at geologically relevant state conditions [67–69]. However, the investigated range of concentrations, temperatures and pressures is still rather limited, and more experimental data are needed to test the validity of the information obtained from molecular-dynamics simulations.

In the present work, in order to expand the range of available experimental data, a NDIS experiment using Cl-isotopes was performed on a 5 molal NaCl-D_2O solution, at temperatures up to 150 °C and pressures up to 33.8 kbar. The method of first-order difference functions was used to provide site-specific information on the solvation of Cl^- ion. A high-concentration solution was chosen in order to maximise the atomic fraction of the Cl^- ions in solution, which is necessary to provide good counting statistics for a NDIS experiment. A molality of 5 was chosen to match the salinity that can be reached in subduction zones [1]. Heavy water was used in order to avoid the large incoherent and inelastic scattering effects associated with light hydrogen nuclei. The NDIS experiment presented in this chapter was performed in two stages. The first part of the experiment was performed in March 2013 using the D4c diffractometer at the ILL, where the use of a Paris-Edinburgh press allowed a maximum pressure of 33.8 kbar to be reached at a temperature of 150 °C. We are not aware of any other NDIS experiments on aqueous solutions for this pressure and temperature range. One of the reasons is the high technical difficulty of performing a NDIS experiment with such a setup. Details of this part of the experiment are described by Dr. Rowlands in her thesis [23]. The second part of the experiment was performed in July 2015, on D4c, using a Ti-Zr pressure cell with a heating system that allowed us to span a pressure range between 0.1 and 1 kbar, which is not readily accessible by using a Paris-Edinburgh press. The development of the Ti-Zr pressure cell setup was part of this thesis work. Aqueous solutions of similar composition have already been studied [70–75], using a setup similar to the one that we developed, but the present work combined improved instrumentation with the diffractometer D4c [46], thus allowing for the collection of data sets with markedly improved quality and statistics. Also, the results obtained with the Ti-Zr pressure cell were necessary to guide in the data analysis and interpretation of the data sets measured with the Paris-Edinburgh press. The results from the different setups allows for insight into the coordination environment of the Cl^- ion, over a temperature and pressure range that has never previously been accessed. The results are required to inform ongoing MD simulations.

In this chapter, the essential theory is outlined in section 4.3. The experimental details for the Ti-Zr heated pressure cell experiment are given in section 4.4. The experimental results are shown in section 4.5.1, where they are compared to those obtained for the higher pressure range using the Paris-Edinburgh press. Discussions and conclusions follow in section 4.6 and 4.7, respectively.

4.2 Units

The concentration of a solution can be expressed in different units. In this chapter, the concentration is expressed in terms of the molality m, as defined by

$$\text{molality} = \frac{\text{numbers of moles of solute}}{\text{1 kg of solvent}}, \tag{4.1}$$

and occasionally in terms of weight percent (wt%), where

$$\text{wt\%} = \frac{\text{mass of solute}}{\text{mass of solution}} \times 100. \tag{4.2}$$

Pressures are given in kilobars and, for reference, 1 kbar = 0.1 GPa.

4.3 Theory

As shown by Eq.(2.17), in a neutron-diffraction experiment the measured differential scattering cross section contains both desired information on the total structure factor and undesired information on the distinct and self inelastic-scattering terms. When dealing with aqueous solutions, inelastic scattering is mostly associated with the presence in the sample of light nuclei, such as hydrogen and deuterium. This scattering manifests itself in the differential scattering cross-section measured in a reactor-based experiment by a characteristic Q-dependent slope, that has to be subtracted in order to obtain $F(Q)$. In this case, a Placzek correction cannot be applied [20, 76], and it is necessary to employ empirical methods.

If two samples are identical in every respect except for their Cl-isotope compositions, the inelasticity terms cancel when a difference function $\Delta F_{\mathrm{Cl}}(Q)$ is formed [70]. For instance, let $\mathrm{Na}^{\mathrm{Nat}}\mathrm{Cl}$-$\mathrm{D_2O}$ be a solution prepared using chlorine with its natural isotopic abundance, $^{\mathrm{Nat}}\mathrm{Cl}$, and let $\mathrm{Na}^{37}\mathrm{Cl}$-$\mathrm{D_2O}$ be a solution prepared using $^{37}\mathrm{Cl}$ isotopes. If the measured differential scattering cross sections are represented by $\frac{d\sigma}{d\Omega}(Q)\Big|^{\mathrm{Nat}}$ and $\frac{d\sigma}{d\Omega}(Q)\Big|^{37}$, respectively, then their subtraction gives

$$\begin{aligned}
&\frac{1}{N_S}\left[\frac{d\sigma}{d\Omega}(\theta)\Big|^{\mathrm{Nat}} - \frac{d\sigma}{d\Omega}(\theta)\Big|^{37}\right] \\
&= \frac{1}{N_S}\left[\frac{1}{A^{\mathrm{Nat}}_{\mathrm{S,SC}}(\theta)}\left(\frac{I^{\mathrm{Nat}}_{\mathrm{SC}}(\theta)}{a(\theta)} - M^{\mathrm{Nat}}_{\mathrm{SC}}(\theta)\right) - \frac{1}{A^{37}_{\mathrm{S,SC}}(\theta)}\left(\frac{I^{37}_{\mathrm{SC}}(\theta)}{a(\theta)} - M^{37}_{\mathrm{SC}}(\theta)\right)\right] + X_c(\theta) \\
&= \Delta F_{\mathrm{Cl}}(Q) + c_{\mathrm{Cl}}(\bar{b}^2_{^{\mathrm{Nat}}\mathrm{Cl}} - \bar{b}^2_{^{37}\mathrm{Cl}}),
\end{aligned} \tag{4.3}$$

where $\mathrm{X}_c(\theta)$ denotes the correction for the cell, as shown in Eq. (3.10),

$$X_c(\theta) = \frac{1}{N_S A_{\mathrm{C,C}}(\theta)}\left(\frac{I^{\mathrm{E}}_{\mathrm{C}}(\theta)}{a(\theta)} - M_{\mathrm{C}}(\theta)\right)\left(\frac{A^{\mathrm{Nat}}_{\mathrm{C,SC}}(\theta)}{A^{\mathrm{Nat}}_{\mathrm{S,SC}}(\theta)} - \frac{A^{37}_{\mathrm{C,SC}}(\theta)}{A^{37}_{\mathrm{S,SC}}(\theta)}\right). \tag{4.4}$$

The superscripts Nat and 37 refer to the attenuation and multiple-scattering terms corresponding to the $\mathrm{Na}^{\mathrm{Nat}}\mathrm{Cl}$-$\mathrm{D_2O}$ and $\mathrm{Na}^{37}\mathrm{Cl}$-$\mathrm{D_2O}$ samples, respectively.
The difference function $\Delta F_{\mathrm{Cl}}(Q)$ is defined by

$$\begin{aligned}
\Delta F_{\mathrm{Cl}}(Q) &\equiv {}^{\mathrm{Nat}}F(Q) - {}^{37}F(Q) \\
&= A[S_{\mathrm{ClD}}(Q) - 1] + B[S_{\mathrm{ClO}}(Q) - 1] + C[S_{\mathrm{ClNa}}(Q) - 1] + D[S_{\mathrm{ClCl}}(Q) - 1],
\end{aligned} \tag{4.5}$$

where the weighting factors are given by

$$A = 2c_{\mathrm{Cl}}c_{\mathrm{D}}b_{\mathrm{D}}(b_{^{\mathrm{Nat}}\mathrm{Cl}} - b_{^{37}\mathrm{Cl}}) \tag{4.6}$$

$$B = 2c_{\mathrm{Cl}}c_{\mathrm{O}}b_{\mathrm{O}}(b_{^{\mathrm{Nat}}\mathrm{Cl}} - b_{^{37}\mathrm{Cl}}) \tag{4.7}$$

$$C = 2c_{\mathrm{Cl}}c_{\mathrm{Na}}b_{\mathrm{Na}}(b_{^{\mathrm{Nat}}\mathrm{Cl}} - b_{^{37}\mathrm{Cl}}) \tag{4.8}$$

$$D = c_{\mathrm{Cl}}^2(b_{^{\mathrm{Nat}}\mathrm{Cl}}^2 - b_{^{37}\mathrm{Cl}}^2). \tag{4.9}$$

The Fourier transform of $\Delta F_{\mathrm{Cl}}(Q)$ gives the corresponding real-space function

$$\begin{aligned}\Delta G_{\mathrm{Cl}}(r) &= \frac{1}{2\pi^2\rho r}\int_0^\infty QM(Q)\Delta F_{\mathrm{Cl}}(Q)\ \sin(Qr)dQ \\ &= A[g_{\mathrm{ClD}}(r)-1] + B[g_{\mathrm{ClO}}(r)-1] + C[g_{\mathrm{ClNa}}(r)-1] + D[g_{\mathrm{ClCl}}(r)-1],\end{aligned} \tag{4.10}$$

where ρ is the atomic number density. The theoretical low-r limit is given by the sum of the weighting factors

$$\Delta G_{\mathrm{Cl}}(r \to 0) = -(A+B+C+D), \tag{4.11}$$

and therefore depends on the isotopic enrichment of the chemical species and the solution concentrations. When the difference function $\Delta G_{\mathrm{Cl}}(r)$ is formed, the Cl-D peak position is expected to be the shortest [70, 77] and, if contributions from the other Cl atom pair-correlations can be neglected at this distance, it follows that

$$g_{\mathrm{ClD}}(r) \approx \frac{\Delta G_{\mathrm{Cl}}(r) - \Delta G_{\mathrm{Cl}}(r \to 0)}{A}. \tag{4.12}$$

In this case, the mean number of D atoms contained in a spherical shell of radii r_1 and r_2, centred on a Cl atom, is given by

$$\bar{n}_{\mathrm{Cl}}^{\mathrm{D}} = 4\pi\rho\int_{r_1}^{r_2} g_{\mathrm{ClD}}(r)r^2dr. \tag{4.13}$$

4.4 Experimental method

The NDIS experiments were performed on Cl-isotopically enriched 5 m NaCl-D_2O samples. Solutions of $Na^{Nat}Cl$-D_2O (Puratronic® 99.999 % metal based purity from Alfa Aesar) and $Na^{37}Cl$-D_2O (95 % isotopic enrichment from SigmaAldrich) were measured on D4c using the Ti-Zr pressure-cell, while solutions of $Na^{Mix}Cl$-D_2O and $Na^{35}Cl$-D_2O (99 % isotopic enrichment from SigmaAldrich) were measured on D4c using the Paris-Edinburgh press. For the $Na^{Mix}Cl$-D_2O solution, ^{Mix}Cl denotes a 50:50 mixture of ^{35}Cl and ^{37}Cl. In both cases, the solutions were prepared in the Liquid and Amorphous Materials group laboratory at the University of Bath by Dr. Zeidler and Dr. Rowlands. Details on the samples preparation are given in reference [23]. The atomic fractions and bound coherent scattering lengths of the elements in the samples are listed in Table 4.1. The total scattering cross sections for the samples, at the incident neutron wavelengths, are given in Table 4.2.

Table 4.1: The atomic fractions and bound coherent scattering lengths [33] for the experiments on 5 m solutions of NaCl-D_2O. The numbers in parenthesis indicate the uncertainty and apply to the least significant digits.

Element	atomic fraction	b_{coh} (fm)	Relative abundance (%)
Na	0.0313(1)	3.62(2)	–
^{Nat}Cl	0.0313(1)	9.57708(8)	–
^{37}Cl	0.0313(1)	3.08(6)	24.23
^{35}Cl	0.0313(1)	11.65(2)	75.77
^{Mix}Cl	0.0313(1)	7.365(5)	–
D	0.6249(1)	6.671(4)	0.015
O	0.3125(1)	5.803(4)	–

Table 4.2: The total scattering cross-sections at the incident neutron wavelengths λ_i for different 5 m solutions of NaCl-D_2O. The value for the total cross-section per nucleon for D_2O, 3.745(4) barn, was taken from reference [78].

Sample	σ_T (barn)	λ_i (Å)
$Na^{Nat}Cl$-D_2O	4.445(3)	0.49873(5)
$Na^{37}Cl$-D_2O	3.339(4)	0.49873(5)
$Na^{35}Cl$-D_2O	4.691(4)	0.4971(8)
$Na^{Mix}Cl$-D_2O	4.181(4)	0.4971(8)

Each measured $F(Q)$ function has contributions from ten partial structure factors, whereas $\Delta F_{Cl}(Q)$ has contributions from only four Cl-β partial structure factors, where

β = D, O, Na or Cl. The weighting factors for the partial structure factors in $F(Q)$ and in $\Delta F_{\mathrm{Cl}}(Q)$ are given in Tables 4.3 and 4.4, respectively.

Table 4.3: The $S_{\alpha\beta}(Q)$ weighting factors in the $F(Q)$ function for a 5 m solution of NaCl-D$_2$O. I-Nat and I-37 refer to the weighting factors in ${}^{\mathrm{Nat}}F(Q)$ and ${}^{37}F(Q)$, respectively, while II-35 and II-Mix refer to the weighting factors in ${}^{35}F(Q)$ and ${}^{\mathrm{Mix}}F(Q)$, respectively.

Weighting factor	I-Nat (mbarn)	I-37 (mbarn)	II-35 (mbarn)	II-Mix (mbarn)
${c_{\mathrm{Na}}}^2{b_{\mathrm{Na}}}^2$	1.3(8) 10^{-4}	1.3(8) 10^{-4}	1.3(8) 10^{-4}	1.3(8) 10^{-4}
${c_{\mathrm{Cl}}}^2{b_{\mathrm{Cl}}}^2$	8.9(3) 10^{-4}	9.28(11) 10^{-5}	1.329(5) 10^{-3}	5.31(9) 10^{-4}
${c_{\mathrm{D}}}^2{b_{\mathrm{D}}}^2$	0.17(2)	0.17(2)	0.17(2)	0.17(2)
${c_{\mathrm{O}}}^2{b_{\mathrm{O}}}^2$	0.03(1)	0.03(1)	0.03(1)	0.03(1)
$2c_{\mathrm{Na}}b_{\mathrm{Na}}c_{\mathrm{Cl}}b_{\mathrm{Cl}}$	6.80(7) 10^{-4}	2.19(5) 10^{-4}	8.27(8) 10^{-4}	5.23(6) 10^{-4}
$2c_{\mathrm{Na}}b_{\mathrm{Na}}c_{\mathrm{D}}b_{\mathrm{D}}$	9.45(3) 10^{-3}	9.45(3) 10^{-3}	9.45(3) 10^{-3}	9.45(3) 10^{-3}
$2c_{\mathrm{Na}}b_{\mathrm{Na}}c_{\mathrm{O}}b_{\mathrm{O}}$	4.12(21) 10^{-3}	4.12(21) 10^{-3}	4.12(21) 10^{-3}	4.12(21) 10^{-3}
$2c_{\mathrm{Cl}}b_{\mathrm{Cl}}c_{\mathrm{D}}b_{\mathrm{D}}$	0.025(4)	8.02(2) 10^{-3}	0.03(1)	0.019(11)
$2c_{\mathrm{Cl}}b_{\mathrm{Cl}}c_{\mathrm{O}}b_{\mathrm{O}}$	0.011(6)	3.49(6) 10^{-3}	0.013(4)	8.36(8) 10^{-3}
$2c_{\mathrm{D}}b_{\mathrm{D}}c_{\mathrm{O}}b_{\mathrm{O}}$	0.151(16)	0.151(16)	0.151(16)	0.151(16)

Table 4.4: The $S_{\alpha\beta}(Q)$ weighting factors in the difference function $\Delta F_{\mathrm{Cl}}(Q)$ for a 5 m solution of NaCl-D$_2$O. In the first case (I), $\Delta F_{\mathrm{Cl}}(Q)$ was obtained by using ${}^{\mathrm{Nat}}$Cl and ^{37}Cl isotope substitution, while in the second case (II), $\Delta F_{\mathrm{Cl}}(Q)$ was obtained by using ^{35}Cl and ${}^{\mathrm{Mix}}$Cl (a 50:50 mixture of ^{35}Cl and ^{37}Cl) isotope substitution.

Cl-β	I (mbarn)	II (mbarn)
Cl-D	16.95(15)	11.16(71)
Cl-O	7.37(8)	4.86(31)
Cl-Na	0.46(2)	0.30(2)
Cl-Cl	0.81(1)	0.79(7)

4.4.1 The Ti-Zr pressure cell

The Ti-Zr cell setup was developed in order to access a pressure range that is complementary to that of the Paris-Edinburgh press, *i.e.* pressures below 2.4 kbar. It comprised a Ti-Zr pressure cell, a fluid-separator, a pressure transducer, a pump and heating system. A sketch for the setup is shown in Figure 4-1, while technical drawings for the cell and separator are shown in Figures 4-2 and 4-3, respectively.

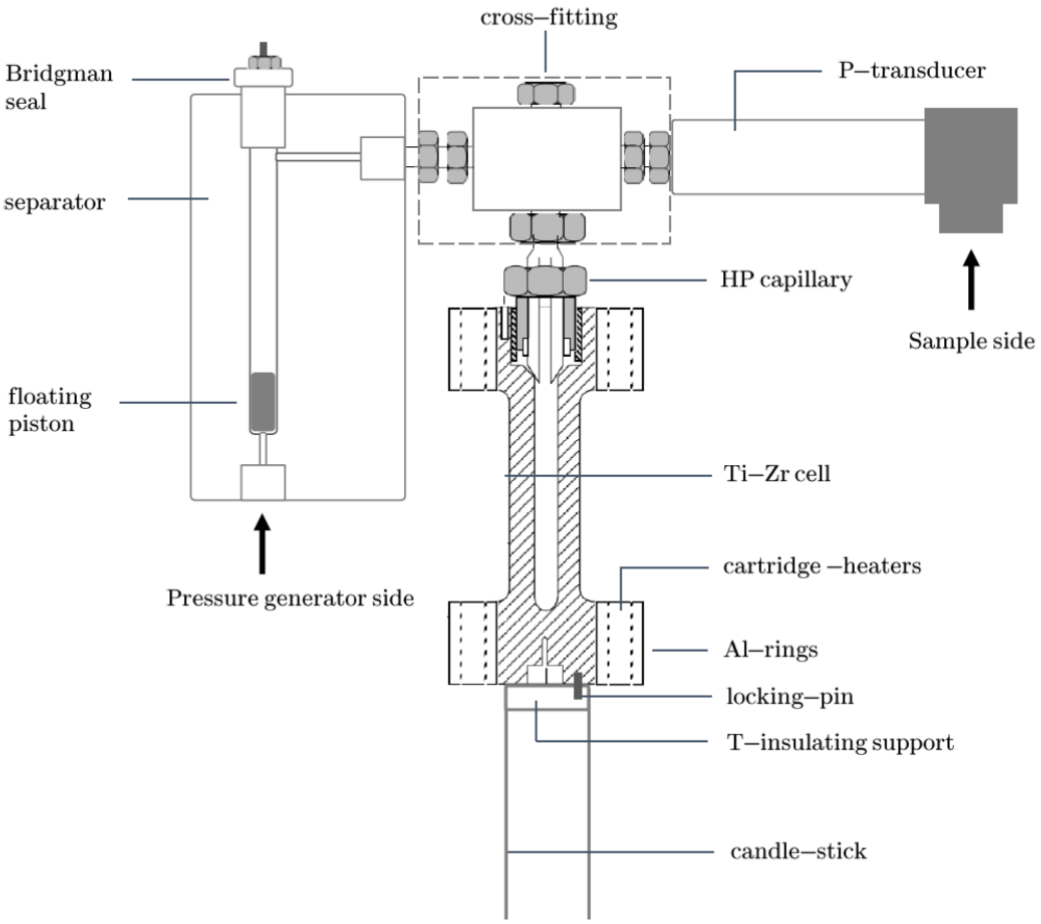

Figure 4-1: Schematic showing the Ti-Zr pressure cell together with the heating and pressure setups (not to scale). The cell sits on a candle-stick in contact with a thermally-insulating support. The cell orientation is fixed with respect to the candle stick via a metal locking-pin. The high-pressure capillary on top of the cell is connected to a cross-fitting, and hence to a separator (pressure generator-side) and to a pressure transducer (sample-side). The cell is heated by using four cartridge heaters embedded in two aluminium rings mounted at the ends of the cell. Two thermocouples are connected to the rings, in order to regulate the power supply, and hence the temperature of the cell.

The Ti-Zr cell

The material for the cell was chosen to be $Ti_{0.676}Zr_{0.324}$, a so-called null-scattering alloy, that has a nominal mean coherent neutron-scattering length of zero. This alloy can be used for high-pressure neutron-scattering research because of its excellent strength properties [79, 80]. $Ti_{0.676}Zr_{0.324}$ also exhibits an exceptionally good corrosion resistance due to the formation of a protective oxide film on the metal surface. This oxide layer, having a thickness of 5-10 nm [81], occurs naturally and prevents chemical attack of the underlying metal surface. In general, water and electrolytic solutions can be highly corrosive at high temperatures, thus altering the mechanical properties of the alloy after dissolving the oxide layer. In fact, even though Ti-Zr cells have been used in several neutron diffraction experiments on aqueous solutions at high temperatures and pressures [72, 73, 82], problems were encountered due to leaks and combustion [72, 83, 84]. For this reason, and because our cell (donated by Dr. George Neilson) had already been used before, we limited our maximum temperature to 150 °C and pressure to 2 kbar, after mechanical tests were performed [81]. The cell-geometry is shown in Figure 4-2. The high-pressure capillary used to seal the top of the cell was made of a stainless steel-alloy, called RESATO HP 160, that is highly resistant to corrosion.

The separator and the pressure transducer

A fluid-separator was used to pressurise the sample, in which a sealed floating piston separates the liquid sample from the pressurising fluid (3M Fluorinert^{TM} FC-770). Hence, the pressure on the generator side was transmitted to the sample via displacement of the piston. Once the piston reaches a stable position, the pressure between the two fluids is in balance, assuming that the piston is frictionless. Although the principle is simple, the practical realisation of a separator optimised for high-temperature and pressure experiments is quite challenging, because the materials that are employed must be chemically resistant. Also, leaks or sample contamination are likely to happen if the piston does not isolate properly the two fluids. In order to avoid these issues, a special separator design, shown in Figure 4-3, was developed by Burkhard Annighöfer.

The seal between the fluids was achieved by using compressed elastomer O-rings (Viton-FKM, Hardness: 70 Shore(A)) that could withstand the accessible pressure and temperature regime. Four O-rings were greased and mounted around the piston, as shown in Figure 4-4(d), by making use of a sliding-tool. The piston was then pushed into the separator's body, and a plunger was used to check it had reached its initial position. Once the vessel's volume was filled with sample, the separator was hermetically sealed using a Bridgman seal. Pressure on the fluid-separator piston was generated by a spindle-pump, making use of 3M Fluorinert^{TM} FC-770 as the pressure-transmitting fluid. Gauges were used to measure the pressure in the pump-reservoir and the pressure applied to the piston. A pressure transducer was also connected to the cell in order to measure the pressure on the sample side of the separator. The high-pressure connections between the cell, the fluid-separator and the pressure transducer, were chosen in order to minimise the overall sample volume. This feature was required because of the high cost of ^{37}Cl-isotopes.

The heating system

The heating system consisted of two aluminium clamps connected at the ends of the cell, as shown in Figures 4-4(b) and (c). Each clamp had four embedded cartridge heaters. A test was made to ensure that the pressure cell could be uniformly heated. It showed that, without the sample, the maximum temperatures measured in the middle part of the cell were 48, 96 and 139 °C when the clamps were heated at 50, 100 and 150 °C. The difference between the measured and the target temperatures diminish in the presence of the sample, due to thermal convection. Two thermocouples were used to regulate the temperature of each clamp, and another was placed in contact with the bottom of the cell.

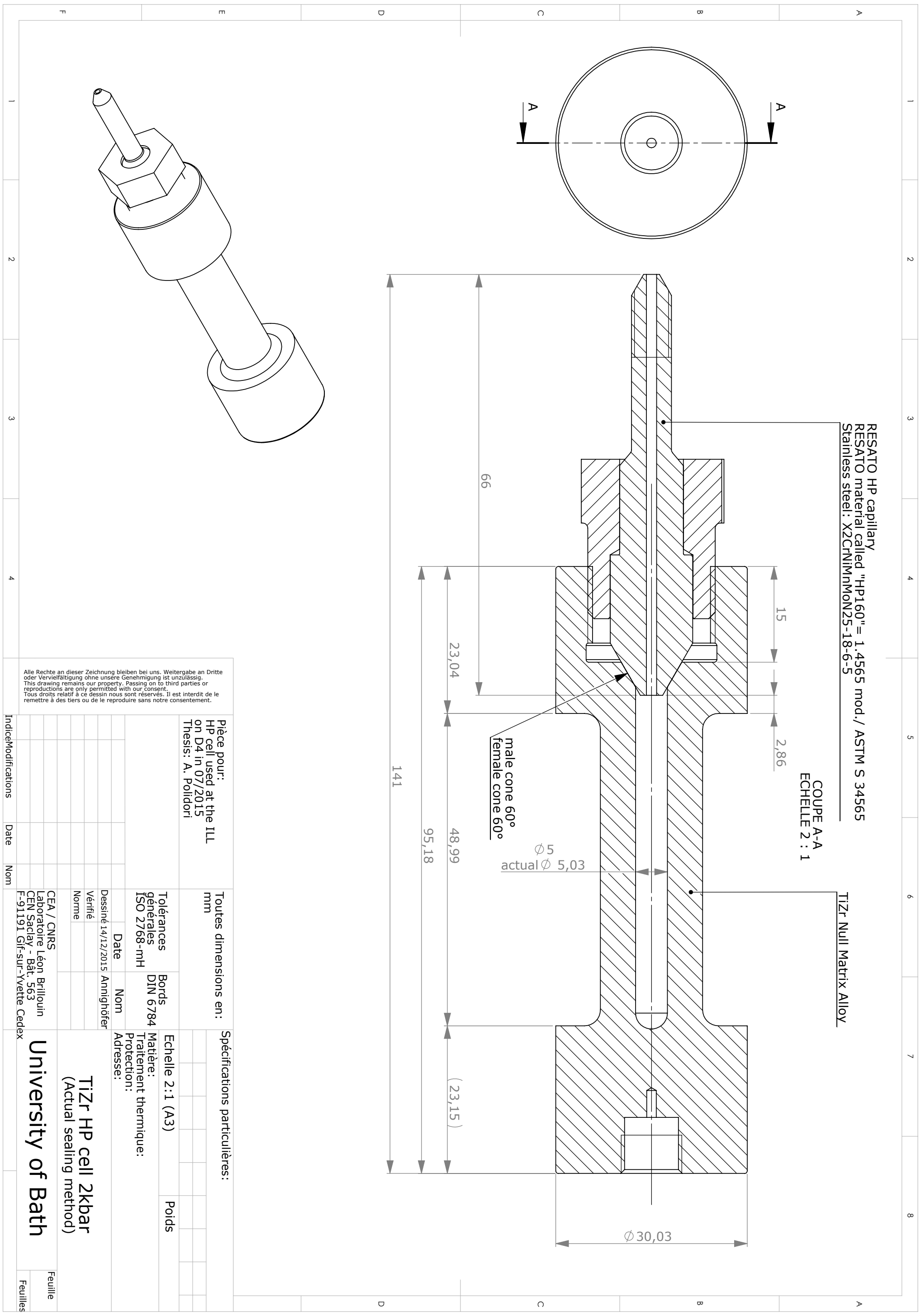

Figure 4-2: Drawing of the Ti-Zr pressure cell used for the D4c experiment on NaCl-D_2O. The high-pressure fitting is shown screwed into the top of the cell. The internal diameter of the cell is 5.03 mm. The overall volume, including the high-pressure fitting, is about 1.2 ml. The drawing was made by Burkhard Annighöfer.

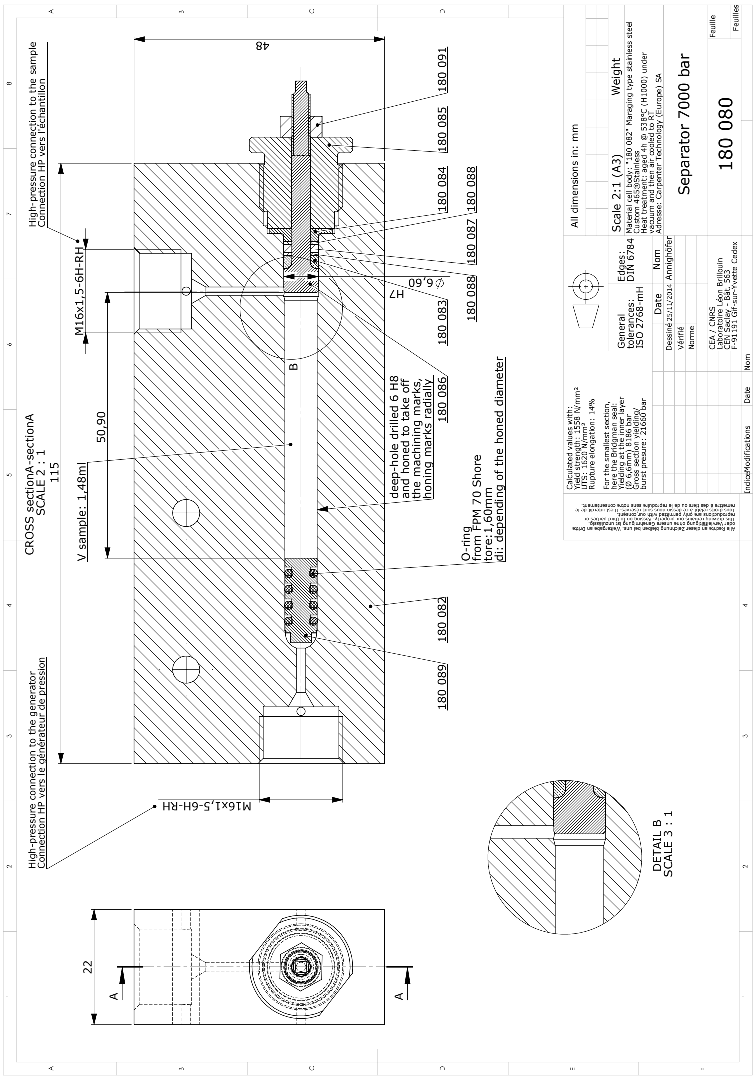

Figure 4-3: Drawing of the fluid-separator developed for the D4c experiment on NaCl-D_2O. The body of the separator has an outlet to the high-pressure generator side (bottom), another to the sample side (top-left) and an outlet into which a mushroom-Bridgman seal is plugged (top), once the sample has been loaded. The sample volume is 1.48 ml. The floating rubbing piston (part labelled as 180 089) is sitting in its starting position, before pressure is applied from the generator. The drawing was made by Burkhard Annighöfer.

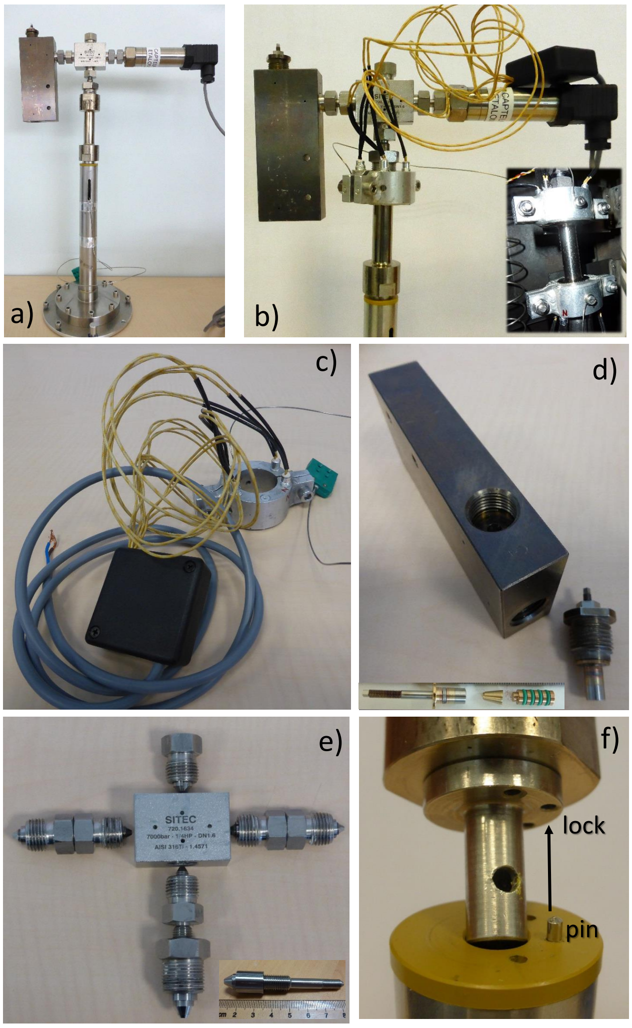

Figure 4-4: In (a) the Ti-Zr cell is mounted as shown in the schematic of Figure 4-1, except that the heating clamps are missing. In (b) one of the heating clamps is mounted at the top-end of the cell, while in the inset both of the heaters are mounted. As shown in (c), each clamp is made of two semi-cylindrical parts, connected by two bolts, in which four cartridge heaters are embedded. These heaters are connected via the yellow wires to the power supply. In (d), the body of the separator, and the Bridgman seal, are shown. The inset shows the mushroom-plug of the Bridgman seal, the piston with four green O-rings (Viton-FKM, Hardness: 70 Shore(A)), and the conical sliding-tool used to mount them. In (e) the high-pressure fittings used to form the central cross are shown. The fitting at the bottom, also shown in the inset, is the one that seals the cell and is made of a strong corrosion-resistant stainless-steel alloy (RESATO HP 160) to avoid leaks. Figure (f) shows the metal pin that locks the cell to the candle-stick to avoid rotation. The thermal-insulating yellow support is made of PAI (Polyamide-imide) “Torlon 4203” that can withstand temperatures up to 250 °C.

4.4.2 D4c neutron-diffraction experiment

The Ti-Zr cell setup was assembled outside the D4c belljar, where the filling stage could be done more easily. The procedure for loading the sample was carefully thought through and was tested several times before the experiment because the filling stage had to be done as quickly as possible in order to minimise contamination of the sample by atmospheric water. In fact, the H/D balance of the measured samples is a key parameter in a neutron-diffraction experiment with deuterated samples, if the slopes arising from inelastic scattering are to cancel once a first-order difference function is taken. Secondly, the filling of the high-pressure capillaries had to be done carefully in order to avoid the presence of air bubbles in the can. Lastly, it was important to establish a procedure to recover the sample prepared from ^{37}Cl. Considerable effort was made to guarantee that the setup could be re-mounted in an identical position for each measurement, in order to maintain a constant background. This is important in experiments using the Ti-Zr alloy, because of the presence in the material of phase-separated crystalline domains, in which the mean coherent neutron-scattering length is not zero, as for the ideal case: small Bragg peaks appear in the diffraction patterns and have preferred orientations.

Procedure for loading the sample and mounting the cell

The following procedure was used for mounting and filling the cell:

1. The high-pressure fitting was screwed into the top of the cell and tightened with spanners. The cell was then placed on the candle-stick as shown in Figure 4-4(f), so that the metal pin would prevent the cell from rotating. Then, the body of the cross-union was screwed into the top of the fitting, (Figure 4-5), and the relative position between the flat cell surface and the body of the cross union was set at about 45° (Figure 4-5).

2. A teflon tube of length 14 cm and outer diameter of 0.6 mm was inserted vertically, from the top entrance of the cross-union down to the bottom of the cell, as shown in Figure 4-6(a). Then, a syringe with a needle was filled with sample and attached to the end of the tube, after making sure that there were no bubbles in either the syringe or needle. The sample was injected into the the teflon tube to ensure that the cell was filled from the bottom, while slowly extracting the tube, up to the central point of the cross union. The rising level of the sample was checked visually using a flash light pointing at the cross union's outlets.

3. The volume of the pressure transducer was filled with sample using the syringe, before the pressure fitting was screwed into the transducer and tightened with

Figure 4-5: On the left: the body of the cross fitting is mounted on the cell via the high-pressure capillary that seals the cell. On the right: the orientation between the fitting and the cell is checked, using as a reference one of the flat surfaces at the end of the cell.

spanners. The pressure fitting volume was also filled with sample, as shown in Figure 4-6(b), and then screwed into one of the outlets on the cross union.

4. The separator vessel was filled from the top outlet (Figure 4-6(c)), after checking that the piston was placed at the very bottom. Once the rising level of the sample reached the height of the lateral outlet, the Bridgman seal was plugged into the top outlet as follows:

    - the gland-nut of the seal was firmly hand tightened so that the Bridgman seal was tight against the body of the separator;
    - the small nut on top of the gland nut was then strongly tightened, keeping the shaft constant in orientation, and allowing the lead washer to flow and therefore to seal the vessel.

    Holding the separator in a horizontal position, its volume was filled from the lateral outlet, a pressure fitting was connected to this outlet, and filled with sample before being screwed into the cross union (Figure 4-6(d)).

5. After all of the parts were connected to the cross union, a small amount of sample was injected into the top outlet of the cross-fitting to fill the remaining volume, as shown in Figure 4-6(e). The needle was then inserted in the cell to break possible air-bubbles, and then removed to check that the level of the sample was constant. The outlet was then closed with a fitting that was tightened with spanners.

6. In order to check that the right amount of sample, corresponding to 3.12 ml, had been injected, the bottle containing the sample, the syringe with needle, and the teflon tube were weighed before and after the filling procedure.

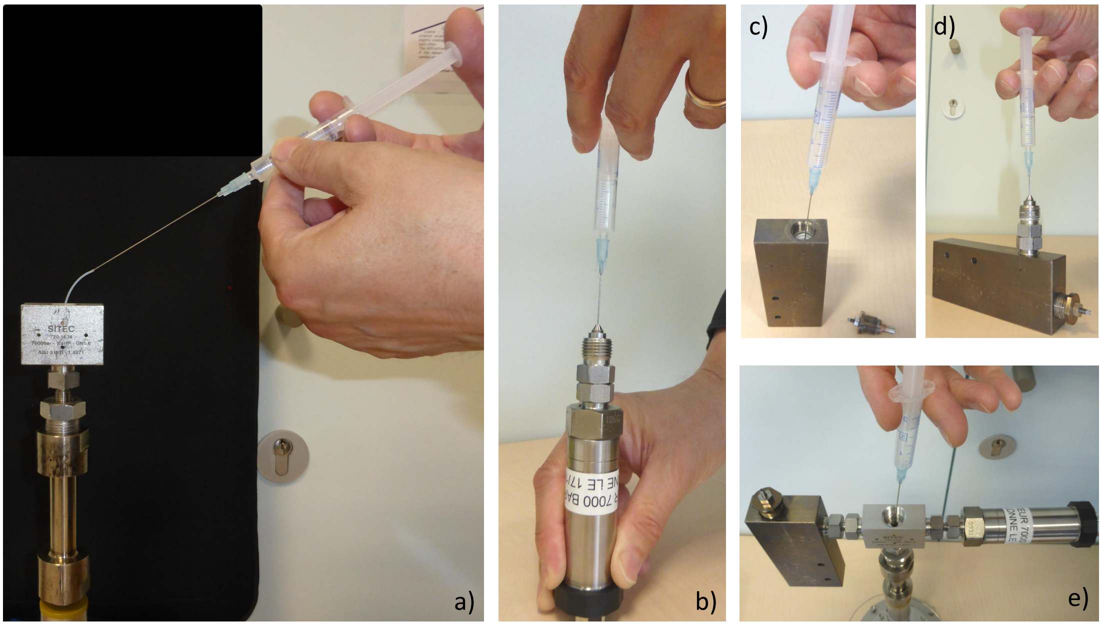

Figure 4-6: Different steps in the filling stage. (a) A teflon tube is inserted in the cell via the cross-union, and is connected to a needle in order to inject the sample in the syringe. (b) The volume of the pressure transducer, and of the connection fitting, is filled. (c) The separator is filled before screwing in the Bridgman seal, and after it is placed horizontally (d) the pressure fitting is connected and the remaining volume filled. Once all the filled components are connected to the cross-union, some more sample is inserted from the top outlet of the cross union, before this outlet is closed.

The setup was then mounted in the D4c belljar. The candle-stick was fixed on a plate with screws. The heating clamps were connected around the ends of the cell, making sure that the aluminium parts were not exposed to the incident neutron beam. The cartridge heater wires were connected to an external power supply via a belljar feed-through. The electrical resistance of each heater was measured after the clamps were fixed, to check that they had not been damaged during the mounting. Three thermocouples were mounted and placed carefully to avoid scattering from the incident beam. Two of them were connected to the heating clamps and one to the bottom of the cell. The separator was mounted in a horizontal position to avoid possible secondary scattering from neutrons diffracted from the pressure cell, and its bottom outlet was connected to the pressure generator with a pig-tail high-pressure fitting. This connection was designed to be flexible and minimise the stress on the other components during the tightening of the junctions. The connections to the external spindle-pump, and to the electrical power supply for the heating system, were realised via two belljar feed-throughs. Neutron-absorbing $^{10}B_4C$ flags were then positioned close to the pressure cell in order to collimate the incident neutron beam. The belljar environment, with the Ti-Zr cell setup, is shown in Figure 4-7. The belljar lid was mounted and the belljar was placed under vacuum once it was checked that everything was in place. The heaters at the top and bottom of the cell were controlled via separate power supplies, and displays were used both to set the temperature and to read the values measured by the thermocouples. Gauges were used to monitor the sample-pressure and check that leaks were not occurring.

Procedure for unloading the sample and cleaning the setup

At the end of each measurement with a NaCl-D_2O sample, the cell and the other parts in contact with salty water had to be carefully cleaned. Also, for the $Na^{37}Cl$-D_2O case, a special procedure was followed to recover the maximum possible amount of sample. At the end of the measurement, the setup was dismounted from the D4c belljar, so that the unloading could be done in the atelier. As each component was disconnected from the cross union, the sample was extracted with a syringe and, if necessary, use was made of a teflon tube. For each component, the procedure was repeated as many times as necessary to ensure that no more sample would be injected into the recovery-sample bottle. After having drawn as much sample as possible, each component was rinsed many times with water and the washings were kept in a separate bottle. In order to check that Cl was no longer contained in the setup, an aqueous solution with $AgNO_3$ was made in a separate container, and a drop of the recovered sample was added to the solution. If the solution turned out to be cloudy, than more rinsing was required.

The cell and the high-pressure fittings were than rinsed with acetone and placed under vacuum to be dried. The piston was removed from the separator and acetone-soaked cotton-buds were used to clean traces of extruded lead on its external surface. After this, the separator's body was ultrasounded for five minutes at 50 °C in a vessel filled with a Gigapur-05 decontamination detergent. Once dried, the separator was rinsed with acetone and again dried by flushing Argon through it. The O-rings in the piston were changed after each loading, and the piston itself was cleaned with acetone.

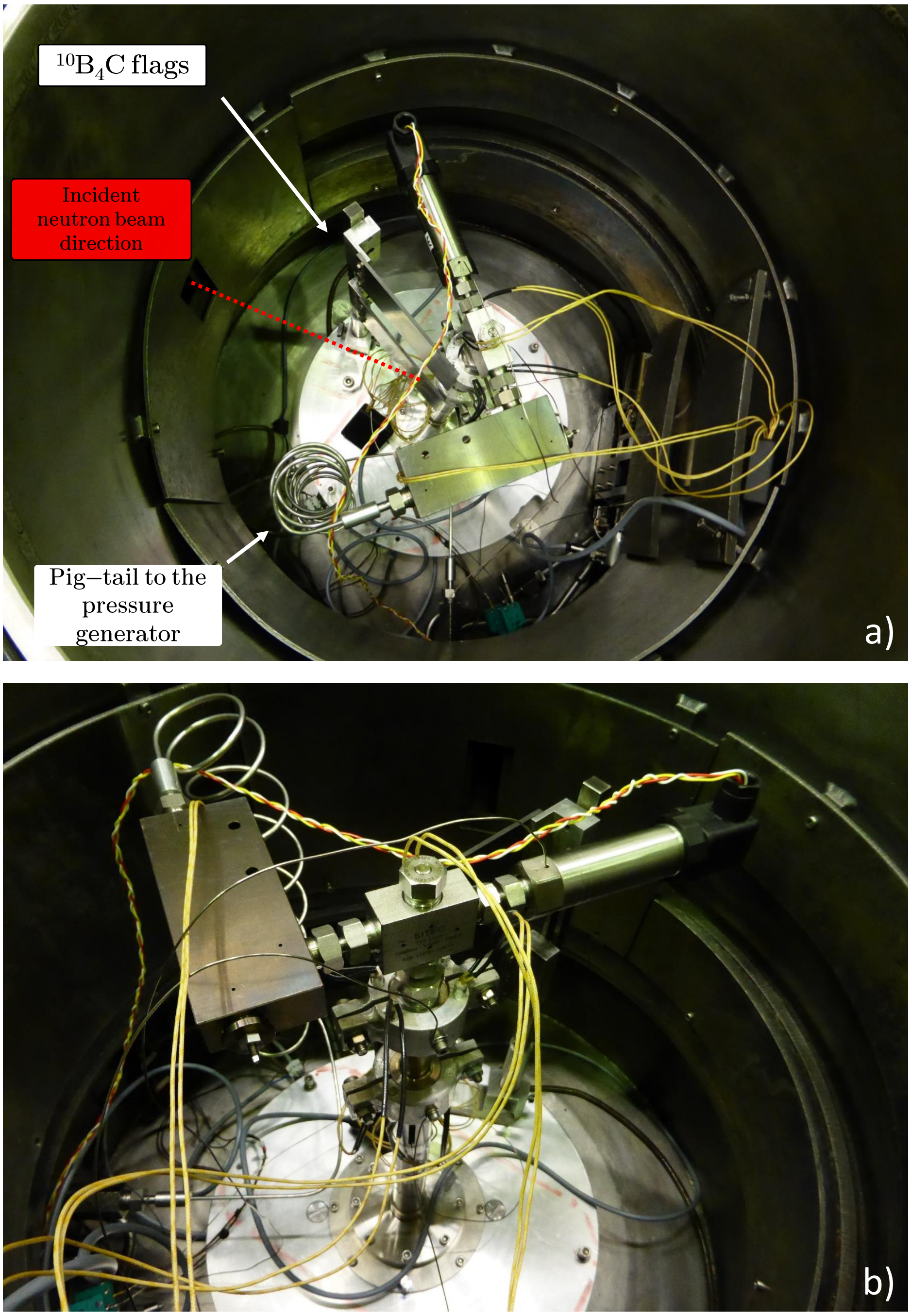

Figure 4-7: View of the D4c belljar once the setup is mounted. (a) The neutron-absorbing flags, made of $^{10}B_4C$, shield the setup by collimating the incident neutron beam. The orientation of the flags is kept constant for the different measurements. The separator is rotated horizontally and is connected to a pig-tail high-pressure capillary. (b) The cell is mounted on the candle-stick, the heating-clamps are connected, and the yellow wires of the cartridge heaters are suspended far from the can. The pressure transducer is to the right of the cross-union, while the separator is placed in a horizontal position and is connected to a pig-tail high-pressure capillary to the left.

4.4.3 The pressure, temperature and density dependence of the NaCl-D_2O solution

The state conditions reached with the Ti-Zr cell setup during the neutron-diffraction experiment are shown in Table 4.5 and Figure 4-8, where they are compared to those reached with the Paris-Edinburgh press. The temperature and pressure dependence of the mass density for the 5 m NaCl-D_2O solution is also shown. Density values for the Ti-Zr cell range were obtained from Potter and Brown [85], but values for a 5 m NaCl-D_2O solution in the Paris-Edinburgh press range are not available in the literature. For the higher pressure range, the density was estimated [23] by making use of diffraction data for D_2O collected with both the Ti-Zr pressure cell and the Paris-Edinburgh press. The principal peak position Q_{PP} in the total structure factor was then plotted as a function of the known number density [86] in the spanned pressure range from ambient to 33.8 kbar, and a linear dependence was found. Then, the Q_{PP} values measured for the NaCl-D_2O D4c experiment with the Ti-Zr pressure cell were plotted as a function of the number density, and an extrapolation was made for higher densities by assuming the same rate of change with pressure as found for D_2O [23]. In Table 4.5, the ratio between the number density ρ, and its value at ambient conditions ρ_0, shows that the number density decreases with increasing temperature at constant pressure, and increases with pressure at constant temperature, such that $\rho/\rho_0 \approx 1$ at 1 kbar and 150 °C.

Table 4.5: The temperature and pressure dependence of the mass density ρ for a 5 m solution of NaCl-D_2O, and its ratio with the number density ρ_0 at ambient conditions. The densities for the Ti-Zr pressure cell range were taken from Potter and Brown [85], while the values for the Paris-Edinburgh press range were estimated [23].

Setup	Temperature (°C)	Pressure (kbar)	ρ (Å^{-3})	ρ / ρ_0
	25	0.001	0.09536	1.00000
Ti-Zr cell	50(1)	0.10(1)	0.09468	0.99287
	100(2)	0.10(1)	0.09233	0.96823
	150(4)	0.10(1)	0.08951	0.93865
	150(4)	0.50(1)	0.09175	0.96214
	150(4)	1.00(2)	0.09377	0.98333
PE-press	150(4)	2.4(5)	0.10177	1.06722
	150(4)	10.0(5)	0.11141	1.16831
	150(4)	22.4(5)	0.12748	1.33683
	150(4)	27.9(5)	0.13390	1.40415
	150(9)	33.8(5)	0.14033	1.47158

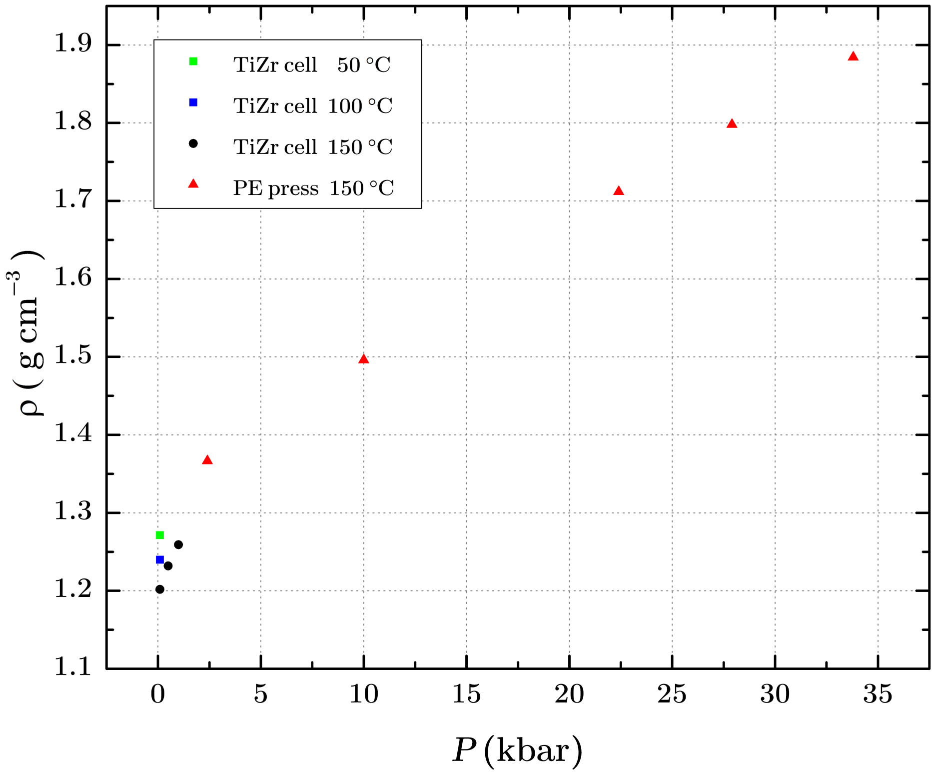

Figure 4-8: Temperature and pressure dependence of the mass density ρ for a 5 m solution of NaCl-D_2O. The values correspond to those reported in Table 4.5.

4.5 Results

In this section, the total structure factors and first-order difference functions obtained from the NDIS experiment for the 5 m NaCl-D_2O samples are presented. The data sets obtained with the Ti-Zr pressure cell are compared with those obtained with a Paris-Edinburgh press.

4.5.1 Total structure factors

Each total structure factor, $F(Q)$, was extracted from the measured differential scattering cross-section by fitting a fifth-order polynomial to $\frac{d\sigma(Q)}{d\Omega}Q$ to remove the Q-dependent slope that originates from inelastic scattering. Figure 4-9 shows examples of the fits obtained for the 5 m $\mathrm{Na}^{\mathrm{Nat}}$Cl-$D_2O$ solutions. This empirical method has previously been applied to the data sets obtained from water and ice Ih [23, 87].

The total structure factors for 5 m solutions of $\mathrm{Na}^{\mathrm{Nat}}$Cl-$D_2O$ and Na^{37}Cl-D_2O measured with the Ti-Zr pressure cell are shown in Figures 4-10 and 4-11, respectively. For comparison, the total structure factors for 5 m solutions of $\mathrm{Na}^{\mathrm{Mix}}$Cl-$D_2O$ and Na^{35}Cl-D_2O measured using the Paris-Edinburgh press are shown in Figure 4-12 and 4-13. The total pair-distribution functions $G(r)$ are shown in Figures 4-14 – 4-15 for the Ti-Zr cell data sets, and in Figures 4-16 – 4-17 for the Paris-Edinburgh press data sets. Table 4.6 gives the temperature and pressure dependence of the oxygen-deuterium peak position and coordination number.

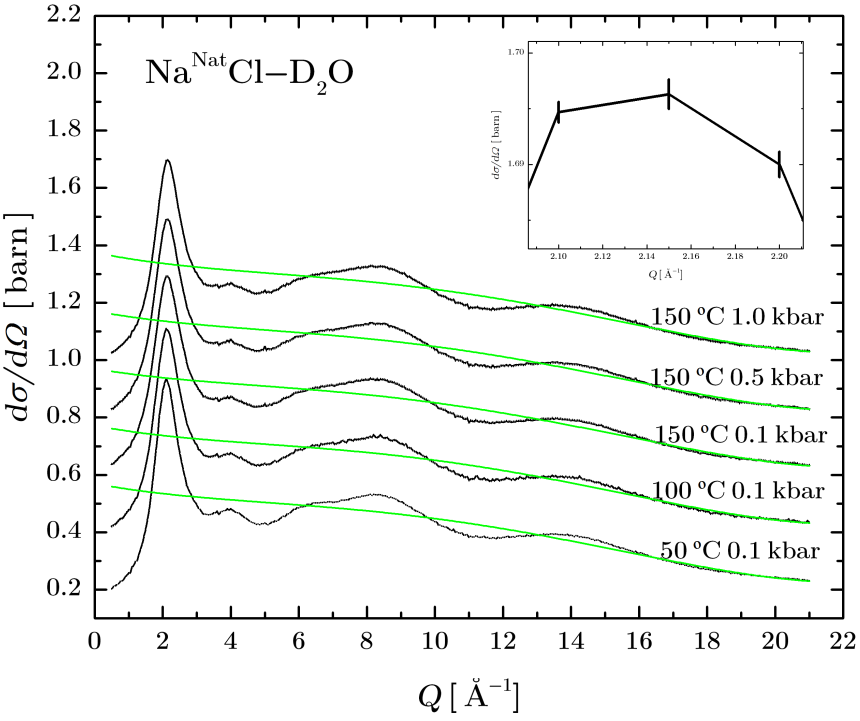

Figure 4-9: The solid black lines with vertical error bars are the differential scattering cross-sections for a 5 *m* $Na^{Nat}Cl-D_2O$ solution measured using the Ti-Zr cell. The solid green lines are the fits used to remove the Q-dependent slope that originates from inelastic scattering. The inset zooms into the the error bars that are hardly distinguishable, given the high-quality counting statistics.

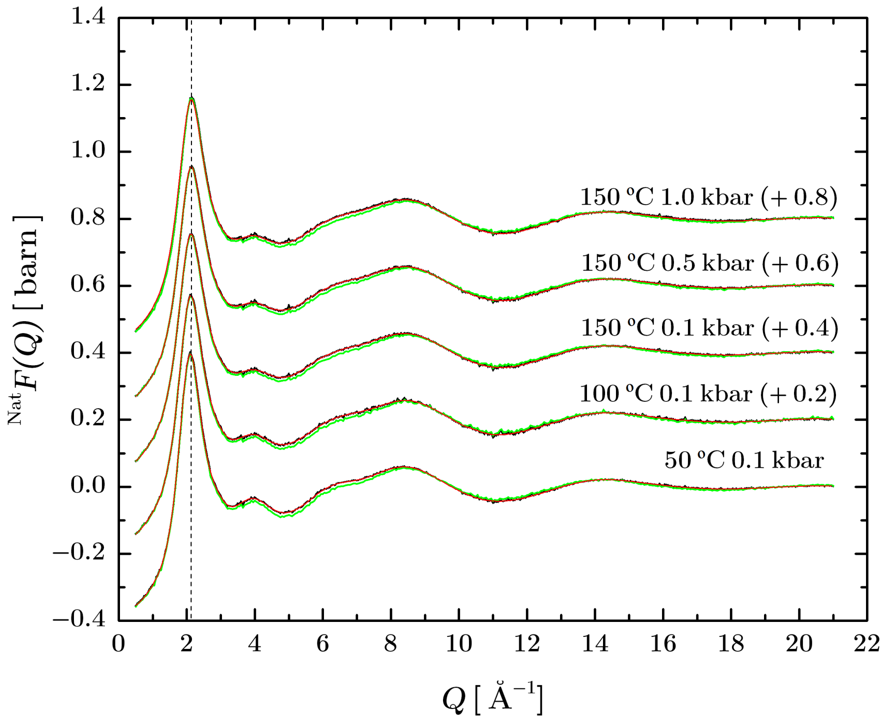

Figure 4-10: The temperature and pressure dependence of the total structure factor $^{\mathrm{Nat}}F(Q)$ for a 5 m Na$^{\mathrm{Nat}}$Cl-D$_2$O solution. The solid black lines are the data sets measured using a Ti-Zr heated pressure-cell, where vertical offsets, indicated in parenthesis, are used for clarity of presentation. The vertical error bars are hardly distinguishable given the high-quality counting statistics. The red curves show spline fits to the experimental datasets. The green curves are the back-Fourier transforms of the $G(r)$ functions shown in Figure 4-14, once the low-r oscillations are set to their theoretical limit. The dashed vertical black line is plotted as a reference for the first peak position at 50 °C and 0.1 kbar.

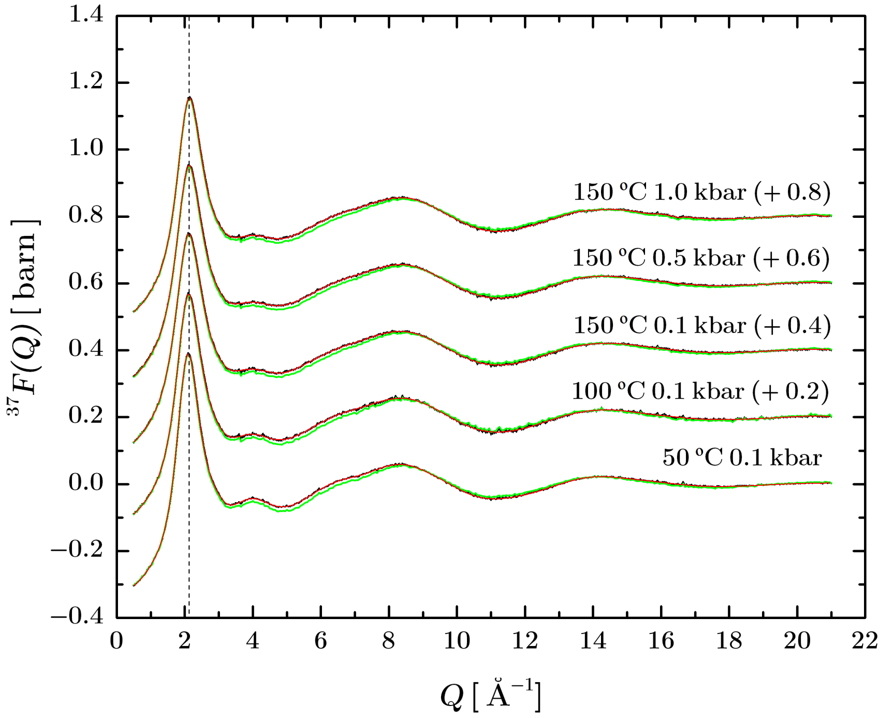

Figure 4-11: The temperature and pressure dependence of the total structure factor $^{37}F(Q)$ for a 5 m Na^{37}Cl-D$_2$O solution. The solid black lines are the data sets measured using a Ti-Zr heated pressure-cell, where vertical offsets, indicated in parenthesis, are used for clarity of presentation. The vertical error bars are hardly distinguishable given the high-quality counting statistics. The red curves show spline fits to the experimental datasets. The green curves are the back-Fourier transforms of the $G(r)$ functions in Figure 4-15, once the low-r oscillations are set to their theoretical limit. The dashed vertical black line is plotted as a reference for the first peak position at 50 °C and 0.1 kbar.

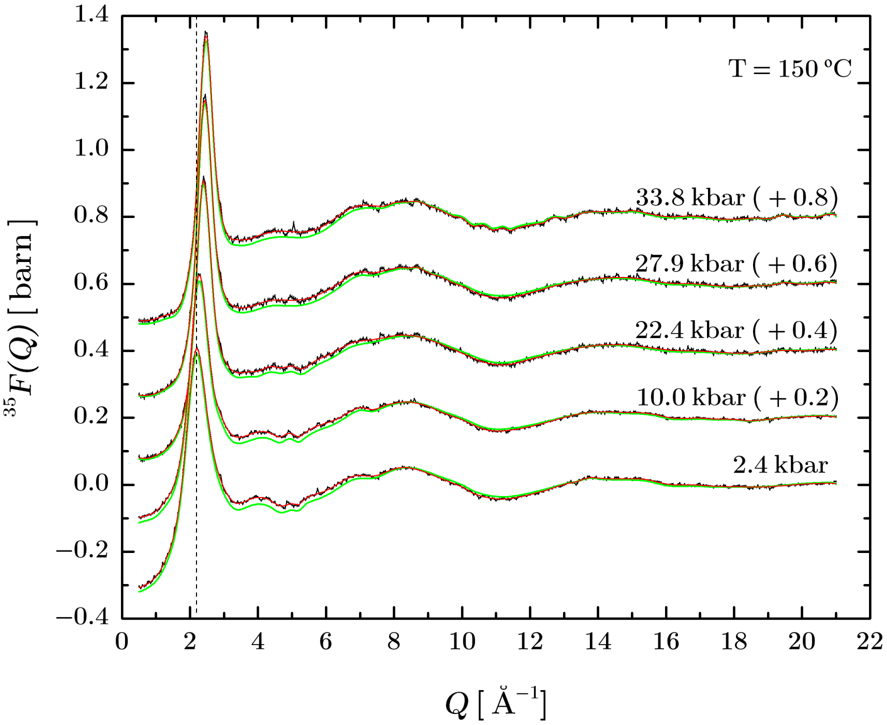

Figure 4-12: The pressure dependence of the total structure factor $^{35}F(Q)$ for a 5 m Na^{35}Cl-D$_2$O solution. The solid black lines are the data sets measured using a Paris-Edinburgh press with heated anvils. Vertical offsets, indicated in parenthesis, are used for clarity of presentation. The vertical error bars are hardly distinguishable given the high-quality counting statistics. The red curves show spline fits to the experimental datasets. The green curves are the back-Fourier transforms of the $G(r)$ functions shown in Figure 4-16, once the low-r oscillations are set to their theoretical limit. The dashed vertical black line is plotted as a reference for the first peak position at 150 °C and 2.4 kbar.

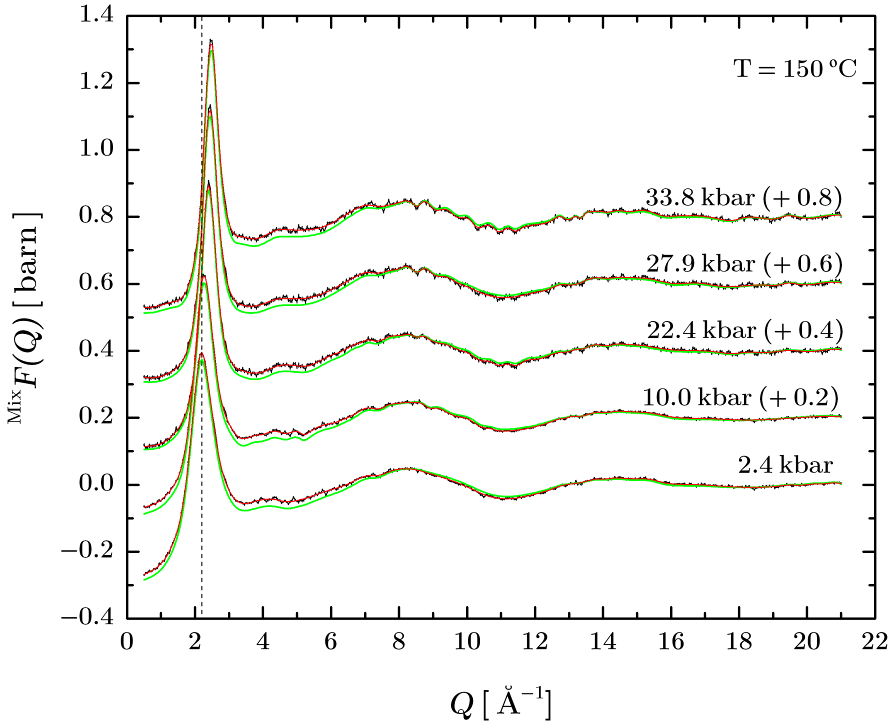

Figure 4-13: The pressure dependence of the total structure factor $^{\mathrm{Mix}}F(Q)$ of a 5 m $\mathrm{Na}^{\mathrm{Mix}}\mathrm{Cl}$-$\mathrm{D_2O}$ solution. The solid black lines are the data sets measured using a Paris-Edinburgh press with heated anvils. Vertical offsets, indicated in parenthesis, are used for clarity of presentation. The vertical error bars are hardly distinguishable given the high-quality counting statistics. The red curves show spline fits to the experimental datasets. The green curves are the back-Fourier transforms of the $G(r)$ functions shown in Figure 4-17, once the low-r oscillations are set to their theoretical limit. The dashed vertical black line is plotted as a reference for the first peak position at 150 °C and 2.4 kbar.

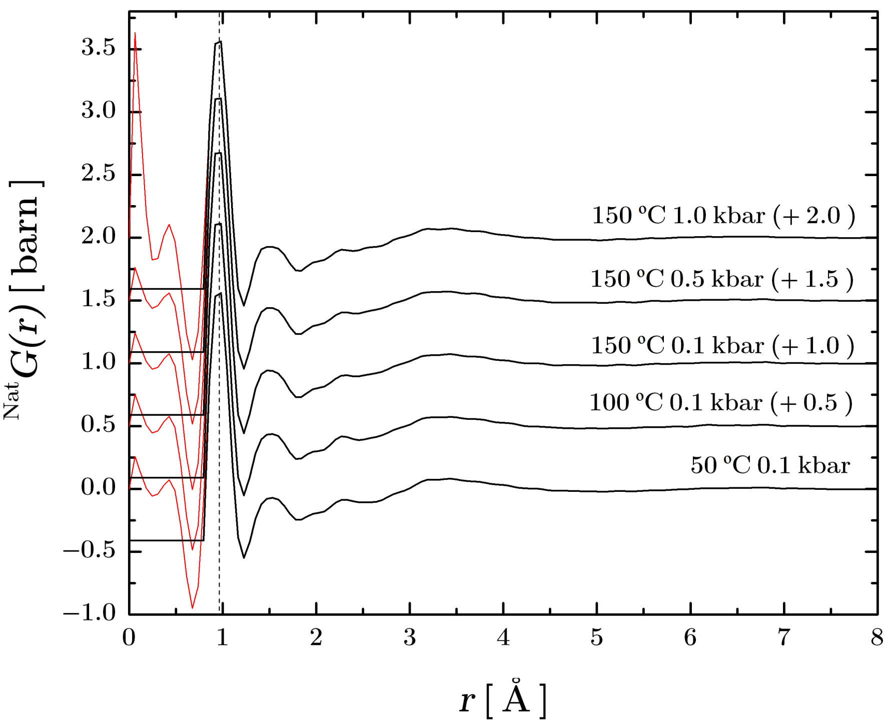

Figure 4-14: The temperature and pressure dependence of the total pair-distribution function ${}^{\mathrm{Nat}}G(r)$ for a 5 m $\mathrm{Na}^{\mathrm{Nat}}\mathrm{Cl}$-$\mathrm{D_2O}$ solution. The solid black curves give the ${}^{\mathrm{Nat}}G(r)$ functions obtained by Fourier-transforming the ${}^{\mathrm{Nat}}F(Q)$ functions of Figure 4-10, and are set to the calculated ${}^{\mathrm{Nat}}G(r \to 0)$ limit at r-values smaller than the distance of closest approach between the centres of two atoms. The solid red curves show the Fourier transform artefacts in the low-r region. The dashed vertical black line is plotted as a reference for the peak position at 50 °C and 0.1 kbar. Vertical offsets, indicated in parenthesis, are used for clarity of presentation.

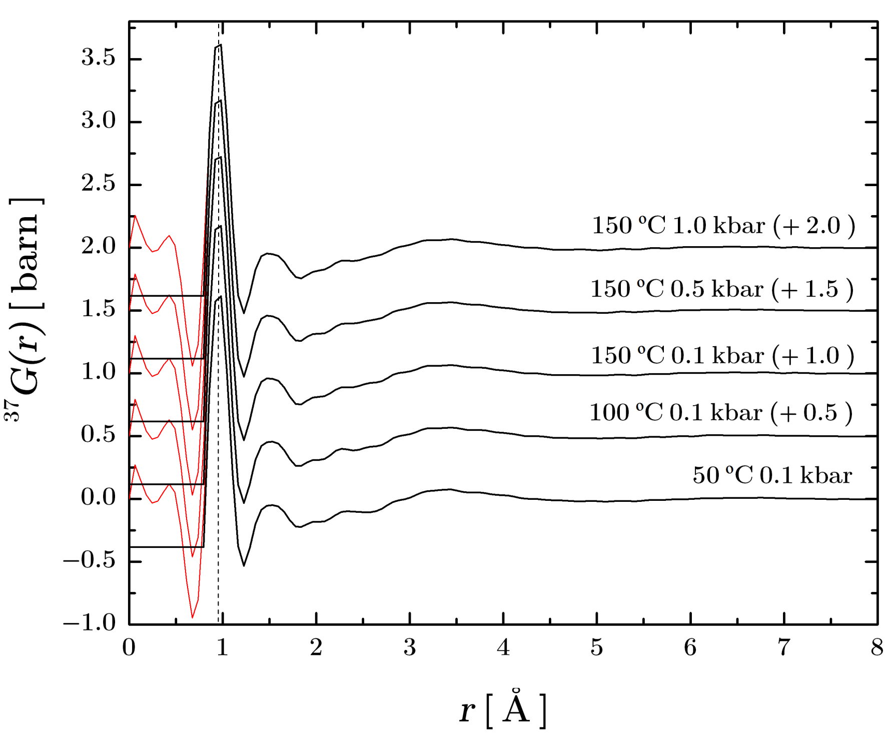

Figure 4-15: The temperature and pressure dependence of the total pair-distribution function $^{37}G(r)$ for a 5 m Na^{37}Cl-D$_2$O solution. The solid black curves give the $^{37}G(r)$ functions obtained by Fourier-transforming the $^{37}F(Q)$ functions in Figure 4-11, and are set to the calculated $^{37}G(r \to 0)$ limit at r-values smaller than the distance of closest approach between the centres of two atoms. The solid red curves show the Fourier transform artefacts in the low-r region. The dashed vertical black line is plotted as a reference for the peak position at 50 °C and 0.1 kbar. Vertical offsets, indicated in parenthesis, are used for clarity of presentation.

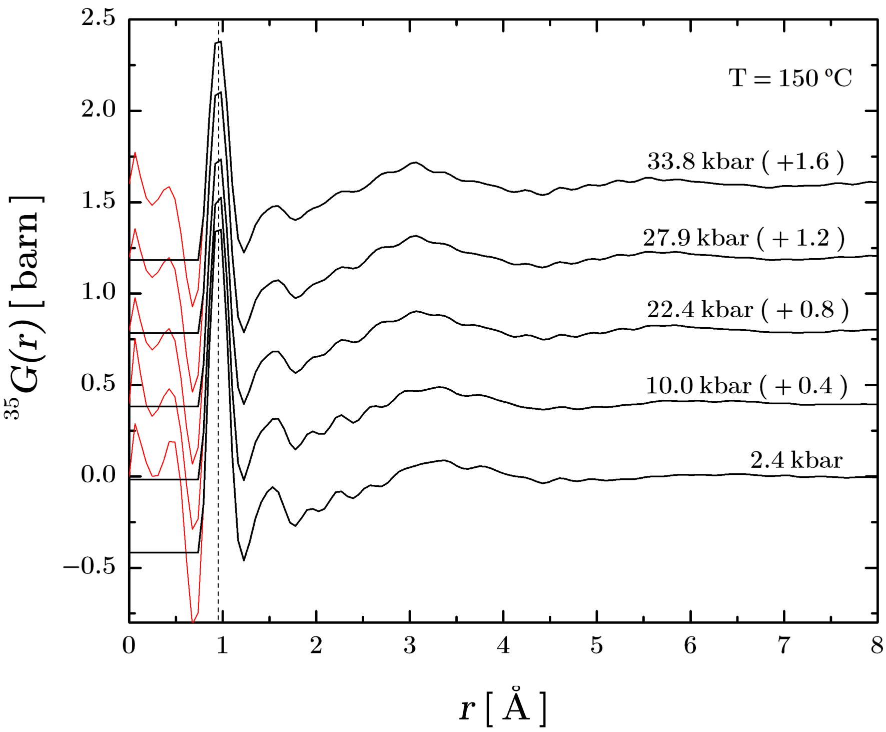

Figure 4-16: The pressure dependence of the total pair-distribution function $^{35}G(r)$ for a 5 m Na^{35}Cl-D$_2$O solution. The solid black curves give the $^{35}G(r)$ functions obtained by Fourier-transforming the $^{35}F(Q)$ functions in Figure 4-12, and are set to the calculated $^{35}G(r \to 0)$ limit at r-values smaller than the distance of closest approach between the centres of two atoms. The solid red curves show the Fourier transform artefacts in the low-r region. The dashed vertical black line is plotted as a reference for the peak position at 150 °C and 2.4 kbar. Vertical offsets, indicated in parenthesis, are used for clarity of presentation.

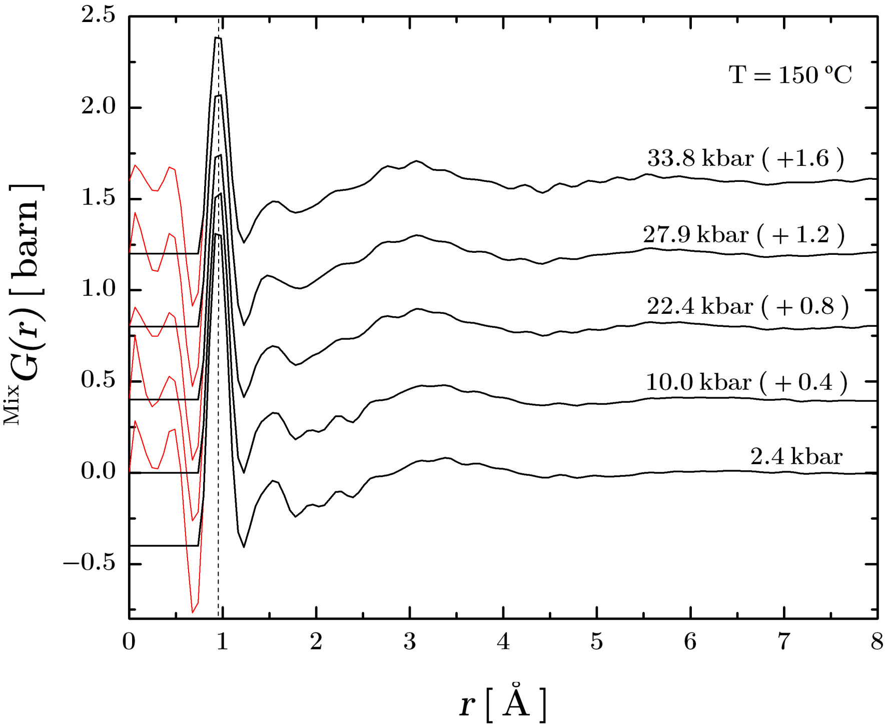

Figure 4-17: The pressure dependence of the total pair-distribution function $^{\rm Mix}G(r)$ for a 5 m Na$^{\rm Mix}$Cl-D$_2$O solution. The solid black curves give the $^{\rm Mix}G(r)$ functions obtained by Fourier-transforming the $^{\rm Mix}F(Q)$ functions in Figure 4-13, and are set to the calculated $^{\rm Mix}G(r \to 0)$ limit at r-values smaller than the distance of closest approach between the centres of two atoms. The solid red curves show the Fourier transform artefacts in the low-r region. The dashed vertical black line is plotted as a reference for the peak position at 150 °C and 2.4 kbar. Vertical offsets, indicated in parenthesis, are used for clarity of presentation.

Sample	Setup	Temperature (°C)	Pressure (kbar)	r_{OD} (Å)	$\overline{n}_{\mathrm{O}}^{\mathrm{D}}$
$\mathrm{Na^{Nat}Cl\text{-}D_2O}$	TiZr cell	50(1)	0.10(1)	0.95(1)	2.04(1)
		100(2)	0.10(1)	0.95(1)	2.02(1)
		150(4)	0.10(1)	0.95(1)	2.02(1)
		150(4)	0.50(1)	0.95(1)	2.02(1)
		150(4)	1.0(5)	0.95(1)	2.01(1)
$\mathrm{Na^{37}Cl\text{-}D_2O}$	TiZr cell	50(1)	0.10(1)	0.96(1)	2.04(1)
		100(2)	0.10(1)	0.95(1)	2.04(1)
		150(4)	0.10(1)	0.95(1)	2.03(1)
		150(4)	0.50(1)	0.95(1)	2.04(1)
		150(4)	1.0(5)	0.95(1)	2.03(1)
$\mathrm{Na^{35}Cl\text{-}D_2O}$	PE press	150(4)	2.4(5)	0.95(2)	2.04(3)
		150(4)	10.0(5)	0.96(2)	1.97(3)
		150(4)	22.4(5)	0.95(2)	2.02(3)
		150(9)	27.9(5)	0.95(2)	2.06(3)
		150(9)	33.8(5)	0.95(2)	2.02(3)
$\mathrm{Na^{Mix}Cl\text{-}D_2O}$	PE press	150(4)	2.4(5)	0.95(2)	1.97(3)
		150(4)	10.0(5)	0.95(2)	1.96(3)
		150(4)	22.4(5)	0.96(2)	2.01(3)
		150(9)	27.9(5)	0.96(2)	2.04(3)
		150(9)	33.8(5)	0.95(2)	2.00(3)

Table 4.6: Pressure dependence of the oxygen-deuterium peak position r_{OD} and coordination number $\overline{n}_{\mathrm{O}}^{\mathrm{D}}$ as found from the first peak in the measured $G(r)$ functions shown in Figures 4-14, 4-15, 4-16 and 4-17.

4.5.2 Difference functions

The first-order difference functions $\Delta F_{\mathrm{Cl}}(Q)$ that were obtained for the Ti-Zr cell setup are shown in Figure 4-18, and those obtained for the Paris-Edinburgh press setup are shown in Figure 4-19. A comparison between the two sets of $\Delta F_{\mathrm{Cl}}(Q)$ functions is shown in Figure 4-20.

The Paris-Edinburgh press difference functions presented here were obtained by using a different method to that used by Rowlands in [23]. In fact, she formed difference functions by using an equation equivalent to Eq.(4.3), by assuming that $A^{35}_{\mathrm{C,SC}}(\theta) = A^{\mathrm{Mix}}_{\mathrm{C,SC}}(\theta)$, $A^{35}_{\mathrm{S,SC}}(\theta) = A^{\mathrm{Mix}}_{\mathrm{S,SC}}(\theta)$ and that the multiple-scattering contributions for both samples are identical, such that

$$\Delta F_{\mathrm{Cl}}(Q) + c_{\mathrm{Cl}}(\bar{b}^2_{^{35}\mathrm{Cl}} - \bar{b}^2_{^{\mathrm{Mix}}\mathrm{Cl}}) = \frac{I^{35}_{\mathrm{SC}}(\theta) - I^{\mathrm{Mix}}_{\mathrm{SC}}(\theta)}{a(\theta) N_S A_{\mathrm{S,SC}}(\theta)}, \tag{4.14}$$

where $A_{\mathrm{S,SC}}(\theta)$ is an average of $A^{35}_{\mathrm{C,SC}}(\theta)$ and $A^{\mathrm{Mix}}_{\mathrm{C,SC}}(\theta)$. This assumption is not valid, however, because there is a difference of about 1% between $A^{35}_{\mathrm{C,SC}}(\theta)$ and $A^{\mathrm{Mix}}_{\mathrm{C,SC}}(\theta)$, which compares to a difference of about 4% between $A^{\mathrm{Nat}}_{\mathrm{C,SC}}(\theta)$ and $A^{37}_{\mathrm{C,SC}}(\theta)$. Difference functions for the Paris-Edinburgh press data sets were therefore formed by subtracting the $\frac{d\sigma(Q)}{d\Omega}$ functions for the Na^{35}Cl-D$_2$O and Na$^{\mathrm{Mix}}$Cl-D$_2$O samples, after the corrections for attenuation and multiple scattering were applied following Eqs. (4.3) – (4.4).

The $\Delta G_{\mathrm{Cl}}(r)$ functions measured using the Ti-Zr cell are shown in Figure 4-21. Figure 4-22 shows the temperature dependence of the first peak in $\Delta G_{\mathrm{Cl}}(r)$ when the pressure is kept constant at 0.1 kbar and the temperature is increased from 50 °C to 150 °C. Figure 4-23 shows the pressure dependence of the first peak in $\Delta G_{\mathrm{Cl}}(r)$ when the temperature is kept constant at 150 °C, and pressure increased from 0.1 to 1 kbar.

The $\Delta G_{\mathrm{Cl}}(r)$ functions measured using the Paris-Edinburgh press are shown in Figure 4-24. A comparison of the real-space functions at 150 °C and in the pressure range between 0.1 and 33.8 kbar is shown in Figure 4-25. To facilitate this comparison, the real-space information is expressed in terms of the normalised function

$$\Delta G'_{\mathrm{Cl}}(r) = \frac{\Delta G_{\mathrm{Cl}}(r) - \Delta G_{\mathrm{Cl}}(r \to 0)}{A}. \tag{4.15}$$

such that the first peak gives $g_{\mathrm{ClD}}(r)$ in the absence of other overlapping partial pair-distribution functions (see Eq.(4.12)). Figure 4-26 shows the temperature dependence of the Cl-D weighted peak position and coordination number at a constant pressure of 0.1 kbar. Figure 4-27 shows the pressure dependence of the Cl-D weighted peak position and coordination number at a constant temperature of 150 °C. Values for the Cl-D bond distances, weighted peak positions and coordination numbers are listed in Tables 4.7 – 4.8.

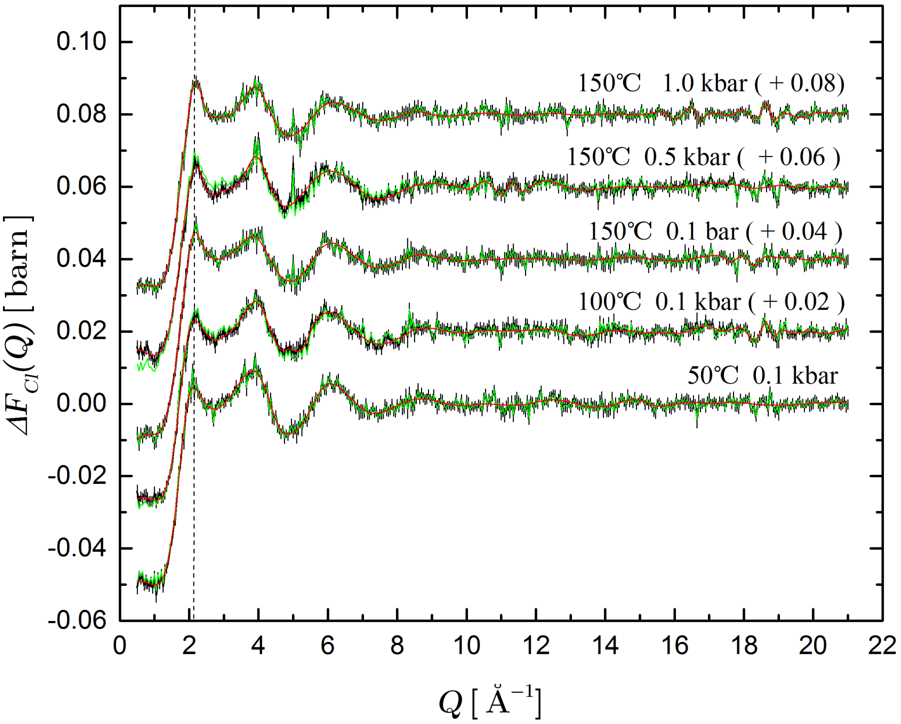

Figure 4-18: The temperature and pressure dependence of the first-order difference function $\Delta F_{\mathrm{Cl}}(Q)$ for a 5 m NaCl-D$_2$O solution. The difference functions were obtained from the total structure factors shown in Figures 4-10 and 4-11. The solid black lines are the measured data sets, with vertical black error bars. The red curves show spline fits to the experimental datasets. The green curves are the back-Fourier transforms of the $\Delta G_{\mathrm{Cl}}(r)$ functions shown in Figure 4-21, once the low-r oscillations are set to their theoretical limit. The data sets are offset vertically, for clarity of presentation, and the offsets are indicated in parenthesis. The dashed vertical black line is plotted as a reference for the first peak position at 50 °C and 0.1 kbar.

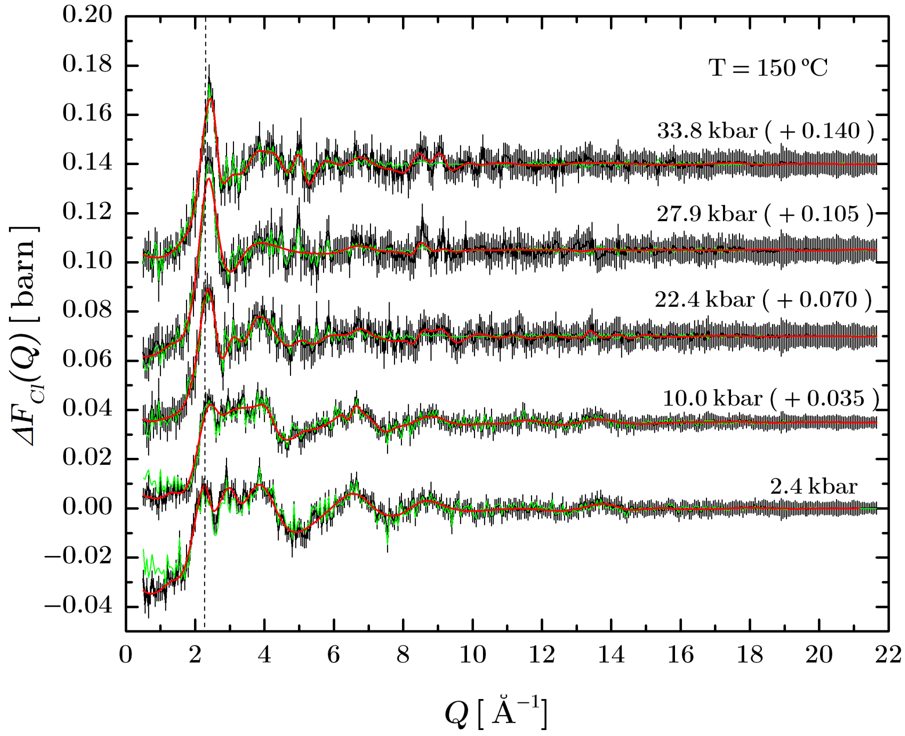

Figure 4-19: The pressure dependence of the first-order difference function $\Delta F_{\mathrm{Cl}}(Q)$ for a 5 m NaCl-D_2O solution. The difference functions were obtained from the total structure factors shown in Figures 4-13 and 4-12. The solid black lines are the measured data sets, with vertical black error bars. The red curves show spline fits to the experimental datasets. The green curves are the back-Fourier transforms of the $\Delta G_{\mathrm{Cl}}(r)$ functions shown in Figure 4-21, once the low-r oscillations are set to their theoretical limit. The data sets are offset vertically, for clarity of presentation, and the offsets are indicated in parenthesis. The dashed vertical black line is plotted as a reference for the first peak position at 150 °C and 2.4 kbar.

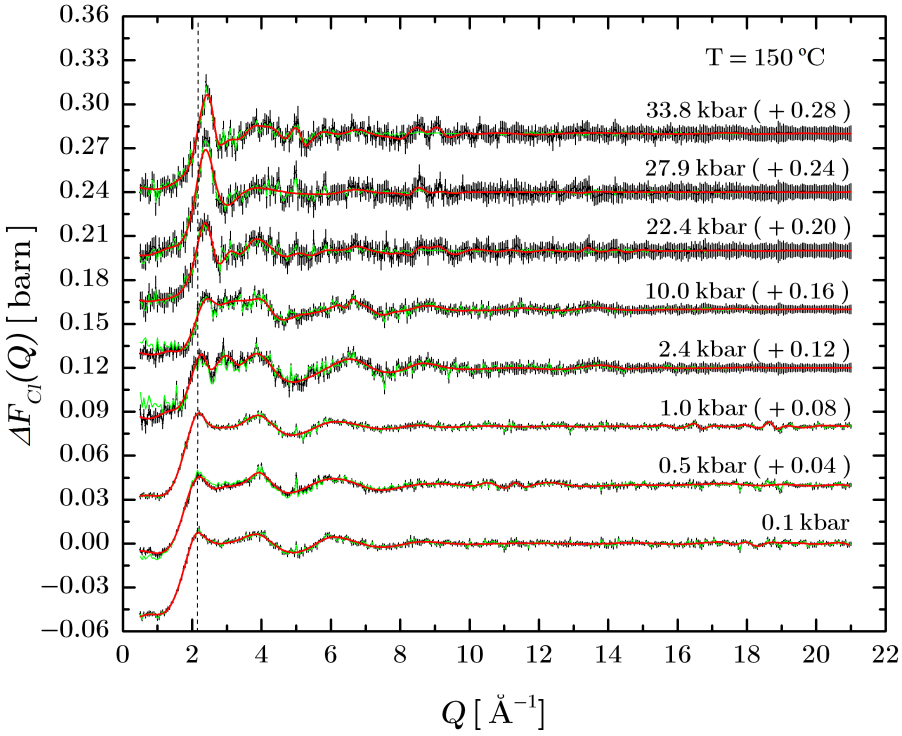

Figure 4-20: The pressure dependence of the first-order difference function $\Delta F_{\mathrm{Cl}}(Q)$ for a 5 m NaCl-D$_2$O solution at 150 °C. The data sets measured at pressures up to 1 kbar were obtained using a heated Ti-Zr pressure cell and are taken from Figure 4-18. The data sets measured at pressures higher than 1 kbar were obtained using a Paris-Edinburgh press with heated anvils and are taken from Figure 4-19. The solid black lines with vertical black error bars represent the measured data sets. The error bars are smaller for the data sets measured with the Ti-Zr pressure cell because the sample volume ($\approx$ 1 ml) was 30 times larger than the volume (30 μl) corresponding to the Ti-Zr gaskets of the PE press. The red curves show spline fits to the experimental datasets. The green curves are the back-Fourier transforms of the respective $\Delta G_{\mathrm{Cl}}(r)$ functions, once the low-r oscillations are set to their theoretical limit. The data sets are offset vertically, for clarity of presentation, and the offsets are indicated in parenthesis. The dashed vertical black line is plotted as a reference for the first peak position at 0.1 kbar.

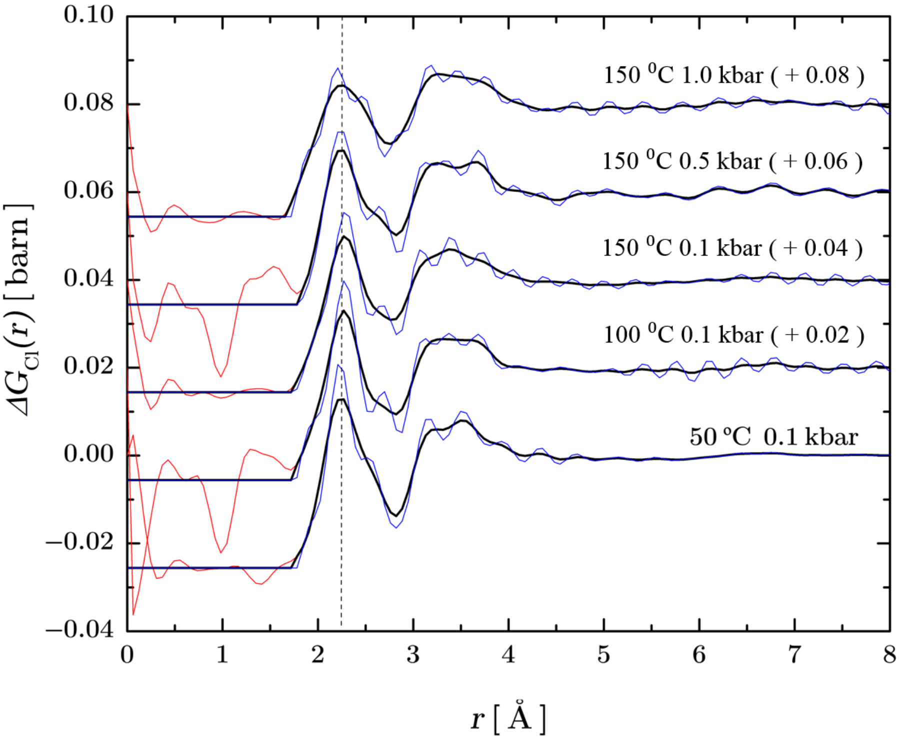

Figure 4-21: The temperature and pressure dependence of the first-order difference function $\Delta G_{\mathrm{Cl}}(r)$ for a 5 m NaCl-D$_2$O solution. The solid black lines were obtained by Fourier transforming the spline-fitted $\Delta F_{\mathrm{Cl}}(Q)$ functions shown in Figure 4-18, using a Lorch modification function with $Q_{\mathrm{max}} = 21$ Å^{-1}, and setting the low-r oscillations (red solid lines) to their theoretical limit. The solid blue lines were obtained by Fourier transforming the spline-fitted $\Delta F_{\mathrm{Cl}}(Q)$ functions shown in Figure 4-18, and setting the low-r oscillations to their theoretical limit. The data sets are offset vertically, for clarity of presentation, and the offsets are indicated in parenthesis. The dashed vertical black line is plotted as a reference for the peak position at 50 °C and 0.1 kbar.

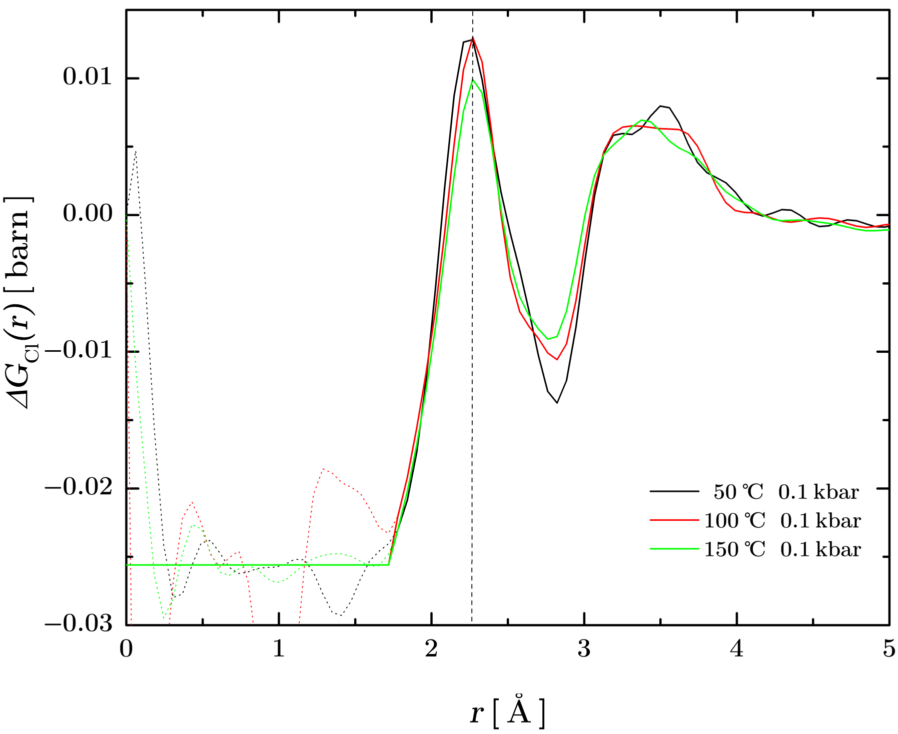

Figure 4-22: The temperature dependence of the first-order difference function $\Delta G_{\mathrm{Cl}}(r)$ for a 5 m NaCl-D_2O solution at 0.1 kbar. The solid lines were obtained by Fourier transforming the spline-fitted $\Delta F_{\mathrm{Cl}}(Q)$ functions at 0.1 kbar, using a Lorch modification function with $Q_{\max} = 21$ Å^{-1}, and setting the low-r oscillations (dashed lines) to their theoretical limit. The dashed vertical black line is plotted as a reference for the peak position at 50 °C.

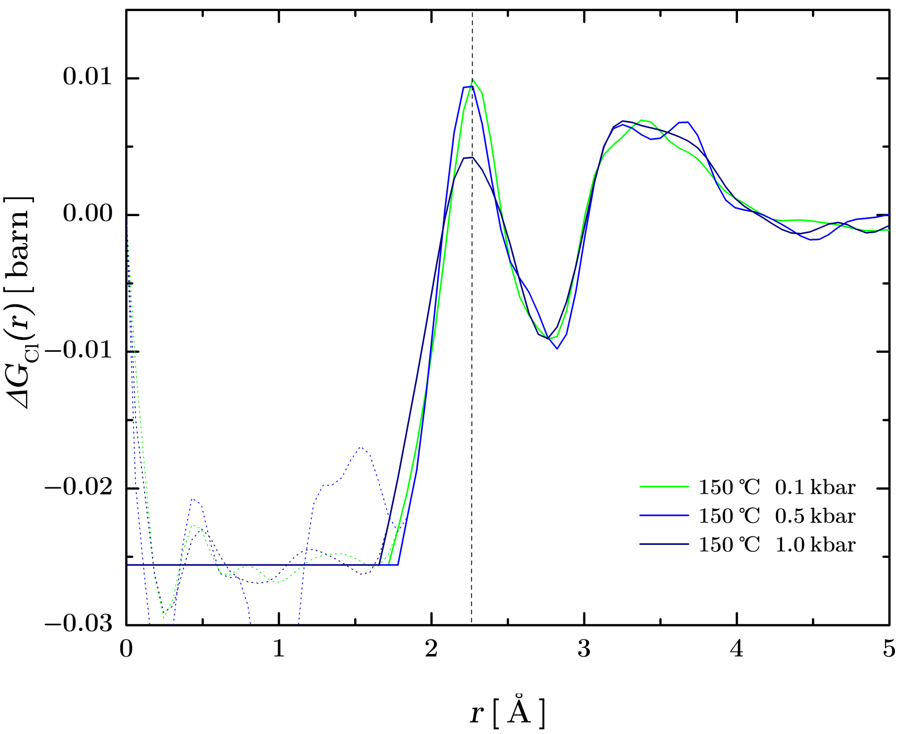

Figure 4-23: The pressure dependence of the first-order difference function $\Delta G_{\mathrm{Cl}}(r)$ for a 5 m NaCl-D_2O solution at 150 °C. The solid lines were obtained by Fourier transforming the spline-fitted $\Delta F_{\mathrm{Cl}}(Q)$ functions shown in Figure 4-18, using a Lorch modification function with $Q_{\mathrm{max}} = 21$ Å^{-1}, and setting the low-r oscillations (dashed lines) to their theoretical limit. The dashed vertical black line is plotted as a reference for the peak position at 0.1 kbar.

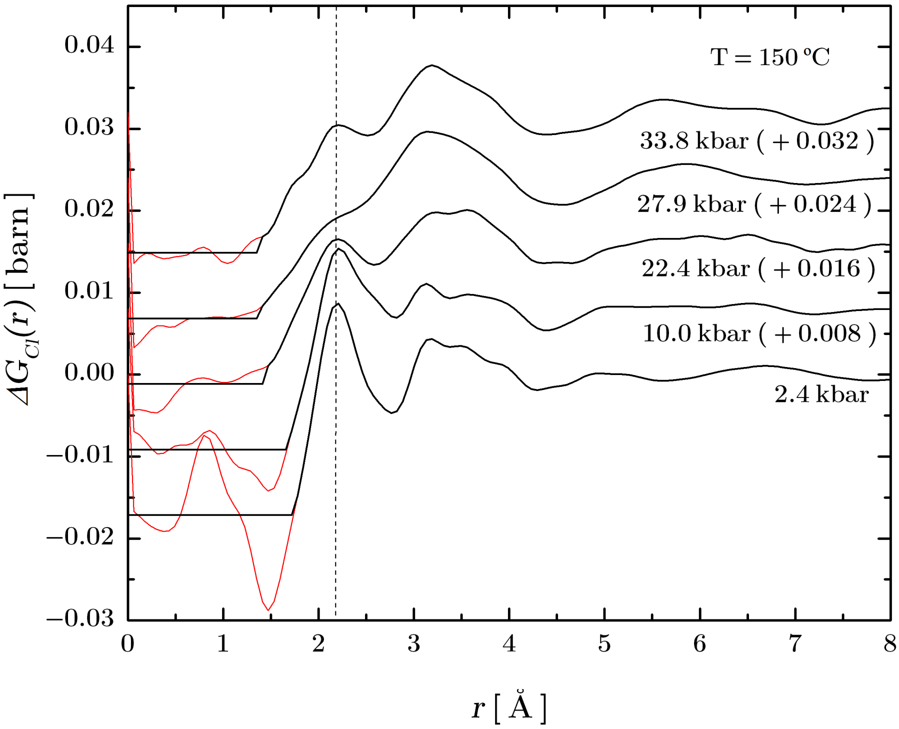

Figure 4-24: The pressure dependence of the first-order difference function $\Delta G_{\text{Cl}}(r)$ for a 5 m NaCl-D_2O solution. The solid black lines were obtained by Fourier transforming the spline- fitted $\Delta F_{\text{Cl}}(Q)$ functions shown in Figure 4-19, using a Lorch modification function with $Q_{\text{max}} = 9.75$ Å^{-1}, and setting the low-r oscillations (red solid lines) to their theoretical limit. The curves are offset vertically, for clarity of presentation, and the offsets are indicated in parenthesis. The dashed vertical black line is plotted as a reference for the peak position at 2.4 kbar.

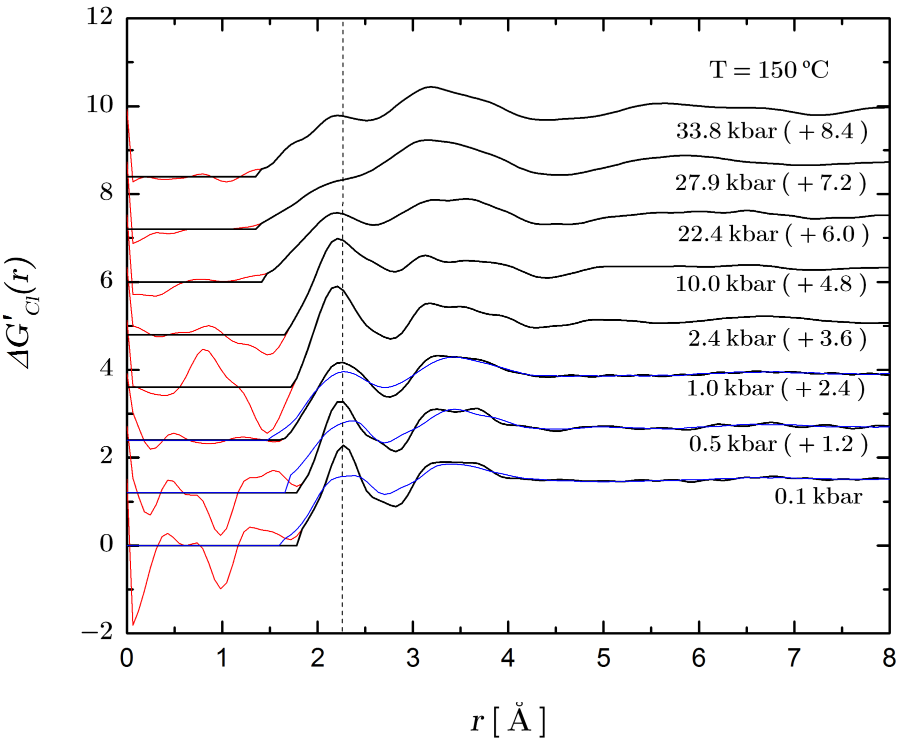

Figure 4-25: The pressure dependence of the normalised first-order difference function $\Delta G'_{\mathrm{Cl}}(r)$ for a 5 m NaCl-D_2O solution. The data sets measured at pressures up to 1 kbar were obtained by using a heated Ti-Zr pressure cell and are shown in Figure 4-21. The data sets measured at pressures higher than 1 kbar were obtained by using a Paris-Edinburgh press with heated anvils and are shown in Figure 4-24. The solid black lines were obtained by Fourier transforming the spline-fitted $\Delta F_{\mathrm{Cl}}(Q)$ functions shown in Figure 4-18 and 4-19, using a Lorch modification function with $Q_{\mathrm{max}} = 21$ Å^{-1} for pressures ≤ 1 kbar and $Q_{\mathrm{max}} = 9.75$ Å^{-1} for pressures > 1 kbar, and setting the low-r oscillations (red solid lines) to their theoretical limit. The solid blue lines were obtained by Fourier transforming the spline-fitted $\Delta F_{\mathrm{Cl}}(Q)$ functions shown in Figure 4-18, using a Lorch modification function with $Q_{\mathrm{max}} = 9.75$ Å^{-1} for pressures ≤ 1 kbar. The functions thus obtained were then normalised following Eq.(4.15). The curves are offset vertically, for clarity of presentation, and the offsets are indicated in parenthesis. The dashed vertical black line is plotted as a reference for the peak position at 0.1 kbar.

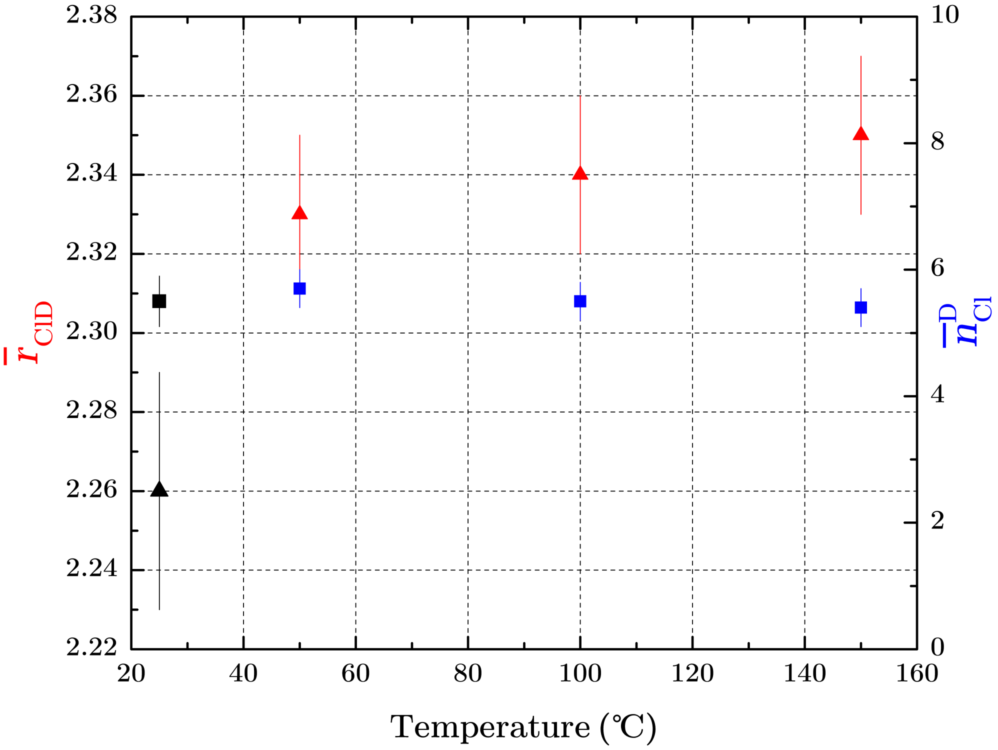

Figure 4-26: Temperature dependence of the chlorine-deuterium peak position $\bar{r}_{\mathrm{ClD}}$ (red triangles with error bars) and coordination number $\bar{n}_{\mathrm{Cl}}^{\mathrm{D}}$ (blue squares with error bars), at a constant pressure of 0.1 kbar, corresponding to a ρ/ρ_0 range that varies by ≈ 6 % (Table 4.5). The weighted peak position and coordination number, at ambient temperature and pressure [88] (black triangles and squares, respectively, with error bars) are also shown, to provide a reference value.

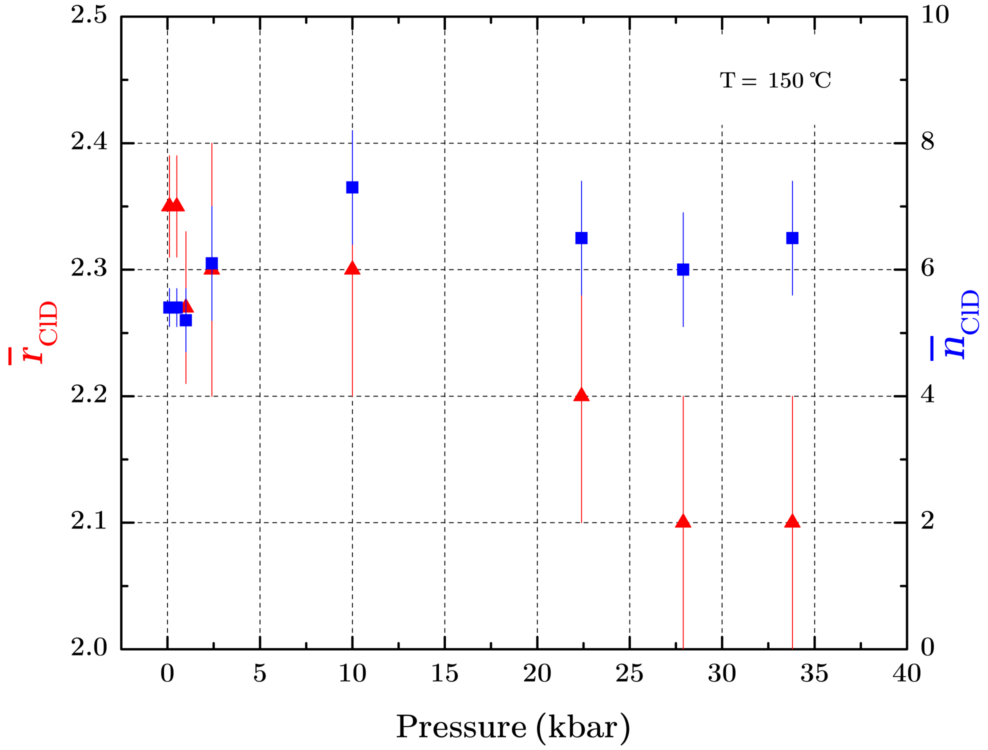

Figure 4-27: Pressure dependence of the chlorine-deuterium weighted peak-position $\overline{r}_{\mathrm{ClD}}$ (red triangles with error bars) and coordination number $\overline{n}_{\mathrm{Cl}}^{\mathrm{D}}$ (blue squares with error bars) at a constant temperature of 150 °C, corresponding to a ρ/ρ_0 range that varies by a ≈ 54 % difference (Table 4.5).

$\Delta G_{\mathrm{Cl}}(r)$	Setup	Temperature (°C)	r_{ClD} (Å)	$\overline{r}_{\mathrm{ClD}}$ (Å)	$\overline{n}_{\mathrm{Cl}}^{\mathrm{D}}$
$\mathrm{Na}^{\mathrm{Nat}-37}\mathrm{Cl}$	TiZr cell	50(1)	2.23(2)	2.33(2)	5.7(3)
		100(2)	2.27(2)	2.34(2)	5.5(3)
		150 (4)	2.28(2)	2.35(2)	5.4(3)

Table 4.7: Temperature dependence of the chlorine-deuterium peak position r_{ClD}, the weighted peak-position $\overline{r}_{\mathrm{ClD}}$, and the coordination number $\overline{n}_{\mathrm{Cl}}^{\mathrm{D}}$, at a pressure of 0.1 kbar. Values were obtained from the measured $\Delta G_{\mathrm{Cl}}(r)$ functions shown in Figures 4-21 and 4-22.

$\Delta G_{\mathrm{Cl}}(r)$	Setup	Pressure (kbar)	r_{ClD} (Å)	$\overline{r}_{\mathrm{ClD}}$ (Å)	$\overline{n}_{\mathrm{Cl}}^{\mathrm{D}}$
$\mathrm{Na}^{\mathrm{Nat}-37}\mathrm{Cl}$	TiZr cell	0.10(1)	2.28(4)	2.35(2)	5.4(3)
		0.50(1)	2.24(4)	2.35(2)	5.4(3)
		1.00(2)	2.24(4)	2.27(2)	5.2(5)
$\mathrm{Na}^{35-\mathrm{Mix}}\mathrm{Cl}$	PE press	2.4(5)	2.19(4)	2.27(6)	6.1(9)
		10.0(5)	2.21(4)	2.33(6)	7.3(9)*
		22.4(5)	2.19(4)	2.16(6)	6.5(9)*
		27.9(5)	2.36(4)	2.04(6)	6.0(9)*
		33.8(5)	2.39(4)	2.07(6)	6.5(9)*

Table 4.8: Pressure dependence of the chlorine-deuterium peak position r_{ClD}, the weighted peak-position $\overline{r}_{\mathrm{ClD}}$, and the coordination number $\overline{n}_{\mathrm{Cl}}^{\mathrm{D}}$ at a temperature of 150 °C. Values were obtained from the measured $\Delta G_{\mathrm{Cl}}(r)$ functions shown in Figures 4-21 and 4-24. Asterisks indicate coordination numbers that are ill-defined because of a broadening of the first peak in $\Delta G_{\mathrm{Cl}}(r)$.

4.6 Discussion

The total structure factors for the $Na^{Nat}Cl$-D_2O and $Na^{37}Cl$-D_2O solutions show a principal peak position at about 2.2 Å^{-1} that remains constant over the spanned temperature at pressures up to 1 kbar (Figures 4-10 and 4-11). For the same system, as studied via NDIS at ambient conditions, Enderby *et al.* also found a principal peak position at about 2.2 Å^{-1} [89]. The total structure factors for the $Na^{35}Cl$-D_2O and $Na^{Mix}Cl$-D_2O solutions are shown in Figures 4-12 and 4-13. In this case, the principal peak position becomes sharper and shifts from about 2.2 Å^{-1} to 2.5 Å^{-1}, as the pressure increases from 2.4 kbar to 33.8 kbar, at a constant temperature of 150 °C. For each $F(Q)$ function, there is good agreement between the measured data set and the back-Fourier transforms of $\Delta G_{\mathrm{Cl}}(r)$ after the low-r oscillations have been removed, except at Q-values between 4 and 6 Å^{-1}, *i.e.* where the fifth-order polynomial used to subtract the inelastic-scattering contribution to $\frac{d\sigma(Q)}{d\Omega}$ does not correct perfectly for the slope.

The first peak in the $G(r)$ functions of Figures 4-14 – 4-17 corresponds to the intra-molecular O-D correlations. The peak position gives the O-D intra-molecular bond distance, and this remains constant at about 0.95(1) Å over the temperature and pressure ranges spanned in both the Ti-Zr pressure cell and Paris-Edinburgh press experiments. Also, the coordination number of deuterium around oxygen is consistent with $\overline{n}_{\mathrm{O}}^{\mathrm{D}} = 2$, as expected for D_2O molecules, and does not evolve with temperature and pressure. These results are in agreement with those found from an NDIS experiment on a 1 m solution of NaCl-D_2O: at the state conditions defined by 300 °C and 0.12 kbar, or by 460 °C and 0.8 kbar, de Jong and Neilson [74] found $r_{\mathrm{OD}} = 0.97(2)$ Å and $\overline{n}_{\mathrm{O}}^{\mathrm{D}} = 2.0(1)$. Also, a bond distance $r_{\mathrm{OD}} = 0.96(2)$ Å is found from neutron-diffraction measurements on D_2O at ambient conditions [87], and in the pressure range between 2.4 and 33.8 kbar [90]. Zeidler *et al.* [91] find an intra-molecular bond distance $r_{\mathrm{OD}} = 0.985(5)$ Å for pure heavy water. Discrepancies between the measured r_{OD} values can arise from the different approaches used to correct data sets for inelastic scattering.

As shown in Figures 4-14 and 4-17, the first peak in $G(r)$ has a constant height and width as the temperature is first increased to 150 °C and the pressure is increased to 1.0 kbar. It then decreases in height and broadens when the pressure is increased to 33.8 kbar at 150 °C. Despite the fact that the first peak position and coordination number do not vary with the experimental conditions, the observed changes are likely to reflect alterations to the structure of water as the density is increased.

In fact, water at ambient conditions favours a tetrahedral hydrogen-bonded arrangement of the H_2O molecules (Fig. 4-28), that differs substantially from the structure

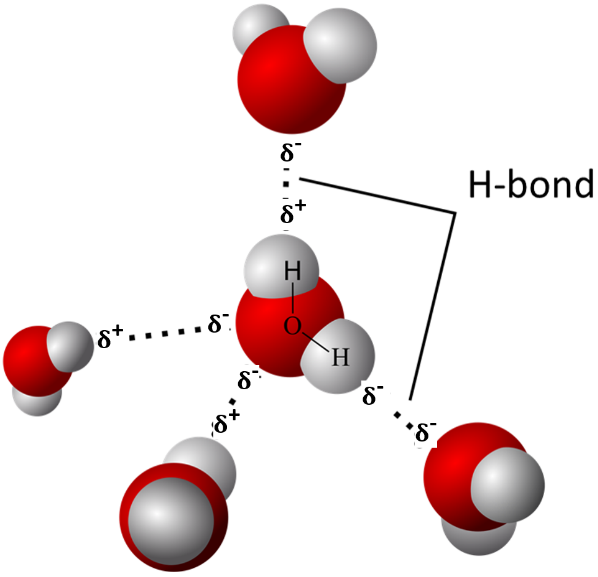

Figure 4-28: A tetrahedral arrangement of hydrogen-bonded water molecules [92]. The δ^- symbol denotes a partial negative charge near the oxygen atom, while the δ^+ symbol denotes a partial positive charge at the hydrogen position.

adopted by simple fluids, *i.e.* a classical system of approximately spherical, non polar molecules interacting via pair potentials. When the pressure is increased, the water structure is progressively modified as to resemble that of a simple fluid, as shown by: (1) neutron diffraction in which pressure and temperature were increased to 6.5 GPa and 670 K [93]; (2) X-ray diffraction in which pressure and temperature were increased to 17 GPa and 850 K [94, 95]; (3) molecular-dynamics simulations at pressures and temperatures up to 1.5 GPa and 500 K, respectively [69, 96]. Interestingly, such modifications are found to occur without a major change to the intra-molecular bond distance, distorting only a little the tetrahedral arrangement of the hydrogen bonds. Thus, the broadening of the first peak in $G(r)$ observed in the present work, which corresponds to a wider distribution of possible intra-molecular bond distances, is consistent with the experimental observations of water under pressure. It should also be pointed out that, as supported by previous studies, the intra-molecular structure of the water molecule is not affected markedly by the presence of ions, even at high concentrations [97].

The first-order difference functions $\Delta F_{\text{Cl}}(Q)$ are shown in Figures 4-18 – 4-20. The counting statistics are significantly better for the data sets measured with the Ti-Zr cell setup, as compared to the Paris-Edinburgh setup, because the sample volume (≈ 1 ml) was 30 times larger than the sample contained in the Ti-Zr gaskets of the PE press (30 μl). Also, there are difficulties in fully removing from $\Delta F_{\text{Cl}}(Q)$ the scattering from the Ti-Zr gaskets used in the PE press. For example, the feature at about $Q = 3$ Å^{-1}

in the 2.4 kbar measurement (Figure 4-20) is likely to originate from unwanted Ti-Zr scattering, as well as the features between 8 and 10 Å^{-1} for the data sets at pressures higher than 10 kbar.

Figure 4-18 shows that, although the first peak in $\Delta F_{\mathrm{Cl}}(Q)$ at 2.2 Å^{-1} becomes sharper with increasing temperature and pressure, its position does not shift significantly up to 150 °C and 1 kbar. This peak position is in agreement with the results found from two previous neutron-diffraction studies at ambient conditions: a peak position at about 2.3 Å^{-1} was found by Soper *et al.* [70] for a 5.32 *m* NaCl-D_2O solution, while Barnes *et al.* [77] report a peak position of about 2.2 Å^{-1} for a 3.62 *m* NaCl-D_2O solution. Figures 4-19–4-20 show a shift in the first peak position in $\Delta F_{\mathrm{Cl}}(Q)$, from $\approx$ 2.2 Å^{-1} to about 2.45 Å^{-1}, as the pressure is increased from 0.1 to 33.8 kbar at 150 °C. Also, the shape of the $\Delta F_{\mathrm{Cl}}(Q)$ becomes similar to that of a simple fluid as the pressure is increased to 33.8 kbar.

In real space, the $\Delta G_{\mathrm{Cl}}(r)$ function of Figure 4-21 show an evolution in the structure of the first peak. These functions were obtained by Fourier transforming the corresponding spline-fitted $\Delta F_{\mathrm{Cl}}(Q)$ functions, using a Lorch function with $Q_{\mathrm{max}} = 21$ Å^{-1}. At a constant pressure of 0.1 kbar, and temperature increasing from 50 °C to 150 °C, there is a shift in r_{ClD} from 2.23(2) to 2.29(2) Å, while $\overline{n}_{\mathrm{Cl}}^{\mathrm{D}}$ decreases from 5.7(3) to 5.4(5) as shown in Figure 4-26. These values for r_{ClD} are consistent with those found from previous experiments on NaCl-D_2O and other Cl-aqueous solutions [70, 77, 88] at ambient conditions. In particular, Soper *et al.* [70, 88] found $r_{\mathrm{ClD}} = 2.26(3)$ Å and $\overline{n}_{\mathrm{Cl}}^{\mathrm{D}} = 5.5(4)$ for a 5.32 *m* NaCl-D_2O solution [70, 88].

In Table 4.7, the weighted peak position is also reported as a function of temperature: $\overline{r}_{\mathrm{ClD}}$ increases from 2.33(2) to 2.35(2) Å, as the temperature is increased from 50 °C to 150 °C at 0.1 kbar, suggesting that the shift in the measured r_{ClD} value is a real effect of temperature rather then being related to the shape of the peak. An expansion of the first peak with increasing temperature therefore seems to be realistic. An analogous effect is also found for a 2 *m* solution of $NiCl_2$ as investigated at a constant pressure of 1 kbar with temperature increasing from 100 °C to 300 °C [72]: in this case, there is an increase of r_{ClD} from 2.30(3) to 2.39(4) Å, and a decrease of the Cl-D coordination number from 6.9(5) to 4.9(5).

Figure 4-22 shows an increase in the height of the $\Delta G_{\mathrm{Cl}}(r)$ function near the first-minimum position at about 2.8 Å, as the temperature is increased from 50 °C to 150 °C at 0.1 kbar, at a distance where the Na-Cl first neighbours are likely to be found [69]. This increase of height might be due to a combination of effects. For instance, thermal effects may lead to an increased rate of exchange between the deuterium atoms at distances corresponding to the first and second peaks around the Cl^-ion. Also, ion-pairing may increases with temperature, although this information cannot be inferred directly from $\Delta G_{\mathrm{Cl}}(r)$, because the contribution to the $\Delta G_{\mathrm{Cl}}(r)$ function from $g_{\mathrm{NaCl}}(r)$ is very small, as indicated by the weighting factors given in Table 4.4. For example, Shen *et al.* [69] performed molecular-dynamics simulations on a 1.7 m sodium chloride solution and found that when the temperature increases from 25 °C to 275 °C, at about 0.1 kbar, there is an increase in ion-pairing and a shift of the Na–Cl peak position towards lower-r values from about 3 to 2.8 Å. Also, they found that the height of the first Cl–D peak at ≈ 2.4 Å decreases with increasing temperature, while the magnitude $g_{\mathrm{ClD}}(r)$ increases at ≈ 3 Å. A simple explanation for this effect is based on the fact that the electrostatic Coulomb interaction between two ions in solution with charges q_1 and q_2 is modified by the presence of water, as expressed by the relative dielectric permittivity ϵ_r in the expression

$$F_{\mathrm{Coulomb}}(r) = \frac{q_1 q_2}{4\pi\epsilon_r\epsilon_0 r^2}. \tag{4.16}$$

As shown in Figure 4-29, at a pressure of 0.1 kbar, an increase in temperature from 50 °C to 150 °C corresponds to a strong decrease in ϵ_r from about 70 to 45. The observed decrease of the coordination number $\overline{n}_{\mathrm{Cl}}^{\mathrm{D}}$ with increasing temperature (Table 4.7), is therefore consistent with a decrease of the dielectric permittivity, which promotes ion-association rather than ion-hydration. The pressure dependence of $\Delta G_{\mathrm{Cl}}(r)$ at 150 °C is shown in Figures 4-23 and Table 4.8. In this case, there is a contraction of r_{ClD} from 2.35(2) Å to 2.07(6) Å, which is particularly marked when the pressure exceeds 1 kbar. The coordination number $\overline{n}_{\mathrm{Cl}}^{\mathrm{D}}$ does not vary substantially, being 5.4(2) at 0.1 kbar and 5.2(4) at 1 kbar. The small change in $\overline{n}_{\mathrm{Cl}}^{\mathrm{D}}$ is consistent with the behaviour of the dielectric permittivity that, at constant temperature, increases slowly with pressure (Figure 4-29), thereby favouring ion-hydration. However, the uncertainty in the measured coordination numbers is such that it is difficult to identify a clear trend.

Figures 4-24 and 4-25 show the $\Delta G_{\mathrm{Cl}}(r)$ functions obtained by Fourier transforming the corresponding spline-fitted $\Delta F_{\mathrm{Cl}}(Q)$ functions after a Lorch function is applied with $Q_{\max} = 9.75$ Å^{-1}. The modification function is used to smooth unphysical features in the $\Delta F_{\mathrm{Cl}}(Q)$ functions, without altering the shape of the main peaks at lower Q-values. As the pressure increases from 2.4 to 33.8 kbar at 150 °C, $\Delta G_{\mathrm{Cl}}(r)$ shows a first peak that becomes progressively broader and merges more-and-more with the second peak. In particular, at pressures higher than 2.4 kbar, the first shell becomes less developed, so that the identification of a first minimum for calculating the Cl-D coordination number becomes unclear. Table 4.8 and Figure 4-27 show a contraction of $\overline{r}_{\mathrm{ClD}}$ with increasing pressure, but the dependence of the Cl-D coordination number is not as clear. Such behaviour is difficult to understand in terms of the dielectric permittivity, because data are available for the latter only up to a maximum pressure of 5 kbar [98, 99]. Figure

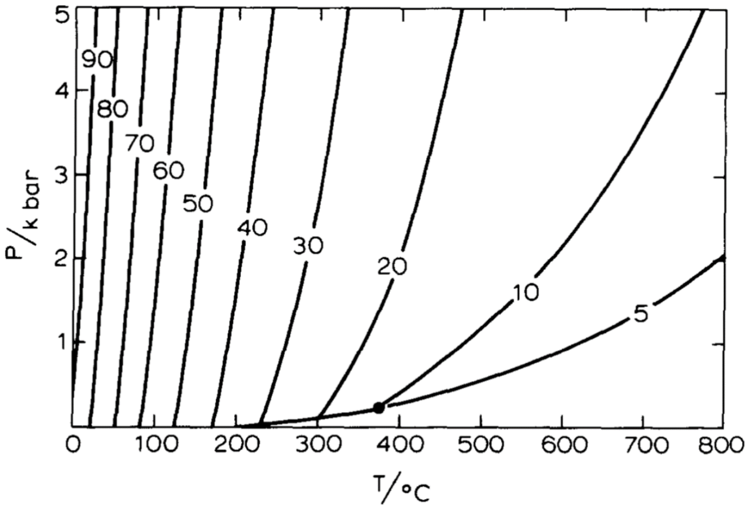

Figure 4-29: Variation of the relative dielectric permittivity ϵ_r with temperature and pressure. The curves are isopleths and are labelled accordingly. The filled circle represents the critical point of water [98].

4-29 shows that, at a constant temperature of 150 °C, ϵ increases from about 45 at ambient pressure to about 55 at 5 kbar, such that the change in dielectric permittivity should promote ion-hydration rather then Na-Cl ion-association. A possible way to interpret this change is that the effect of increasing pressure is to push both the first and second coordination shells closer to the Cl^-ion. The system progressively undergoes more frustration that leads to a broader angular and Cl-D bond-length distribution. However, it has to be noted that some of the broadening at these highest pressures arises from the limited Q-range ($Q_{\max} = 9.75$ Å^{-1}) used to form the $\Delta G'_{\mathrm{Cl}}(r)$ functions (Figure 4-25).

4.7 Conclusions

The neutron diffraction with isotope substitution experiments have provided new insight into the Cl^-ion coordination environment in a 5 m NaCl-D_2O solution, for a temperature and pressure range that had not been previously investigated. Two different setups involving either a Ti-Zr pressure cell or a Paris-Edinburgh press were employed. These setups allowed, in the first case, for a substantial improvement in the quality of data obtained under high-pressure conditions and, in the second case, to increase for the first time the investigated pressures up to 33.8 kbar.

The total structure factors and pair distribution functions show that the water molecules remain intact. At 150 °C and pressures up to 33.8 kbar the total structure factor evolves, becoming more simple-fluid like. In real space, this is accompanied by a broader range of possible O-D intra-molecular bond distances. However, the coordination number $\overline{n}_{\mathrm{O}}^{\mathrm{D}}$ is consistent with 2 over the entire temperature and pressure range that was spanned, suggesting that, even though pressure changes the distribution of intra-molecular O-D bond distances, it does not break these O-D intra-molecular bonds.

The difference functions formed in real space show that, at a constant pressure of 0.1 kbar and temperature increasing from 50 °C to 150 °C, the first shell expands. This effect, and the decrease of $\overline{n}_{\mathrm{Cl}}^{\mathrm{D}}$, can be related to the behaviour of the dielectric permittivity of water, which decreases with increasing temperature, thus favouring ion-association. At a constant temperature of 150 °C, an increase in pressure up to 1 kbar shows a compression of r_{ClD}, and a slight decrease in the Cl-D coordination number that is expected, given the behaviour of water's dielectric permittivity.

At higher pressures, the difference functions measured with the Paris-Edinburgh setup have lower-quality counting statistics as compared to the Ti-Zr pressure cell datasets. Despite this, the reciprocal-space functions show clear pressure-driven changes to the solution structure, which evolves, as for water, to become more simple-fluid like. In real space, these changes are reflected by a progressive evolution of the first and second peaks. The weighted peak position indicates a progressive shift towards lower r-values for the Cl first peak . The height of the minimum after the first peak position in $\Delta G_{\mathrm{Cl}}(r)$ becomes large at pressures higher than 2.4 kbar, making it difficult to identify reliable Cl-D coordination numbers.

A comparison of the present experimental results with those obtained from ongoing molecular-dynamics simulations should help to understand the contributions of the different $g_{\mathrm{Cl}\beta}(r)$ partial pair-distribution functions to $\Delta G_{\mathrm{Cl}}(r)$. Our findings emphasise the importance of a joint approach between neutron diffraction and molecular-dynamics simulations, in order to help in the interpretation of the new experimental information.

5. The structure of As_xSe_{1-x} glasses ($0.3 \leq x \leq 0.4$)

5.1 Introduction

Chalcogenide glasses (ChGs) are systems formed by one or more of the chalcogen elements S, Se and Te. The chalcogen is usually covalently bonded to a network-forming element such as As, Ge, Sb, Ga, Si or P. ChG-based technological applications include infra-red transmitting materials such as prisms, windows and wave-guides. They are also used as the host-matrix for infra-red lasers [2, 3]. The functionality of ChGs depends on the flexible or rigid nature of their underlying networks, and therefore a detailed understanding of the atomic-scale structure is required in order to tailor specific optical, electronic and mechanical properties. The structure of a network-forming glass can change its topology when the chemical composition is varied. Mean-field constraint-counting theory predicts that a change in the structure will occur, from an elastically floppy to a stressed-rigid phase, when the mean number of Lagrangian bonding constraints per atom, $\overline{N_c}$, equals three, the number of degrees of freedom per atom in three dimensions. An elastically-floppy phase is under-constrained ($\overline{N_c} < 3$) whereas a stressed-rigid phase is over-constrained ($\overline{N_c} > 3$). A system in which all of the bond-stretching and bond-bending constraints are intact, and which has no dangling bonds, is expected to undergo a transition between these phases at a mean coordination number $\bar{n} = 2.4$ [100, 101]. Furthermore, if the network can self-organise during its formation, by including structures that minimise over-constrained regions, two transitions can occur such that the floppy and stressed-rigid phases are separated by a composition range known as the intermediate phase (IP) [102].

Boolchand *et al.* [103] performed temperature-modulated differential scanning calorimetry experiments on the As_xSe_{1-x} system, finding an IP for the composition range $0.291(1) < x < 0.37(1)$. For these As-Se glasses, under the assumptions that: (1) As is 3 fold-coordinated; (2) Se is 2 fold-coordinated; (3) that there are no dangling bonds; the mean coordination number $\bar{n} = 2.4$ occurs when $x = 0.4$, meaning that the intermediate phase is shifted markedly from the mean-field expectation. First-principles molecular dynamics (FPMD) simulations for amorphous and liquid As_xSe_{1-x} systems, with $0.2 \leq x \leq 0.4$, point to thresholds and anomalies in the behavior of the reciprocal space functions, that can be linked to the IP region [24]. In the present work, the method of neutron diffraction with isotope substitution will be used to investigate the reciprocal-space features of the As_xSe_{1-x} glassy system.

In addition, the extent of the chemical ordering will be assessed. Here, two contrasting models exist to describe the chemical ordering in network glasses [104]. Both of these models are based on the so-called "8-N" bonding rule, where N is the total number of *s* and *p* electrons in the outmost shell of an atom [105]. In the random covalent network (RCN) model, the bond distribution is treated as purely statistical, depending only on the local coordination environment and on the concentration of the atomic species [106]. This implies that effects that would enforce chemical ordering can be neglected, as for example the relative bond energies, and that heteropolar and homopolar bonds are both allowed at all compositions. In contrast, in the chemically ordered network (CON) model, differences between the chemical bonds are taken into account such that heteropolar bonds are preferred [107, 108].

Figure 5-1 show the crystal structure for As_2Se_3 with 3 fold-coordinated As atoms in corner-sharing $AsSe_{3/2}$ pyramids [109].

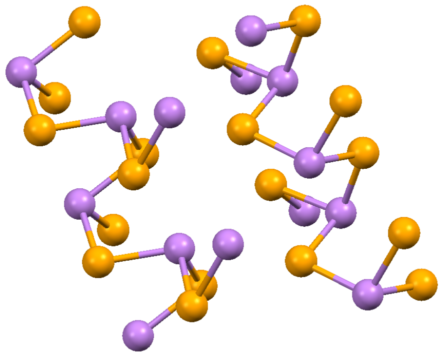

Figure 5-1: Crystal structure for As_2Se_3 [109]. The As atoms are in purple and the Se atoms are in yellow.

The predominant structural motifs for As_xSe_{1-x} glasses are pyramidal $AsSe_{3/2}$ units that are crossed-linked by Se_n chains. However, Boolchand *et al.* [103] found that, in addition to Se_n chains and $As(Se_{1/2})_3$ pyramids, quasi-tetrahedral $Se{=}AsSe_{3/2}$ units are present for the Se-rich compositions, allowing 4 fold-coordinated As atoms to exist, against the prediction of the "8-N" bonding rule. Bauchy *et al.* [24] found the existence of homopolar As-As bonds via first-principles molecular dynamics (FPMD) simulations for $x > 0.3$, which lead to the growth of ethylene-like structures that contain these

As-As bonds. Hosakawa *et al.* [26] investigated $\mathrm{As}_x\mathrm{Se}_{1-x}$ glasses ($x = 0.29$, 0.33 and 0.40) by combining anomalous X-ray scattering experiments and reverse Monte Carlo modelling. They found a breakdown of the "8-N" bonding rule around As, and a fraction of homopolar bonds As-As that is in agreement with the FPMD results found by Bauchy *et al.* [24, 25]. However, their results showed discrepancies in the region of the pre-peak of $S_{\mathrm{AsSe}}(Q)$.

In order to provide experimental information for a deeper understanding of these glassy networks, and to test the validity of the RMC and FPMD simulations, NDIS experiments were made using the GEM diffractometer at ISIS. Three compositions in the $0.3 \leq x \leq 0.4$ range were investigated to span the IP, namely $\mathrm{As}_{0.30}\mathrm{Se}_{0.70}$, $\mathrm{As}_{0.35}\mathrm{Se}_{0.65}$ and $\mathrm{As}_{0.40}\mathrm{Se}_{0.60}$.

5.2 Theory

The method of NDIS exploits the variation between the coherent neutron-scattering lengths of isotopes of the same chemical species. Diffraction patterns are measured for samples that are identical in every respect, except for the isotopic composition of one or more of the chemical elements. Consider, for example, the $\mathrm{As}_{0.30}\mathrm{Se}_{0.70}$ composition. Because As is a monoisotopic element, it is possible to use only Se isotope substitution. Let ${}^{\mathrm{Nat}}F(Q)$ be the total structure factor measured for $\mathrm{As}_{0.30}{}^{\mathrm{Nat}}\mathrm{Se}_{0.70}$, where Nat indicates the natural isotopic abundance for Se, and let ${}^{76}F(Q)$ be the total structure factor measured for an isotopically-enriched sample of $\mathrm{As}_{0.30}{}^{76}\mathrm{Se}_{0.70}$. The diffraction patterns can be Fourier transformed to give the corresponding total pair distribution functions $G(r)$ by using Eq.(2.25). For example, in the case of the natural sample, ${}^{\mathrm{Nat}}G(r)$ is given by

$$\begin{aligned}{}^{\mathrm{Nat}}G(r) &= \frac{1}{2\pi^2\rho r}\int_0^\infty {}^{\mathrm{Nat}}F(Q)Q\sin(Qr)dQ \\ &= c_{\mathrm{As}}^2 b_{\mathrm{As}}^2[g_{\mathrm{AsAs}}(r)-1] + c_{\mathrm{Se}}^2 b_{{}^{\mathrm{Nat}}\mathrm{Se}}^2[g_{\mathrm{SeSe}}(r)-1] + 2c_{\mathrm{As}}c_{\mathrm{Se}}b_{\mathrm{As}}b_{{}^{\mathrm{Nat}}\mathrm{Se}}[g_{\mathrm{AsSe}}(r)-1],\end{aligned} \tag{5.1}$$

where ρ is the atomic number density of the system, and the partial pair-distribution functions $g_{\alpha\beta}(r)$ are defined in Section 2.2. At r-values smaller than the distance of closest approach between the centres of two atoms

$${}^{\mathrm{Nat}}G(r\to 0) = {}^{\mathrm{Nat}}G(0) = -(c_{\mathrm{As}}b_{\mathrm{As}} + c_{\mathrm{Se}}b_{{}^{\mathrm{Nat}}\mathrm{Se}})^2, \tag{5.2}$$

and the average coordination number can be defined as

$$\overline{n}_{\text{Nat}} = 4\pi\rho \int_{r_1}^{r_2} \frac{\left[{}^{\text{Nat}}G(r) - {}^{\text{Nat}}G(0)\right]}{|{}^{\text{Nat}}G(0)|} r^2 dr \tag{5.3}$$

$$\begin{aligned} &= \frac{c_{\text{As}}^2 b_{\text{As}}^2 4\pi\rho}{|{}^{\text{Nat}}G(0)|} \int_{r_1}^{r_2} g_{\text{AsAs}}(r) r^2 dr + \frac{c_{\text{Se}}^2 b_{\text{Nat}_{\text{Se}}}^2 4\pi\rho}{|{}^{\text{Nat}}G(0)|} \int_{r_1}^{r_2} g_{\text{SeSe}}(r) r^2 dr \\ &+ \frac{2c_{\text{As}} b_{\text{As}} c_{\text{Se}} b_{\text{Nat}_{\text{Se}}} 4\pi\rho}{|{}^{\text{Nat}}G(0)|} \int_{r_1}^{r_2} g_{\text{AsSe}}(r) r^2 dr \\ &= \frac{c_{\text{As}} b_{\text{As}}^2}{|{}^{\text{Nat}}G(0)|} \overline{n}_{\text{As}}^{\text{As}} + \frac{c_{\text{Se}} b_{\text{Nat}_{\text{Se}}}^2}{|{}^{\text{Nat}}G(0)|} \overline{n}_{\text{Se}}^{\text{Se}} + \frac{2c_{\text{As}} b_{\text{As}} b_{\text{Nat}_{\text{Se}}}}{|{}^{\text{Nat}}G(0)|} \overline{n}_{\text{As}}^{\text{Se}}. \end{aligned} \tag{5.4}$$

The same formalism is valid for the isotopically enriched sample, and an average coordination number $\overline{n}_{76}$ can be calculated by replacing $b_{\text{Nat}_{\text{Se}}}$ by $b_{76_{\text{Se}}}$ in Eqs.(5.1)-(5.4), such that:

$$\overline{n}_{76} = 4\pi\rho \int_{r_1}^{r_2} \frac{\left[{}^{76}G(r) - {}^{76}G(0)\right]}{|{}^{76}G(0)|} r^2 dr \tag{5.5}$$

$$= \frac{c_{\text{As}} b_{\text{As}}^2}{|{}^{76}G(0)|} \overline{n}_{\text{As}}^{\text{As}} + \frac{c_{\text{Se}} b_{76_{\text{Se}}}^2}{|{}^{76}G(0)|} \overline{n}_{\text{Se}}^{\text{Se}} + \frac{2c_{\text{As}} b_{\text{As}} b_{76_{\text{Se}}}}{|{}^{76}G(0)|} \overline{n}_{\text{As}}^{\text{Se}}. \tag{5.6}$$

The measured diffraction patterns ${}^{\text{Nat}}F(Q)$ and ${}^{76}F(Q)$ can be combined to form first-order difference functions, where different partial structure factors can be eliminated in turn (Section 2.4). For example, the difference function

$$\begin{aligned} \Delta F_{\text{Se}}(Q) &= {}^{76}F(Q) - {}^{\text{Nat}}F(Q) \\ &= 2c_{\text{As}} c_{\text{Se}} b_{\text{As}} (b_{76_{\text{Se}}} - b_{\text{Nat}_{\text{Se}}})[S_{\text{AsSe}}(Q) - 1] + c_{\text{Se}}^2 (b_{76_{\text{Se}}}^2 - b_{\text{Nat}_{\text{Se}}}^2)[S_{\text{SeSe}}(Q) - 1], \end{aligned} \tag{5.7}$$

removes $S_{\text{AsAs}}(Q)$, whereas the weighted difference function

$$\begin{aligned} \Delta F_{\text{X}}(Q) &= \left(\frac{b_{\text{Nat}_{\text{Se}}}}{b_{76_{\text{Se}}}}\right) {}^{76}F(Q) - {}^{\text{Nat}}F(Q) \\ &= c_{\text{As}}^2 b_{\text{As}}^2 \left(\frac{b_{\text{Nat}_{\text{Se}}}}{b_{76_{\text{Se}}}} - 1\right) [S_{\text{AsAs}}(Q) - 1] + c_{\text{Se}}^2 b_{\text{Nat}_{\text{Se}}} (b_{76_{\text{Se}}} - b_{\text{Nat}_{\text{Se}}})[S_{\text{SeSe}}(Q) - 1], \end{aligned} \tag{5.8}$$

removes $S_{\mathrm{AsSe}}(Q)$, and

$$\begin{aligned}\Delta F_{\mathrm{As}}(Q) &= {}^{\mathrm{Nat}}F(Q) - \left(\frac{b_{^{\mathrm{Nat}}\mathrm{Se}}}{b_{^{76}\mathrm{Se}}}\right)^2 {}^{76}F(Q) \\ &= 2c_{\mathrm{As}}c_{\mathrm{Se}}b_{\mathrm{As}}b_{^{\mathrm{Nat}}\mathrm{Se}}\left(1 - \frac{b_{^{\mathrm{Nat}}\mathrm{Se}}}{b_{^{76}\mathrm{Se}}}\right)[S_{\mathrm{AsSe}}(Q) - 1] \\ &+ c_{\mathrm{As}}^2 b_{\mathrm{As}}^2\left[1 - \left(\frac{b_{^{\mathrm{Nat}}\mathrm{Se}}}{b_{^{76}\mathrm{Se}}}\right)^2\right][S_{\mathrm{AsAs}}(Q) - 1] \end{aligned} \tag{5.9}$$

removes $S_{\mathrm{SeSe}}(Q)$. The Fourier transform of a difference function provides the corresponding real-space information. For instance, the Fourier transform of Eq.(5.7) gives

$$\begin{aligned}\Delta G_{\mathrm{Se}}(r) &= \frac{1}{2\pi^2\rho r}\int\limits_0^\infty Q\Delta F_{\mathrm{Se}}(Q)\sin(Qr)dQ \\ &= \frac{1}{2\pi^2\rho r}\left[2c_{\mathrm{As}}c_{\mathrm{Se}}b_{\mathrm{As}}(b_{^{76}\mathrm{Se}} - b_{^{\mathrm{N}}\mathrm{Se}})\right]\int\limits_0^\infty Q[S_{\mathrm{AsSe}}(Q) - 1]\sin(Qr)dQ \\ &+ \frac{1}{2\pi^2\rho r}\left[c_{\mathrm{Se}}^2(b_{^{76}\mathrm{Se}}^2 - b_{^{\mathrm{N}}\mathrm{Se}}^2)\right]\int\limits_0^\infty Q[S_{\mathrm{SeSe}}(Q) - 1]\sin(Qr)dQ \\ &= \left[2c_{\mathrm{As}}c_{\mathrm{Se}}b_{\mathrm{As}}(b_{^{76}\mathrm{Se}} - b_{^{\mathrm{N}}\mathrm{Se}})\right]\left[g_{\mathrm{AsSe}}(r) - 1\right] + \left[c_{\mathrm{Se}}^2(b_{^{76}\mathrm{Se}}^2 - b_{^{\mathrm{N}}\mathrm{Se}}^2)\right]\left[g_{\mathrm{SeSe}}(r) - 1\right].\end{aligned} \tag{5.10}$$

Here, the low-r limit is given by

$$\Delta G_{\mathrm{Se}}(0) = -2c_{\mathrm{As}}c_{\mathrm{Se}}b_{\mathrm{As}}(b_{^{76}\mathrm{Se}} - b_{^{\mathrm{Nat}}\mathrm{Se}}) - c_{\mathrm{Se}}^2(b_{^{76}\mathrm{Se}}^2 - b_{^{\mathrm{Nat}}\mathrm{Se}}^2), \tag{5.11}$$

and an averaged coordination number can be defined by

$$\begin{aligned}\overline{n}_{\mathrm{Se}} &= \frac{4\pi\rho}{|\Delta G_{\mathrm{Se}}(0)|}\int\limits_{r_1}^{r_2}\left[\Delta G_{\mathrm{Se}}(r)-\Delta G_{\mathrm{Se}}(0)\right] r^2 dr \qquad (5.12)\\
&= \frac{2c_{\mathrm{As}}b_{\mathrm{As}}(b_{^{76}\mathrm{Se}}-b_{^{\mathrm{Nat}}\mathrm{Se}})c_{\mathrm{Se}}4\pi\rho}{|\Delta G_{\mathrm{Se}}(0)|}\int\limits_{r_1}^{r_2} g_{\mathrm{AsSe}}(r)r^2 dr\\
&+ \frac{c_{\mathrm{Se}}(b^2_{^{76}\mathrm{Se}}-b^2_{^{\mathrm{Nat}}\mathrm{Se}})c_{\mathrm{Se}}4\pi\rho}{|\Delta G_{\mathrm{Se}}(0)|}\int\limits_{r_1}^{r_2} g_{\mathrm{SeSe}}(r)r^2 dr\\
&= \frac{2c_{\mathrm{As}}b_{\mathrm{As}}(b_{^{76}\mathrm{Se}}-b_{^{\mathrm{Nat}}\mathrm{Se}})}{|\Delta G_{\mathrm{Se}}(0)|}\bar{n}^{\mathrm{Se}}_{\mathrm{As}} + \frac{c_{\mathrm{Se}}(b^2_{^{76}\mathrm{Se}}-b^2_{^{\mathrm{Nat}}\mathrm{Se}})}{|\Delta G_{\mathrm{Se}}(0)|}\bar{n}^{\mathrm{Se}}_{\mathrm{Se}}.\end{aligned} \tag{5.13}$$

Likewise, average coordination numbers can be defined for the Fourier transforms of Eqs.(5.8) and (5.9):

$$\overline{n}_{\mathrm{X}} = \frac{c_{\mathrm{As}}b^2_{\mathrm{As}}\left(\frac{b_{^{\mathrm{Nat}}\mathrm{Se}}}{b_{^{76}\mathrm{Se}}}-1\right)}{|\Delta G_{\mathrm{X}}(0)|}\bar{n}^{\mathrm{As}}_{\mathrm{As}} + \frac{c_{\mathrm{Se}}b_{^{\mathrm{Nat}}\mathrm{Se}}(b_{^{76}\mathrm{Se}}-b_{^{\mathrm{Nat}}\mathrm{Se}})}{|\Delta G_{\mathrm{X}}(0)|}\bar{n}^{\mathrm{Se}}_{\mathrm{Se}} \tag{5.14}$$

$$\overline{n}_{\mathrm{As}} = \frac{2c_{\mathrm{As}}b_{\mathrm{As}}b_{^{\mathrm{Nat}}\mathrm{Se}}\left(1-\frac{b_{^{\mathrm{Nat}}\mathrm{Se}}}{b_{^{76}\mathrm{Se}}}\right)}{|\Delta G_{\mathrm{As}}(0)|}\bar{n}^{\mathrm{Se}}_{\mathrm{As}} + \frac{c_{\mathrm{As}}b^2_{\mathrm{As}}\left[1-\left(\frac{b_{^{\mathrm{Nat}}\mathrm{Se}}}{b_{^{76}\mathrm{Se}}}\right)^2\right]}{|\Delta G_{\mathrm{As}}(0)|}\bar{n}^{\mathrm{As}}_{\mathrm{As}}. \tag{5.15}$$

5.3 Experimental method

5.3.1 Sample preparation

The samples were prepared in the Liquid and Amorphous Materials laboratory at Bath. For each composition, two different glassy samples were prepared that were identical in every respect, except that one contained Se of natural isotopic abundance, $^{\mathrm{Nat}}$Se, whilst the other contained the isotope ^{76}Se. Silica ampoules were etched with HF acid, then thoroughly rinsed with water and acetone. Once dried by heating under vacuum at 800 °C, the ampoules were loaded with As (99.99999+% purity from Alfa Aesar) and $^{\mathrm{Nat}}$Se (purity $\geq$ 99.999% from Sigma Aldrich) or ^{76}Se (99.8% ^{76}Se, relative abundance

9.0%, and 0.2% ^{77}Se, relative abundance 7.6%, from Isoflex USA) in the desired ratio, inside an argon-filled glove-box. Once loaded, an ampoule was evacuated to $\approx 10^{-6}$ Torr, sealed, and then placed into a rocking furnace. The temperature was increased at 1 °C/min to 685 °C, dwelling for 4 hours each at the Se melting point (221 °C) and at the As melting point (614 °C). At the Se boiling point (685 °C), the samples were left to dwell for 47 hours. The furnace was then placed vertically and left for another hour before the temperature was ramped down, at 1 °C/min, to 400 °C, where the sample was left to equilibrate for 4 hours. Finally, the ampoule was quenched by dropping it into a container filled with an ice-water mixture.

The glasses were prepared in three different stages. Firstly, the $\mathrm{As_{0.30}Se_{0.70}}$ samples were prepared for the first part of the neutron-diffraction experiment. These samples were used to prepare the $\mathrm{As_{0.35}Se_{0.65}}$ samples, by adding the required amount of Se, for the second part of the NDIS experiment. Similarly, these samples were then used to prepare the $\mathrm{As_{0.40}Se_{0.60}}$ samples to carry out the third part of the NDIS experiment. The chemical compositions of the prepared glasses were not measured. All of the prepared samples were glassy, except for $\mathrm{As_{0.40}{}^{76}Se_{0.60}}$, which was found to be crystalline during the diffraction experiment, although the procedure used to prepare it was the same as that used for the other samples. Thus far, an explanation for this crystallisation has not been found. In order to form difference functions for the $\mathrm{As_{0.40}Se_{0.60}}$ composition, a $\mathrm{As_{0.40}{}^{Mix}Se_{0.60}}$ sample was investigated, where $^{\mathrm{Mix}}$Se indicates a mixture of 50% $^{\mathrm{Nat}}$Se and 50% ^{76}Se. The density of the samples was measured using a He pycnometer. The mean bound coherent scattering lengths $\bar{b}_{\mathrm{coh}}$, the total neutron-scattering cross sections σ_{T} and the measured number densities of the samples are listed in Table 5.1.

Table 5.1: Parameters describing the samples used for the neutron-diffraction experiments. Values for $\bar{b}_{\mathrm{coh}}$ and σ_{T} were calculated using the data given by Sears [33]. The tabulated neutron-absorption cross section for ^{76}Se (σ_{abs}=85(7) barn) is incorrect. Instead, it was estimated from neutron-diffraction data analysis to be σ_{abs}=115(23) barn [110].

Sample	$\bar{b}_{\mathrm{coh}}$ (fm)	σ_{T} (barn) @ λ_{i} = 1.798 (Å))	ρ (Å^{-3})
$\mathrm{As_{0.30}{}^{Nat}Se_{0.70}}$	7.553(9)	17.0(3)	0.03475(7)
$\mathrm{As_{0.30}{}^{76}Se_{0.70}}$	10.508(7)	96.6(16.4)	0.03475(7)
$\mathrm{As_{0.35}{}^{Nat}Se_{0.65}}$	7.484(6)	16.5(6)	0.0349(1)
$\mathrm{As_{0.35}{}^{76}Se_{0.65}}$	10.23(6)	90.4(15.3)	0.0349(1)
$\mathrm{As_{0.40}{}^{Nat}Se_{0.60}}$	7.414(7)	16.0(2)	0.0354(1)
$\mathrm{As_{0.40}{}^{Mix}Se_{0.60}}$	8.68(3)	50.11(7.06)	0.0354(1)
$\mathrm{As_{0.40}{}^{76}Se_{0.60}}$	9.947(5)	128.42(7.06)	0.0354(1)

5.3.2 GEM experiment

The three parts of the NDIS experiment were carried out on the GEM diffractometer at ISIS, which is described in Section 3.2. The $\mathrm{As}_{0.30}\mathrm{Se}_{0.70}$, $\mathrm{As}_{0.35}\mathrm{Se}_{0.65}$ and $\mathrm{As}_{0.40}\mathrm{Se}_{0.60}$ compositions were investigated in October 2013, March 2014 and August 2014, respectively. The samples were coarsely ground inside an argon-filled glove-box, and then loaded into a vanadium can (outer diameter = 5 mm, wall thickness = 0.1 mm). The loaded can was closed under argon, and then taken out of the glove-box. In order to achieve a higher packing fraction, and hence a higher number of scattering centres in the neutron beam, each can was placed into a ultrasound bath for a couple of minutes. The packing fraction values reached using this procedure were in the range 57-64 %. The loaded can was mounted on a stick to be centred in the neutron beam. In each part of the NDIS experiment, diffraction patterns were measured for each of the samples, the empty vanadium can, the empty belljar, and a vanadium rod for normalisation purposes.

5.4 Results

5.4.1 Total structure factors

The measured total structure factors are shown in Figures 5-2 – 5-4. In Figure 5-5, a comparison is shown between the diffraction patterns measured for $\mathrm{As}_{0.40}\mathrm{Se}_{0.60}$ using D4c (from [90]) and GEM. In Figure 5-6, the neutron-diffraction results from [90] are shown for $\mathrm{As}_{0.40}\mathrm{Se}_{0.60}$, where the isotopically-enriched sample was $\mathrm{As}_{0.40}{}^{76}\mathrm{Se}_{0.60}$ instead of $\mathrm{As}_{0.40}{}^{\mathrm{Mix}}\mathrm{Se}_{0.60}$.

The total structure factors show similar features across the composition range, with oscillations that die out at $Q \approx 30$ Å^{-1}. Figure 5-5 show good agreement between the total structure factors measured using GEM and D4c for the $\mathrm{As}_{0.40}\mathrm{Se}_{0.60}$ composition, and the small discrepancy most likely originates from the difference in the resolution functions between the two diffractometers. For all of the compositions, there is a difference in the total structure factors such that, in terms of magnitude, ${}^{76}F(Q)$ (or ${}^{\mathrm{Mix}}F(Q)$) > ${}^{\mathrm{Nat}}F(Q)$. The reason lies in the difference between the coherent neutron-scattering lengths of the Se isotopes employed in the NDIS experiment, as indicated by Table 5.1. At $Q \approx 1.25$ Å^{-1}, a pre-peak manifests itself in all of the total structure factors. This feature, also known as a first sharp diffraction peak (FSDP), is a signature of the presence of intermediate range order (IRO), having a periodicity given by $2\pi/Q_{\mathrm{FSDP}}$ and correlation length given by $2\pi/\Delta Q_{\mathrm{FSDP}}$, where ΔQ_{FSDP} is the full-width at half-maximum [7, 111]. The FSDP position found in the present work is consistent with the value $Q \approx 1.2$ Å^{-1} found for liquid and glassy $\mathrm{As}_{0.40}\mathrm{Se}_{0.60}$ by

Hosokawa *et al.* [112]. In particular, they found via AXS that the IRO is dominated by the As-As pair-distribution function with a correlation length of about 5.2 Å. The total pair-distribution functions are shown in Figures 5-7 – 5-11. The comparison in Figure 5-10 shows that there is good agreement between the $G(r)$ functions measured on GEM and on D4c for the $\mathrm{As}_{0.40}{}^{\mathrm{Nat}}\mathrm{Se}_{0.60}$ and $\mathrm{As}_{0.40}{}^{\mathrm{Mix}}\mathrm{Se}_{0.60}$ samples. The first peak position, at about 2.40(3) Å, does not vary substantially across the compositions and the same value is found for the crystalline, glassy and liquid structures of many different $\mathrm{As}_x\mathrm{Se}_{1-x}$ compositions [112–117].

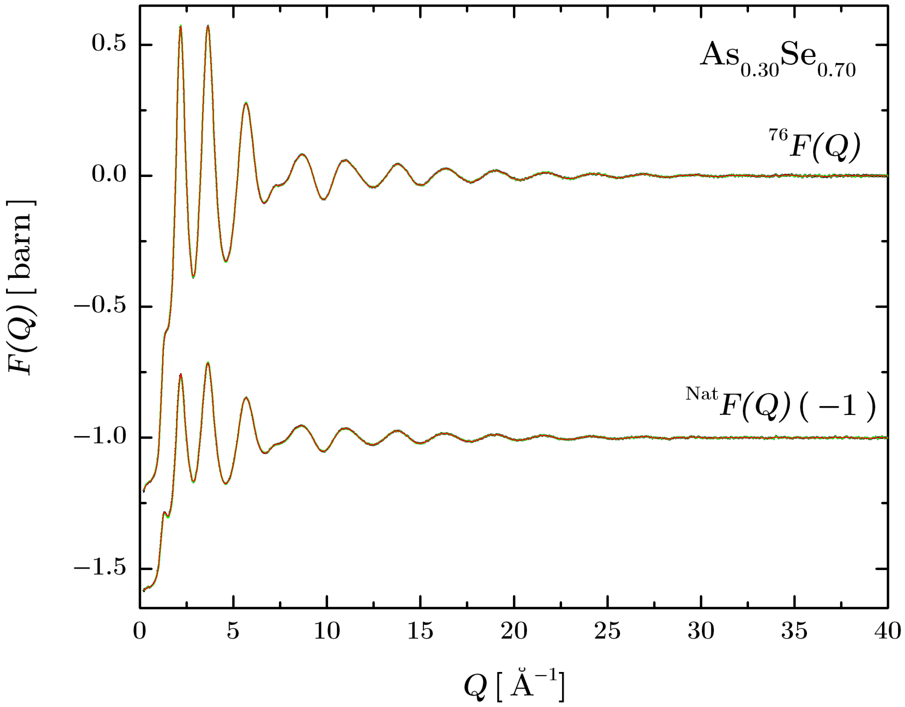

Figure 5-2: Total structure factors $^{76}F(Q)$ and $^{\mathrm{Nat}}F(Q)$ for $\mathrm{As}_{0.30}{}^{76}\mathrm{Se}_{0.70}$ and $\mathrm{As}_{0.30}{}^{\mathrm{Nat}}\mathrm{Se}_{0.70}$, respectively. The solid black lines with vertical error bars are the measured data sets. The error bars are hardly distinguishable, given the high-quality counting statistics. The red curves show spline fits to the measured data sets. The green curves are the back-Fourier transforms of the $G(r)$ functions shown in Figure 5-7, once the low-r oscillations are set to their theoretical $G(r \to 0)$ limit. The curves for $^{\mathrm{Nat}}F(Q)$ have been offset vertically, for clarity of presentation, and the offsets are indicated in parenthesis.

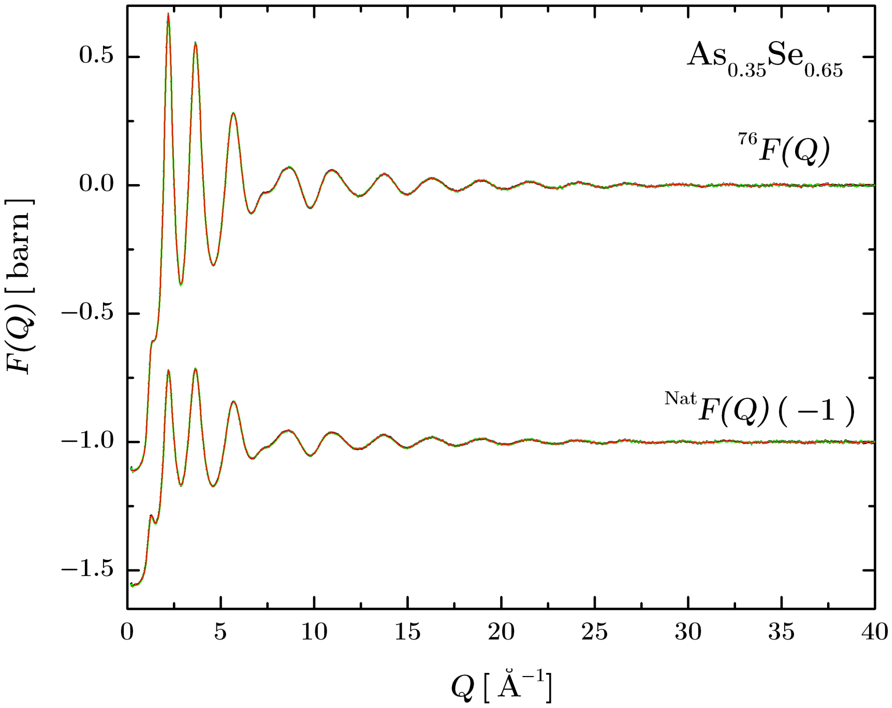

Figure 5-3: Total structure factors $^{76}F(Q)$ and $^{\mathrm{Nat}}F(Q)$ for As$_{0.35}$^{76}Se$_{0.65}$ and As$_{0.35}$$^{\mathrm{Nat}}Se_{0.65}$, respectively. The solid black lines with vertical error bars are the measured data sets. The error bars are hardly distinguishable, given the high-quality counting statistics. The red curves show spline fits to the measured data sets. The green curves are the back- Fourier transforms of the $G(r)$ functions shown in Figure 5-8, once the low-r oscillations are set to their theoretical $G(r \to 0)$ limit. The curves for $^{\mathrm{Nat}}F(Q)$ have been offset vertically, for clarity of presentation, and the offsets are indicated in parenthesis.

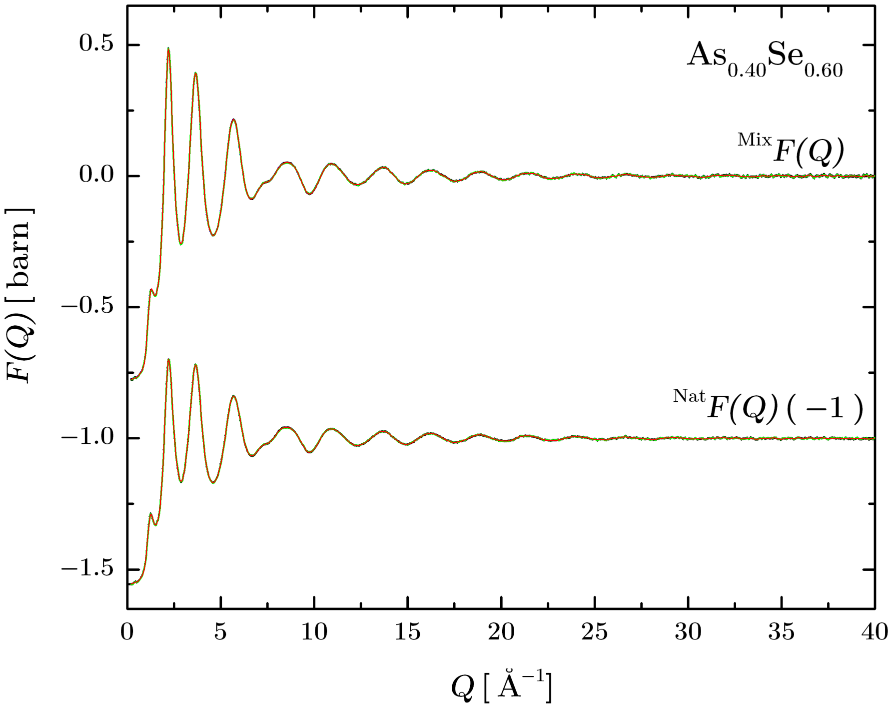

Figure 5-4: Total structure factors ${}^{\mathrm{Mix}}F(Q)$ and ${}^{\mathrm{Nat}}F(Q)$ for $\mathrm{As}_{0.40}{}^{\mathrm{Mix}}\mathrm{Se}_{0.60}$ and $\mathrm{As}_{0.40}{}^{\mathrm{Nat}}\mathrm{Se}_{0.60}$, respectively. The solid black lines with vertical error bars are the measured data sets. The error bars are hardly distinguishable, given the high-quality counting statistics. The red curves show spline fits to the measured data sets. The green curves are the back-Fourier transforms of the $G(r)$ functions shown in Figure 5-9, once the low-r oscillations are set to their theoretical $G(r \to 0)$ limit. The curves for ${}^{\mathrm{Nat}}F(Q)$ have been offset vertically, for clarity of presentation, and the offsets are indicated in parenthesis.

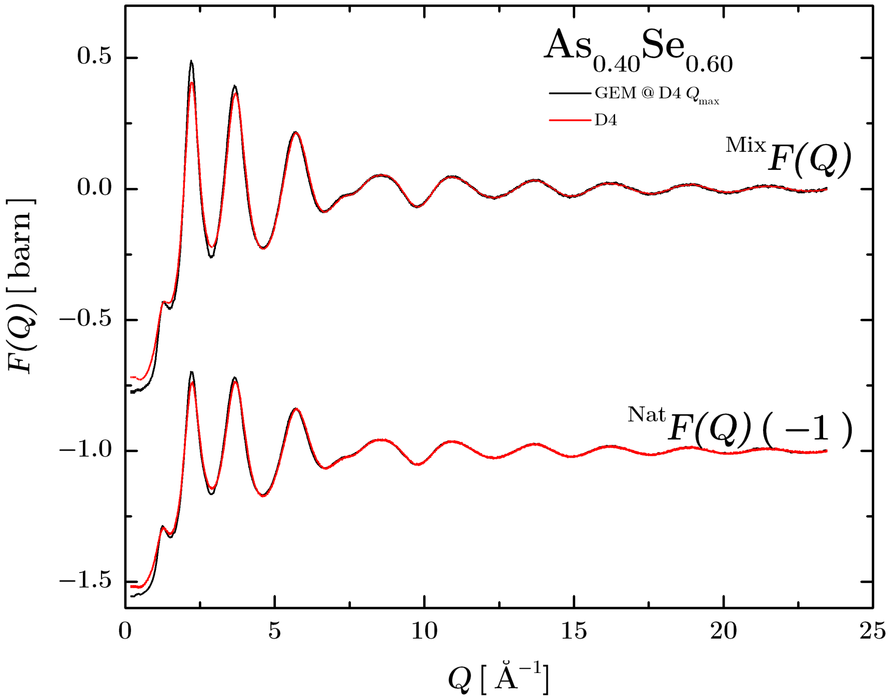

Figure 5-5: Comparison between the total structure factors ${}^{\mathrm{Mix}}F(Q)$ and ${}^{\mathrm{Nat}}F(Q)$ for $\mathrm{As}_{0.40}{}^{\mathrm{Mix}}\mathrm{Se}_{0.60}$ and $\mathrm{As}_{0.40}{}^{\mathrm{Nat}}\mathrm{Se}_{0.60}$, respectively, as measured on GEM or on D4c. The solid black lines represent the data sets measured on GEM with Q_{max} set to the D4c value of 23.45 Å^{-1}. The solid red lines represent the data sets measured on D4c [90]. In both cases, the vertical error bars are hardly distinguishable, given the high-quality counting statistics. The curves for ${}^{\mathrm{Nat}}F(Q)$ have been offset vertically, for clarity of presentation, and the offsets are indicated in parenthesis.

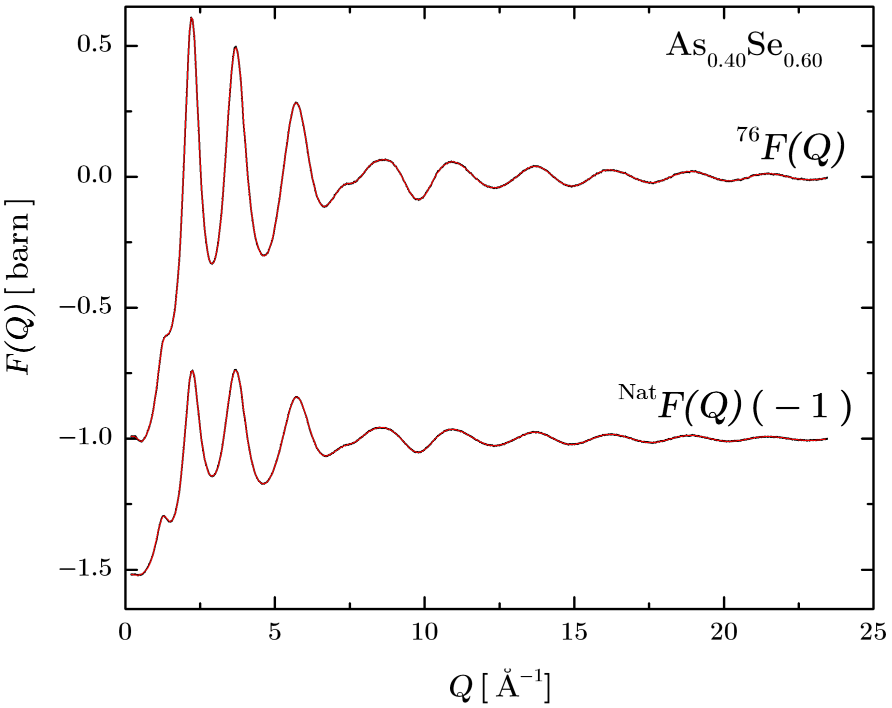

Figure 5-6: Total structure factors $^{76}F(Q)$ and $^{\mathrm{Nat}}F(Q)$ for $\mathrm{As}_{0.40}{}^{76}\mathrm{Se}_{0.60}$ and $\mathrm{As}_{0.40}{}^{\mathrm{Nat}}\mathrm{Se}_{0.60}$, respectively. The solid black lines with vertical error bars are the data sets measured on D4c [90]. The error bars are hardly distinguishable, given the high-quality counting statistics. The red curves show spline fits to the measured data sets. The curves for $^{\mathrm{Nat}}F(Q)$ have been offset vertically, for clarity of presentation, and the offsets are indicated in parenthesis.

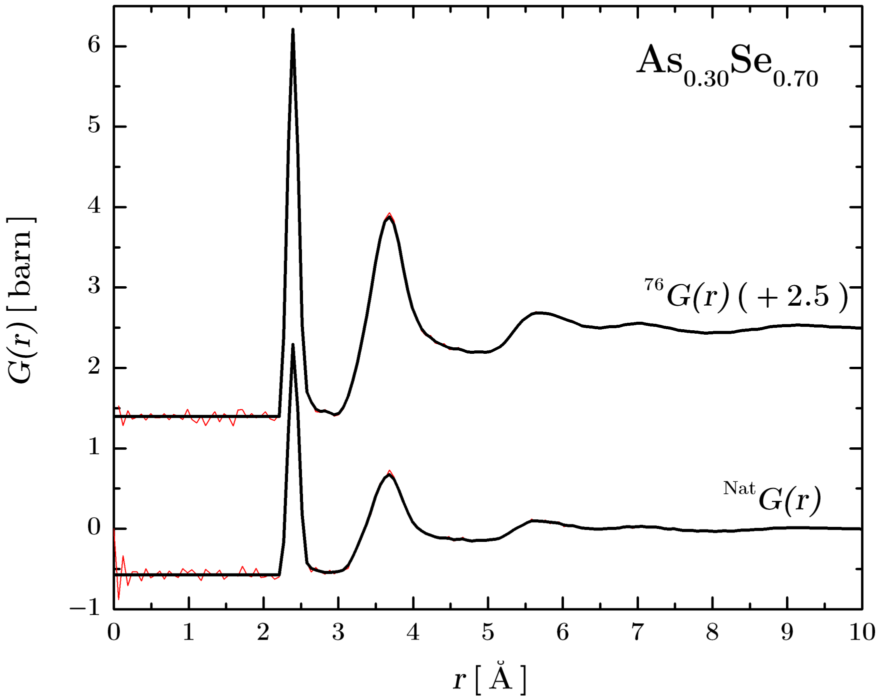

Figure 5-7: Total pair-distribution functions $^{76}G(r)$ and $^{\mathrm{Nat}}G(r)$ for $\mathrm{As}_{0.30}{}^{76}\mathrm{Se}_{0.70}$ and $\mathrm{As}_{0.30}{}^{\mathrm{Nat}}\mathrm{Se}_{0.70}$, respectively. The solid red lines show the Fourier transforms of the spline-fitted data sets shown in Figure 5-2. The solid black curves also show the Fourier transforms of these spline-fitted data sets after the low-r oscillations are set to their theoretical $G(r \to 0)$ limit but, in this case, a Lorch modification function was applied, with $Q_{\max} = 40$ Å^{-1}, to smooth the data after the first peak. The curves for $^{76}G(r)$ are offset vertically, for clarity of presentation, and the offsets are indicated in parenthesis.

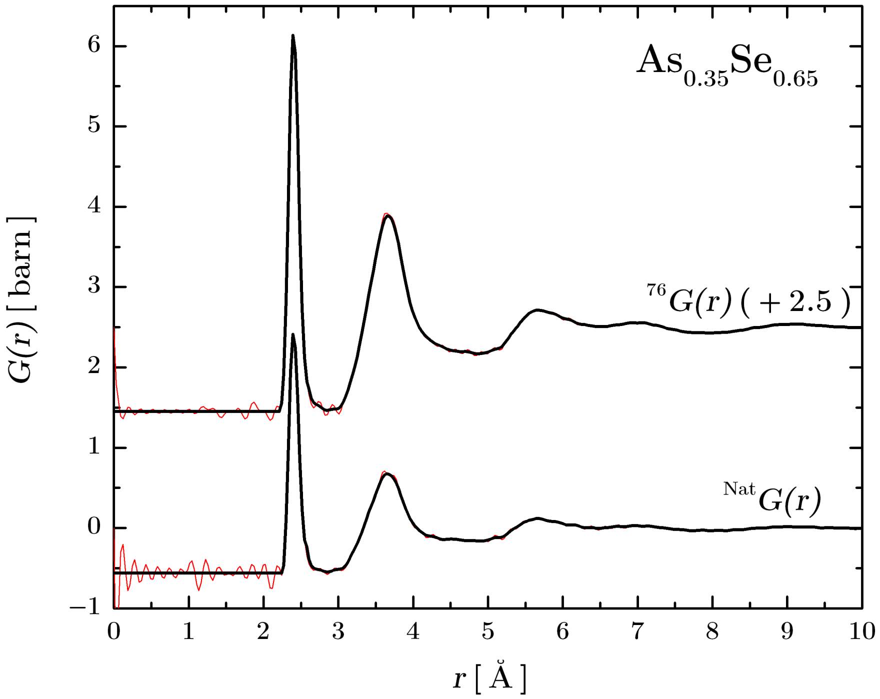

Figure 5-8: Total pair-distribution functions $^{76}G(r)$ and $^{\mathrm{Nat}}G(r)$ for $\mathrm{As}_{0.35}{}^{76}\mathrm{Se}_{0.65}$ and $\mathrm{As}_{0.35}{}^{\mathrm{Nat}}\mathrm{Se}_{0.65}$, respectively. The solid red lines show the Fourier transform of the spline-fitted data sets shown in Figure 5-3. The solid black curves also show the Fourier transforms of these spline-fitted data sets after the low-r oscillations are set to their theoretical $G(r \to 0)$ limit, but, in this case, a Lorch modification function was applied, with $Q_{\mathrm{max}} = 40$ Å^{-1}, to smooth the data after the first peak. The curves for $^{76}G(r)$ are offset vertically, for clarity of presentation, and the offset is indicated in parenthesis.

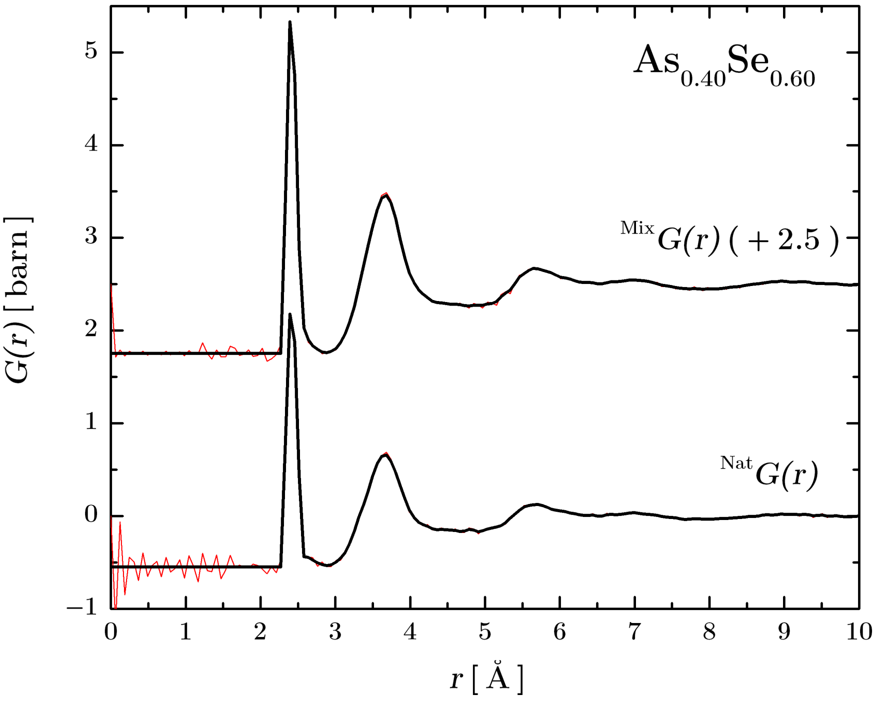

Figure 5-9: Total pair-distribution functions $^{\mathrm{Mix}}G(r)$ and $^{\mathrm{Nat}}G(r)$ for $\mathrm{As}_{0.40}{}^{\mathrm{Mix}}\mathrm{Se}_{0.60}$ and $\mathrm{As}_{0.40}{}^{\mathrm{Nat}}\mathrm{Se}_{0.60}$, respectively. The solid red lines show the Fourier transform of the spline-fitted data sets shown in Figure 5-4. The solid black curves also show the Fourier transforms of these spline-fitted data sets after the low-r oscillations are set to their theoretical $G(r \to 0)$ limit, but, in this case, a Lorch modification function was applied, with $Q_{\max} = 40$ Å^{-1}, to smooth the data after the first peak. The curves for $^{\mathrm{Mix}}G(r)$ are offset vertically. for clarity of presentation, and the offset is indicated in parenthesis.

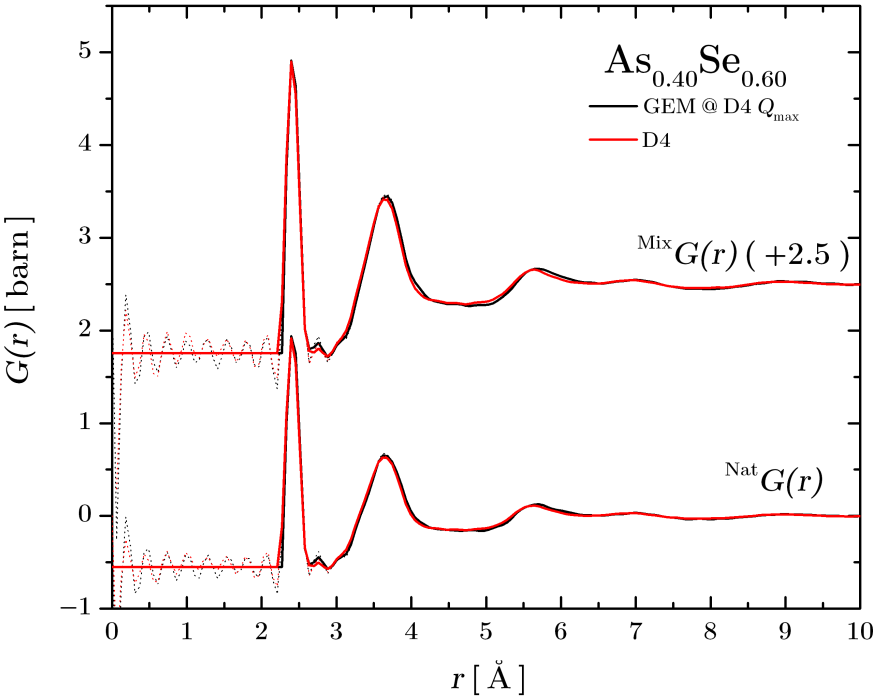

Figure 5-10: Comparison between the total pair-distribution functions $^{\mathrm{Mix}}G(r)$ and $^{\mathrm{Nat}}G(r)$ for As$_{0.40}{}^{\mathrm{Mix}}$Se$_{0.60}$ and As$_{0.40}{}^{\mathrm{Nat}}$Se$_{0.60}$, respectively, as measured on GEM or D4c. The solid black lines represent the Fourier transforms of the GEM spline-fitted data, after Q_{max} is set to the D4c value of 23.45 Å^{-1}, and the low-r oscillations (black dashed lines) are set to their theoretical $G(r \to 0)$ limit. The solid red lines, taken from [90], represent the Fourier transforms of the D4c spline-fitted data, once the low-r oscillations (red dashed lines) are set to their theoretical limit $G(r \to 0)$. In both cases, a Lorch function was applied to smooth the data after the first peak. The curves for $^{\mathrm{Mix}}G(r)$ are offset vertically, for clarity of presentation, and the offsets are indicated in parenthesis.

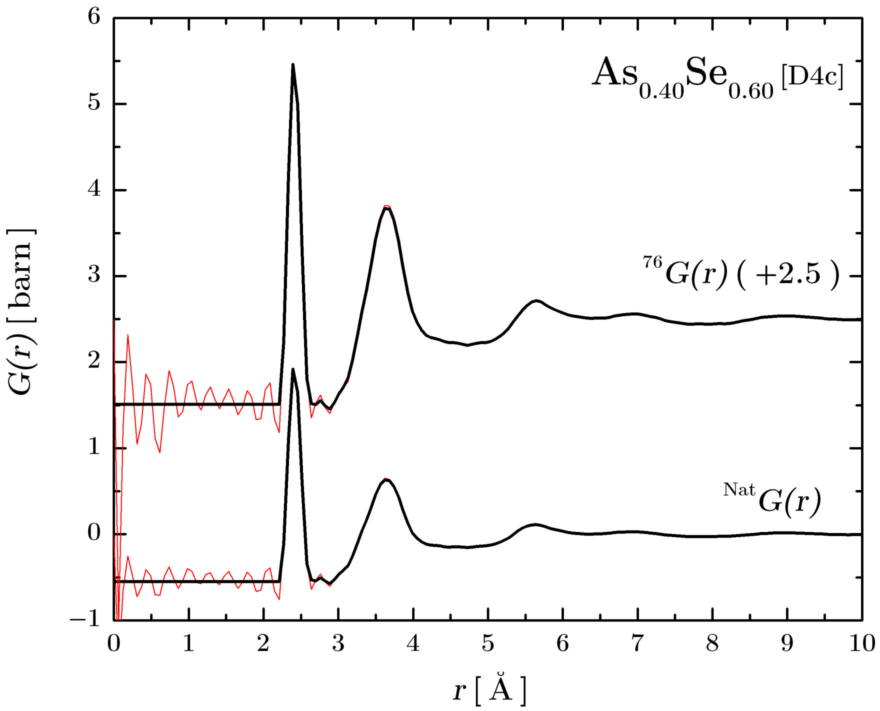

Figure 5-11: Total pair-distribution functions $^{76}G(r)$ and $^{\mathrm{Nat}}G(r)$ for $\mathrm{As}_{0.40}{}^{76}\mathrm{Se}_{0.60}$ and $\mathrm{As}_{0.40}{}^{\mathrm{Nat}}\mathrm{Se}_{0.60}$, respectively, as measured on D4c [90]. The solid red lines show the Fourier transforms of the spline-fitted data sets shown in Figure 5-6, with $Q_{\mathrm{max}} = 23.45$ Å^{-1}. The solid black curves also show the Fourier transforms of these spline-fitted data sets after the low-r oscillations are set to their theoretical $G(r \to 0)$ limit but, in this case, a Lorch function was applied, with $Q_{\mathrm{max}} = 23.45$ Å^{-1}, to smooth the data after the first peak. The curves for $^{76}G(r)$ are offset vertically, for clarity of presentation, and the offsets are indicated in parenthesis.

5.4.2 First-order difference functions

The total pair-correlation functions in Figures 5-7 – 5-11 show a first peak at about 2.40(3) Å. As found for other chalcogenide glasses, such as $\mathrm{Ge}_x\mathrm{Se}_{1-x}$ [108], the homopolar As-As and Se-Se bonds are expected to be comparable in length to heteropolar As-Se bonds. The first-order difference functions introduced in Section 5.2 can be used to eliminate, in turn, one of the $g_{\alpha\beta}(r)$ functions from $G(r)$. These difference functions can be re-written as

$$\Delta G_{\mathrm{Se}}(r) = a_1[g_{\mathrm{AsSe}}(r) - 1] + a_2[g_{\mathrm{SeSe}}(r) - 1] \tag{5.16}$$

with $a_1 = 2c_{\mathrm{As}}c_{\mathrm{Se}}b_{\mathrm{As}}(b_{^{76}\mathrm{Se}} - b_{^{\mathrm{Nat}}\mathrm{Se}})$ and $a_2 = c_{\mathrm{Se}}^2(b_{^{76}\mathrm{Se}}^2 - b_{^{\mathrm{Nat}}\mathrm{Se}}^2)$;

$$\Delta G_{\mathrm{X}}(r) = b_1[g_{\mathrm{AsAs}}(r) - 1] + b_2[g_{\mathrm{SeSe}}(r) - 1] \tag{5.17}$$

with $b_1 = c_{\mathrm{As}}^2 b_{\mathrm{As}}^2\left(\frac{b_{^{\mathrm{Nat}}\mathrm{Se}}}{b_{^{76}\mathrm{Se}}} - 1\right)$, $b_2 = c_{\mathrm{Se}}^2 b_{^{\mathrm{Nat}}\mathrm{Se}}(b_{^{76}\mathrm{Se}} - b_{^{\mathrm{Nat}}\mathrm{Se}})$, and where the symbol X refers to the homopolar As-As and Se-Se bonds;

$$\Delta G_{\mathrm{As}}(r) = c_1[g_{\mathrm{AsSe}}(r) - 1] + c_2[g_{\mathrm{AsAs}}(r) - 1], \tag{5.18}$$

with $c_1 = 2c_{\mathrm{As}}c_{\mathrm{Se}}b_{\mathrm{As}}b_{^{\mathrm{Nat}}\mathrm{Se}}\left(1 - \frac{b_{^{\mathrm{Nat}}\mathrm{Se}}}{b_{^{76}\mathrm{Se}}}\right)$ and $c_2 = c_{\mathrm{As}}^2 b_{\mathrm{As}}^2\left[1 - \left(\frac{b_{^{\mathrm{Nat}}\mathrm{Se}}}{b_{^{76}\mathrm{Se}}}\right)^2\right]$.

The same formalism holds for the difference functions formed when $^{\mathrm{Mix}}\mathrm{Se}$ was used in place of $^{76}\mathrm{Se}$. By looking at the weighting factors listed in Table 5.2, it is possible to understand which partial pair-correlation function receives the largest weighting. For instance, in the case of $\Delta G_{\mathrm{Se}}(r)$, the weighting factor for the Se-Se correlations (a_2) is larger than that for the As-Se correlations (a_1) for all of the compositions. In the case of $\Delta G_{\mathrm{X}}(r)$, the weighting factor (b_2) for the Se-Se correlations is larger than that for the As-As correlations (b_1) for all of the compositions, and the latter is also negative. In the case of $\Delta G_{\mathrm{As}}(r)$, the weighting factor ($c_1$) for the As-Se correlations is larger than that for the As-As correlations (c_2) for all of the compositions.

The measured first-order difference functions are shown in Figures 5-12 – 5-16. Figures 5-12 – 5-14 give the functions measured on GEM and Figure 5-15 shows a comparison between the functions measured for $\mathrm{As}_{0.40}\mathrm{Se}_{0.60}$ using GEM or D4c (from [90]). Figure 5-16 shows the difference functions measured for $\mathrm{As}_{0.40}\mathrm{Se}_{0.60}$ on D4c using

Table 5.2: Weighting factors for the first-order difference functions of Eqs. 5.16 – 5.18. The difference functions for $As_{0.30}Se_{0.70}$ (I-GEM), $As_{0.35}Se_{0.65}$ (II-GEM) and $As_{0.40}Se_{0.60}$ (III-D4c) were obtained using ^{76}Se isotope substitution, while the difference functions for $As_{0.40}Se_{0.60}$ (III-GEM) were obtained using $^{\mathrm{Mix}}$Se isotope substitution

Weighting factor	I-GEM (barn)	II-GEM (barn)	III-GEM (barn)	III-D4c (barn)
a_1	0.1170(6)	0.1270(6)	0.0640(4)	0.133
a_2	0.418(12)	0.36(1)	0.131(4)	0.306
b_1	-0.0135(1)	-0.0180(1)	-0.0140(1)	-0.024
b_2	0.165(4)	0.142(3)	0.058(2)	0.121
c_1	0.076(2)	0.083(2)	0.051(1)	0.087
c_2	0.0220(3)	0.0300(4)	0.0252(5)	0.04

^{76}Se isotope substitution (from [90]). The features for a given difference function do not change substantially with the glass composition. For instance, the $\Delta F_{\mathrm{As}}(Q)$ functions show a clear FSDP at $Q \approx 1.25$ Å^{-1}, while the $\Delta F_{\mathrm{Se}}(Q)$ and $\Delta F_{\mathrm{X}}(Q)$ functions exhibit a shoulder in this low-Q region.

The real-space difference functions are shown in Figures 5-17–5-22. These were obtained by Fourier transforming the corresponding reciprocal-space functions with $Q_{\mathrm{max}} = 30$ Å^{-1}, where the oscillations have already died out, in order to avoid Fourier transforming statistical noise. The first peak position in $\Delta G_{\mathrm{Se}}(r)$ is at 2.38(3) Å for $As_{0.30}Se_{0.70}$, 2.40(3) Å for $As_{0.35}Se_{0.65}$ and 2.41(3) Å for $As_{0.40}Se_{0.60}$. These average bond distances compare well with the As-Se bond distances of 2.38 Å and 2.40 Å found in crystalline $As_{0.50}Se_{0.50}$ and $As_{0.40}Se_{0.60}$ [113, 115], respectively. Also, the Se-Se bond distance is found to vary between 2.30 and 2.34 Å in liquid and glassy Ge–Se systems [108], and the value 2.32 Å is found in amorphous Selenium [118].

The first peak position in $\Delta G_{\mathrm{X}}(r)$ varies between 2.30(2) Å and 2.39(2) Å. These values can be compared with the average As-As bond distance of 2.44 Å found for crystalline $As_{0.50}Se_{0.50}$ [115], and with the Se-Se bond distance of 2.30 - 2.34 Å found in [108]. In Figure 5-19, the $\Delta G_{\mathrm{X}}(r)$ function measured on GEM for $As_{0.40}Se_{0.60}$ shows a double peak in the region between 2.27 Å and 2.69 Å. Figure 5-21 shows a comparison between the first peaks in the $\Delta G_{\mathrm{X}}(r)$ functions measured on GEM, obtained with or without the application of a Lorch function, and the same function measured on D4c. Figures 5-22 shows again the $\Delta G_{\mathrm{X}}(r)$ function as measured on D4c, but this time by using ^{76}Se isotope substitution. The functions measured on D4c both show a single peak. Also, the dip in the GEM data at ≈ 2.5 Å occurs at a larger distance than the As-As bond length of 2.44 Å found in crystalline $As_{0.50}Se_{0.50}$ [115], and the second peak in the GEM data at ≈ 2.60 Å is much larger than typical Se-Se homopolar bond distances [108]. Thus, although the As-As correlations receive a negative weighting in $\Delta G_{\mathrm{X}}(r)$ (Table 5.2), it is likely that the double-peak feature in the GEM data originates from poor counting statistics for the $\mathrm{As}_{0.40}{}^{\mathrm{Mix}}\mathrm{Se}_{0.60}$ sample. The first peak position in $\Delta G_{\mathrm{As}}(r)$ varies between 2.40(2) Å and 2.42(2) Å. These distances compare well with the value of 2.42(2) Å found by Benmore and Salmon [116] for the As-As and As-Se bond distances in glassy $\mathrm{Ag_2As_3Se_4}$ and $\mathrm{Cu_2As_3Se_4}$.

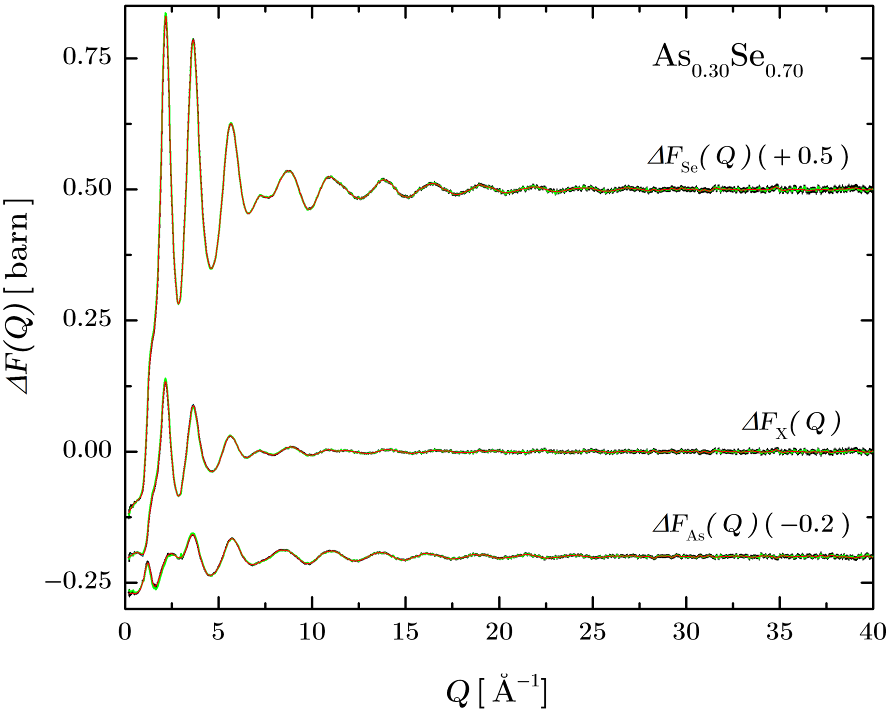

Figure 5-12: First-order difference functions for $\mathrm{As_{0.30}Se_{0.70}}$, as obtained from the total structure factors ${}^{76}F(Q)$ and ${}^{\mathrm{Nat}}F(Q)$ shown in Figure 5-2. The solid black lines with vertical error bars are the first-order difference functions measured on GEM. The error bars are hardly distinguishable, given the high-quality counting statistics. The red curves show spline fits to the measured data sets. The green curves are the back-Fourier transforms of the $\Delta G(r)$ functions shown in Figure 5-17, once the low-r oscillations are set to their theoretical $\Delta G(r \to 0)$ limit. The curves have been offset vertically, for clarity of presentation, and the offsets are indicated in parenthesis.

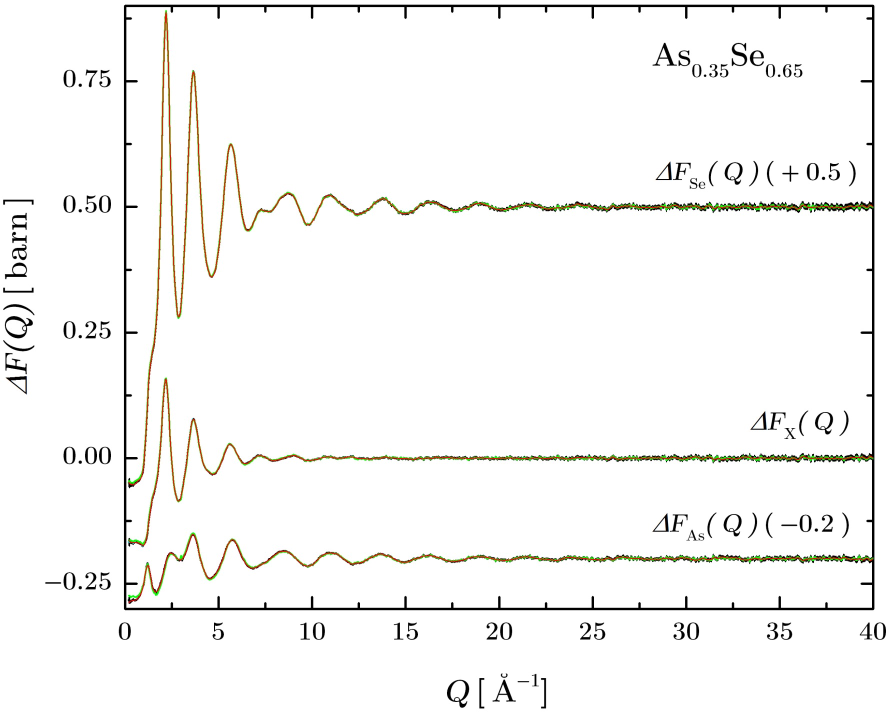

Figure 5-13: First-order difference functions for $\mathrm{As}_{0.35}\mathrm{Se}_{0.65}$, as obtained from the total structure factors ${}^{76}F(Q)$ and ${}^{\mathrm{Nat}}F(Q)$ shown in Figure 5-3. The solid black lines with vertical error bars are the first-order difference functions measured on GEM. The error bars are hardly distinguishable, given the high-quality counting statistics. The red curves show spline fits to the measured data sets. The green curves are the back-Fourier transforms of the $\Delta G(r)$ functions shown in Figure 5-18, once the low-r oscillations are set to their theoretical $\Delta G(r \to 0)$ limit. The curves have been offset vertically, for clarity of presentation, and the offsets are indicated in parenthesis.

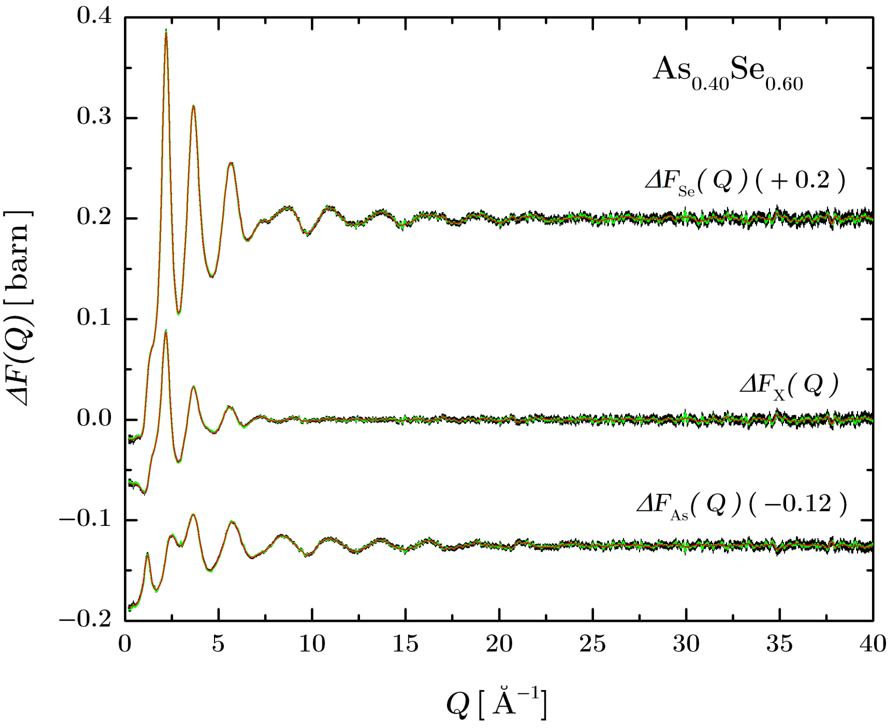

Figure 5-14: First-order difference functions for As$_{0.40}$Se$_{0.60}$, as obtained from the total structure factors $^{\mathrm{Mix}}F(Q)$ and $^{\mathrm{Nat}}F(Q)$ shown in Figure 5-4. The solid black lines with vertical error bars are the first-order difference measured on GEM. The error bars are hardly distinguishable, given the high-quality counting statistics. The red curves show spline fits to the experimental data sets. The green curves are the back-Fourier transforms of the $\Delta G(r)$ functions shown in Figure 5-19, once the low-r oscillations are set to their theoretical $\Delta G(r \to 0)$ limit. The curves have been offset vertically, for clarity of presentation, and the offsets are indicated in parenthesis.

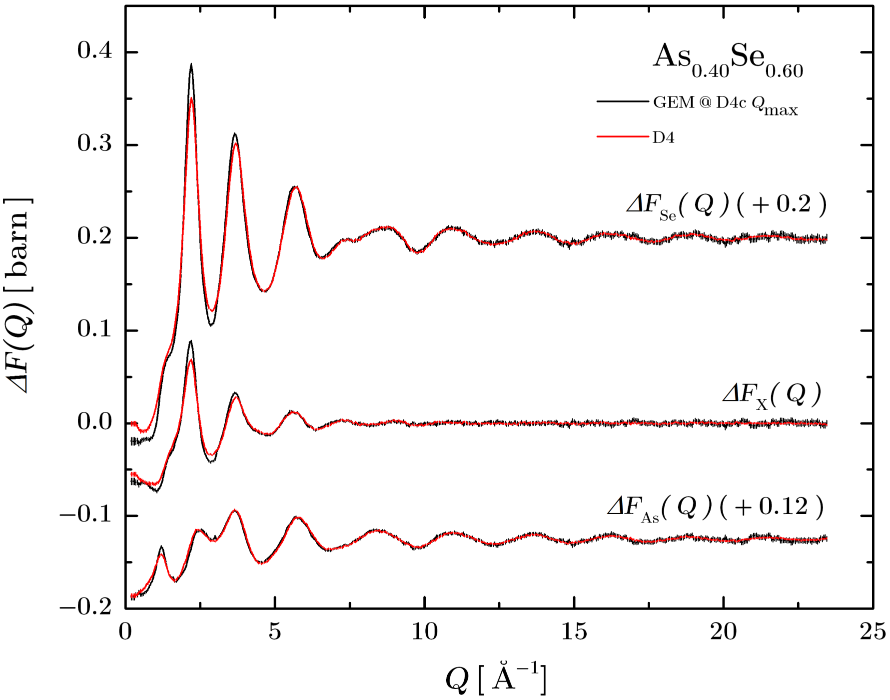

Figure 5-15: First-order difference functions for $As_{0.40}Se_{0.60}$, as obtained from the total structure factors ${}^{\mathrm{Mix}}F(Q)$ and ${}^{\mathrm{Nat}}F(Q)$ shown in Figure 5-4. The solid black lines with vertical error bars are the first-order difference functions measured on GEM, after Q_{max} is set to the D4c value of 23.45 $\mathrm{\AA}^{-1}$. The red solid lines with vertical error bars are the first-order difference functions measured on D4c [90]. The vertical error bars are in both cases hardly distinguishable, given the high-quality counting statistics. The curves have been offset vertically, for clarity of presentation, and the offsets are indicated in parenthesis.

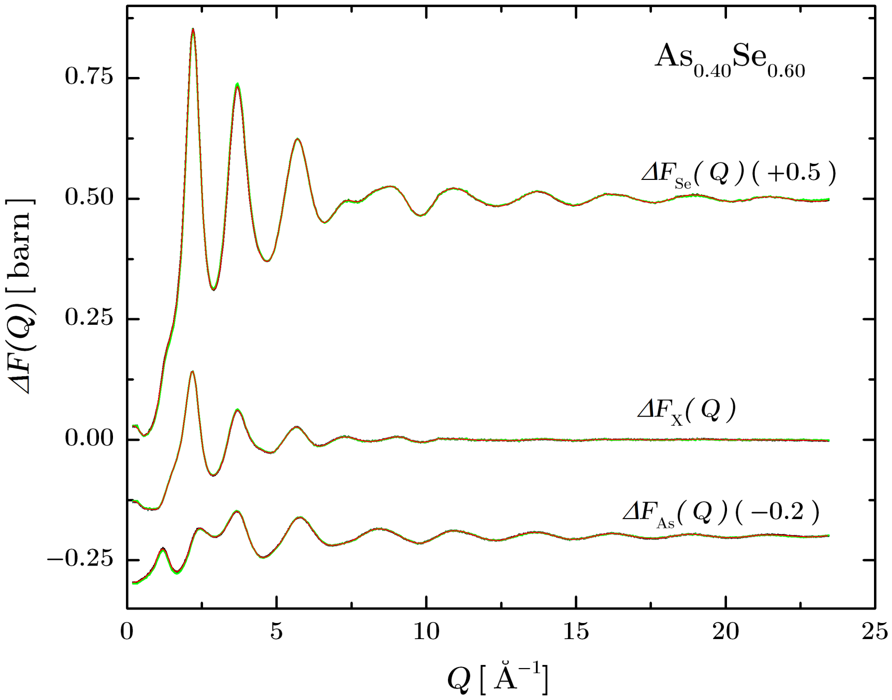

Figure 5-16: First-order difference functions for As$_{0.40}$Se$_{0.60}$, as obtained from the total structure factors $^{76}F(Q)$ and $^{\mathrm{Nat}}F(Q)$ shown in Figure 5-6. The solid black lines with vertical error bars are the first-order difference functions measured on D4c (from [90]). The vertical error bars are hardly distinguishable, given the high-quality counting statistics. The red curves show spline fits to the measured data sets. The green curves are the back-Fourier transforms of the $\Delta G(r)$ functions in Figure 5-19, once the low-r oscillations are set to their theoretical $\Delta G(r \to 0)$ limit. The curves have been offset vertically, for clarity of presentation, and the offsets are indicated in parenthesis.

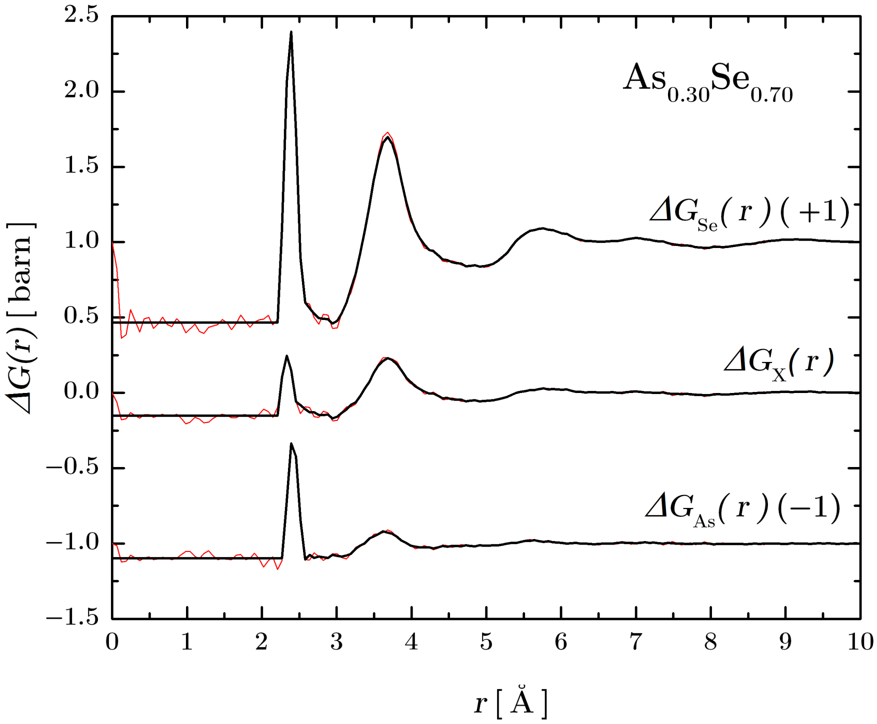

Figure 5-17: Real-space first-order difference functions $\Delta G(r)$ for $As_{0.30}Se_{0.70}$. The solid red lines show the Fourier transforms of the spline-fitted data sets shown in Figure 5-12 with $Q_{\max} = 30$ Å^{-1}. The solid black curves also show the Fourier transforms of these spline-fitted data sets, after the low-r oscillations are set to their theoretical $\Delta G(r \to 0)$ limit but, in this case, a Lorch function was applied, with $Q_{\max} = 30$ Å^{-1}, to smooth the data after the first peak. The curves for $\Delta G_{Se}(r)$ and $\Delta G_{As}(r)$ are offset vertically, for clarity of presentation, and the offsets are indicated in parenthesis.

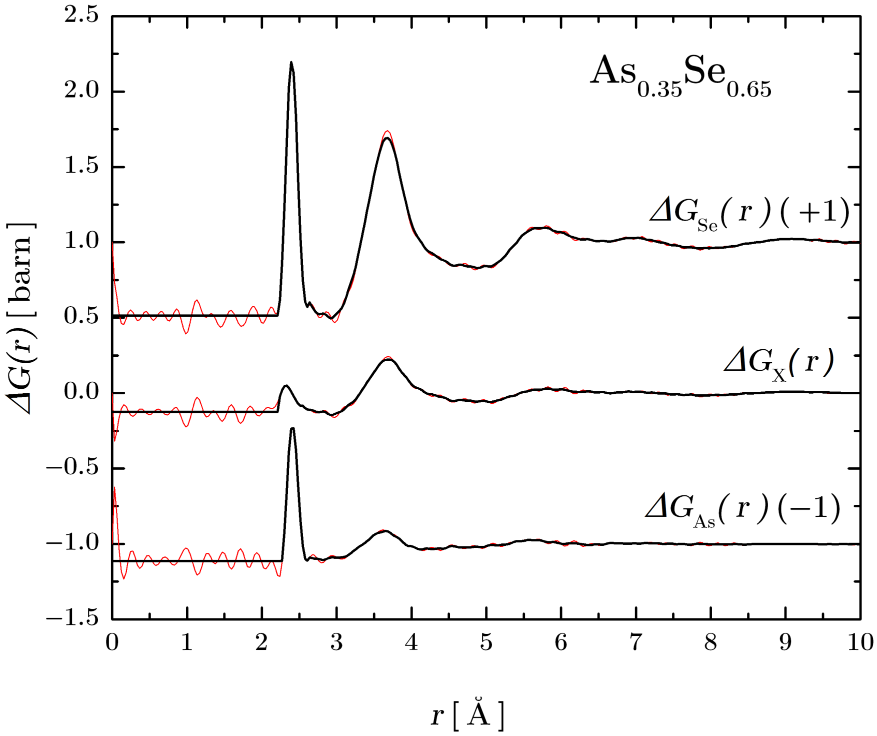

Figure 5-18: Real-space first-order difference functions $\Delta G(r)$ for As$_{0.35}$Se$_{0.65}$. The solid red lines show the Fourier transforms of the spline-fitted data sets shown in Figure 5-13 with $Q_{\mathrm{max}} = 30$ Å^{-1}. The solid black curves also show the Fourier transforms of these spline-fitted data sets, after the low-r oscillations are set to their theoretical $\Delta G(r \to 0)$ limit but, in this case, a Lorch function was applied, with $Q_{\mathrm{max}} = 30$ Å^{-1}, to smooth the data after the first peak. The curves for $\Delta G_{\mathrm{Se}}(r)$ and $\Delta G_{\mathrm{As}}(r)$ are offset vertically, for clarity of presentation, and the offsets are indicated in parenthesis.

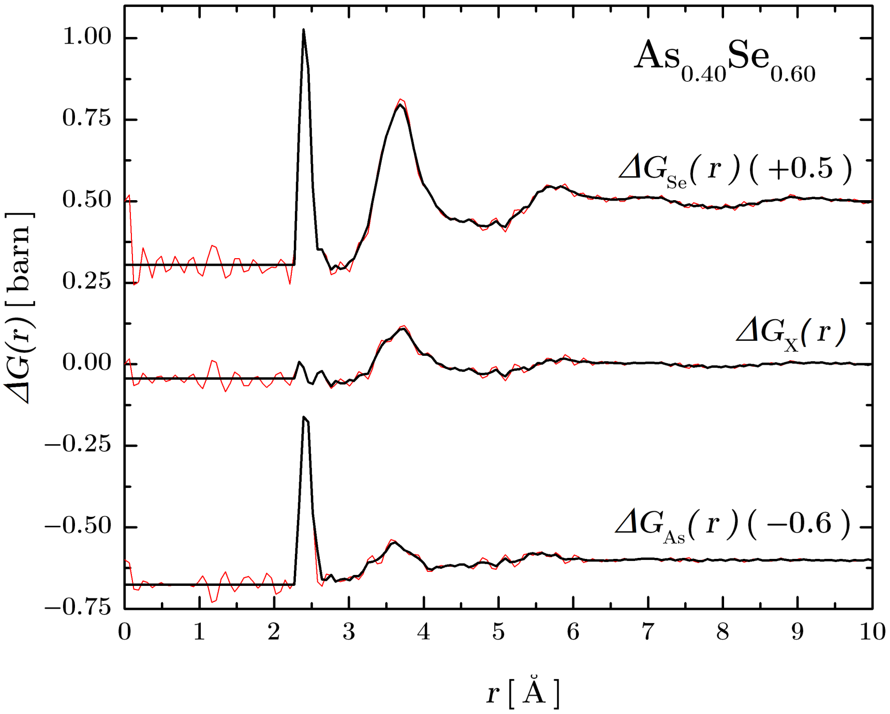

Figure 5-19: Real-space first-order difference functions $\Delta G(r)$ for $\mathrm{As_{0.40}Se_{0.60}}$. The solid red lines show the Fourier transforms of the spline-fitted data sets shown in Figure 5-14 with $Q_{\max} = 30$ Å^{-1}. The solid black curves also show the Fourier transforms of these spline-fitted data sets, after the low-r oscillations are set to their theoretical $\Delta G(r \to 0)$ limit but, in this case, a Lorch function was applied, with $Q_{\max} = 30$ Å^{-1}, to smooth the data after the first peak. The curves for $\Delta G_{\mathrm{Se}}(r)$ and $\Delta G_{\mathrm{As}}(r)$ are offset vertically, for clarity of presentation, and the offsets are indicated in parenthesis.

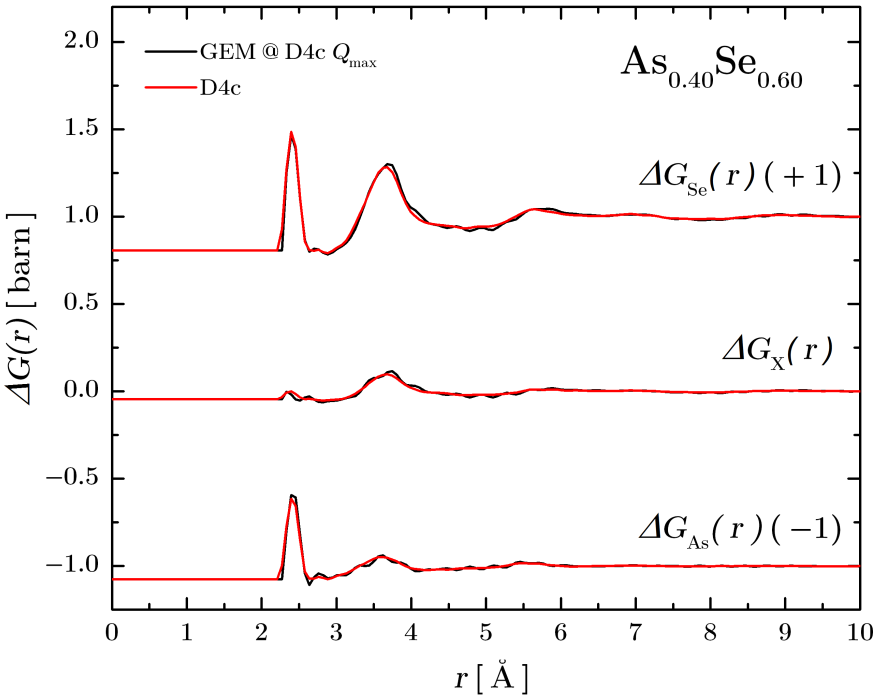

Figure 5-20: Comparison between the real-space first-order difference functions $\Delta G(r)$ for $As_{0.40}Se_{0.60}$. The solid black lines are the Fourier transforms of the GEM spline-fitted data sets shown in Figure 5-15 ($Q_{\max} = 23.45$ Å^{-1}), after the low-r oscillations are set to their theoretical $\Delta G(r \to 0)$ limit, and with a Lorch function applied (with $Q_{\max} = 23.45$ Å^{-1}) to smooth the data after the first peak. The solid red lines are the Fourier transforms of the D4c spline-fitted data sets shown in Figure 5-15, after the low-r oscillations are set to their theoretical $\Delta G(r \to 0)$ limit, and with a Lorch function applied (with $Q_{\max} = 23.45$ Å^{-1}) to smooth the data after the first peak. The curves for $\Delta G_{\mathrm{Se}}(r)$ and $\Delta G_{\mathrm{As}}(r)$ are offset vertically, for clarity of presentation, and the offsets are indicated in parenthesis.

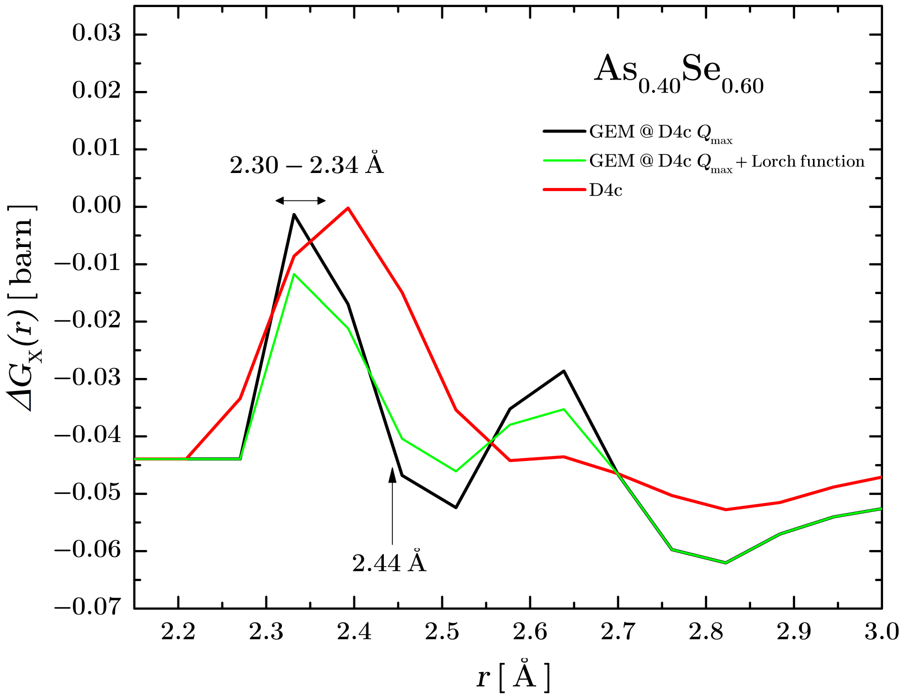

Figure 5-21: Zoom into the first-peak region of the $\Delta G_{\mathrm{X}}(r)$ first-order difference functions for $As_{0.40}Se_{0.60}$ shown in Figures 5-20 and 5-22. The solid black line is the Fourier transform of the GEM spline-fitted data, after Q_{max} was set to the D4c value of 23.45 Å^{-1}. The green solid line is also the Fourier transform of the GEM spline-fitted data after Q_{max} was set to the D4c value, but in this case a Lorch modification function was applied. The solid red line is the Fourier transform of the D4c difference function. The position of typical Se-Se distances (2.30–2.34 Å) [108] and the As-As distance in crystalline $As_{0.50}Se_{0.50}$ (2.44 Å) [115] are also shown. The dip after the first peak for the GEM data sets could originate from the nearest-neighbour As-As correlations that receive a negative weighting factor in the equation for $\Delta G_{\mathrm{X}}(r)$ (Table 5.2), but the As-As bond length would be much larger than found for crystalline $As_{0.50}Se_{0.50}$. The peak in the GEM data sets in the range $\approx$ 2.5–2.7 Å does not correspond to typical Se-Se bond distances and may therefore be a Fourier-transform artefact.

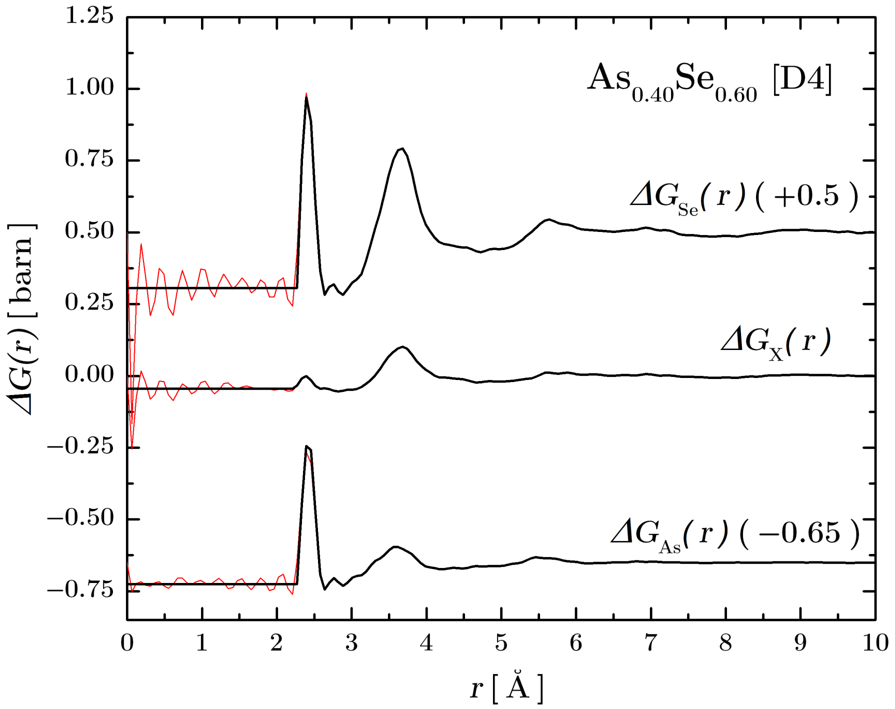

Figure 5-22: Real-space first-order difference functions $\Delta G(r)$ for As$_{0.40}$Se$_{0.60}$ as obtained from [90]. The solid red lines show the Fourier transforms of the spline-fitted data sets shown in Figure 5-16 with $Q_{\max} = 23.45$ Å^{-1}. The solid black curves also show the Fourier transforms of these spline-fitted data sets, after the low-r oscillations are set to their theoretical $\Delta G(r \to 0)$ limit but, in this case, a Lorch function was applied, with $Q_{\max} = 23.45$ Å^{-1}, to smooth the data after the first peak. The curves for $\Delta G_{\mathrm{Se}}(r)$ and $\Delta G_{\mathrm{As}}(r)$ are offset vertically, for clarity of presentation, and the offsets are indicated in parenthesis..

In order to facilitate a comparison between difference functions having different weighting factors, the real-space information can be expressed in terms of the normalised function

$$\Delta G'(r) = \frac{\Delta G(r) - \Delta G(0)}{|\Delta G(0)|}. \tag{5.19}$$

The normalised weighting factors corresponding to the $\Delta G'(r)$ functions formed using ^{76}Se isotope substitution are given in Table 5.3.

Table 5.3: Normalised weighting factors for the $\Delta G'(r)$ difference functions. The difference functions for $\mathrm{As_{0.30}Se_{0.70}}$ (I-GEM), $\mathrm{As_{0.35}Se_{0.65}}$ (II-GEM) and $\mathrm{As_{0.40}Se_{0.60}}$ (III-D4c) were obtained using ^{76}Se isotope substitution.

Weighting factor	I-GEM (barn)	II-GEM (barn)	III-D4c (barn)
$a'_1 = a_1/\lvert\Delta G_{\mathrm{Se}}(0)\rvert$	0.219(6)	0.26(1)	0.303
$a'_2 = a_2/\lvert\Delta G_{\mathrm{Se}}(0)\rvert$	0.781(12)	0.74(2)	0.697
$b'_1 = b_1/\lvert\Delta G_{\mathrm{X}}(0)\rvert$	-0.089(9)	-0.148(14)	-0.247
$b'_2 = b_2/\lvert\Delta G_{\mathrm{X}}(0)\rvert$	1.089(79)	1.148(84)	1.247
$c'_1 = c_1/\lvert\Delta G_{\mathrm{As}}(0)\rvert$	0.774(2)	0.731(6)	0.687
$c'_2 = c_2/\lvert\Delta G_{\mathrm{As}}(0)\rvert$	0.226(2)	0.296(9)	0.313

Figure 5-23 shows a comparison between the normalised $\Delta G'(r)$ functions obtained for the three investigated compositions using ^{76}Se isotope substitution, and offers a starting point for some qualitative remarks on the contribution of the different pair-correlation functions to the difference functions. The data sets shown for $\mathrm{As_{0.30}Se_{0.70}}$ and $\mathrm{As_{0.35}Se_{0.65}}$ were measured on GEM, and Q_{max} was set to the D4c value of 23.45 Å^{-1}. The data sets shown for $\mathrm{As_{0.40}Se_{0.60}}$ were measured [90] using D4c (Figure 5-22).

The first peak in $\Delta G'_{\mathrm{Se}}(r)$, which is likely to have contributions from both As-Se and Se-Se bonds, has a constant height across the composition range, despite the fact that the Se-Se correlations have weighting factors (a'_2) higher than those for the As-Se correlations (a'_1) (see Table 5.3). This may be an indication that most of the bonds are heteropolar or that the fraction of Se-Se bonds does not vary strongly with the Se concentration. The height of the first peak in $\Delta G'_{\mathrm{X}}(r)$, to which homopolar As-As and Se-Se correlations can both contribute, decreases with the Se concentration. In this case, the Se-Se correlations have weighting factors (b'_2) higher than those for the As-As correlations (b'_1), which are negative. Therefore, the reduction of the peak's height, with increasing As content, may be due to either a decrease in the fraction of Se-Se bonds and/or to an increase in the fraction of As-As bonds.

The first peak in $\Delta G'_{\mathrm{As}}(r)$ can have contributions from both As-Se and As-As bonds, where the weighting factors for the As-Se correlations (c'_1) are higher than those for the As-As correlations (c'_2). The height of the first peak does not vary strongly between $\mathrm{As_{0.30}Se_{0.70}}$ and $\mathrm{As_{0.35}Se_{0.65}}$ but shows a decrease for $\mathrm{As_{0.40}Se_{0.60}}$, and is accompanied by a small broadening of the peak width, so that the total area does not change considerably. This might be consistent with the fact that most of the bonds are heteropolar, and that the fraction of As-Se bonds does not change very much with the composition. The global trend seems to suggest: (1) that most of the bonds are heteropolar; (2) that the fraction of Se-Se bonds decreases and the fraction of As-As bonds increases, as the composition is changed from $\mathrm{As_{0.30}Se_{0.70}}$ to $\mathrm{As_{0.40}Se_{0.60}}$. However, these observations are speculative because the different compositions have different weighting factors.

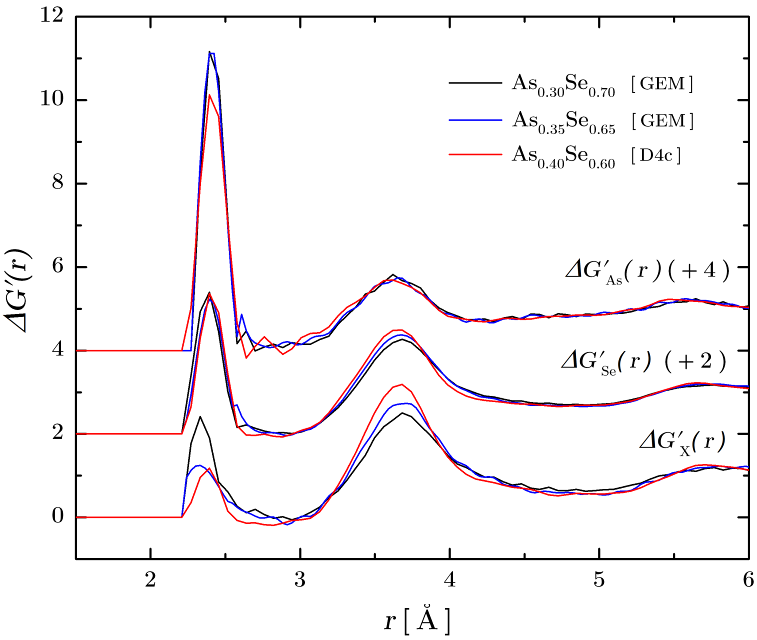

Figure 5-23: Comparison between the normalised first-order difference functions for $As_{0.30}Se_{0.70}$ (GEM - Figure 5-17), $As_{0.35}Se_{0.65}$ (GEM - Figure 5-18) and $As_{0.40}Se_{0.60}$ (D4c - Figure 5-22). For $As_{0.30}Se_{0.70}$ and $As_{0.35}Se_{0.65}$ the $\Delta G'(r)$ functions were obtained by setting $Q_{\max}$ to the D4c value of 23.45 Å^{-1}. The solid black lines represent $As_{0.30}Se_{0.70}$, the solid blue lines represent $As_{0.35}Se_{0.65}$, and the solid red lines represent $As_{0.40}Se_{0.60}$, after the unphysical low-r oscillations are set to their theoretical $\Delta G(r \to 0)$ limits. The data sets obtained by Fourier transforming without a Lorch modification function are joined smoothly to those obtained by Fourier transforming with a Lorch modification function at an r-value after the first peak. The curves for $\Delta G'_{Se}(r)$ and $\Delta G'_{As}(r)$ are offset vertically, for clarity of presentation, and the offsets are indicated in parenthesis.

5.5 Discussion

In order to understand more quantitatively the contributions of the different partial pair-distribution functions to the $\Delta G(\mathrm{r})$ functions, a comparison will be made of the present experimental results with those obtained from first-principles molecular dynamics (FPMD) simulations [25] and from reverse Monte Carlo (RMC) modelling [26], both in reciprocal and real space. Note that, while Bauchy *et al.* [25] investigated the $\mathrm{As}_{0.30}\mathrm{Se}_{0.70}$, $\mathrm{As}_{0.35}\mathrm{Se}_{0.65}$ and $\mathrm{As}_{0.40}\mathrm{Se}_{0.60}$ compositions via FPMD simulations, Hosokawa *et al.* [26] combined Anomalous X-ray Scattering (AXS) measurements and RMC modelling for the $\mathrm{As}_{0.29}\mathrm{Se}_{0.71}$, $\mathrm{As}_{0.33}\mathrm{Se}_{0.67}$ and $\mathrm{As}_{0.40}\mathrm{Se}_{0.60}$ compositions.

5.5.1 Comparison with FPMD simulations and RMC modelling

In Figures 5-24 – 5-25, the total structure factors for $\mathrm{As}_{0.30}\mathrm{Se}_{0.70}$, $\mathrm{As}_{0.35}\mathrm{Se}_{0.65}$ and $\mathrm{As}_{0.40}\mathrm{Se}_{0.60}$ measured via NDIS are compared to those obtained from the FPMD simulation and RMC methods. The total structure factors for the latter were obtained from a neutron-weighted linear combination of the partial structure factors given by Bauchy *et al.* [25] or by Hosokawa *et al.* [26], respectively. There is qualitative agreement between the RMC and NDIS results, but the heights of the peaks are not perfectly reproduced. This might be due, in part, to the fact that the RMC data were modelled by using AXS measurements having a different resolution function as compared to the data sets measured via NDIS. The agreement between the NDIS results and FPMD simulations is not as good. In particular, the pre-peak at about 1.25 Å^{-1} appears as a shoulder as opposed to a peak. Figures 5-26 – 5-27 give the corresponding real-space information, and show that the average first-peak position from the RMC data sets is systematically smaller than found from NDIS. In comparison, the real-space functions obtained by FPMD simulations show an average peak position that is systematically larger than found from NDIS.

Figures 5-28 – 5-30 compare the first-order difference functions. In this case, the RMC data agree better with the NDIS results as compared to the FPMD simulations. The corresponding real-space information is presented in Figures 5-31 – 5-33. Again, the average first-peak positions are systematically shifted towards smaller or larger values for the RMC and FPMD results, as compared to the NDIS results, respectively.

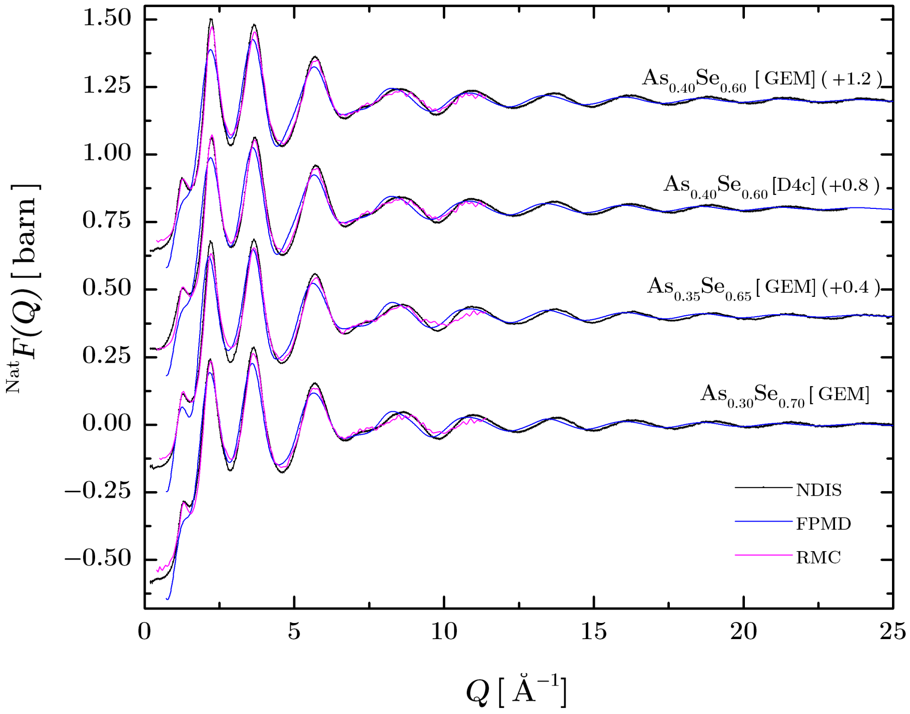

Figure 5-24: Total structure factors $^{\mathrm{Nat}}F(Q)$ for $As_{0.30}Se_{0.70}$, $As_{0.35}Se_{0.65}$ and $As_{0.40}Se_{0.60}$. The solid black lines with vertical error bars are the experimental data sets measured using GEM or D4c. The vertical error bars are hardly distinguishable, given the high-quality counting statistics. The solid blue lines are the FPMD simulations obtained from a neutron-weighted linear combination of the partial structure factors given in [25]. The solid magenta lines are the RMC-modelled total structure factors for $As_{0.29}Se_{0.71}$, $As_{0.33}Se_{0.67}$ and $As_{0.40}Se_{0.60}$, obtained from a neutron-weighted linear combination of the partial structure factors given in [26]. The curves have been offset vertically, for clarity of presentation, and the maximum Q-value has been reduced to 25 Å^{-1}. The offsets are indicated in parenthesis.

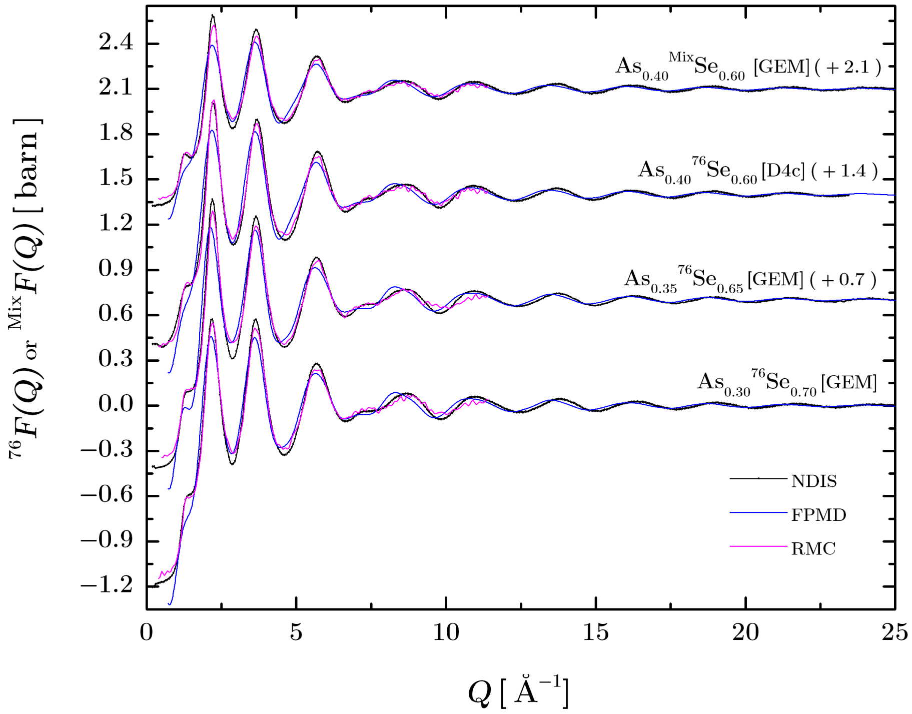

Figure 5-25: Total structure factors $^{76}F(Q)$ or $^{\mathrm{Mix}}F(Q)$ obtained for the Se-isotope enriched samples. The solid black lines with vertical error bars are the measured data sets for As$_{0.30}$^{76}Se$_{0.70}$ (GEM), As$_{0.35}$^{76}Se$_{0.65}$ (GEM), As$_{0.40}$^{76}Se$_{0.60}$ (D4c) or As$_{0.40}$$^{\mathrm{Mix}}Se_{0.60}$ (GEM). The vertical error bars are hardly distinguishable, given the high-quality counting statistics. The solid blue lines are the FPMD simulations obtained from a neutron-weighted linear combination of the partial structure factors given in [25]. The solid magenta lines are the RMC-modelled total structure factors for As$_{0.29}$^{76}Se$_{0.71}$, As$_{0.33}$^{76}Se$_{0.67}$ and As$_{0.40}$$^{\mathrm{Mix}}Se_{0.60}$ for comparison with the GEM data, and for As$_{0.40}$^{76}Se$_{0.60}$ for comparison with the D4c data. The latter were obtained from a neutron-weighted linear combination of the partial structure factors given in [26]. The curves have been offset vertically, for clarity of presentation, and the maximum Q-value has been reduced to 25 Å^{-1}. The offsets are indicated in parenthesis.

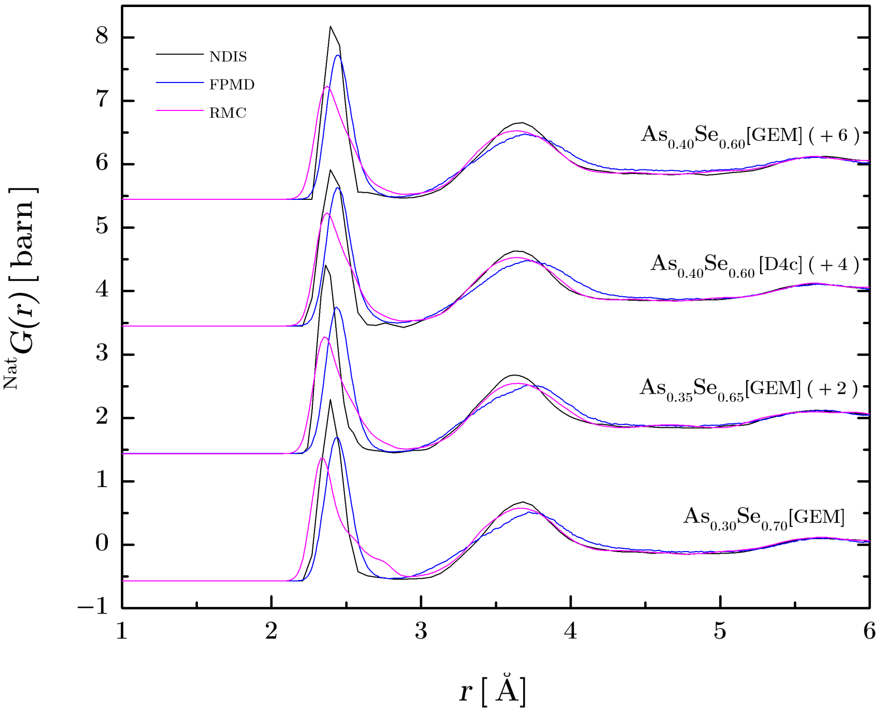

Figure 5-26: Total pair-distribution functions $^{\mathrm{Nat}}G(r)$ for $As_{0.30}Se_{0.70}$, $As_{0.35}Se_{0.65}$ and $As_{0.40}Se_{0.60}$. The solid black lines were obtained by Fourier transforming the $^{\mathrm{Nat}}F(Q)$ functions of Figure 5-24, and were set to the calculated $^{\mathrm{Nat}}G(r \to 0)$ limit at r-values smaller than the distance of closest approach between the centres of two atoms. A Lorch function was applied, with $Q_{\mathrm{max}} = 40$ Å^{-1}, to smooth the data after the first peak. The solid blue lines are the FPMD simulations obtained from a neutron-weighted linear combination of the partial pair-correlation functions given in [25]. The solid magenta lines are the RMC-modelled total pair-distribution functions for $As_{0.29}Se_{0.71}$, $As_{0.33}Se_{0.67}$ and $As_{0.40}Se_{0.60}$, as obtained from a neutron-weighted linear combination of the partial pair-distribution functions given in [26]. The curves have been offset vertically, for clarity of presentation, and the offsets are indicated in parenthesis.

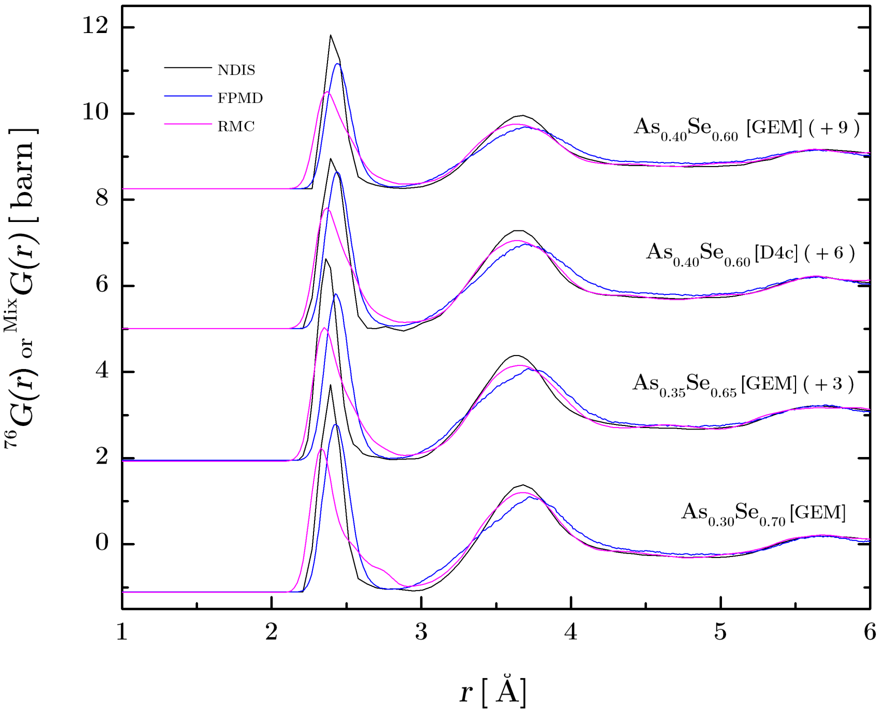

Figure 5-27: Total pair-distribution functions $^{76}G(r)$ or $^{\mathrm{Mix}}G(r)$ for $\mathrm{As_{0.30}Se_{0.70}}$, $\mathrm{As_{0.35}Se_{0.65}}$ and $\mathrm{As_{0.40}Se_{0.60}}$. The solid black lines were obtained by Fourier transforming the $F(Q)$ functions of Figure 5-25, and were set to the calculated $^{76}G(r \to 0)$ or $^{\mathrm{Mix}}G(r \to 0)$ limit at r-values smaller than the distance of closest approach between the centres of two atoms. A Lorch function was applied, with $Q_{\mathrm{max}} = 40$ Å^{-1}, to smooth the data after the first peak. The solid blue lines are the FPMD simulations obtained from a neutron-weighted linear combination of the partial pair-correlation functions given in [25]. The solid magenta lines are the RMC-modelled total pair-distribution functions for $\mathrm{As_{0.29}{}^{76}Se_{0.71}}$, $\mathrm{As_{0.33}{}^{76}Se_{0.67}}$ and $\mathrm{As_{0.40}{}^{Mix}Se_{0.60}}$ for comparison with the GEM data, and for $\mathrm{As_{0.40}{}^{76}Se_{0.60}}$ for comparison with the D4c data. The latter were obtained from a neutron-weighted linear combination of the partial pair-distribution functions given in [26]. The curves have been offset vertically, for clarity of presentation, and the offsets are indicated in parenthesis.

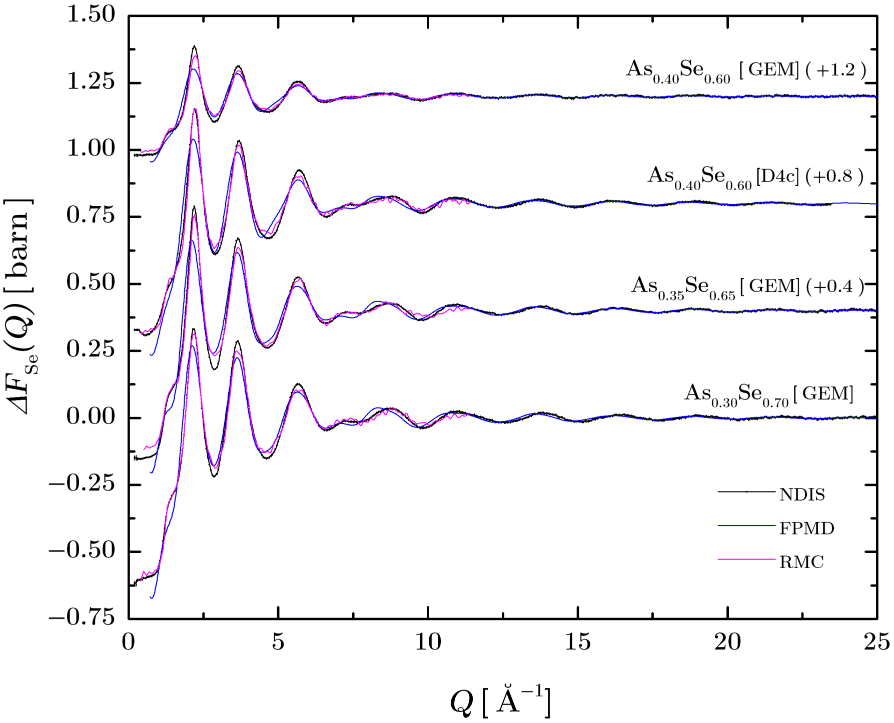

Figure 5-28: First-order difference functions $\Delta F_{\mathrm{Se}}(Q)$ for $\mathrm{As}_{0.30}\mathrm{Se}_{0.70}$, $\mathrm{As}_{0.35}\mathrm{Se}_{0.65}$ and $\mathrm{As}_{0.40}\mathrm{Se}_{0.60}$. The solid black lines with vertical error bars are the experimental data sets measured on GEM or D4c. The vertical error bars are hardly distinguishable, given the high-quality counting statistics. The solid blue lines are the FPMD simulations obtained from a neutron-weighted linear combination of the partial structure factors given in [25]. The solid magenta lines are the RMC-modelled $\Delta F_{\mathrm{Se}}(Q)$ functions for $\mathrm{As}_{0.29}\mathrm{Se}_{0.71}$, $\mathrm{As}_{0.33}\mathrm{Se}_{0.67}$ and $\mathrm{As}_{0.40}\mathrm{Se}_{0.60}$, as obtained from a neutron-weighted linear combination of the partial structure factors given in [26]. The curves have been offset vertically, for clarity of presentation, and the maximum Q-value set at 25 Å^{-1}. The offsets are indicated in parenthesis.

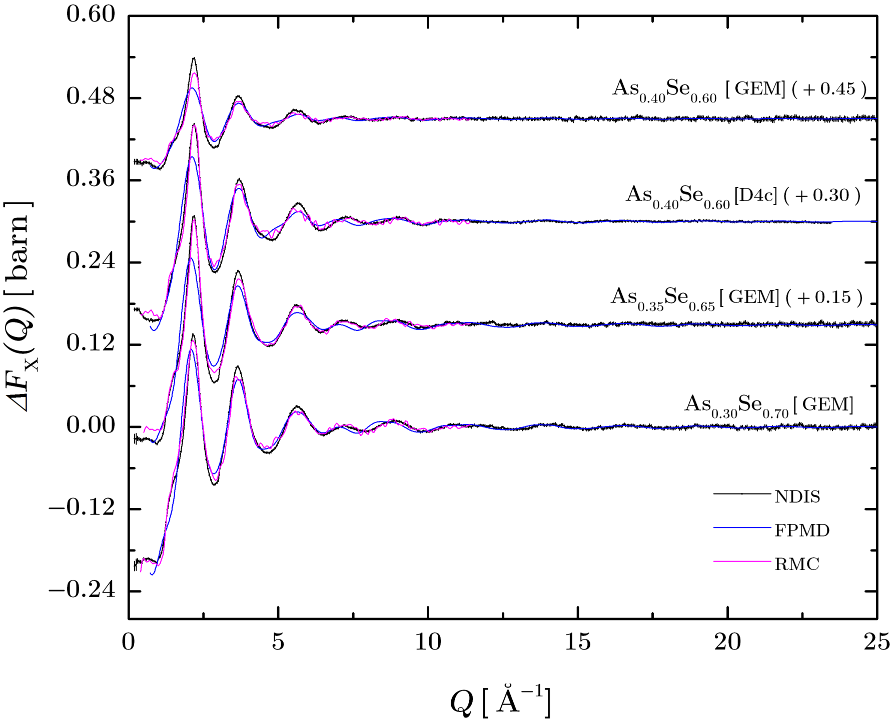

Figure 5-29: First-order difference functions $\Delta F_X(Q)$ for $As_{0.30}Se_{0.70}$, $As_{0.35}Se_{0.65}$ and $As_{0.40}Se_{0.60}$. The solid black lines with vertical error bars are the experimental data sets measured on GEM or D4c. The vertical error bars are hardly distinguishable, given the high-quality counting statistics. The solid blue lines are the FPMD simulations obtained from a neutron-weighted linear combination of the partial structure factors given in [25]. The solid magenta lines are the RMC-modelled $\Delta F_X(Q)$ function for $As_{0.29}Se_{0.71}$, $As_{0.33}Se_{0.67}$ and $As_{0.40}Se_{0.60}$, as obtained from a neutron-weighted linear combination of the partial structure factors given in [26]. The curves have been offset vertically, for clarity of presentation, and the maximum Q-value set at 25 Å^{-1}. The offsets are indicated in parenthesis.

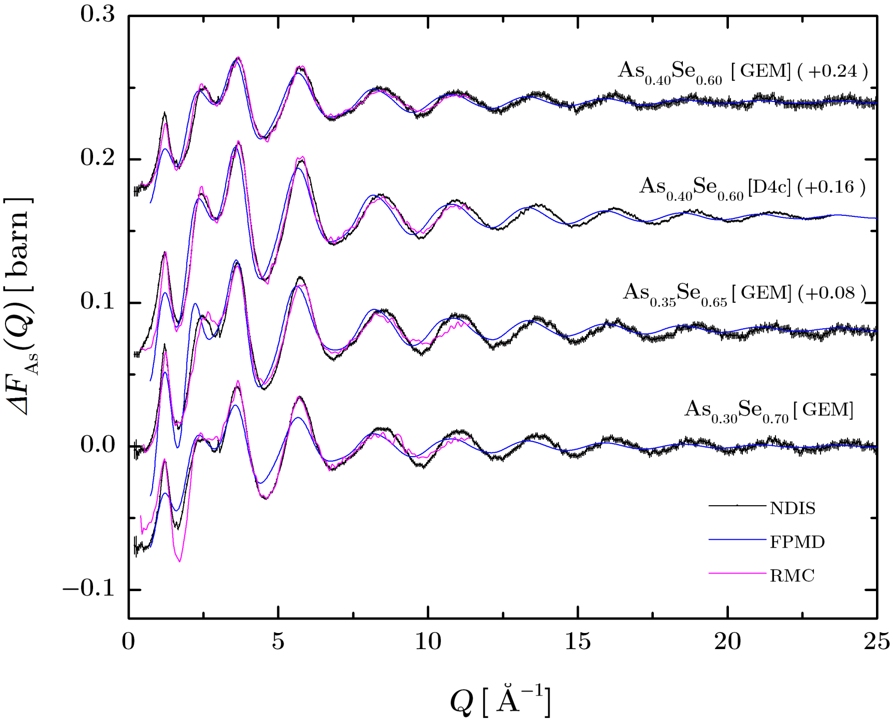

Figure 5-30: First-order difference functions $\Delta F_{\mathrm{As}}(Q)$ for $\mathrm{As_{0.30}Se_{0.70}}$, $\mathrm{As_{0.35}Se_{0.65}}$ and $\mathrm{As_{0.40}Se_{0.60}}$. The solid black lines with vertical error bars are the experimental data sets measured on GEM or D4c. The vertical error bars are hardly distinguishable, given the high-quality counting statistics. The solid blue lines are the FPMD simulations obtained from a neutron-weighted linear combination of the partial structure factors given in [25]. The solid magenta lines are the RMC-modelled $\Delta F_{\mathrm{As}}(Q)$ functions for $\mathrm{As_{0.29}Se_{0.71}}$, $\mathrm{As_{0.33}Se_{0.67}}$ and $\mathrm{As_{0.40}Se_{0.60}}$, as obtained from a neutron-weighted linear combination of the partial structure factors given in [26]. The curves have been offset vertically, for clarity of presentation, and the maximum Q-value has been set at 25 $\mathrm{\AA}^{-1}$. The offsets are indicated in parenthesis.

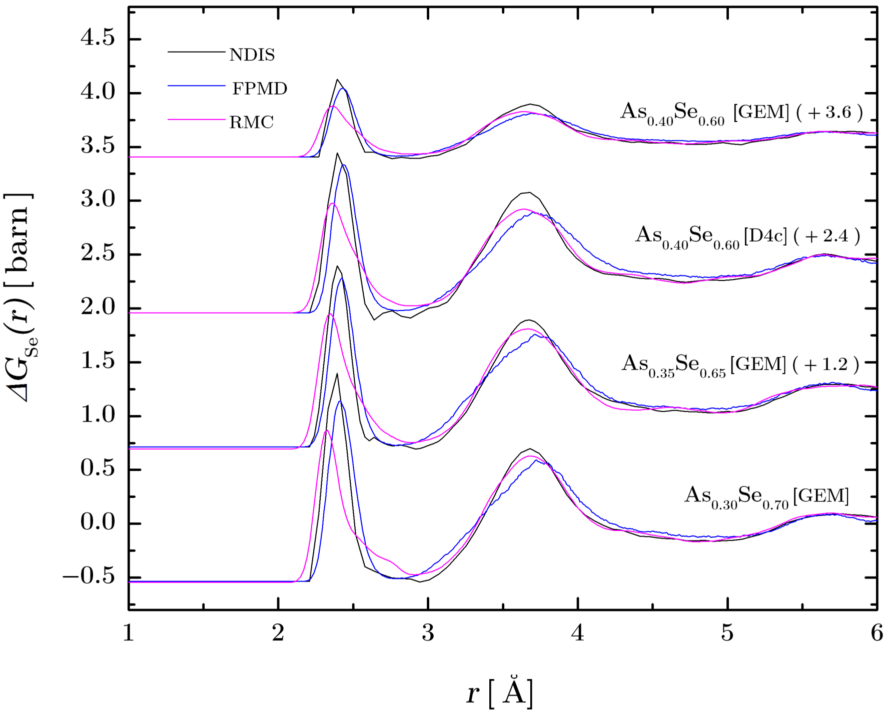

Figure 5-31: Real-space first-order difference functions $\Delta G_{\mathrm{Se}}(r)$ for $\mathrm{As_{0.30}Se_{0.70}}$, $\mathrm{As_{0.35}Se_{0.65}}$ and $\mathrm{As_{0.40}Se_{0.60}}$. The solid black lines are the experimental data sets measured on GEM or D4c, with a Lorch function applied ($Q_{\max} = 30$ Å^{-1}) to smooth the data after the first peak. The solid blue lines are the FPMD simulations obtained from a neutron-weighted linear combination of the partial pair-distribution functions given in [25]. The solid magenta lines are the RMC-modelled $\Delta G_{\mathrm{Se}}(r)$ functions for $\mathrm{As_{0.29}Se_{0.71}}$, $\mathrm{As_{0.33}Se_{0.67}}$ and $\mathrm{As_{0.40}Se_{0.60}}$, obtained from a neutron-weighted linear combination of the partial pair-distribution functions given in [26]. The curves have been offset vertically, for clarity of presentation, and the offsets are indicated in parenthesis.

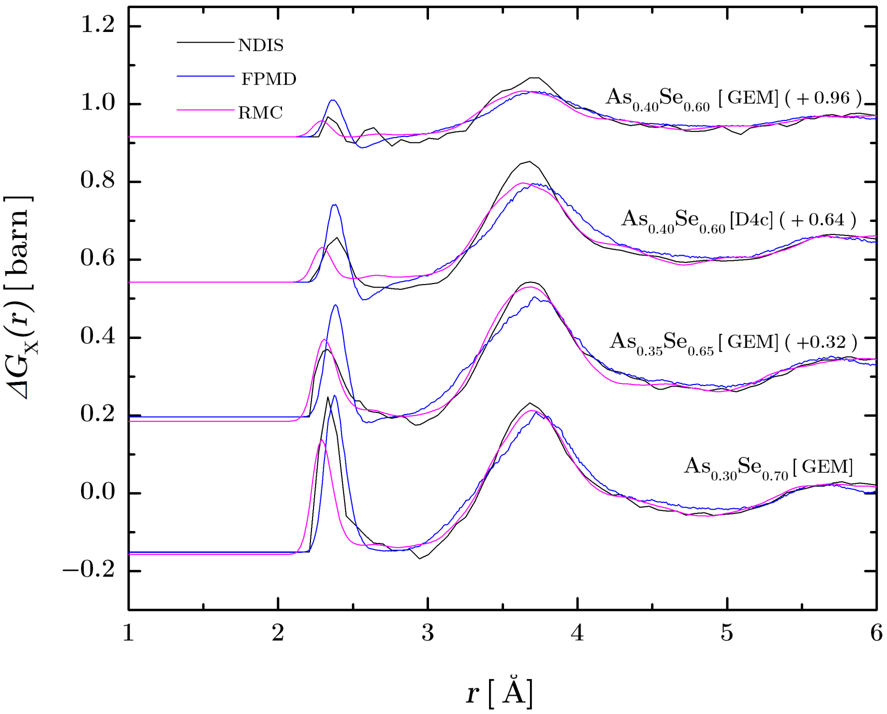

Figure 5-32: Real-space first-order difference functions $\Delta G_{\mathrm{X}}(r)$ for $\mathrm{As}_{0.30}\mathrm{Se}_{0.70}$, $\mathrm{As}_{0.35}\mathrm{Se}_{0.65}$ and $\mathrm{As}_{0.40}\mathrm{Se}_{0.60}$. The solid black lines are the experimental data sets measured on GEM or D4c, with a Lorch function applied ($Q_{\mathrm{max}} = 30$ Å^{-1}) to smooth the data after the first peak. The solid blue lines are the FPMD simulations obtained from a neutron-weighted linear combination of the partial pair-distribution functions given in [25]. The solid magenta lines are the RMC-modelled $\Delta G_{\mathrm{X}}(r)$ functions for $\mathrm{As}_{0.29}\mathrm{Se}_{0.71}$, $\mathrm{As}_{0.33}\mathrm{Se}_{0.67}$ and $\mathrm{As}_{0.40}\mathrm{Se}_{0.60}$, obtained from a neutron-weighted linear combination of the partial pair-distribution functions given in [26]. The curves have been offset vertically, for clarity of presentation, and the offsets are indicated in parenthesis.

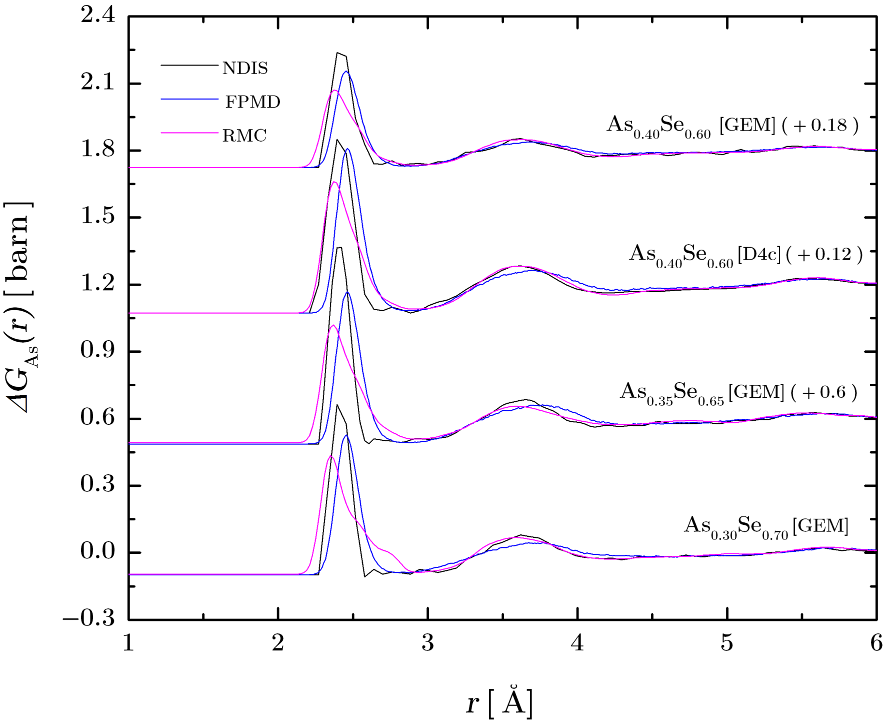

Figure 5-33: Real-space first-order difference functions $\Delta G_{\mathrm{As}}(r)$ for $\mathrm{As}_{0.30}\mathrm{Se}_{0.70}$, $\mathrm{As}_{0.35}\mathrm{Se}_{0.65}$ and $\mathrm{As}_{0.40}\mathrm{Se}_{0.60}$. The solid black lines are the experimental data sets measured on GEM or D4c, with a Lorch function applied ($Q_{\mathrm{max}} = 30$ Å^{-1}) to smooth the data after the first peak. The solid blue lines are the FPMD simulations obtained from a neutron-weighted linear combination of the partial pair-distribution functions given in [25]. The solid magenta lines are the RMC-modelled $\Delta G_{\mathrm{As}}(r)$ functions for $\mathrm{As}_{0.29}\mathrm{Se}_{0.71}$, $\mathrm{As}_{0.33}\mathrm{Se}_{0.67}$ and $\mathrm{As}_{0.40}\mathrm{Se}_{0.60}$, obtained from a neutron-weighted linear combination of the partial pair-distribution functions given in [26]. The curves have been offset vertically, for clarity of presentation, and the offsets are indicated in parenthesis.

The first-peak positions and partial coordination numbers given by Bauchy *et al.* [25] and by Hosokawa *et al.* [26] for the partial pair-distribution functions are given in Tables 5.4–5.5. Although the RMC and FPMD values do not match, they both show the same trends, *i.e.* when the As content increases, the coordination number $\bar{n}_{\mathrm{As}}^{\mathrm{As}}$ increases, whereas the coordination numbers $\bar{n}_{\mathrm{As}}^{\mathrm{Se}}$ and $\bar{n}_{\mathrm{Se}}^{\mathrm{Se}}$ both decrease. Tables 5.6 – 5.9 show a comparison between the neutron-weighted coordination numbers and peak positions obtained from RMC or FPMD, and the values obtained using NDIS. The results show that, as the As concentration increases:

- the coordination numbers $\overline{n}_{\mathrm{exp}}$, $\overline{n}_{\mathrm{RMC}}$ and $\overline{n}_{\mathrm{MD}}$ associated with $\Delta G_{\mathrm{X}}(r)$ decrease. This trend is consistent with both a decrease of $\bar{n}_{\mathrm{Se}}^{\mathrm{Se}}$ and an increase of $\bar{n}_{\mathrm{As}}^{\mathrm{As}}$, given that $g_{\mathrm{AsAs}}(r)$ has a negative weighting factor in $\Delta G_{\mathrm{X}}(r)$ (Table 5.2);
- the coordination numbers $\overline{n}_{\mathrm{exp}}$, $\overline{n}_{\mathrm{RMC}}$ and $\overline{n}_{\mathrm{MD}}$ associated with $\Delta G_{\mathrm{Se}}(r)$ remain about constant;
- the coordination numbers $\overline{n}_{\mathrm{exp}}$ and $\overline{n}_{\mathrm{MD}}$ associated with $\Delta G_{\mathrm{As}}(r)$ remain constant, whereas $\overline{n}_{\mathrm{RMC}}$ decreases. Since both $\bar{n}_{\mathrm{As}}^{\mathrm{Se}}$ and $\bar{n}_{\mathrm{As}}^{\mathrm{As}}$ contribute to these total coordination numbers, and the first decreases while the second increases, the trend for $\overline{n}_{\mathrm{RMC}}$ is due to a decrease in $\bar{n}_{\mathrm{As}}^{\mathrm{Se}}$ by 41% between the compositions $\mathrm{As}_{0.30}\mathrm{Se}_{0.70}$ and $\mathrm{As}_{0.40}\mathrm{Se}_{0.60}$, as compared to a 18% decrease in the corresponding FPMD values.

The discrepancy between the coordination numbers obtained using NDIS versus RMC or FPMD can be quantified as

$$\Delta n = \frac{\left|\overline{n} - \overline{n}_{\mathrm{exp}}\right|}{\left|\overline{n}_{\mathrm{exp}}\right|}, \tag{5.20}$$

where $\overline{n}$ refers to a coordination number obtained via RMC or FPMD, and $\overline{n}_{\mathrm{exp}}$ refers to a coordination number obtained from NDIS. For the $\mathrm{As}_{0.30}\mathrm{Se}_{0.70}$ and $\mathrm{As}_{0.35}\mathrm{Se}_{0.65}$ compositions (Tables 5.6 – 5.7), the discrepancy between the coordination numbers obtained via RMC and NDIS varies between 0 and 27.3%. In both cases, the largest discrepancy is obtained for the difference function $\Delta G_{\mathrm{X}}(r)$, which involves both As-As and Se-Se correlations. For the FPMD and NDIS values, the discrepancy varies between 0 and 2% for $\mathrm{As}_{0.30}\mathrm{Se}_{0.70}$, and between 0 – 18% for $\mathrm{As}_{0.35}\mathrm{Se}_{0.65}$. For the $\mathrm{As}_{0.40}\mathrm{Se}_{0.60}$ composition (Tables 5.8 – 5.10), the discrepancy between the coordination numbers obtained from RMC and NDIS reaches 60-76% for $\Delta G_{\mathrm{X}}(r)$, as compared to a discrepancy of 0-33% for FPMD and NDIS. Hence, the coordination numbers obtained via NDIS are in better agreement with those obtained using FPMD simulations rather than from RMC modelling.

RMC compositions	$\overline{n}_{\mathrm{As}}^{\mathrm{As}}$	$\overline{r}_{\mathrm{AsAs}}$	$\overline{n}_{\mathrm{As}}^{\mathrm{Se}}$	$\overline{r}_{\mathrm{AsSe}}$	$\overline{n}_{\mathrm{Se}}^{\mathrm{Se}}$	$\overline{r}_{\mathrm{SeSe}}$
$\mathrm{As}_{0.29}\mathrm{Se}_{0.71}$	0.12	2.41	3.57	2.35	0.54	2.29
$\mathrm{As}_{0.33}\mathrm{Se}_{0.67}$	0.24	2.45	3.05	2.37	0.50	2.31
$\mathrm{As}_{0.40}\mathrm{Se}_{0.60}$	0.73	2.41	2.53	2.37	0.32	2.25

Table 5.4: Coordination numbers and peak positions from the partial-pair correlation functions for $\mathrm{As}_{0.29}\mathrm{Se}_{0.71}$, $\mathrm{As}_{0.33}\mathrm{Se}_{0.67}$ and $\mathrm{As}_{0.40}\mathrm{Se}_{0.60}$ obtained using RMC [26].

FPMD compositions	$\overline{n}_{\mathrm{As}}^{\mathrm{As}}$	$\overline{r}_{\mathrm{AsAs}}$	$\overline{n}_{\mathrm{As}}^{\mathrm{Se}}$	$\overline{r}_{\mathrm{AsSe}}$	$\overline{n}_{\mathrm{Se}}^{\mathrm{Se}}$	$\overline{r}_{\mathrm{SeSe}}$
$\mathrm{As}_{0.30}\mathrm{Se}_{0.70}$	0.07	2.57	2.94	2.47	0.74	2.39
$\mathrm{As}_{0.35}\mathrm{Se}_{0.65}$	0.37	2.53	2.66	2.46	0.59	2.41
$\mathrm{As}_{0.40}\mathrm{Se}_{0.60}$	0.65	2.55	2.40	2.45	0.42	2.37

Table 5.5: Coordination numbers and peak positions from the partial-pair correlation functions for $\mathrm{As}_{0.30}\mathrm{Se}_{0.70}$, $\mathrm{As}_{0.35}\mathrm{Se}_{0.65}$ and $\mathrm{As}_{0.40}\mathrm{Se}_{0.60}$ obtained using FPMD simulations [25].

$\mathrm{As}_{0.30}\mathrm{Se}_{0.70}$	$\overline{r}_{\mathrm{exp}}$ (Å)	$\overline{n}_{\mathrm{exp}}$	$\overline{r}_{\mathrm{RMC}}$ (Å)	$\overline{n}_{\mathrm{RMC}}$	$\overline{r}_{\mathrm{MD}}$ (Å)	$\overline{n}_{\mathrm{MD}}$
$^{\mathrm{Nat}}G(r)$	2.40(3)	2.2(1)	2.34	2.3	2.43	2.2
$^{76}G(r)$	2.40(3)	1.96(4)	2.33	2.0	2.43	2.0
$\Delta G_{\mathrm{Se}}(r)$	2.38(3)	1.7(1)	2.32	1.7	2.41	1.7
$\Delta G_{\mathrm{X}}(r)$	2.34(3)	1.1(1)	2.29	0.8	2.38	1.1
$\Delta G_{\mathrm{As}}(r)$	2.40(3)	3.3(1)	2.35	4.0	2.45	3.3

Table 5.6: The average peak positions and coordination numbers ($\overline{r}_{\mathrm{exp}}$, $\overline{n}_{\mathrm{exp}}$) for the real-space functions obtained for $\mathrm{As}_{0.30}\mathrm{Se}_{0.70}$ on GEM, as well as the average peak positions and coordination numbers obtained from the RMC modelling of $\mathrm{As}_{0.29}\mathrm{Se}_{0.71}$ ($\overline{r}_{\mathrm{RMC}}$, $\overline{n}_{\mathrm{RMC}}$) [26], and from the FPMD simulations of $\mathrm{As}_{0.30}\mathrm{Se}_{0.70}$ ($\overline{r}_{\mathrm{MD}}$, $\overline{n}_{\mathrm{MD}}$) [25].

$\mathrm{As}_{0.35}\mathrm{Se}_{0.65}$	$\overline{r}_{\mathrm{exp}}$ (Å)	$\overline{n}_{\mathrm{exp}}$	$\overline{r}_{\mathrm{RMC}}$ (Å)	$\overline{n}_{\mathrm{RMC}}$	$\overline{r}_{\mathrm{MD}}$ (Å)	$\overline{n}_{\mathrm{MD}}$
$^{\mathrm{Nat}}G(r)$	2.40(3)	2.2(1)	2.36	2.3	2.43	2.3
$^{76}G(r)$	2.40(3)	1.93(4)	2.36	1.9	2.43	2.0
$\Delta G_{\mathrm{Se}}(r)$	2.40(3)	1.7(1)	2.35	1.7	2.42	1.7
$\Delta G_{\mathrm{X}}(r)$	2.32(3)	0.8(1)	2.31	0.8	2.38	0.9
$\Delta G_{\mathrm{As}}(r)$	2.40(3)	3.3(1)	2.37	3.6	2.45	3.3

Table 5.7: The average peak positions and coordination numbers ($\overline{r}_{\mathrm{exp}}$, $\overline{n}_{\mathrm{exp}}$) for the real-space functions obtained for $\mathrm{As}_{0.35}\mathrm{Se}_{0.65}$ on GEM, as well as the average peak positions and coordination numbers obtained from the RMC modelling of $\mathrm{As}_{0.33}\mathrm{Se}_{0.67}$ ($\overline{r}_{\mathrm{RMC}}$, $\overline{n}_{\mathrm{RMC}}$) [26] and from the FPMD simulations of $\mathrm{As}_{0.35}\mathrm{Se}_{0.65}$ ($\overline{r}_{\mathrm{MD}}$, $\overline{n}_{\mathrm{MD}}$) [25].

$\mathrm{As}_{0.40}\mathrm{Se}_{0.60}$	$\overline{r}_{\mathrm{exp}}$ (Å)	$\overline{n}_{\mathrm{exp}}$	$\overline{r}_{\mathrm{RMC}}$ (Å)	$\overline{n}_{\mathrm{RMC}}$	$\overline{r}_{\mathrm{MD}}$ (Å)	$\overline{n}_{\mathrm{MD}}$
$^{\mathrm{Nat}}G(r)$	2.41(3)	2.2(1)	2.37	2.4	2.44	2.3
$^{\mathrm{Mix}}G(r)$	2.41(3)	2.1(1)	2.37	2.1	2.44	2.2
$\Delta G_{\mathrm{Se}}(r)$	2.40(3)	1.7(1)	2.36	1.7	2.43	1.8
$\Delta G_{\mathrm{X}}(r)$	2.39(3)	0.3(2)	2.29	0.12	2.37	0.4
$\Delta G_{\mathrm{As}}(r)$	2.42(3)	3.1(1)	2.38	3.4	2.45	3.2

Table 5.8: The average peak positions and coordination numbers ($\overline{r}_{\mathrm{exp}}$, $\overline{n}_{\mathrm{exp}}$) for the real-space functions obtained for $\mathrm{As}_{0.40}\mathrm{Se}_{0.60}$ on GEM, as well as the average peak positions and coordination numbers obtained from the RMC modelling of $\mathrm{As}_{0.40}\mathrm{Se}_{0.60}$ ($\overline{r}_{\mathrm{RMC}}$, $\overline{n}_{\mathrm{RMC}}$) [26] and from the FPMD simulations of $\mathrm{As}_{0.40}\mathrm{Se}_{0.60}$ ($\overline{r}_{\mathrm{MD}}$, $\overline{n}_{\mathrm{MD}}$) [25].

$\mathrm{As}_{0.40}\mathrm{Se}_{0.60}$	$\overline{r}_{\mathrm{exp}}$ (Å)	$\overline{n}_{\mathrm{exp}}$	$\overline{r}_{\mathrm{RMC}}$ (Å)	$\overline{n}_{\mathrm{RMC}}$	$\overline{r}_{\mathrm{MD}}$ (Å)	$\overline{n}_{\mathrm{MD}}$
$^{\mathrm{Nat}}G(r)$	2.41(3)	2.3(1)	2.37	2.4	2.44	2.3
$^{\mathrm{Mix}}G(r)$	2.41(3)	2.1(1)	2.37	2.1	2.44	2.2
$\Delta G_{\mathrm{Se}}(r)$	2.41(3)	1.8(1)	2.36	1.7	2.43	1.8
$\Delta G_{\mathrm{X}}(r)$	2.39(3)	0.5(2)	2.29	0.12	2.37	0.4
$\Delta G_{\mathrm{As}}(r)$	2.41(3)	3.2(1)	2.38	3.4	2.45	3.2

Table 5.9: The average peak positions and coordination numbers ($\overline{r}_{\mathrm{exp}}$, $\overline{n}_{\mathrm{exp}}$) for the real-space functions obtained for $\mathrm{As}_{0.40}\mathrm{Se}_{0.60}$ on D4c ([90]), as well as the average peak positions and coordination numbers obtained from the RMC modelling of $\mathrm{As}_{0.40}\mathrm{Se}_{0.60}$ ($\overline{r}_{\mathrm{RMC}}$, $\overline{n}_{\mathrm{RMC}}$) [26] and from the FPMD simulations of $\mathrm{As}_{0.40}\mathrm{Se}_{0.60}$ ($\overline{r}_{\mathrm{MD}}$, $\overline{n}_{\mathrm{MD}}$) [25].

$\mathrm{As}_{0.40}\mathrm{Se}_{0.60}$	$\overline{r}_{\mathrm{exp}}$ (Å)	$\overline{n}_{\mathrm{exp}}$	$\overline{r}_{\mathrm{RMC}}$ (Å)	$\overline{n}_{\mathrm{RMC}}$	$\overline{r}_{\mathrm{MD}}$ (Å)	$\overline{n}_{\mathrm{MD}}$
$^{\mathrm{Nat}}G(r)$	2.41(3)	2.3(1)	2.37	2.4	2.44	2.3
$^{76}G(r)$	2.41(3)	2.0(1)	2.37	1.8	2.44	2.0
$\Delta G_{\mathrm{Se}}(r)$	2.41(3)	1.7(1)	2.36	1.7	2.43	1.7
$\Delta G_{\mathrm{X}}(r)$	2.38(3)	0.5(2)	2.29	0.2	2.37	0.5
$\Delta G_{\mathrm{As}}(r)$	2.41(3)	3.3(1)	2.38	3.5	2.45	3.3

Table 5.10: The average peak positions and coordination numbers ($\overline{r}_{\mathrm{exp}}$, $\overline{n}_{\mathrm{exp}}$) for the real-space functions obtained for $\mathrm{As}_{0.40}\mathrm{Se}_{0.60}$ on D4c ([90]), as well as the average peak positions and coordination numbers obtained from the RMC modelling of $\mathrm{As}_{0.40}\mathrm{Se}_{0.60}$ ($\overline{r}_{\mathrm{RMC}}$, $\overline{n}_{\mathrm{RMC}}$) [26] and from the FPMD simulations of $\mathrm{As}_{0.40}\mathrm{Se}_{0.60}$ ($\overline{r}_{\mathrm{MD}}$, $\overline{n}_{\mathrm{MD}}$) [25].

5.5.2 Network models

The coordination numbers obtained from the NDIS, RMC and FPMD methods can be compared to those calculated by assuming either the RCN or CON model. Both models assume that the “8-N” rule holds [108], such that As is 3-fold coordinated and Se is 2-fold coordinated. Then, the number of nearest-neighbour atoms for As can be denoted by $z_{\mathrm{As}} = 3$, and the number of nearest-neighbour atoms for Se can be denoted by $z_{\mathrm{Se}} = 2$. The RCN model assumes that there is no difference between the bond energies or any other effect that could lead to preferential ordering, *i.e.* the distribution of the bond types is purely statistical. In this case, by defining the total number of bonds as

$$z = \frac{c_{\mathrm{As}} z_{\mathrm{As}} + c_{\mathrm{Se}} z_{\mathrm{Se}}}{2}, \tag{5.21}$$

the coordination numbers for homopolar and heteropolar bonds are given by [106]

$$\begin{aligned} \bar{n}_{\mathrm{As}}^{\mathrm{As}} &= c_{\mathrm{As}} \frac{z_{\mathrm{As}}^2}{2z}, \\ \bar{n}_{\mathrm{Se}}^{\mathrm{Se}} &= c_{\mathrm{Se}} \frac{z_{\mathrm{Se}}^2}{2z}, \\ \bar{n}_{\mathrm{As}}^{\mathrm{Se}} &= c_{\mathrm{Se}} \frac{z_{\mathrm{Se}} z_{\mathrm{As}}}{2z}. \end{aligned} \tag{5.22}$$

In the CON model, heteropolar bonds are favoured, such that only As-Se and Se-Se bonds are allowed for the Se-rich region of the phase diagram ($\mathrm{c}_{\mathrm{As}} < 0.4$), while only As-Se and As-As bonds are allowed for the As-rich side ($\mathrm{c}_{\mathrm{As}} > 0.4$). At the stoichiometric composition,

$$c_{\mathrm{As}} = \frac{z_{\mathrm{Se}}}{z_{\mathrm{Se}} + z_{\mathrm{As}}} = 0.4 \tag{5.23}$$

and only As-Se bonds are allowed, such that

$$\begin{aligned} \bar{n}_{\mathrm{As}}^{\mathrm{As}} &= \bar{n}_{\mathrm{Se}}^{\mathrm{Se}} = 0, \\ \bar{n}_{\mathrm{As}}^{\mathrm{Se}} &= 3, \end{aligned}$$

i.e. the network is expected to be completely chemically ordered for $\mathrm{As}_{0.40}\mathrm{Se}_{0.60}$ [108]. The $\mathrm{As}_{0.30}\mathrm{Se}_{0.70}$ and $\mathrm{As}_{0.35}\mathrm{Se}_{0.65}$ compositions are in the Se-rich region $0 \le c_{\mathrm{As}} < 0.4$ where

$$\begin{aligned} \bar{n}_{\mathrm{As}}^{\mathrm{Se}} &= z_{\mathrm{As}} = 3, \\ \bar{n}_{\mathrm{Se}}^{\mathrm{Se}} &= z_{\mathrm{Se}} - \frac{c_{\mathrm{As}}}{c_{\mathrm{Se}}} z_{\mathrm{As}}. \end{aligned} \tag{5.24}$$

In Figures 5-34 – 5-41, the coordination numbers obtained from the NDIS, RMC and FPMD methods are compared to those calculated by assuming either the RCN or the CON model. The results show that neither of these models perfectly describe the structure of the investigated $\mathrm{As}_x\mathrm{Se}_{1-x}$ glassy networks for the spanned composition range. In particular, even if the CON model seems to be more realistic for the $\mathrm{As}_{0.30}\mathrm{Se}_{0.70}$ and $\mathrm{As}_{0.35}\mathrm{Se}_{0.65}$ compositions, it fails in describing the coordination numbers for $\mathrm{As}_{0.40}\mathrm{Se}_{0.60}$, especially in the case of the $\Delta G_\mathrm{X}(r)$ functions for which the nearest-neighbour coordination number involves only homopolar bonds. In fact, for the CON model, only heteropolar bonds are allowed at the stoichiometric composition, whereas the NDIS, RMC and FPMD results are all consistent with the presence of homopolar As-As and Se-Se bonds.

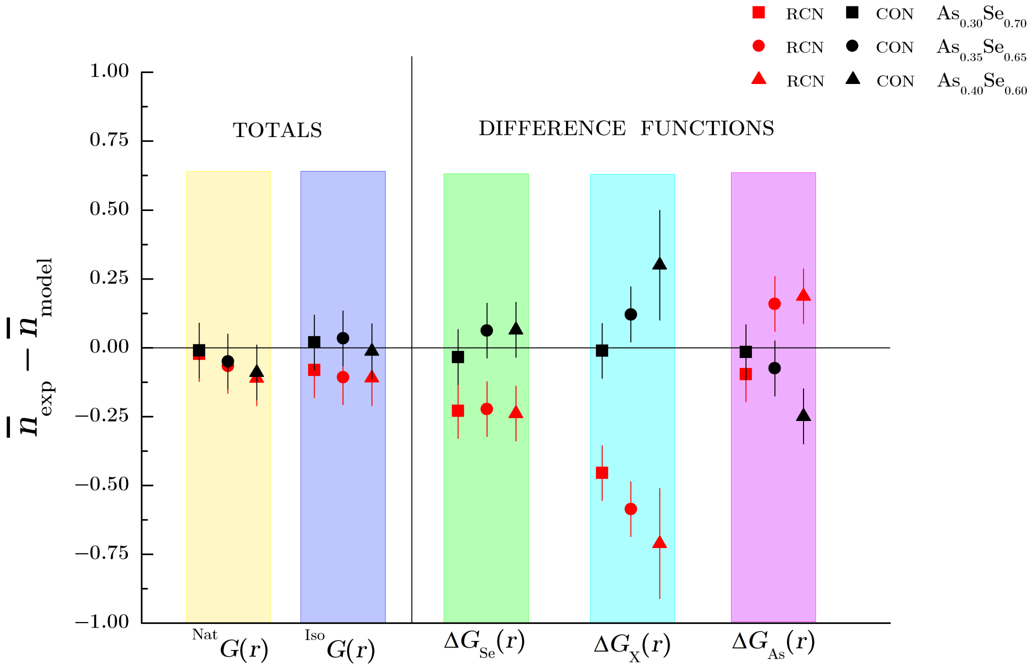

Figure 5-34: The differences between the coordination numbers obtained from the GEM data and the values obtained from either the RCN (red markers) or CON (black markers) model. The values for $\mathrm{As}_{0.30}\mathrm{Se}_{0.70}$ are represented by squares (■, 🟥), the values for $\mathrm{As}_{0.35}\mathrm{Se}_{0.65}$ are represented by circles (•, 🔴), and the values for $\mathrm{As}_{0.40}\mathrm{Se}_{0.60}$ are represented by triangles (▲, 🔺). The values related to the total pair-distribution functions are highlighted in yellow for $^\mathrm{Nat}G(r)$ and in blue for $^\mathrm{Iso}G(r)$, where Iso = 76 for $\mathrm{As}_{0.30}{}^\mathrm{Iso}\mathrm{Se}_{0.70}$ and $\mathrm{As}_{0.35}{}^\mathrm{Iso}\mathrm{Se}_{0.65}$, or Iso = Mix for $\mathrm{As}_{0.40}{}^\mathrm{Iso}\mathrm{Se}_{0.60}$. The values obtained from the difference functions are highlighted in green for $\Delta G_\mathrm{Se}(r)$, cyan for $\Delta G_\mathrm{X}(r)$ and magenta for $\Delta G_\mathrm{As}(r)$.

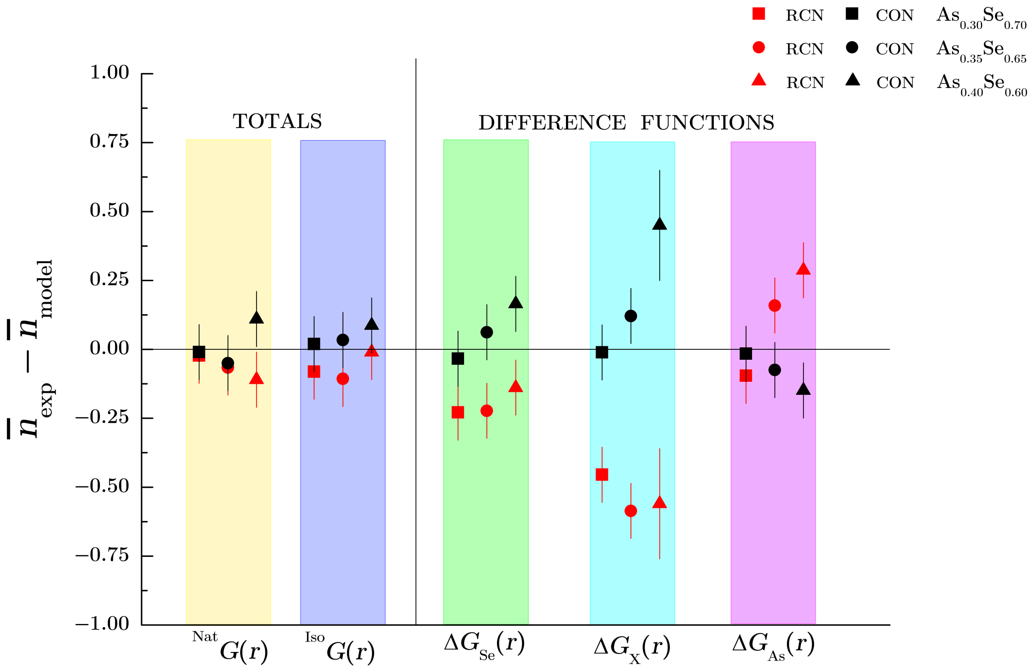

Figure 5-35: The differences between the coordination numbers obtained from the GEM or D4c data and the values obtained from either the RCN (red markers) or CON (black markers) model. The plot is identical to the one in Figure 5-34, but in this case the values for $As_{0.40}Se_{0.60}$ are from D4c with ${}^{Mix}Se$ isotope substitution. The values for $As_{0.30}Se_{0.70}$ (GEM) are represented by squares (■, 🟥), the values for $As_{0.35}Se_{0.65}$ (GEM) are represented by circles (●, ●), and the values for $As_{0.40}Se_{0.60}$ (D4c) are represented by triangles (▲, ▲). The values related to the total pair-distribution functions are highlighted in yellow for ${}^{Nat}G(r)$ and in blue for ${}^{Iso}G(r)$, where Iso = 76 for $As_{0.30}{}^{Iso}Se_{0.70}$ and $As_{0.35}{}^{Iso}Se_{0.65}$, or Iso = Mix for $As_{0.40}{}^{Iso}Se_{0.60}$. The values obtained from the difference functions are highlighted in green for $\Delta G_{Se}(r)$, cyan for $\Delta G_{X}(r)$ and magenta for $\Delta G_{As}(r)$.

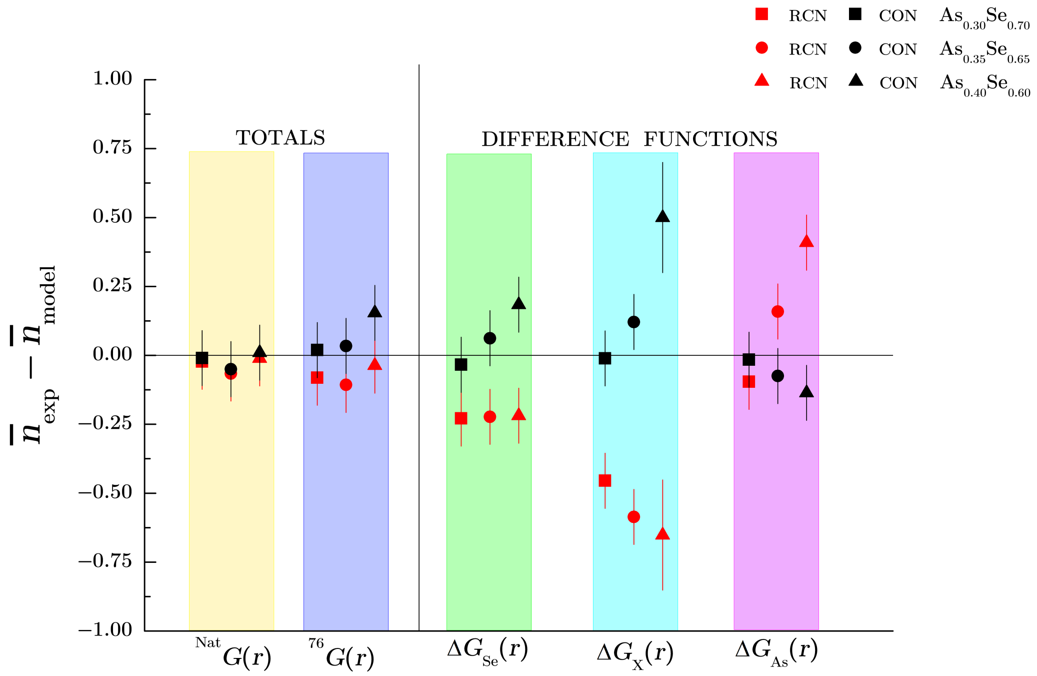

Figure 5-36: The differences between the coordination numbers obtained from the GEM or D4c data and the values obtained from either the RCN (red markers) or CON (black markers) model. The plot is identical to the one in Figure 5-35, but in this case the values for $As_{0.40}Se_{0.60}$ are from D4c with ^{76}Se isotope substitution. The values for $As_{0.30}Se_{0.70}$ (GEM) are represented by squares (■, ■), the values for $As_{0.35}Se_{0.65}$ (GEM) are represented by circles (•, •), and the values for $As_{0.40}Se_{0.60}$ (D4c) are represented by triangles (▲, ▲). The values related to the total pair-distribution functions are highlighted in yellow for $^{\mathrm{Nat}}G(r)$ and in blue for $^{76}G(r)$. The values obtained from the difference functions are highlighted in green for $\Delta G_{\mathrm{Se}}(r)$, cyan for $\Delta G_{\mathrm{X}}(r)$ and magenta for $\Delta G_{\mathrm{As}}(r)$.

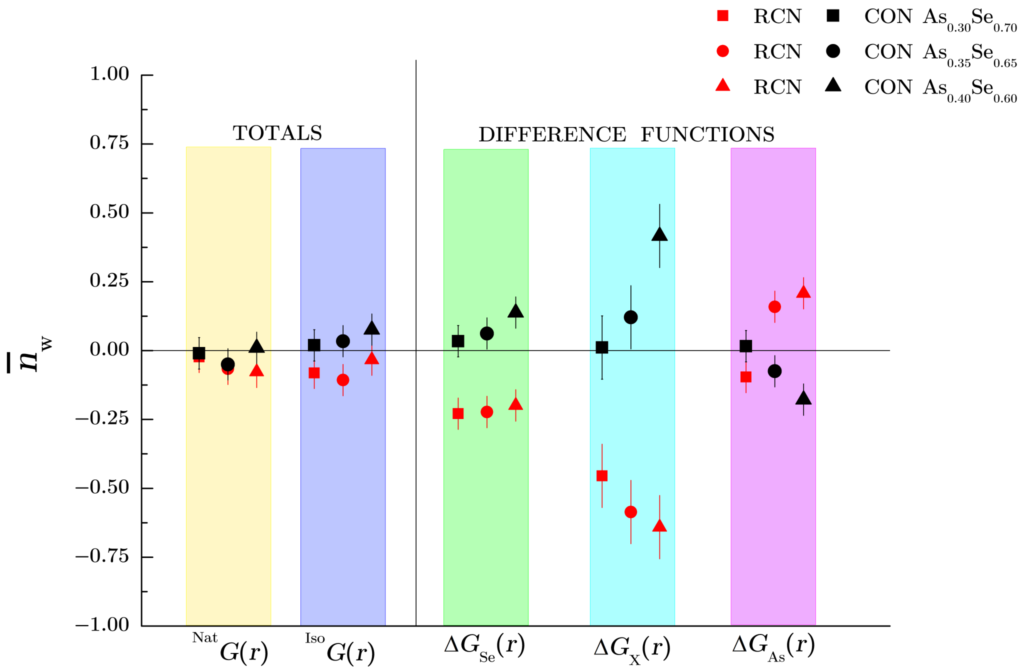

Figure 5-37: The differences between the coordination numbers obtained from the NDIS experiments (GEM and D4c data) and the values obtained from either the RCN (red markers) or CON (black markers) model. The graph summarises the information contained in Figures 5-34 – 5-36 by taking, for a given composition and function i, the weighted average of $(x_i \pm \sigma_i)$, where $x_i = \bar{n}_{\mathrm{exp}} - \bar{n}_{\mathrm{model}}$n and σ_i is the associated error. The weighted average is defined by $\bar{n}_{\mathrm{w}} = \sum_{i=1}^{3} w_i x_i / \sum_{i=1}^{3} w_i$, where $w_i = 1/\sigma_i^2$. The values for $As_{0.30}Se_{0.70}$ (GEM) are represented by squares (■, 🟥), the values for $As_{0.35}Se_{0.65}$ (GEM) are represented by circles (•, •), and the values for $As_{0.40}Se_{0.60}$ (GEM and D4c) are represented by triangles (▲, ▲). The values related to the total pair-distribution functions are highlighted in yellow for $^{\mathrm{Nat}}G(r)$ and in blue for $^{\mathrm{Iso}}G(r)$. The values obtained from the difference functions are highlighted in green for $\Delta G_{\mathrm{Se}}(r)$, cyan for $\Delta G_{\mathrm{X}}(r)$ and magenta for $\Delta G_{\mathrm{As}}(r)$.

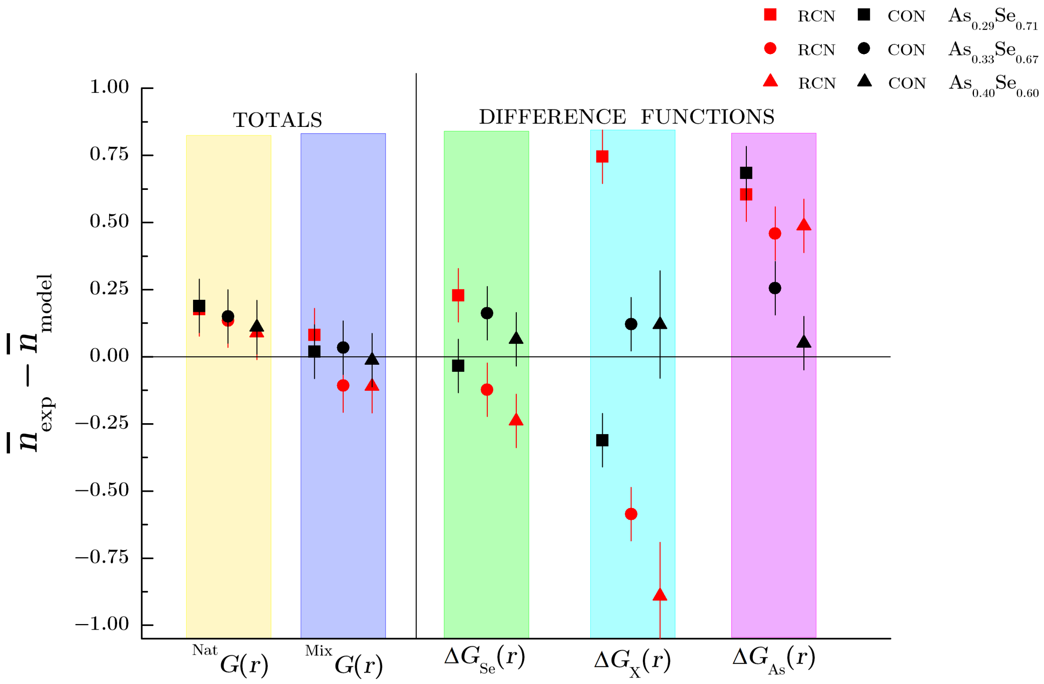

Figure 5-38: The differences between the coordination numbers obtained from the RMC-modelled data [26] and the values obtained from either the RCN (red markers) or CON (black markers) model. The values for $As_{0.30}Se_{0.70}$ are represented by squares (■, ■), the values for $As_{0.35}Se_{0.65}$ are represented by circles (•, •), and the values for $As_{0.40}Se_{0.60}$ are represented by triangles (▲, ▲). The values related to the total pair-distribution functions are highlighted in yellow for $^{\text{Nat}}G(r)$ and in blue for $^{\text{Mix}}G(r)$. The values obtained from the difference functions are highlighted in green for $\Delta G_{\text{Se}}(r)$, cyan for $\Delta G_{\text{X}}(r)$ and magenta for $\Delta G_{\text{As}}(r)$.

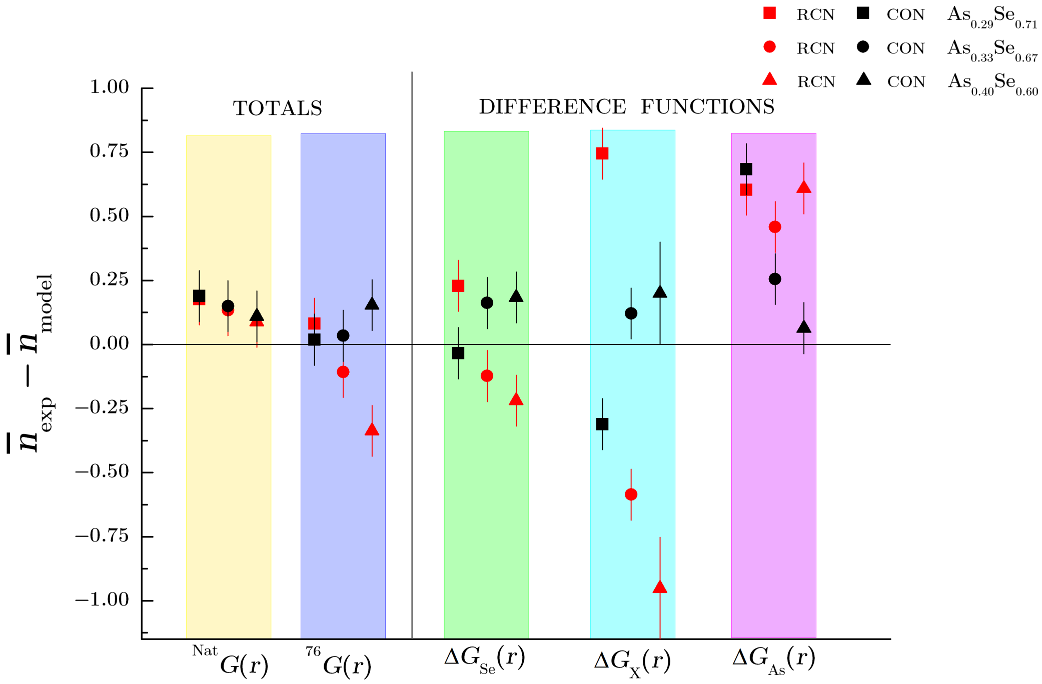

Figure 5-39: The differences between the coordination numbers obtained from the RMC-modelled data [26] and the values obtained from either the RCN (red markers) or CON (black markers) model. The values for $As_{0.30}Se_{0.70}$ are represented by squares (■, ■), the values for $As_{0.35}Se_{0.65}$ are represented by circles (•, •), and the values for $As_{0.40}Se_{0.60}$ are represented by triangles (▲, ▲). The values related to the total pair-distribution functions are highlighted in red for $^{Nat}G(r)$ and in blue for $^{76}G(r)$. The values obtained from the difference functions are highlighted in green for $\Delta G_{Se}(r)$, cyan for $\Delta G_{X}(r)$ and magenta for $\Delta G_{As}(r)$.

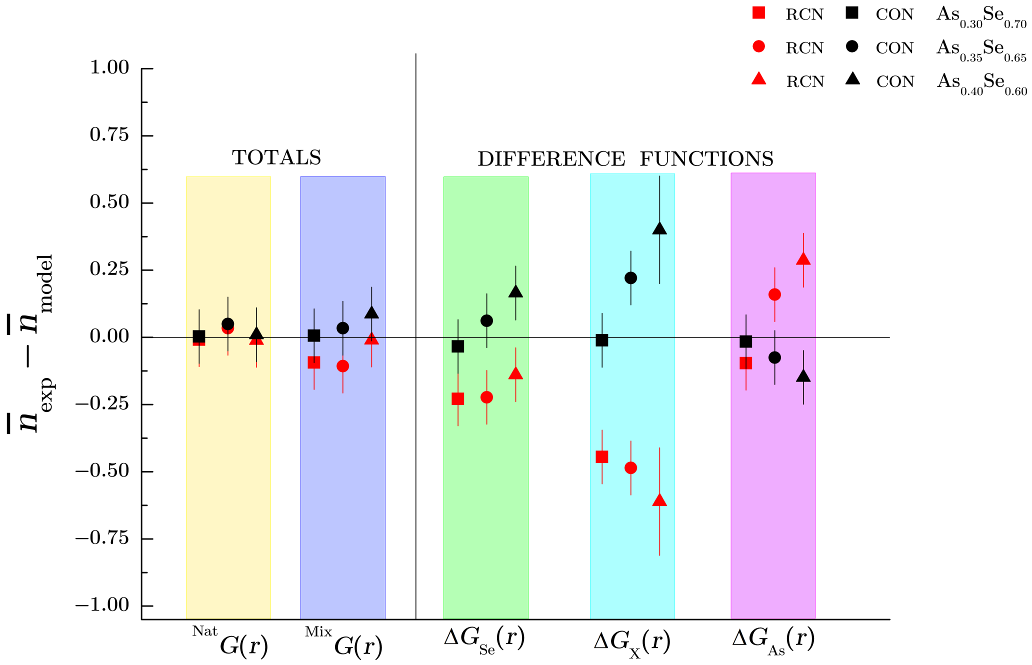

Figure 5-40: The differences between the coordination numbers obtained from the FPMD simulations [25] and the values obtained from either the RCN (red markers) or CON (black markers) model. The values for $\text{As}_{0.30}\text{Se}_{0.70}$ are represented by squares (■, ■), the values for $\text{As}_{0.35}\text{Se}_{0.65}$ are represented by circles (•, •), and the values for $\text{As}_{0.40}\text{Se}_{0.60}$ are represented by triangles (▲, ▲). The values related to the total pair distribution functions are highlighted in yellow for $^{\text{Nat}}G(r)$ and in blue for $^{\text{Mix}}G(r)$. The values obtained from the difference functions are highlighted in green for $\Delta G_{\text{Se}}(r)$, cyan for $\Delta G_{\text{X}}(r)$ and magenta for $\Delta G_{\text{As}}(r)$.

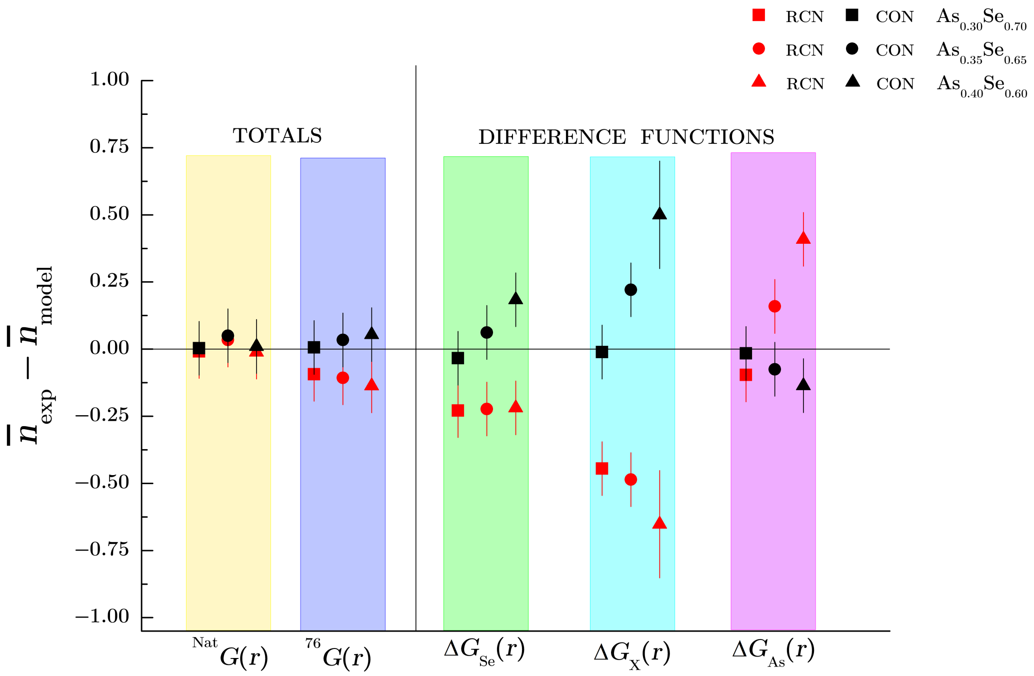

Figure 5-41: The differences between the coordination numbers obtained from the FPMD simulations [25] and the values obtained from either the RCN (red markers) or CON (black markers) model. The values for $As_{0.30}Se_{0.70}$ are represented by squares (■, ■), the values for $As_{0.35}Se_{0.65}$ are represented by circles (•, •), and the values for $As_{0.40}Se_{0.60}$ are represented by triangles (▲, ▲). The values related to the total pair distribution functions are highlighted in yellow for $^{\mathrm{Nat}}G(r)$ and in blue for $^{76}G(r)$. The values obtained from the difference functions are highlighted in green for $\Delta G_{\mathrm{Se}}(r)$, cyan for $\Delta G_{\mathrm{X}}(r)$ and magenta for $\Delta G_{\mathrm{As}}(r)$.

5.6 Conclusion

The atomic structures of glassy $As_{0.30}Se_{0.70}$, $As_{0.35}Se_{0.65}$ and $As_{0.40}Se_{0.60}$ have been investigated using NDIS on GEM. The total structure factors and first-order difference functions were compared, both in reciprocal and real space, with the neutron diffraction measurements performed on D4c for the $As_{0.40}Se_{0.60}$ composition. The results are in good overall agreement.

The functions measured via NDIS were also compared with the RMC results from Hosokawa *et al.* [26] and with the FPMD results from Bauchy *et al.* [25]. The reciprocal-space functions measured by NDIS are better reproduced by RMC as compared to FPMD, especially in the region of the pre-peak at low-Q.

In real space, a systematic shift towards smaller r-values is found for the first peak position of the RMC functions as compared to the NDIS functions. This disagreement may originate from the fact that the RMC models were obtained by using AXS measurements that have a limited $Q_{\text{max}} = 11.5$ Å^{-1} as compared to $Q_{\text{max}} = 40$ Å^{-1} for NDIS. In comparison, the first peak in the FPMD real-space functions is systematically shifted towards larger r-values as compared to the NDIS results. Globally, neither the RMC nor the FPMD results match the NDIS real-space functions, even though the FPMD and RMC partial coordination numbers show the same trend, *i.e.* as the As content increases the coordination number $\bar{n}_{\text{As}}^{\text{As}}$ increases, whereas the coordination numbers $\bar{n}_{\text{As}}^{\text{Se}}$ and $\bar{n}_{\text{Se}}^{\text{Se}}$ both decrease. However, the coordination numbers obtained from NDIS are in better agreement with the FPMD rather than with the RMC results.

A comparison of the coordination numbers obtained from the NDIS, RMC and FPMD methods, with those predicted from the CON and RCN models, reveals that neither of these models describe the investigated glasses in an exhaustive way. However, the CON seems to better describe the network structures for the $As_{0.30}Se_{0.70}$ and $As_{0.35}Se_{0.65}$ compositions, but fails to predict the observed homopolar bonds for the stoichiometric composition.

Our NDIS results provide a severe test of the RMC and FPMD models, and reveal discrepancies both in reciprocal and real-space. The reliability of the RMC results is related, in part, to the sensitivity of the experimental AXS data to the relevant correlations in the system, and the measurements suffer from a limited Q-range. Also, constraints related to the choice of minimum bond distances and bond angles can affect the reliability of the RMC results.

In respect of the simulations, the FPMD results may suffer from the presence of a residual pressure, as found from simulations of the $GeSe_2$ system [119]. A comparison between the present results and those obtained from the full set of partial structure factors, measured for $As_{0.40}Se_{0.60}$ on D4c using NDIS [90], will allow for a more complete understanding of the contributions of the different partial pair-distribution functions $g_{\alpha\beta}(r)$ to the $\Delta G(r)$ difference functions.

6. Structure of Large Rare-Earth Aluminosilicate Glasses

6.1 Introduction

The rare-earths belong to a group of chemical elements that includes the lanthanides (La, Ce, Pr, Nd, Pm, Sm, Eu, Gd, Tb, Dy, Ho, Er, Tm, Yb, Lu), yttrium and scandium. Y and Sc are regarded as rare-earth elements because they tend to occur in the same ore deposits as the lanthanides and exhibit similar chemical properties [120]. Due to their electronic, optical and magnetic properties, these chemical elements play a major role in many modern technologies and are extensively used in many different fields, including aeronautics, cancer-treatment and bioprobe applications, and they have also been proposed as candidates for the storage matrices of radioactive waste [121, 122]. Also, the incorporation of optically active rare-earth ions into oxide glasses yields materials that can act as lasers and optical amplifiers for all-fibre optical systems [123]. Because the energy transfer between the rare-earth ions has a strong dependence on their separation, it is desirable to control the rare-earth to rare-earth nearest-neighbour distance in these materials [41]. In silicate glasses, this can be achieved by co-doping the rare-earth oxides with Al_2O_3. However, in order to tailor specific optical, electronic and mechanical properties, it is necessary to develop realistic microscopic models. To this end, information on the atomic-scale structure of these glassy systems is required.

The structure of aluminosilicate (AS) glasses can be understood in terms of a network of corner-sharing SiO_4 and AlO_4 units, linked via bridging oxygen atoms [124]. When all the oxygen atoms in SiO_4 are bridging oxygen atoms, the charge on each unit is neutral. In contrast, an AlO_4 unit having four bridging oxygen atoms will have a net charge of $[AlO_4]^-$. When the rare-earth R^{3+} species are introduced into AS glasses, they tend to induce topological disorder, because they act as network modifiers. This modifying behaviour is found to be stronger with increasing cation field strength (CFS), where CFS$= z/R^2$ (z is the ion valence and R the ionic radius), and as the SiO_2 content decreases [125].

However, there is still an open debate on the structural features of these glasses. For instance, while for decades both Si and Al were thought to be 4-fold coordinated by O, unless the network modifier content is too low for charge-balancing the AlO_4 species, recent work on R_2O_3-Al_2O_3-SiO_2 glasses shows that a significant population of AlO_5 and AlO_6 units are present over the entire range of compositions, especially for decreasing SiO_2 content and for increasing CFS [124]. Figure 6-1 shows examples of sites where a three-fold coordinated oxygen atom, denoted as $O^{[3]}$, is linked to (a) two AlO_4 units and one SiO_4 unit or to (b) one SiO_4 unit and with edge-shared AlO_4/AlO_6 polyhedra.

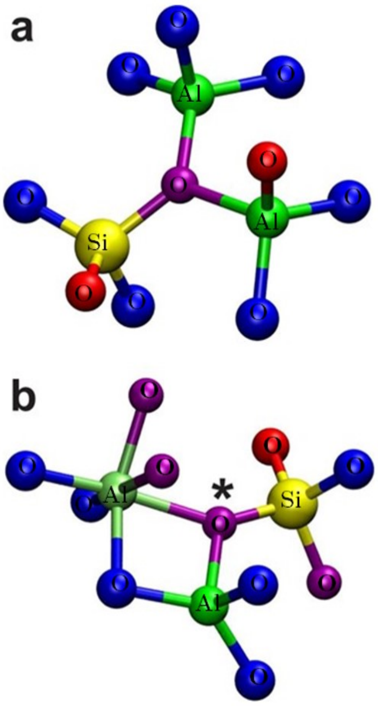

Figure 6-1: Examples of two different configurations containing three-fold coordinated oxygen atom sites (magenta spheres) obtained via MD simulations on RAS glass [124]: (a) $O^{[3]}$–$SiAl_2^{[4]}$ with solely corner-sharing among all Si/Al groups; (b) $O^{[3]}$–$SiAl^{[4]}Al^{[6]}$ (marked by an asterisk) with edge-shared AlO_4/AlO_6 polyhedra. $O^{[1]}$ and $O^{[2]}$ species are given in red and blue, respectively, whereas green and yellow atoms depict Al and Si, respectively.

Different methods can be used to investigate the structure of these systems. Nuclear Magnetic Resonance (NMR) spectroscopy is one of the most powerful techniques for accessing information on the local structure around nuclei such as ^{17}O, ^{27}Al and ^{29}Si. However, for glasses rich in rare-earth content, and with unpaired electron spins, accurate NMR experiments are difficult because of paramagnetic broadening and resonance shifts. Thus, NMR studies have largely been confined to systems containing Y, La, Lu, or Sc, which do not have unpaired electron spins, and are diamagnetic. For these elements, the CFS increases along the series $La^{3+} < Y^{3+} < Lu^{3+} < Sc^{3+}$, as the ion radius shrinks [126–128].

An alternative method to investigate the structure of rare-earth AS (RAS) glasses is by using neutron diffraction with isomorphic substitution (NDIS), as explained in Section 2.1.1. In the present chapter, NDIS will refer to isomorphic as opposed to isotope substitution. In the present work, a ND experiment was performed on the $(R_2O_3)_{0.2}(Al_2O_3)_{0.2}(SiO_2)_{0.6}$ glassy system, where the chosen isomorphic rare-earth species were Neodymium and Praseodymium. The Nd^{3+} and Pr^{3+} ions are at the large-size end of the rare-earth series, are adjacent to one another in the periodic table and exhibit a similar structural chemistry, as indicated by their Pettifor chemical parameters (0.6975 and 0.70) [129] [1]. Also, they have similar ionic radii, namely 0.983 Å and 0.99 Å when they are six-fold coordinated, respectively [126]. However, their coherent neutron scattering lengths are quite different (b_{Nd}=7.69(5) fm versus b_{Pr}=4.58(5) fm), which makes them ideal candidates for applying NDIS. In order to access the $g_{\mathrm{RR}}(r)$ partial pair-correlation function, which contains the desired information on the R-R nearest-neighbour distance, an additional measurement was made on a sample prepared using a 50:50 mixture of Nd and Pr, where the rare-earth ions in this sample will be denoted by Mix.

The results of this work will be compared with those obtained by P. Chirawatkul [27], who investigated the structure of $(R_2O_3)_{0.2}(Al_2O_3)_{0.2}(SiO_2)_{0.6}$ glasses, by using ND with isomorphic substitution. The rare-earth species employed were Dy^{3+} and Ho^{3+}, which are at the small-sized end of the rare-earth series, and are comparable in size. Comparisons will also be made with La-AS glasses, because the La^{3+} ion has an ionic radius of 1.032 Å, a Pettifor chemical parameter that is similar to Nd and Pr, and is non-paramagnetic, which makes feasible a detailed study via NMR.

---

[1] In the phenomenological scale proposed by Pettifor, the elements are arranged in order to reproduce the structural stability of binary compounds.

6.2 Theory

Consider three isomorphic samples of a four-component $(\mathrm{R_2O_3})_{0.2}(\mathrm{Al_2O_3})_{0.2}(\mathrm{SiO_2})_{0.6}$ glassy system, with R = Nd, Pr or Mix (a 50:50 mixture of Nd and Pr), that are identical in every respect except for the coherent neutron scattering length of the RE species $b_{\mathrm{Nd}} > b_{\mathrm{Mix}} > b_{\mathrm{Pr}}$. The corresponding total structure factors, denoted by ${}^{\mathrm{Nd}}F(Q)$, ${}^{\mathrm{Mix}}F(Q)$ and ${}^{\mathrm{Pr}}F(Q)$, are given by

$$\begin{aligned}
{}^{\mathrm{Nd}}F(Q) &= c_{\mathrm{Al}}^2 b_{\mathrm{Al}}^2 \left[S_{\mathrm{AlAl}}(Q)-1\right] + c_{\mathrm{Si}}^2 b_{\mathrm{Si}}^2 \left[S_{\mathrm{SiSi}}(Q)-1\right] \\
&+ c_{\mathrm{O}}^2 b_{\mathrm{O}}^2 \left[S_{\mathrm{OO}}(Q)-1\right] + c_{\mathrm{R}}^2 b_{\mathrm{Nd}}^2 \left[S_{\mathrm{RR}}(Q)-1\right] \\
&+ 2c_{\mathrm{Al}}c_{\mathrm{Si}}b_{\mathrm{Al}}b_{\mathrm{Si}} \left[S_{\mathrm{AlSi}}(Q)-1\right] + 2c_{\mathrm{Al}}c_{\mathrm{O}}b_{\mathrm{Al}}b_{\mathrm{O}} \left[S_{\mathrm{AlO}}(Q)-1\right] \\
&+ 2c_{\mathrm{Al}}c_{\mathrm{R}}b_{\mathrm{Al}}b_{\mathrm{Nd}} \left[S_{\mathrm{RAl}}(Q)-1\right] + 2c_{\mathrm{Si}}c_{\mathrm{O}}b_{\mathrm{Si}}b_{\mathrm{O}} \left[S_{\mathrm{SiO}}(Q)-1\right] \\
&+ 2c_{\mathrm{Si}}c_{\mathrm{R}}b_{\mathrm{Si}}b_{\mathrm{Nd}} \left[S_{\mathrm{RSi}}(Q)-1\right] + 2c_{\mathrm{O}}c_{\mathrm{R}}b_{\mathrm{O}}b_{\mathrm{Nd}} \left[S_{\mathrm{RO}}(Q)-1\right], \qquad (6.1)
\end{aligned}$$

$$\begin{aligned}
{}^{\mathrm{Mix}}F(Q) &= c_{\mathrm{Al}}^2 b_{\mathrm{Al}}^2 \left[S_{\mathrm{AlAl}}(Q)-1\right] + c_{\mathrm{Si}}^2 b_{\mathrm{Si}}^2 \left[S_{\mathrm{SiSi}}(Q)-1\right] \\
&+ c_{\mathrm{O}}^2 b_{\mathrm{O}}^2 \left[S_{\mathrm{OO}}(Q)-1\right] + c_{\mathrm{R}}^2 b_{\mathrm{Mix}}^2 \left[S_{\mathrm{RR}}(Q)-1\right] \\
&+ 2c_{\mathrm{Al}}c_{\mathrm{Si}}b_{\mathrm{Al}}b_{\mathrm{Si}} \left[S_{\mathrm{AlSi}}(Q)-1\right] + 2c_{\mathrm{Al}}c_{\mathrm{O}}b_{\mathrm{Al}}b_{\mathrm{O}} \left[S_{\mathrm{AlO}}(Q)-1\right] \\
&+ 2c_{\mathrm{Al}}c_{\mathrm{R}}b_{\mathrm{Al}}b_{\mathrm{Mix}} \left[S_{\mathrm{RAl}}(Q)-1\right] + 2c_{\mathrm{Si}}c_{\mathrm{O}}b_{\mathrm{Si}}b_{\mathrm{O}} \left[S_{\mathrm{SiO}}(Q)-1\right] \\
&+ 2c_{\mathrm{Si}}c_{\mathrm{R}}b_{\mathrm{Si}}b_{\mathrm{Mix}} \left[S_{\mathrm{RSi}}(Q)-1\right] + 2c_{\mathrm{O}}c_{\mathrm{R}}b_{\mathrm{O}}b_{\mathrm{Mix}} \left[S_{\mathrm{RO}}(Q)-1\right], \qquad (6.2)
\end{aligned}$$

$$\begin{aligned}
{}^{\mathrm{Pr}}F(Q) &= c_{\mathrm{Al}}^2 b_{\mathrm{Al}}^2 \left[S_{\mathrm{AlAl}}(Q)-1\right] + c_{\mathrm{Si}}^2 b_{\mathrm{Si}}^2 \left[S_{\mathrm{SiSi}}(Q)-1\right] \\
&+ c_{\mathrm{O}}^2 b_{\mathrm{O}}^2 \left[S_{\mathrm{OO}}(Q)-1\right] + c_{\mathrm{R}}^2 b_{\mathrm{Pr}}^2 \left[S_{\mathrm{RR}}(Q)-1\right] \\
&+ 2c_{\mathrm{Al}}c_{\mathrm{Si}}b_{\mathrm{Al}}b_{\mathrm{Si}} \left[S_{\mathrm{AlSi}}(Q)-1\right] + 2c_{\mathrm{Al}}c_{\mathrm{O}}b_{\mathrm{Al}}b_{\mathrm{O}} \left[S_{\mathrm{AlO}}(Q)-1\right] \\
&+ 2c_{\mathrm{Al}}c_{\mathrm{R}}b_{\mathrm{Al}}b_{\mathrm{Pr}} \left[S_{\mathrm{RAl}}(Q)-1\right] + 2c_{\mathrm{Si}}c_{\mathrm{O}}b_{\mathrm{Si}}b_{\mathrm{O}} \left[S_{\mathrm{SiO}}(Q)-1\right] \\
&+ 2c_{\mathrm{Si}}c_{\mathrm{R}}b_{\mathrm{Si}}b_{\mathrm{Pr}} \left[S_{\mathrm{RSi}}(Q)-1\right] + 2c_{\mathrm{O}}c_{\mathrm{R}}b_{\mathrm{O}}b_{\mathrm{Pr}} \left[S_{\mathrm{RO}}(Q)-1\right]. \qquad (6.3)
\end{aligned}$$

The weighting factors for the pair-correlation functions involving only the matrix atoms (Al, Si and O) do not change between the samples, unlike those for the pair-correlation functions involving the rare-earth species. Hence, first-order difference functions $\Delta F_{\mathrm{R}}^{(i)}(Q)$ can be formed to eliminate the matrix-to-matrix atom $(\mu - \mu')$ pair-correlation functions, where

$$\begin{aligned}\Delta F_{\mathrm{R}}^{(1)}(Q) &= {}^{\mathrm{Nd}}F(Q) - {}^{\mathrm{Pr}}F(Q) \\ &= c_{\mathrm{R}}^{2}\left(b_{\mathrm{Nd}}^{2} - b_{\mathrm{Pr}}^{2}\right)\left[S_{\mathrm{RR}}(Q) - 1\right] + \Delta_{\mathrm{R}\mu}^{(1)}(Q),\end{aligned} \tag{6.4}$$

$$\begin{aligned}\Delta F_{\mathrm{R}}^{(2)}(Q) &= {}^{\mathrm{Nd}}F(Q) -{}^{\mathrm{Mix}} F(Q) \\ &= c_{\mathrm{R}}^{2}\left(b_{\mathrm{Nd}}^{2} - b_{\mathrm{Mix}}^{2}\right)\left[S_{\mathrm{RR}}(Q) - 1\right] + \Delta_{\mathrm{R}\mu}^{(2)}(Q),\end{aligned} \tag{6.5}$$

$$\begin{aligned}\Delta F_{\mathrm{R}}^{(3)}(Q) &= {}^{\mathrm{Mix}}F(Q) -{}^{\mathrm{Pr}} F(Q) \\ &= c_{\mathrm{R}}^{2}\left(b_{\mathrm{Mix}}^{2} - b_{\mathrm{Pr}}^{2}\right)\left[S_{\mathrm{RR}}(Q) - 1\right] + \Delta_{\mathrm{R}\mu}^{(3)}(Q),\end{aligned} \tag{6.6}$$

and where the $\Delta_{\mathrm{R}\mu}^{(i)}(Q)$ (i = 1, 2 or 3) difference functions involve only the $\mathrm{R} - \mu$ atom pair-correlation functions :-

$$\begin{aligned}\Delta_{\mathrm{R}\mu}^{(1)}(Q) &= 2c_{\mathrm{Al}}c_{R}b_{\mathrm{Al}}\left(b_{\mathrm{Nd}} - b_{\mathrm{Pr}}\right)\left[S_{\mathrm{RAl}}(Q) - 1\right] \\ &+ 2c_{\mathrm{Si}}c_{R}b_{\mathrm{Si}}\left(b_{\mathrm{Nd}} - b_{\mathrm{Pr}}\right)\left[S_{\mathrm{RSi}}(Q) - 1\right] \\ &+ 2c_{\mathrm{O}}c_{R}b_{\mathrm{O}}\left(b_{\mathrm{Nd}} - b_{\mathrm{Pr}}\right)\left[S_{\mathrm{RO}}(Q) - 1\right],\end{aligned} \tag{6.7}$$

$$\begin{aligned}\Delta_{\mathrm{R}\mu}^{(2)}(Q) &= 2c_{\mathrm{Al}}c_{R}b_{\mathrm{Al}}\left(b_{\mathrm{Nd}} - b_{\mathrm{Mix}}\right)\left[S_{\mathrm{RAl}}(Q) - 1\right] \\ &+ 2c_{\mathrm{Si}}c_{R}b_{\mathrm{Si}}\left(b_{\mathrm{Nd}} - b_{\mathrm{Mix}}\right)\left[S_{\mathrm{RSi}}(Q) - 1\right] \\ &+ 2c_{\mathrm{O}}c_{R}b_{\mathrm{O}}\left(b_{\mathrm{Nd}} - b_{\mathrm{Mix}}\right)\left[S_{\mathrm{RO}}(Q) - 1\right],\end{aligned} \tag{6.8}$$

$$\begin{aligned}\Delta_{\mathrm{R}\mu}^{(3)}(Q) &= 2c_{\mathrm{Al}}c_{\mathrm{R}}b_{\mathrm{Al}}\left(b_{\mathrm{Mix}} - b_{\mathrm{Pr}}\right)\left[S_{\mathrm{RAl}}(Q) - 1\right] \\ &+ 2c_{\mathrm{Si}}c_{\mathrm{R}}b_{\mathrm{Si}}\left(b_{\mathrm{Mix}} - b_{\mathrm{Pr}}\right)\left[S_{\mathrm{RSi}}(Q) - 1\right] \\ &+ 2c_{\mathrm{O}}c_{\mathrm{R}}b_{\mathrm{O}}\left(b_{\mathrm{Mix}} - b_{\mathrm{Pr}}\right)\left[S_{\mathrm{RO}}(Q) - 1\right].\end{aligned} \tag{6.9}$$

Let the matrix-matrix difference function be defined by

$$\begin{aligned}\Delta_{\mu\mu}(Q) &= c_{\rm Al}^2 b_{\rm Al}^2\left[S_{\rm AlAl}(Q)-1\right]+c_{\rm Si}^2 b_{\rm Si}^2\left[S_{\rm SiSi}(Q)-1\right] \\ &+ c_{\rm O}^2 b_{\rm O}^2\left[S_{\rm OO}(Q)-1\right]+2c_{\rm Al}c_{\rm Si}b_{\rm Al}b_{\rm Si}\left[S_{\rm AlSi}(Q)-1\right] \\ &+ 2c_{\rm Al}c_{\rm O}b_{\rm Al}b_{\rm O}\left[S_{\rm AlO}(Q)-1\right]+2c_{\rm Si}c_{\rm O}b_{\rm Si}b_{\rm O}\left[S_{\rm SiO}(Q)-1\right].\end{aligned} \tag{6.10}$$

Then the total structure factors given by Eqs.(6.1) – (6.3) can be re-written as

$$^{\rm Nd}F(Q) = \Delta_{\mu\mu}(Q)+\frac{b_{\rm Nd}}{b_{\rm Nd}-b_{\rm Pr}}\Delta_{{\rm R}\mu}^{(1)}(Q)+c_{\rm R}^2 b_{\rm Nd}^2\left[S_{\rm RR}(Q)-1\right], \tag{6.11}$$

$$^{\rm Mix}F(Q) = \Delta_{\mu\mu}(Q)+\frac{b_{\rm Nd}}{b_{\rm Nd}-b_{\rm Mix}}\Delta_{{\rm R}\mu}^{(2)}(Q)+c_{\rm R}^2 b_{\rm Mix}^2\left[S_{\rm RR}(Q)-1\right], \tag{6.12}$$

$$^{\rm Pr}F(Q) = \Delta_{\mu\mu}(Q)+\frac{b_{\rm Mix}}{b_{\rm Mix}-b_{\rm Pr}}\Delta_{{\rm R}\mu}^{(3)}(Q)+c_{\rm R}^2 b_{\rm Pr}^2\left[S_{\rm RR}(Q)-1\right]. \tag{6.13}$$

By subtracting a weighted first-order difference function from a total structure factor, the $\mathrm{R}-\mu$ correlations can be eliminated to leave only the $\mu-\mu'$ and $\mathrm{R}-\mathrm{R}$ correlations. These so-called "total minus weighted difference functions" are given by

$$\begin{aligned}\Delta F^{(1)}(Q) &= {}^{\rm Nd}F(Q)-\frac{b_{\rm Nd}}{b_{\rm Nd}-b_{\rm Pr}}\Delta F_{\rm R}^{(1)}(Q) \\ &= \Delta_{\mu\mu}(Q)-c_{\rm R}^2 b_{\rm Nd}b_{\rm Pr}\left[S_{\rm RR}(Q)-1\right] \\ &= \frac{b_{\rm Nd}\ {}^{\rm Pr}F(Q)-b_{\rm Pr}\ {}^{\rm Nd}F(Q)}{b_{\rm Nd}-b_{\rm Pr}},\end{aligned} \tag{6.14}$$

$$\begin{aligned}\Delta F^{(2)}(Q) &= {}^{\rm Nd}F(Q)-\frac{b_{\rm Nd}}{b_{\rm Nd}-b_{\rm Mix}}\Delta F_{\rm R}^{(2)}(Q) \\ &= \Delta_{\mu\mu}(Q)-c_{\rm R}^2 b_{\rm Nd}b_{\rm Mix}\left[S_{\rm RR}(Q)-1\right] \\ &= \frac{b_{\rm Nd}\ {}^{\rm Mix}F(Q)-b_{\rm Mix}\ {}^{\rm Nd}F(Q)}{b_{\rm Nd}-b_{\rm Mix}},\end{aligned} \tag{6.15}$$

$$\begin{aligned}\Delta F^{(3)}(Q) &= {}^{\mathrm{Mix}}F(Q) - \frac{b_{\mathrm{Mix}}}{b_{\mathrm{Mix}} - b_{\mathrm{Pr}}}\Delta F_{\mathrm{R}}^{(3)}(Q) \\ &= \Delta_{\mu\mu}(Q) - c_{\mathrm{R}}^2 b_{\mathrm{Mix}} b_{\mathrm{Pr}}\left[S_{\mathrm{RR}}(Q) - 1\right] \\ &= \frac{b_{\mathrm{Mix}}\,{}^{\mathrm{Pr}}F(Q) - b_{\mathrm{Pr}}\,{}^{\mathrm{Mix}}F(Q)}{b_{\mathrm{Mix}} - b_{\mathrm{Pr}}}.\end{aligned} \tag{6.16}$$

The set of total structure factors for the samples can be written in matrix notation as $\mathbf{F}(Q) = \mathbf{A}\cdot\mathbf{S}(Q)$ (Eq.(2.39)), *i.e.*

$$\begin{pmatrix} {}^{\mathrm{Nd}}F(Q) \\ {}^{\mathrm{Mix}}F(Q) \\ {}^{\mathrm{Pr}}F(Q) \end{pmatrix} = \begin{pmatrix} c_{\mathrm{R}}^2 b_{\mathrm{Nd}}^2 & 2c_{\mathrm{R}} b_{\mathrm{Nd}} & 1 \\ c_{\mathrm{R}}^2 b_{\mathrm{Mix}}^2 & 2c_{\mathrm{R}} b_{\mathrm{Mix}} & 1 \\ c_{\mathrm{R}}^2 b_{\mathrm{Pr}}^2 & 2c_{\mathrm{R}} b_{\mathrm{Pr}} & 1 \end{pmatrix} \cdot \begin{pmatrix} S_{\mathrm{RR}}(Q) - 1 \\ \delta_{\mathrm{R}\mu}(Q) \\ \Delta_{\mu\mu}(Q) \end{pmatrix}, \tag{6.17}$$

where

$$\delta_{\mathrm{R}\mu}(Q) = c_{\mathrm{Al}} b_{\mathrm{Al}}\left[S_{\mathrm{RAl}}(Q) - 1\right] + c_{\mathrm{Si}} b_{\mathrm{Si}}\left[S_{\mathrm{RSi}}(Q) - 1\right] + c_{\mathrm{O}} b_{\mathrm{O}}\left[S_{\mathrm{RO}}(Q) - 1\right] \tag{6.18}$$

involves only the $\mathrm{R} - \mu$ pair-correlation functions. The values of the weighting factors in the total and various difference functions are listed in Table 6.1.

The matrix $\mathbf{A}$ is given by

$$\frac{\mathbf{A}}{(\mathrm{mbarn})} = \begin{pmatrix} 6.5(10)10^{-3} & 0.162(1) & 1 \\ 4.2(10)10^{-3} & 0.129(1) & 1 \\ 2.3(10)10^{-3} & 0.096(1) & 1 \end{pmatrix}, \tag{6.19}$$

and the inverse matrix $\mathbf{A}^{-1}$

$$\frac{\mathbf{A}^{-1}}{(\mathrm{mbarn})^{-1}} = \begin{pmatrix} 1866 & -3733 & 1866 \\ -105.25 & 241.04 & -135.794 \\ 5.81 & -14.566 & 9.756 \end{pmatrix}, \tag{6.20}$$

will enable the reciprocal-space functions $S_{\mathrm{RR}}(Q)$, $\delta_{\mathrm{R}\mu}(Q)$ and $\Delta_{\mu\mu}(Q)$ to be determined individually.

	R-R	R-O	R-Al	R-Si	Al-Al	Al-Si	Al-O	Si-Si	Si-O	O-O
${}^{\mathrm{Nd}}F(Q)$	6.6(2)	59.3(4)	5.88(4)	10.6(7)	1.318(4)	4.757(7)	26.61(4)	4.292(2)	48.02(4)	134.3(2)
${}^{\mathrm{Mix}}F(Q)$	4.2(1)	47.3(4)	4.69(4)	8.46(7)	1.318(4)	4.757(7)	26.61(4)	4.292(2)	48.02(4)	134.3(2)
${}^{\mathrm{Pr}}F(Q)$	2.3(1)	35.3(6)	3.50(6)	6.32(1)	1.318(4)	4.757(7)	26.61(4)	4.292(2)	48.02(4)	134.3(2)
$\Delta F_{\mathrm{R}}^{(1)}(Q)$	4.2(2)	23.9(7)	2.37(7)	4.3(1)	-	-	-	-	-	-
$\Delta F_{\mathrm{R}}^{(2)}(Q)$	2.4(2)	11.9(5)	1.18(5)	2.1(6)	-	-	-	-	-	-
$\Delta F_{\mathrm{R}}^{(3)}(Q)$	1.8(2)	11.9(5)	1.18(5)	2.1(6)	-	-	-	-	-	-
$\Delta F^{(1)}(Q)$	3.9(1)	-	-	-	1.318(4)	4.757(7)	26.61(4)	4.292(2)	48.02(4)	134.3(2)
$\Delta F^{(2)}(Q)$	5.2(1)	-	-	-	1.318(4)	4.757(7)	26.61(4)	4.292(2)	48.02(4)	134.3(2)
$\Delta F^{(3)}(Q)$	3.1(1)	-	-	-	1.318(4)	4.757(7)	26.61(4)	4.292(2)	48.02(4)	134.3(2)
$\delta_{\mathrm{R}\mu}(Q)$	-	366.5(5)	36.3	65.5(4)	-	-	-	-	-	-
$\Delta_{\mu\mu}(Q)$	-	-	-	-	1.318(4)	4.757(7)	26.61(4)	4.292(2)	48.02(4)	134.3(2)

Table 6.1: Weighting factors expressed for the $S_{\alpha\beta}(Q)$ functions present in the ${}^{\mathrm{R}}F(Q)$, $\Delta F_{\mathrm{R}}^{(\mathrm{i})}(Q)$, $\Delta F^{(\mathrm{i})}(Q)$ ($i = 1$, 2 or 3) and $\Delta_{\mu\mu}(Q)$ functions. The values are given in units of mbarn, except in the case of the $\delta_{\mathrm{R}\mu}(Q)$ function, where the values are given in units of fm.

For all of these functions, the corresponding real-space information can be accessed via Fourier transformation. The total pair-distribution functions corresponding to the total structure factors in Eqs.(6.1)–(6.3) are given by

$$ {}^{\mathrm{R}}G(r) = \frac{1}{2\pi^2 \rho r} \int_0^\infty {}^{\mathrm{R}}F(Q) Q \sin(Qr) dQ, \tag{6.21} $$

with R = Nd, Mix or Nd. The real-space difference functions corresponding to Eqs.(6.4)–(6.6) are given by

$$ \Delta G_{\mathrm{R}}^{(i)}(r) = \frac{1}{2\pi^2 \rho r} \int_0^\infty \Delta F_{\mathrm{R}}^{(i)}(Q) Q \sin(Qr) dQ. \tag{6.22} $$

The real-space "total minus weighted" difference functions corresponding to Eqs. (6.14)–(6.16) are given by

$$ \Delta G^{(i)}(r) = \frac{1}{2\pi^2 \rho r} \int_0^\infty \Delta F^{(i)}(Q) Q \sin(Qr) dQ. \tag{6.23} $$

The Fourier transform of the R-R partial structure factor gives the partial pair-distribution function

$$ g_{\mathrm{RR}}(r) - 1 = \frac{1}{2\pi^2 \rho r} \int_0^\infty [S_{\mathrm{RR}}(Q) - 1] Q \sin(Qr) dQ. \tag{6.24} $$

The real-space information corresponding to the $\delta_{\mathrm{R}\mu}(Q)$ function is given by

$$ \delta_{\mathrm{R}\mu}(r) = \frac{1}{2\pi^2 \rho r} \int_0^\infty \delta_{\mathrm{R}\mu}(Q) Q \sin(Qr) dQ, \tag{6.25} $$

and for the $\Delta_{\mu\mu}(Q)$ function it is given by

$$ \Delta_{\mu\mu}(r) = \frac{1}{2\pi^2 \rho r} \int_0^\infty \Delta_{\mu\mu}(Q) Q \sin(Qr) dQ. \tag{6.26} $$

6.3 Experimental method

6.3.1 Sample preparation

The glassy samples were prepared in the Liquid and Amorphous Materials laboratory in Bath by Dr. Zeidler and Dr. Drewitt. In order to employ the method of isomorphic substitution, three different $(R_2O_3)_{0.2}(Al_2O_3)_{0.2}(SiO_2)_{0.6}$ samples were prepared, with RE = Nd, Pr or Mix, a 50:50 mixture of Nd and Pr. The glasses were prepared by dry mixing powders of Nd_2O_3 (purity 99.99% from Alfa-Aeser) and/or Pr_2O_3 (purity 99.99% from Alfa-Aeser), SiO_2 (purity 99.995% from Alfa-Aeser) and Al_2O_3 (purity 99.998% from Sigma-Aldrich) in a Pt-Rh crucible in the desired ratio. The crucible was then put inside a furnace and left at 1600 °C for one hour. Because these samples are not hygroscopic they were quenched in air on a liquid-N_2 cooled Cu block while dousing with liquid N_2. The density of the samples was measured using a He pycnometer. The mean bound coherent scattering lengths $\bar{b}_{\mathrm{coh}}$, the total neutron-scattering cross sections σ_{T}, and the measured number densities of the samples are listed in Table 6.2.

Table 6.2: Parameters describing the $(R_2O_3)_{0.2}(Al_2O_3)_{0.2}(SiO_2)_{0.6}$ samples, with R = Nd, Mix and Nd, investigated via the NDIS method. Values for $\bar{b}_{\mathrm{coh}}$ and σ_{T} were calculated using the data given by Sears [33].

Samples	$\bar{b}_{\mathrm{coh}}$ (fm)	σ_{T} (barn) @ $\lambda_{\mathrm{i}} = 1.798$ (Å)	ρ (Å^{-3})
R = Nd	5.49(5)	10.3(9)	0.083(1)
R = Mix	5.33(4)	7.5(4)	0.083(1)
R = Pr	5.17(3)	4.72(6)	0.083(1)

6.3.2 D4c experiment

The diffraction patterns were measured using the D4c diffractometer at the ILL by Dr. Zeidler and Dr. Drewitt. Each sample was coarsely ground and then loaded into a vanadium can (outer diameter = 5 mm, wall thickness = 0.1 mm). The vanadium can was then placed inside the evacuated belljar of the instrument. The measurements were performed at room temperature with an incident neutron wavelength of 0.49672(1) Å. The diffraction patterns were also measured for the empty vanadium can, the empty belljar, and a vanadium rod of dimensions comparable to the sample for normalisation purposes.

6.4 Results

6.4.1 Total structure factors

The $(R_2O_3)_{0.2}(Al_2O_3)_{0.2}(SiO_2)_{0.6}$ samples exhibit paramagnetic behaviour due to the presence of the rare-earth species Nd^{3+} and Pr^{3+}. Therefore, the measured total differential scattering cross sections have both nuclear and magnetic components, as shown in the example in Figure 6-2. In order to extract the former, the latter was calculated for each rare-earth ion according to Eq. (2.21), and was then subtracted from the corresponding total differential scattering cross section. Thereafter, the data sets were corrected and analysed following the procedure explained in Section 3.3.

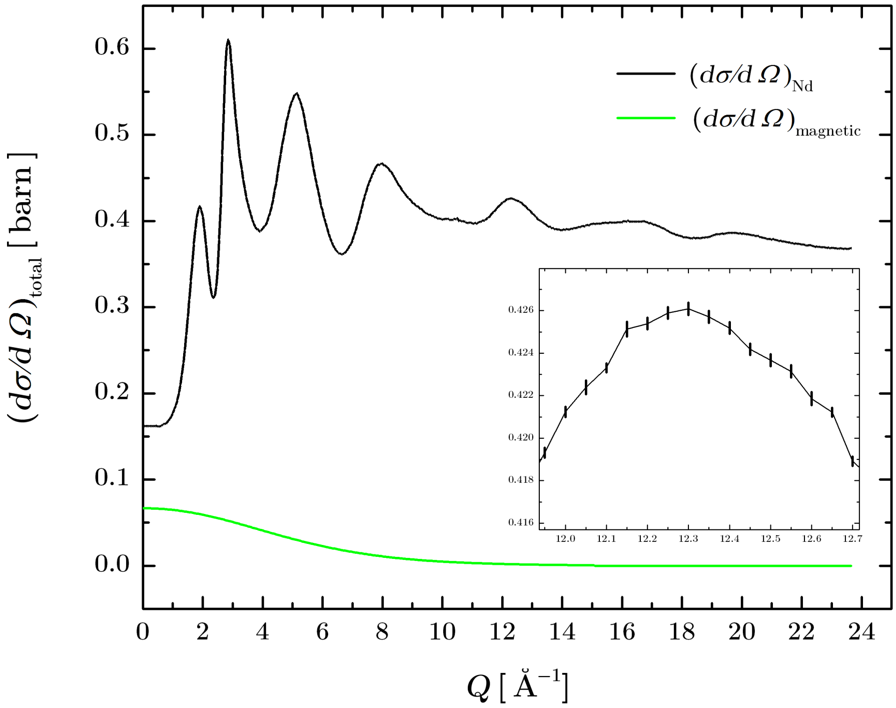

Figure 6-2: The solid black line with vertical error bars is the measured total differential scattering cross section for the $(R_2O_3)_{0.2}(Al_2O_3)_{0.2}(SiO_2)_{0.6}$ sample, with R = Nd. The inset zooms into the the error bars that are hardly distinguishable, given the high-quality counting statistics. The solid green line is the magnetic component of the total differential scattering cross section, given by Eq. (2.21).

Figure 6-3 shows the corrected total structure factors ${}^{\text{Nd}}F(Q)$, ${}^{\text{Mix}}F(Q)$ and ${}^{\text{Pr}}F(Q)$. Figure 6-4 superposes these total structure factors and shows that they have common structural features. There are, however, systematic discrepancies, that can be seen more clearly in the inset, that arise from the difference between the coherent scattering lengths of the rare-earth elements ($b_{\mathrm{Nd}} > b_{\mathrm{Mix}} > b_{\mathrm{Pr}}$). The corresponding real-space functions ${}^{\mathrm{R}}G(r)$ are represented in Figure 6-5. The ringing around each first peak is due to the truncation of each $F(Q)$ function at a finite Q_{max} value. The first low-r oscillation before the first peak in ${}^{\mathrm{R}}G(r)$ was not set to the theoretical $G(r \to 0)$ limit before the back-Fourier transform, in order to ensure that the data sets are correctly normalised. Following Eqs.(6.1)–(6.3) and Eq.(6.21), the $G(r \to 0)$ limit is given by

$$ {}^{\mathrm{R}}G(r \to 0) = {}^{\mathrm{R}}G(0) = -(c_{\mathrm{Al}}b_{\mathrm{Al}} + c_{\mathrm{Si}}b_{\mathrm{Si}} + c_{\mathrm{O}}b_{\mathrm{O}} + c_{\mathrm{R}}b_{\mathrm{R}})^2. \qquad (6.27) $$

The first peak in ${}^{\mathrm{R}}G(r)$ at about 1.65 Å is well separated from the second peak and is associated with Si–O and Al–O correlations. Figures 6-6 – 6-8 show the results obtained by fitting the first peak in the $D(r)$ functions (Eq. (2.32)), to three Gaussian functions convoluted with a sinc function (Eq.(2.35)), with $Q_{\mathrm{max}} = 23.15$ Å^{-1}. The Gaussian functions represent the Si-O and Al-O correlations contained under the first peak. The Si-O parameters were set to $\bar{r}_{\mathrm{SiO}} = 1.61$ Å and $\bar{n}_{\mathrm{Si}}^{\mathrm{O}} = 4.0$, where the latter are found from NMR studies on glassy diamagnetic systems such as $\mathrm{La_{0.66}SiAl_{0.55}O_{3.81}}$ [130] and $\mathrm{(La_2O_3)(Al_2O_3)(SiO_2)}$[124]. The average bond distances and coordination numbers for the Al-O correlations were determined by using a program called RDFgenie, and are listed in Table 6.3. This program implements the procedure described by Martin *et al.* [41] and is a Fortan code written by Prof. Salmon. The Al-O correlations are well described by two Gaussian functions, which indicate the presence of both 4- and 5-fold coordinated Al atoms, as suggested by the NMR experiments of Schaller and Stebbins in [125]. By using the RDFgenie fitting program, the relative fractions of the $\mathrm{AlO_4}$ and $\mathrm{AlO_5}$ units is found to be 80(3)% and 20(3)%, respectively. The goodness-of-fit parameter R_χ, defined by [42]

$$ R_\chi\left(r_{\alpha\beta}, \overline{n}_{\alpha}^{\beta}, \sigma_{\alpha\beta}\right) = \sqrt{\frac{\sum_i \left[D_{\mathrm{exp}}(r_i) - D_{\mathrm{fit}}(r_i)\right]^2}{\sum_i D_{\mathrm{exp}}^2(r_i)}}, \qquad (6.28) $$

is also reported in Table 6.3, along with the fitted r-space range.

Table 6.3: The average coordination numbers and bond distances for AlO_4 and AlO_5 units in glassy $(R_2O_3)_{0.2}(Al_2O_3)_{0.2}(SiO_2)_{0.6}$ samples (with R = Nd, Mix or Pr), as obtained from the first peak in the measured ${}^{\mathrm{R}}D(r)$ functions. The R_χ value, defined in Eq. (2.38), gives the goodness-of-fit parameter for the fitted r-space range.

${}^{\mathrm{R}}G(r)$	$\bar{n}_{\mathrm{Al}}^{\mathrm{O}}$	$\bar{r}_{\mathrm{AlO}}$ (Å)	$\bar{n}_{\mathrm{Al}}^{\mathrm{O}}$	$\bar{r}_{\mathrm{AlO}}$ (Å)	R_χ	range (Å)
R = Nd	4.0(2)	1.75(2)	5.0(1)	1.80(2)	0.052	0 - 1.9
R = Mix	4.0(2)	1.75(2)	5.0(1)	1.82(2)	0.053	0 - 1.9
R = Pr	4.0(2)	1.75(2)	5.0(1)	1.82(2)	0.041	0 - 1.9

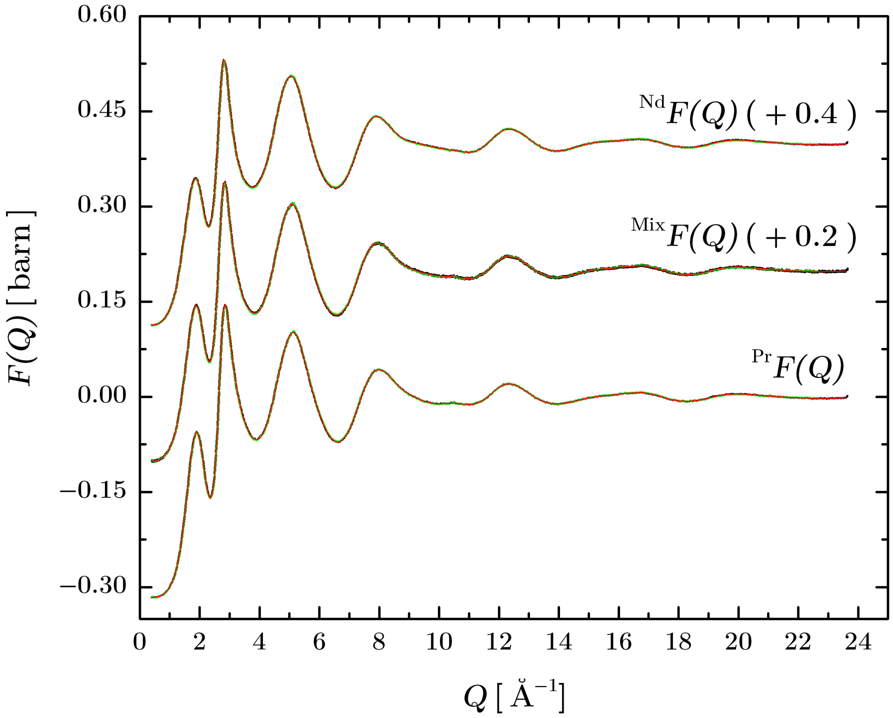

Figure 6-3: Total structure factors ${}^{\mathrm{Nd}}F(Q)$, ${}^{\mathrm{Mix}}F(Q)$ and ${}^{\mathrm{Pr}}F(Q)$ for $(R_2O_3)_{0.2}(Al_2O_3)_{0.2}(SiO_2)_{0.6}$ with R = Nd, Mix or Pr, respectively. The solid black lines with vertical error bars are the measured data sets. The error bars are hardly distinguishable, given the high-quality counting statistics. The red curves show spline fits to the measured data sets. The green curves are the back-Fourier transforms of the ${}^{\mathrm{R}}G(r)$ functions shown in Figure 6-5, once the low-r oscillations are set to their theoretical $G(r \to 0)$ limit. The curves for ${}^{\mathrm{Nd}}F(Q)$ and ${}^{\mathrm{Mix}}F(Q)$ have been offset vertically, for clarity of presentation, and the offsets are indicated in parenthesis.

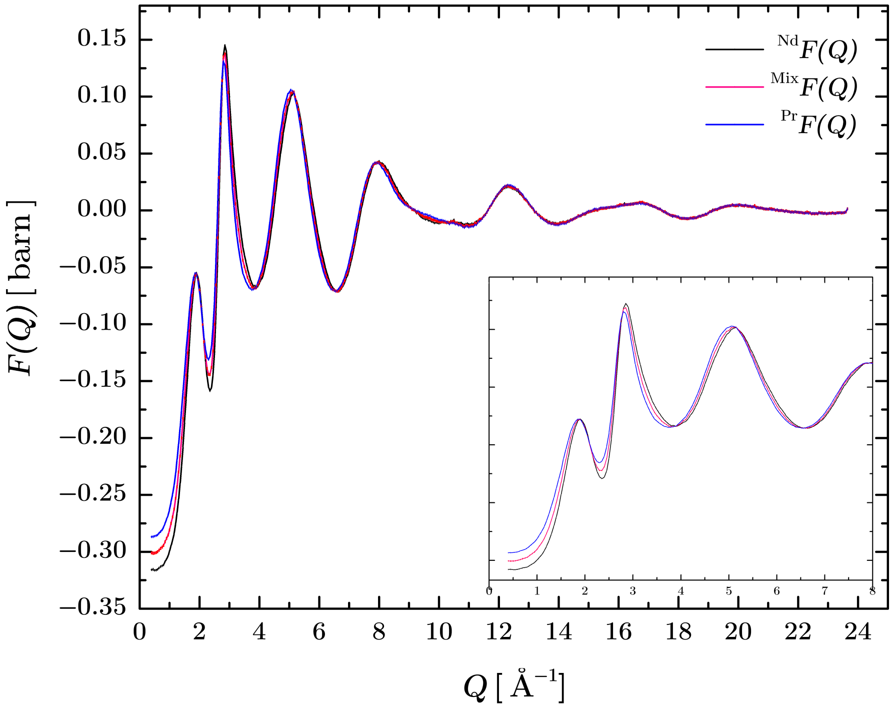

Figure 6-4: Superposition of the total structure factors $^{\mathrm{Nd}}F(Q)$, $^{\mathrm{Mix}}F(Q)$ and $^{\mathrm{Pr}}F(Q)$ for $(\mathrm{R_2O_3})_{0.2}(\mathrm{Al_2O_3})_{0.2}(\mathrm{SiO_2})_{0.6}$ with R = Nd, Mix or Pr, respectively. The solid black, red and blue lines, with vertical error bars, are the measured data sets for $^{\mathrm{Nd}}F(Q)$, $^{\mathrm{Mix}}F(Q)$ and $^{\mathrm{Pr}}F(Q)$, respectively. The error bars are hardly distinguishable, given the high-quality counting statistics. The inset zooms into the low-Q region, where the maximum Q-value is set at 8 Å^{-1}, for clarity of presentation.

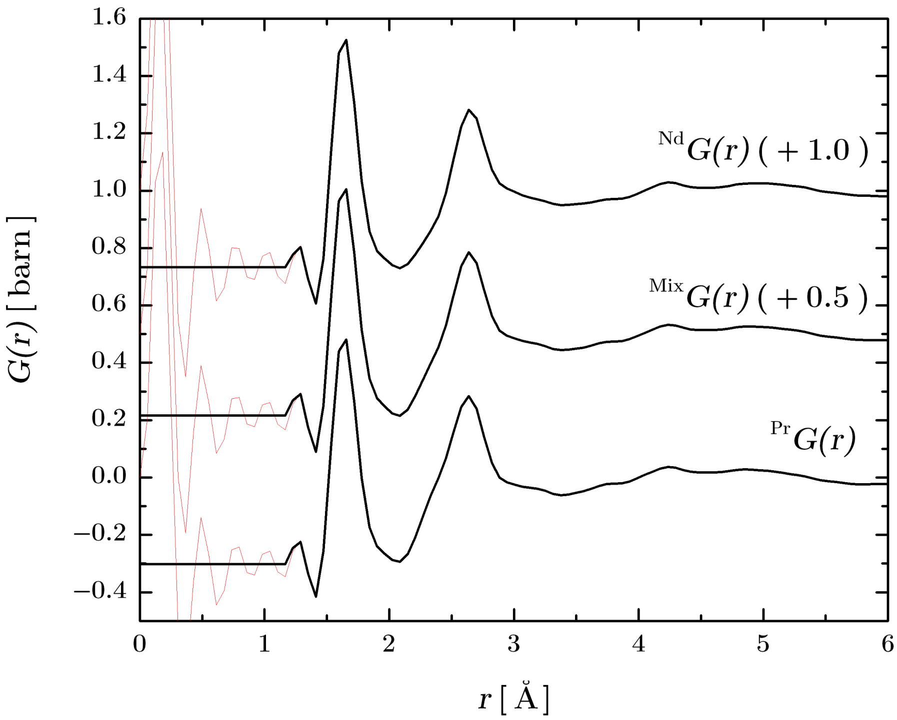

Figure 6-5: Total pair-distribution functions ${}^{\mathrm{Nd}}G(r)$, ${}^{\mathrm{Mix}}G(r)$ and ${}^{\mathrm{Pr}}G(r)$ for $(R_2O_3)_{0.2}(Al_2O_3)_{0.2}(SiO_2)_{0.6}$ with R = Nd, Mix or Pr, respectively. The solid black lines are the Fourier transforms of the spline-fitted data sets shown in Figure 6-3, after the majority of the low-r oscillations (solid red lines) are set to their theoretical ${}^{\mathrm{R}}G(r \to 0)$ limit. The curves for ${}^{\mathrm{Nd}}G(r)$ and ${}^{\mathrm{Mix}}G(r)$ have been offset vertically, for clarity of presentation, and the offsets are indicated in parenthesis.

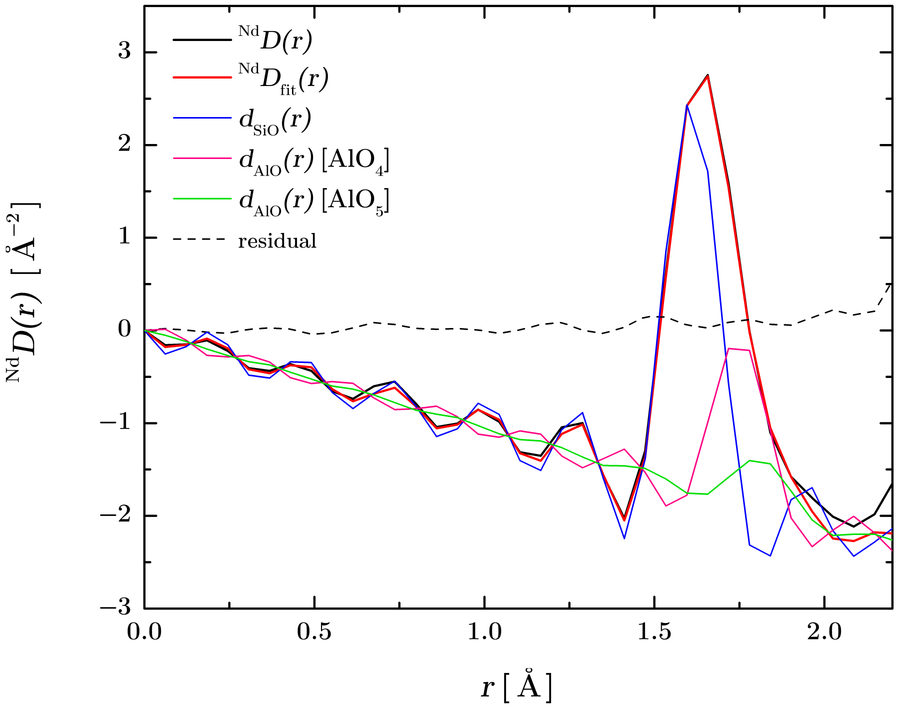

Figure 6-6: The first peak in the $^{\mathrm{Nd}}D(r)$ function for $(\mathrm{R_2O_3})_{0.2}(\mathrm{Al_2O_3})_{0.2}(\mathrm{SiO_2})_{0.6}$ with R = Nd. The solid black line is the measured $D(r)$ function, and is fitted with three Gaussians convoluted with a sinc function using RDFgenie (solid red curve). The solid blue, pink and green curves show the contributions from $d_{\mathrm{SiO}}(r)$, $d_{\mathrm{AlO}}(r)$ for $\mathrm{AlO_4}$ units, and $d_{\mathrm{AlO}}(r)$ for $\mathrm{AlO_5}$ units, respectively. The dashed black line shows the residual. The fit gives $R_\chi = 0.052$ in the fitted range 0 – 1.9 Å.

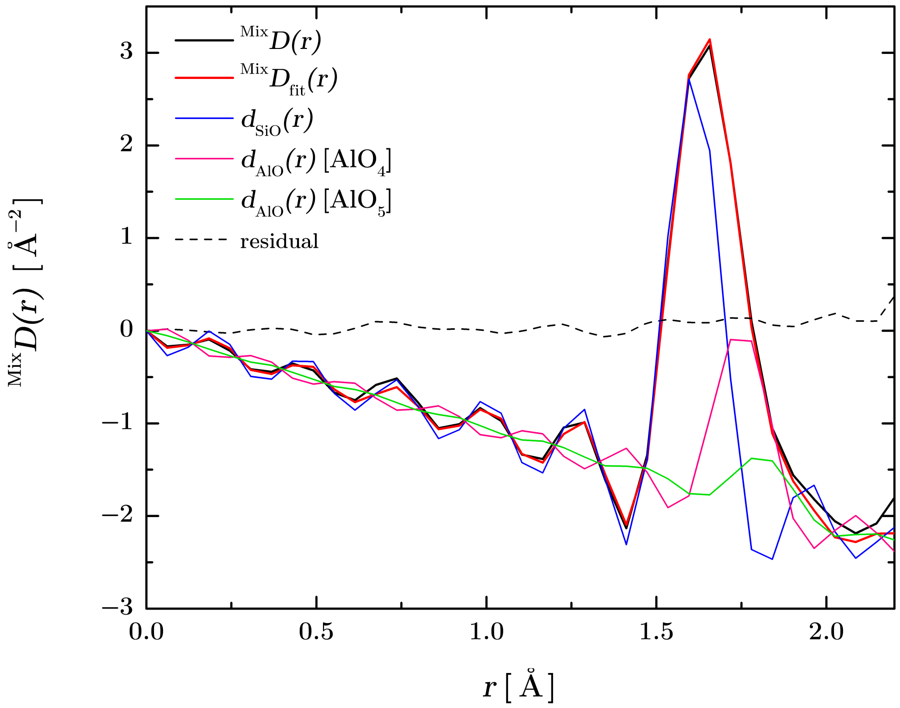

Figure 6-7: The first peak in the ${}^{\mathrm{Mix}}D(r)$ function for $(R_2O_3)_{0.2}(Al_2O_3)_{0.2}(SiO_2)_{0.6}$ with R = Mix. The solid black line is the measured $D(r)$ function, and is fitted with three Gaussians convoluted with a sinc function using RDFgenie (solid red curve). The solid blue, pink and green curves show the contributions from $d_{\mathrm{SiO}}(r)$, $d_{\mathrm{AlO}}(r)$ for AlO_4 units, and $d_{\mathrm{AlO}}(r)$ for AlO_5 units, respectively. The dashed black line shows the residual. The fit gives $R_\chi = 0.053$ in the fitted range 0 – 1.9 Å.

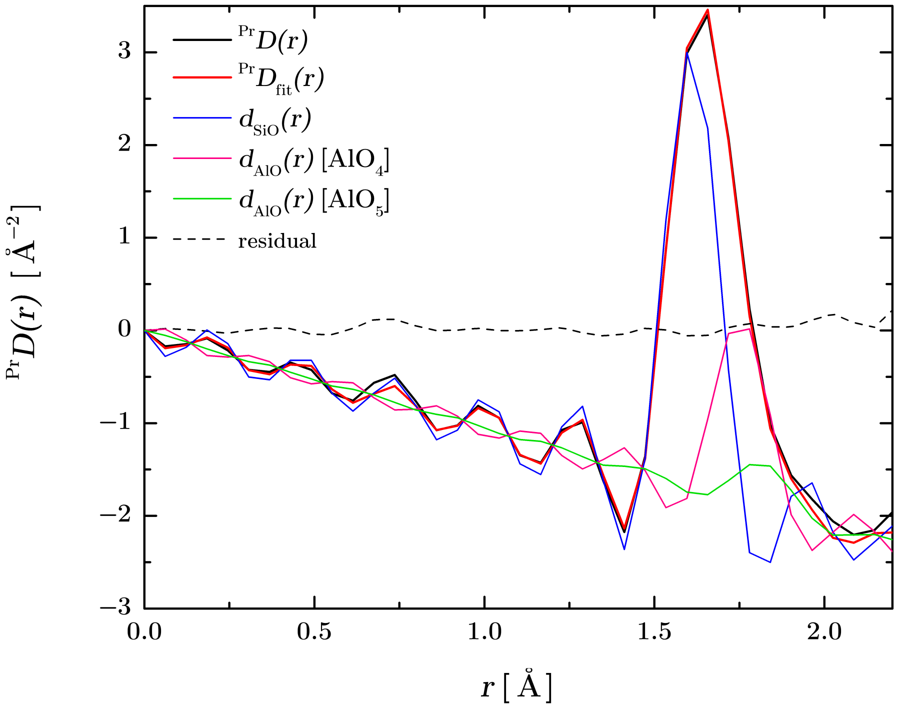

Figure 6-8: The first peak in the $^{\mathrm{Pr}}D(r)$ function for $(\mathrm{R_2O_3})_{0.2}(\mathrm{Al_2O_3})_{0.2}(\mathrm{SiO_2})_{0.6}$ with R = Pr. The solid black line is the measured $D(r)$ function, and is fitted with three Gaussians convoluted with a sinc function using RDFgenie (solid red curve). The solid blue, pink and green curves show the contributions from $d_{\mathrm{SiO}}(r)$, $d_{\mathrm{AlO}}(r)$ for $\mathrm{AlO_4}$ units and $d_{\mathrm{AlO}}(r)$ for $\mathrm{AlO_5}$ units, respectively. The dashed black line shows the residual. The fit gives $R_\chi = 0.051$ in the fitted range 0 – 1.9 Å.

6.4.2 First-order difference functions

The first-order difference functions $\Delta F_{\mathrm{R}}^{(i)}(Q)$ shown in Figure 6-9 were obtained from the total structure factors following Eqs. (6.4)–(6.6). The real-space $\Delta G_{\mathrm{R}}^{(i)}(r)$ functions are shown in Figure 6-10. The first peak at about 2.43(1) Å is well separated from the remaining peaks. Because the nearest-neighbour atoms to the rare-earth species are expected to be oxygen, this peak position will correspond to the R-O bond distance. For instance, in crystalline $\mathrm{Nd_2O_3}$, the Nd-O distance is at about 2.39 Å [131]. The average coordination number of O around R can be calculated using the equation

$$\bar{n}_{\mathrm{R}}^{\mathrm{O}} = 4\pi\rho c_{\mathrm{O}} \int_{r_1}^{r_2} \left[\frac{\Delta G_{\mathrm{R}}^{(i)}(r) - \Delta G_{\mathrm{R}}^{(i)}(0)}{2c_{\mathrm{R}}c_{\mathrm{O}}\Delta b_{\mathrm{R}} b_{\mathrm{O}}} \right] r^2 dr, \tag{6.29}$$

where r_1 and r_2 are the integration limits of the first-peak region, because

$$g_{\mathrm{RO}}(r) = \frac{\Delta G_{\mathrm{R}}^{(i)}(r) - \Delta G_{\mathrm{R}}^{(i)}(0)}{2c_{\mathrm{R}}c_{\mathrm{O}}\Delta b_{\mathrm{R}} b_{\mathrm{O}}}, \tag{6.30}$$

where

$$\Delta b_{\mathrm{R}} = \begin{cases} (b_{\mathrm{Nd}} - b_{\mathrm{Pr}}) & \text{for } i = 1 \\ (b_{\mathrm{Nd}} - b_{\mathrm{Mix}}) & \text{for } i = 2 \\ (b_{\mathrm{Mix}} - b_{\mathrm{Pr}}) & \text{for } i = 3. \end{cases} \tag{6.31}$$

Following the definitions given by Eqs.(6.4)-(6.6) and Eq.(6.22), the $\Delta G_{\mathrm{R}}^{(i)}(r \to 0)$ limits for the difference functions are given by

$$\Delta G_{\mathrm{R}}^{(1)}(r \to 0) = {}^{\mathrm{Nd}}G(0) - {}^{\mathrm{Pr}}G(0) \tag{6.32}$$

$$\Delta G_{\mathrm{R}}^{(2)}(r \to 0) = {}^{\mathrm{Nd}}G(0) - {}^{\mathrm{Mix}}G(0) \tag{6.33}$$

$$\Delta G_{\mathrm{R}}^{(2)}(r \to 0) = {}^{\mathrm{Mix}}G(0) - {}^{\mathrm{Pr}}G(0). \tag{6.34}$$

The $\bar{n}_{\mathrm{R}}^{\mathrm{O}}$ values and average R-O bond distances obtained from the first-peak positions in the $\Delta G_{\mathrm{R}}^{(i)}(r)$ functions are summarised in Table 6.4.

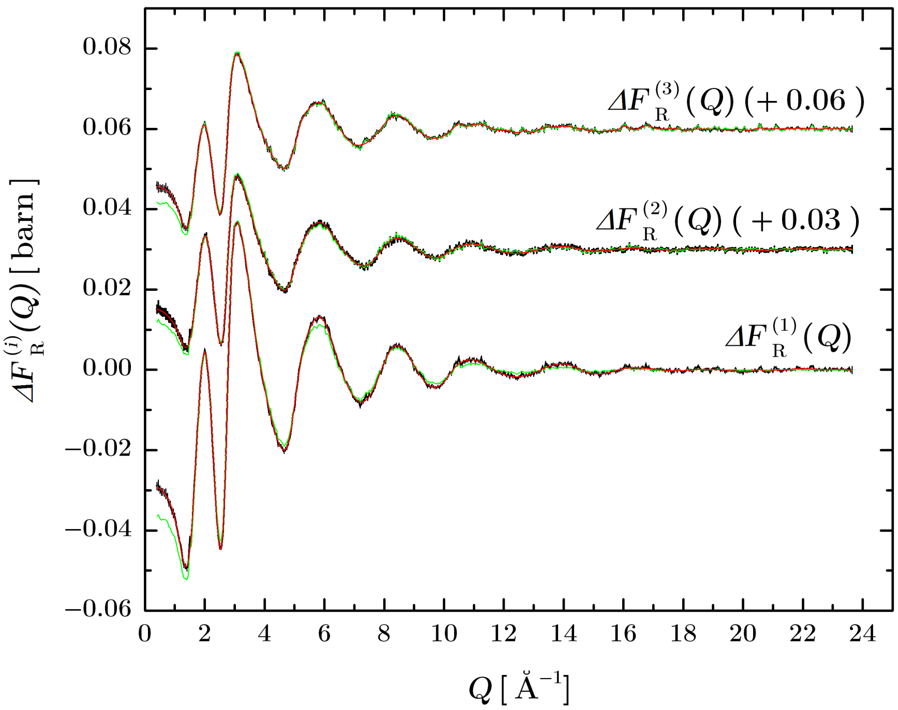

Figure 6-9: First-order difference functions $\Delta F_{\mathrm{R}}^{(i)}(Q)$, for $i = 1$, 2 and 3, as obtained from the total structure factors shown in Fig. 6-3. The solid black lines with vertical error bars are the measured data sets. The red curves show spline fits to these measured data sets. The green curves are the back-Fourier transforms of the $\Delta G_{\mathrm{R}}^{(i)}(r)$ functions shown in Figure 6-10, after the low-r oscillations are set to their theoretical $\Delta G_{\mathrm{R}}^{(i)}(r \to 0)$ limit. The curves for $i = 1$ and 2 have been offset vertically, for clarity of presentation, and the offsets are indicated in parenthesis.

Table 6.4: The average R-O coordination numbers and bond distances obtained from the $\Delta G_{\mathrm{R}}^{(i)}(r)$ functions.

$\Delta G_{\mathrm{R}}^{(i)}(r)$	$\bar{n}_{\mathrm{R}}^{\mathrm{O}}$	$\bar{r}_{\mathrm{RO}}$ (Å)
$i = 1$	7.3(2)	2.43(2)
$i = 2$	7.1(2)	2.41(2)
$i = 3$	7.4(2)	2.41(2)

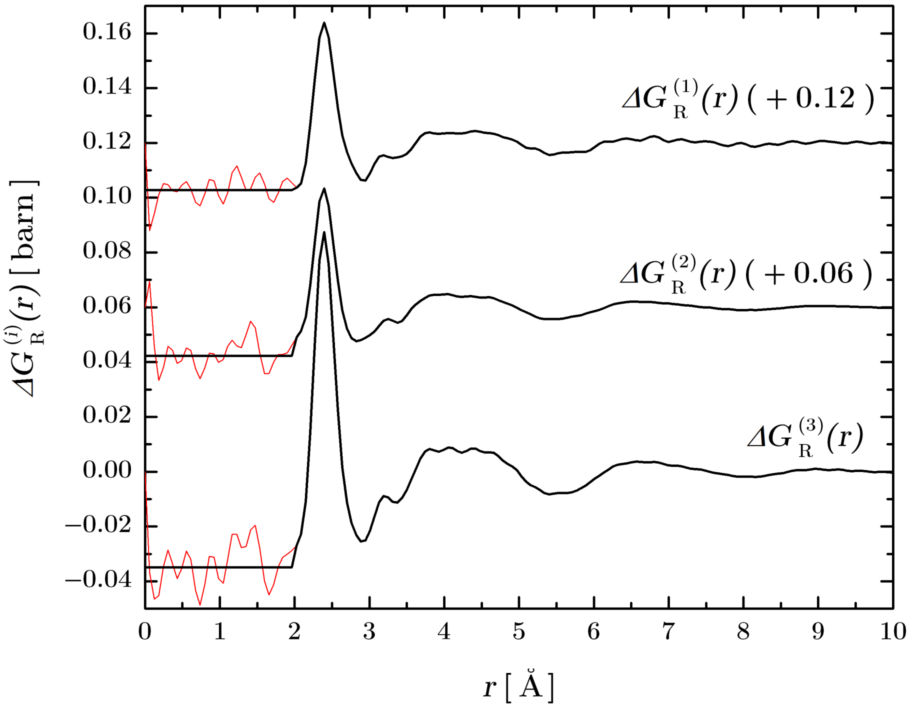

Figure 6-10: Real-space first-order difference functions $\Delta G_{\mathrm{R}}^{(i)}(r)$, for $i = 1$, 2 and 3. The solid black lines are the Fourier transforms of the spline-fitted data sets shown in Figure 6-9, after the low-r oscillations (solid red lines) are set to their theoretical $\Delta G_{\mathrm{R}}^{(i)}(r \rightarrow 0)$ limit. The curves for $i = 1$ and 2 have been offset vertically, for clarity of presentation, and the offsets are indicated in parenthesis.

6.4.3 "Total minus weighted" difference functions

The "total minus weighted" difference (TMWD) functions obtained following Eqs.(6.14)–(6.16) are shown in Figures 6-11 – 6-12. In this case, the R-μ correlations are removed to leave only the R-R and μ-μ correlations. The comparison in Fig.6-12 shows that there is very good agreement between the $\Delta F^{(i)}(Q)$ functions. The real-space information is shown in Figure 6-13. The "ringing" around each first peak is due to the truncation of the $\Delta F^{(i)}(Q)$ functions at a finite $Q_{\rm max}$ value. The first oscillation before the peak was not set to the theoretical $\Delta G^{(i)}(r \to 0)$ limit before the back-Fourier transform, in order to aid in the correct normalisation of the datasets. Following Eqs.(6.14)–(6.16) and Eq.(6.23), the $\Delta G^{(i)}(r \to 0)$ limit for each of the "total minus weighted" difference functions is given by

$$\Delta G^{(1)}(r \to 0) = \frac{b_{\rm Nd}\ {}^{\rm Pr}G(0) - b_{\rm Pr}\ {}^{\rm Nd}G(0)}{b_{\rm Nd} - b_{\rm Pr}} \tag{6.35}$$

$$\Delta G^{(2)}(r \to 0) = \frac{b_{\rm Nd}\ {}^{\rm Mix}G(0) - b_{\rm Mix}\ {}^{\rm Nd}G(0)}{b_{\rm Nd} - b_{\rm Mix}} \tag{6.36}$$

$$\Delta G^{(3)}(r \to 0) = \frac{b_{\rm Mix}\ {}^{\rm Pr}G(0) - b_{\rm Pr}\ {}^{\rm Mix}G(0)}{b_{\rm Mix} - b_{\rm Pr}}. \tag{6.37}$$

The first peak at about 1.65 Å in the $\Delta G^{(i)}(r)$ functions is well separated from the second peak, as in the case of the $G(r)$ functions shown in Figure 6-5, and can be assigned to the Si-O and Al-O correlations. Figures 6-14 – 6-16 show the results obtained by fitting the first peak in the $\Delta D^{(\rm i)}(r)$ functions, with three Gaussian functions convoluted with a sinc function (Eq.(2.35)), where $Q_{\rm max} = 23.15$ Å^{-1}. These Gaussian functions represent the Si-O and Al-O pair-correlations contained under the first peak. The Si-O parameters were set to $\bar{r}_{\rm SiO} = 1.61$ Å and $\bar{n}_{\rm Si}^{\rm O} = 4$. The Al-O correlations are well described by two Gaussian functions, which indicate the presence of both AlO$_4$ and AlO$_5$ units, as suggested by the NMR results of Schaller and Stebbins in [125]. By using the RDFgenie fitting program, the relative fractions of the AlO$_4$ and AlO$_5$ units were found to be 80(3)% and 20(3)%, respectively. The fitted Al-O bond distances and coordination numbers are listed in Table 6.5.

Table 6.5: The average coordination numbers and bond distances for the AlO_4 and AlO_5 units in glassy $(R_2O_3)_{0.2}(Al_2O_3)_{0.2}(SiO_2)_{0.6}$ samples (with R = Nd, Mix or Pr), as obtained from the first peak in the measured $\Delta D^{(i)}(r)$ functions, for $i = 1$, 2 and 3. The goodness-of-fit parameter R_χ is given, along with the fitted r-space range.

$\Delta G^{(i)}(r)$	$\bar{n}_{Al}^{O}$	$\bar{r}_{AlO}$ (Å)	$\bar{n}_{Al}^{O}$	$\bar{r}_{AlO}$ (Å)	R_χ	range (Å)
$i = 1$	4.0(2)	1.75(2)	5.0(1)	1.82(2)	0.070	0 - 1.9
$i = 2$	4.0(2)	1.75(2)	5.0(1)	1.82(2)	0.093	0 - 1.9
$i = 3$	4.0(2)	1.75(2)	5.0(1)	1.80(2)	0.056	0 - 1.9

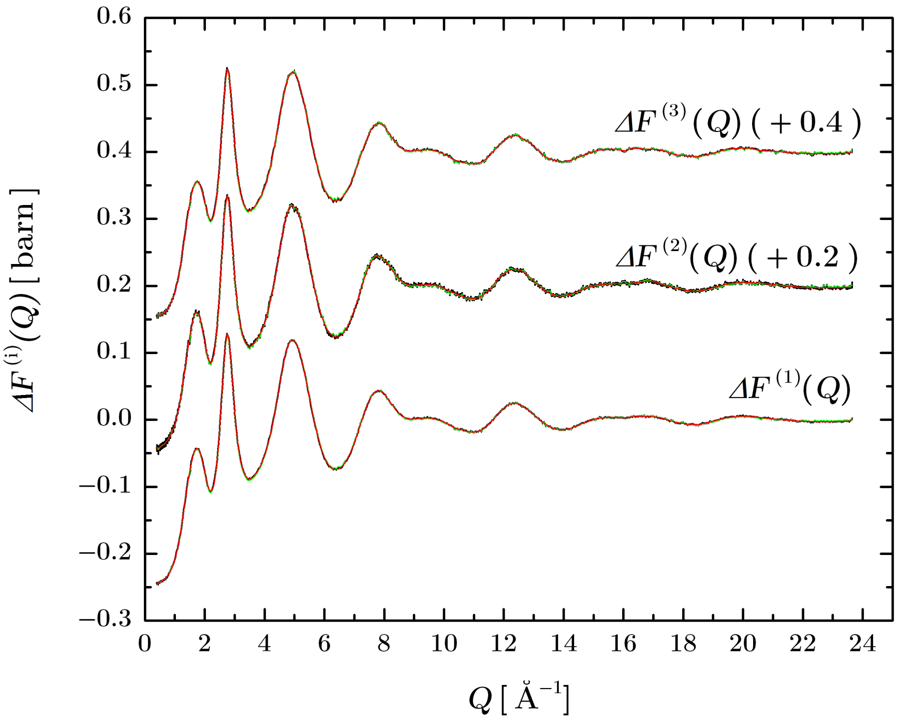

Figure 6-11: "Total minus weighted" difference functions $\Delta F^{(i)}(Q)$, for $i = 1$, 2 and 3. The solid black lines with vertical error bars are the measured data sets. The red curves show spline fits to the measured data sets. The green curves are the back-Fourier transforms of the $\Delta G^{(i)}(r)$ functions shown in Figure 6-13, after the low-r oscillations are set to their theoretical $\Delta G^{(i)}(r \to 0)$ limit. The curves for $i = 1$ and 2 have been offset vertically, for clarity of presentation, and the offsets are indicated in parenthesis.

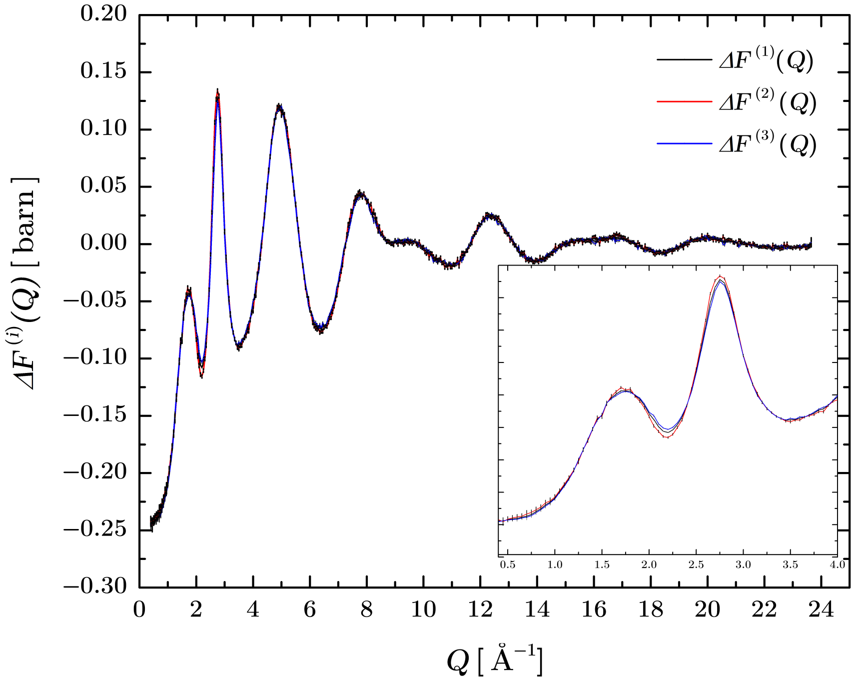

Figure 6-12: Superposition of the "total minus weighted" difference functions $\Delta F^{(i)}(Q)$, for $i = 1$, 2 and 3, shown in Figure 6-11. The solid black, red and blue lines, with vertical error bars, are the measured data sets for $\Delta F^{(1)}(Q)$, $\Delta F^{(2)}(Q)$ and $\Delta F^{(3)}(Q)$, respectively. The error bars are hardly distinguishable, given the high-quality counting statistics. The inset zooms into the low-Q region, where the maximum Q-value is set at 4 Å^{-1}, for clarity of presentation.

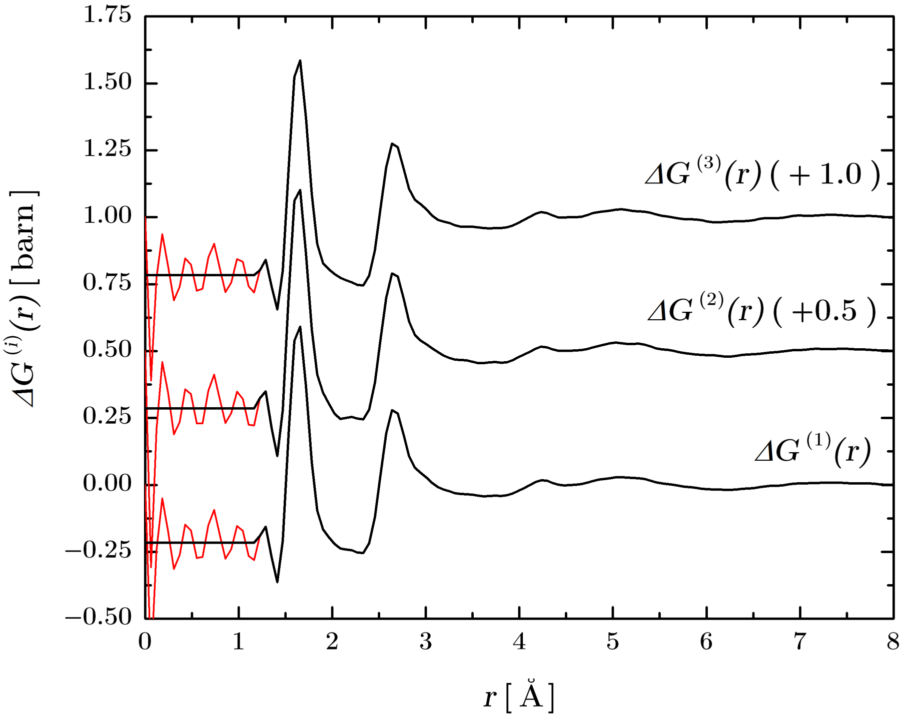

Figure 6-13: Real-space “total minus weighted” difference functions $\Delta G^{(i)}(r)$, for $i = 1$, 2 and 3. The solid black lines are the Fourier transforms of the spline-fitted data sets shown in Figure 6-11, after the low-r oscillations (solid red lines) are set to their theoretical $\Delta G^{(i)}(r \to 0)$ limit. The curves for $i = 1$ and 2 have been offset vertically, for clarity of presentation, and the offsets are indicated in parenthesis.

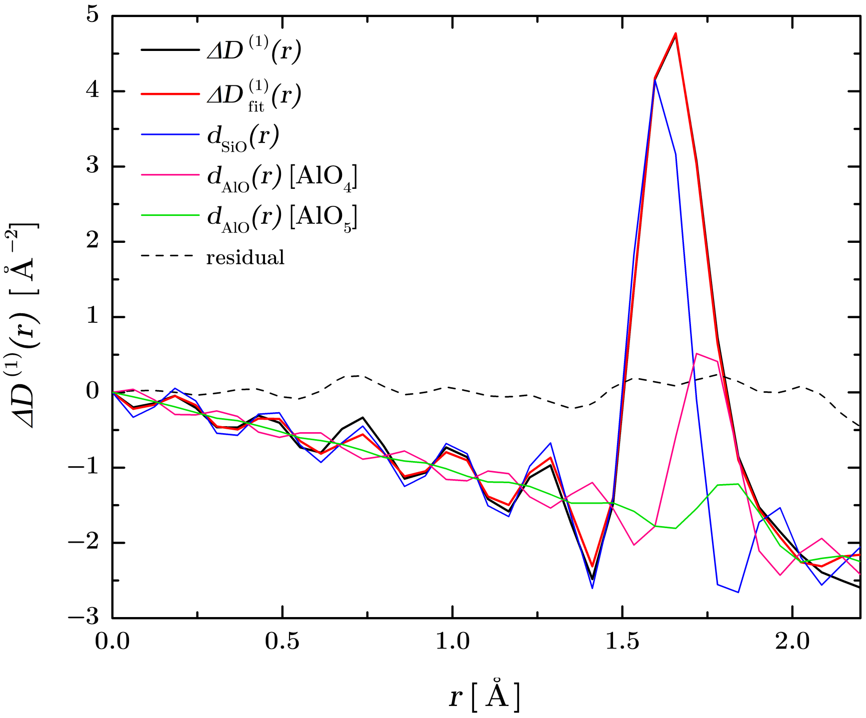

Figure 6-14: The first peak in the $\Delta D^{(1)}(r)$ function. The solid black line is the measured $\Delta D^{(1)}(r)$ function, and is fitted with three Gaussians convoluted with a sinc function using RDFgenie (solid red curve). The solid blue, pink and green curves show the contributions from $d_{\mathrm{SiO}}(r)$, $d_{\mathrm{AlO}}(r)$ for AlO_4 units, and $d_{\mathrm{AlO}}(r)$ for AlO_5 units, respectively. The fit gives $R_\chi = 0.070$ for the range 0 – 1.9 Å.

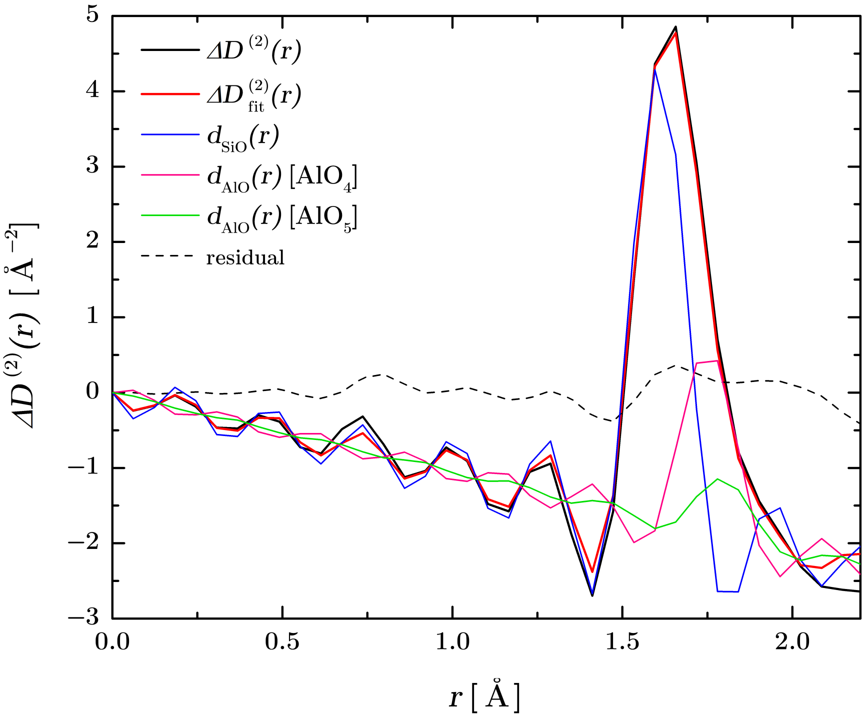

Figure 6-15: The first peak in the $\Delta D^{(2)}(r)$ function. The solid black line is the measured $\Delta D^{(2)}(r)$ function, and is fitted with three Gaussians convoluted with a sinc function using RDFgenie (solid red curve). The solid blue, pink and green curves show the contributions from $d_{\text{SiO}}(r)$, $d_{\text{AlO}}(r)$ for AlO_4 units, and $d_{\text{AlO}}(r)$ for AlO_5 units, respectively. The fit gives $R_\chi = 0.093$ for the range 0 – 1.9 Å.

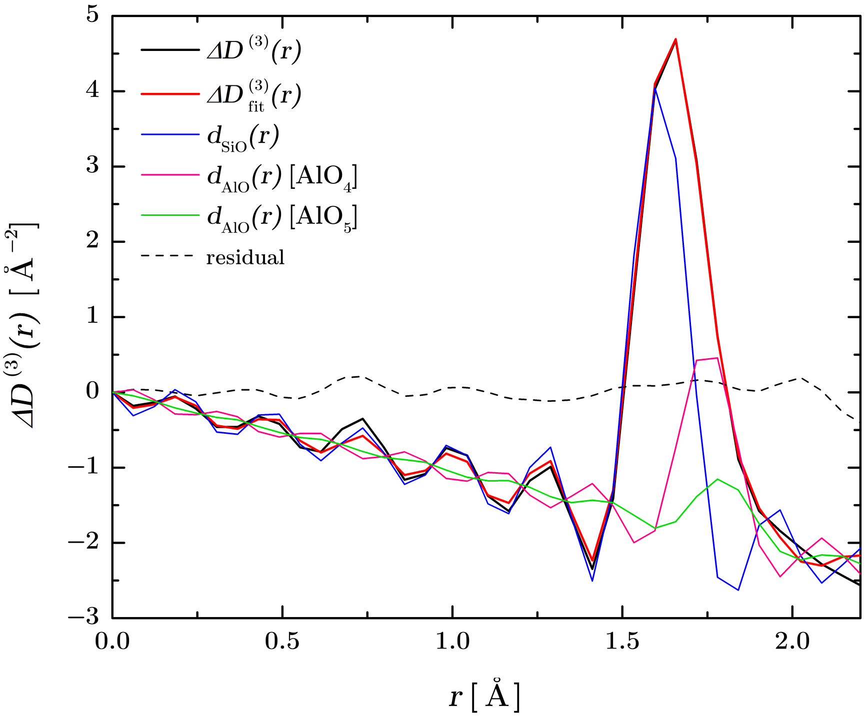

Figure 6-16: The first peak in the $\Delta D^{(3)}(r)$ function. The solid black line is the measured $\Delta D^{(3)}(r)$ function, and is fitted with three Gaussians convoluted with a sinc function using RDFgenie (solid red curve). The solid blue, pink and green curves show the contributions from $d_{\text{SiO}}(r)$, $d_{\text{AlO}}(r)$ for AlO$_4$ units, and $d_{\text{AlO}}(r)$ for AlO$_5$ units, respectively. The fit gives $R_\chi = 0.056$ for the range 0 – 1.9 Å.

6.4.4 The $S_{\mathrm{RR}}(Q)$ partial structure factor, $\delta_{\mathrm{R}\mu}(Q)$ and $\Delta_{\mu\mu}(Q)$ functions

The reciprocal-space functions $S_{\mathrm{RR}}(Q)$, $\delta_{\mathrm{R}\mu}(Q)$ and $\Delta_{\mu\mu}(Q)$, obtained by solving Eq. (6.17), are shown in Figures 6-17 – 6-19, and the corresponding real-space functions are given in Figures 6-20 – 6-22.

The $S_{\mathrm{RR}}(Q)$ partial structure factor and the $g_{\mathrm{RR}}(r)$ partial pair-distribution function contain information on the correlations between the rare-earth atoms. The data are quite noisy, especially for $Q \geq 16$ Å^{-1}. In order to to reduce effectively the statistical noise, a cosine and a Lorch functions were both applied to the spline-fitted data, for $Q \geq 12$ Å^{-1}. The average R-R coordination number is given by

$$\bar{n}_{\mathrm{R}}^{\mathrm{R}} = 4\pi\rho c_{\mathrm{R}} \int_{r_1}^{r_2} g_{\mathrm{RR}}(r) r^2 dr \tag{6.38}$$

and the calculated value is listed in Table 6.6.

The $\delta_{\mathrm{R}\mu}(Q)$ function, defined in Eq.(6.18), has contributions solely from the R-μ correlations. The data are quite noisy, especially for $Q \geq 16$ Å^{-1}. In this case, the use uniquely of a Lorch function, with $Q_{\max} = 15$ Å^{-1}, was sufficient to reduce effectively the statistical noise. The first peak in $\delta_{R\mu}(Q)$ corresponds to the R-O correlations. The average coordination number of O around R can be calculated using the equation

$$\bar{n}_{\mathrm{R}}^{\mathrm{O}} = \frac{4\pi\rho}{b_{\mathrm{O}}} \int_{r_1}^{r_2} \left[\delta_{\mathrm{R}\mu}(r) - \delta_{\mathrm{R}\mu}(0)\right] r^2 dr, \tag{6.39}$$

where r_1 and r_2 are the integration limits for the first-peak region, in which

$$g_{\mathrm{RO}}(r) = \frac{\delta_{R\mu}(r) - \delta_{R\mu}(0)}{b_{\mathrm{O}} c_{\mathrm{O}}}, \tag{6.40}$$

and the limit $\delta_{\mathrm{R}\mu}(r \to 0)$ is given by

$$\delta_{\mathrm{R}\mu}(r \to 0) = \delta_{\mathrm{R}\mu}(0) = -(c_{\mathrm{O}} b_{\mathrm{O}} + c_{\mathrm{Al}} b_{\mathrm{Al}} + c_{\mathrm{Si}} b_{\mathrm{Si}}). \tag{6.41}$$

The $\Delta_{\mu\mu}(Q)$ function contains only those correlations between the matrix elements. The corresponding real-space function has a first peak at 1.65(2) Å, which is associated with the Si-O and Al-O correlations as for the case of the $G(r)$ and $\Delta G^{(i)}(r)$ functions. The "ringing" around the first peak is due to the truncation of $\Delta_{\mu\mu}(Q)$ at a finite $Q_{\max}$ value. The first oscillation before the first peak was not set to the theoretical $\Delta_{\mu\mu}(r \to 0)$ limit before the back-Fourier transform in order to help ensuring that the data set is correctly normalised.

The low-r limit is given by

$$\Delta_{\mu\mu}(r \to 0) = \Delta_{\mu\mu}(0) = -(c_{\mathrm{O}}b_{\mathrm{O}} + c_{\mathrm{Al}}b_{\mathrm{Al}} + c_{\mathrm{Si}}b_{\mathrm{Si}})^2. \tag{6.42}$$

Figure 6-23 shows the result of fitting the first peak in $\Delta\mu\mu(r)$ to three Gaussian functions convoluted with a sinc function (Eq.(2.35)). The Gaussian functions represent the Si-O and Al-O correlations within the region of the first peak. The Si-O parameters were set to $\bar{r}_{\mathrm{SiO}} = 1.61$ Å and $\bar{n}_{\mathrm{Si}}^{\mathrm{O}} = 4$. The Al-O correlations are well described by two Gaussian functions, which indicate the presence of both $\mathrm{AlO_4}$ and $\mathrm{AlO_5}$ units, as suggested by the NMR results of Schaller and Stebbins [125]. By using the RDFgenie fitting program, the relative fractions of $\mathrm{AlO_4}$ and $\mathrm{AlO_5}$ units are found to be 80(3)% and 20(3)%, respectively. The average Al-O bond distances and coordination numbers and listed in Table 6.7.

Table 6.6: The average coordination numbers and bond distances for glassy $(\mathrm{R_2O_3})_{0.2}(\mathrm{Al_2O_3})_{0.2}(\mathrm{SiO_2})_{0.6}$, with R = Nd, Mix or Pr, as obtained from the first peak in the measured $g_{\mathrm{RR}}(r)$ and $\delta_{\mathrm{R}\mu}(r)$ functions.

r-space function	Coordination number	Peak position (Å)
$g_{RR}(r)$	$\bar{n}_{\mathrm{R}}^{\mathrm{R}} = 4.4(2)$	$\bar{r}_{\mathrm{RR}} = 3.9(4)$
$\delta_{R\mu}(r)$	$\bar{n}_{\mathrm{R}}^{\mathrm{O}} = 7.4(2)$	$\bar{r}_{\mathrm{RO}} = 2.44(4)$

Table 6.7: The average coordination numbers and bond distances for the $\mathrm{AlO_4}$ and $\mathrm{AlO_5}$ units in glassy $(\mathrm{R_2O_3})_{0.2}(\mathrm{Al_2O_3})_{0.2}(\mathrm{SiO_2})_{0.6}$ samples with R = Nd, Mix or Pr, as obtained from the first peak in the $\Delta_{\mu\mu}(r)$ function. The goodness-of-fit parameter R_χ is given, along with the fitted r-space range.

r-space function	$\bar{n}_{\mathrm{Al}}^{\mathrm{O}}$	$\bar{r}_{\mathrm{AlO}}$ (Å)	$\bar{n}_{\mathrm{Al}}^{\mathrm{O}}$	$\bar{r}_{\mathrm{AlO}}$ (Å)	R_χ	range (Å)
$\Delta_{\mu\mu}(r)$	4.0(2)	1.74(2)	5.0(1)	1.81(2)	0.092	0.0 - 1.90

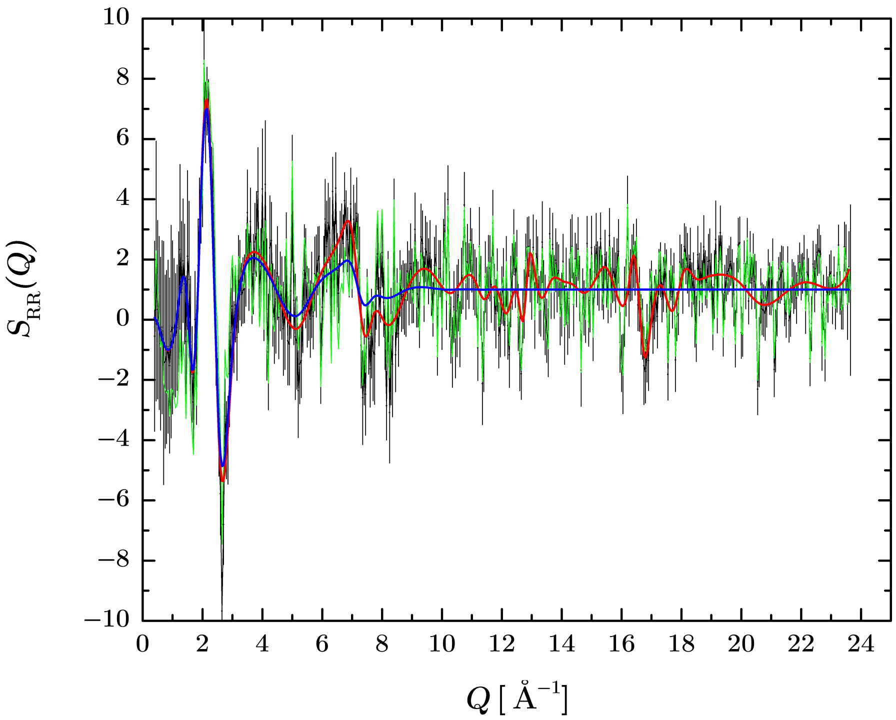

Figure 6-17: Partial structure factor $S_{\mathrm{RR}}(Q)$. The solid black line with vertical error bars is the measured data set. The red curve shows a spline fit to the measured data set. The green curve is the back-Fourier transform of the $g_{\mathrm{RR}}(r)$ function (blue curve in Figure 6-20), after the low-r oscillations are set to their theoretical $g_{\mathrm{RR}}(r \to 0)$ limit. The blue curve is the spline-fitted data, after a cosine and a Lorch functions are applied.

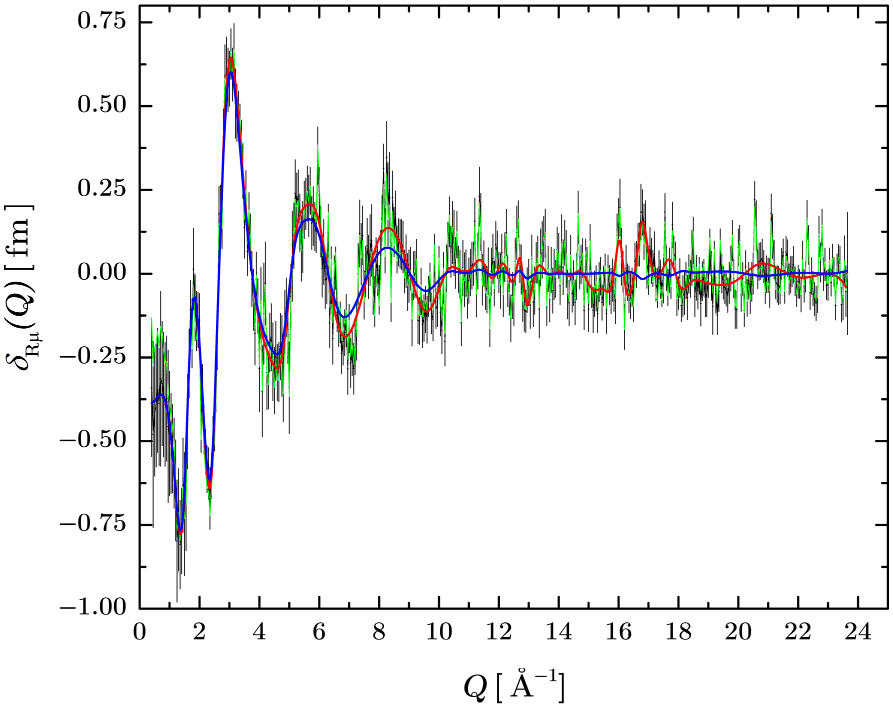

Figure 6-18: Difference function $\delta_{\mathrm{R}\mu}(Q)$. The solid black line with vertical error bars is the measured data set. The red curve shows a spline fit to the measured data set. The green curve is the back-Fourier transform of the $\delta_{\mathrm{R}\mu}(r)$ function shown by the blue curve in Figure 6-21, after the low-r oscillations are set to their theoretical $\delta_{\mathrm{R}\mu}(r \to 0)$ limit. The blue curve is the spline-fitted data after a Lorch functions is applied.

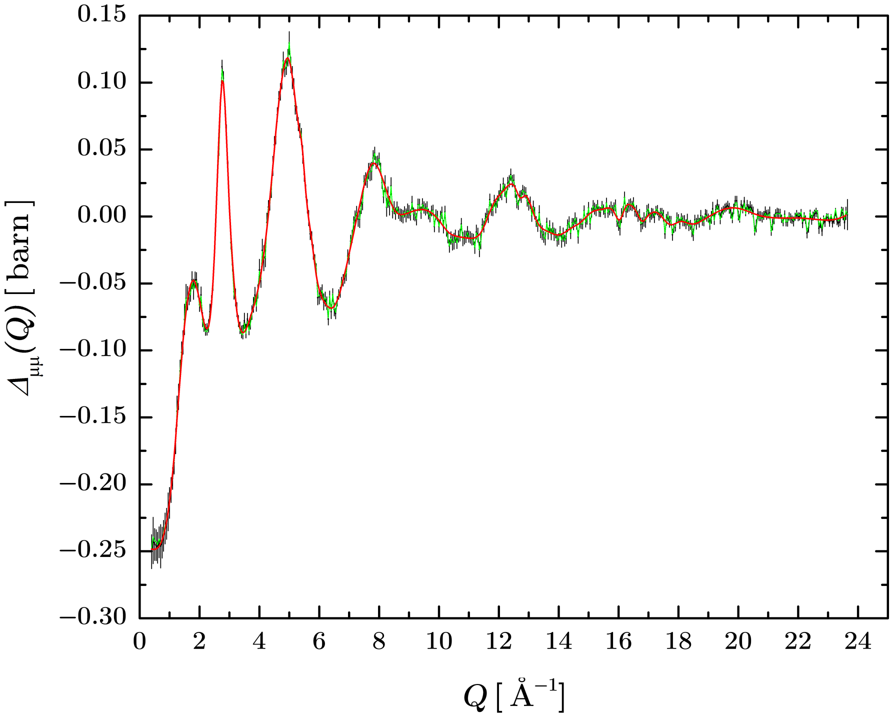

Figure 6-19: Difference function $\Delta_{\mu\mu}(Q)$. The solid black line with vertical error bars is the measured data set. The red curve shows a spline fit to the measured data set. The green curve is the back-Fourier transform of the $\Delta_{\mu\mu}(r)$ function shown in Figure 6-22, after the low-r oscillations are set to their theoretical $\Delta_{\mu\mu}(r \rightarrow 0)$ limit.

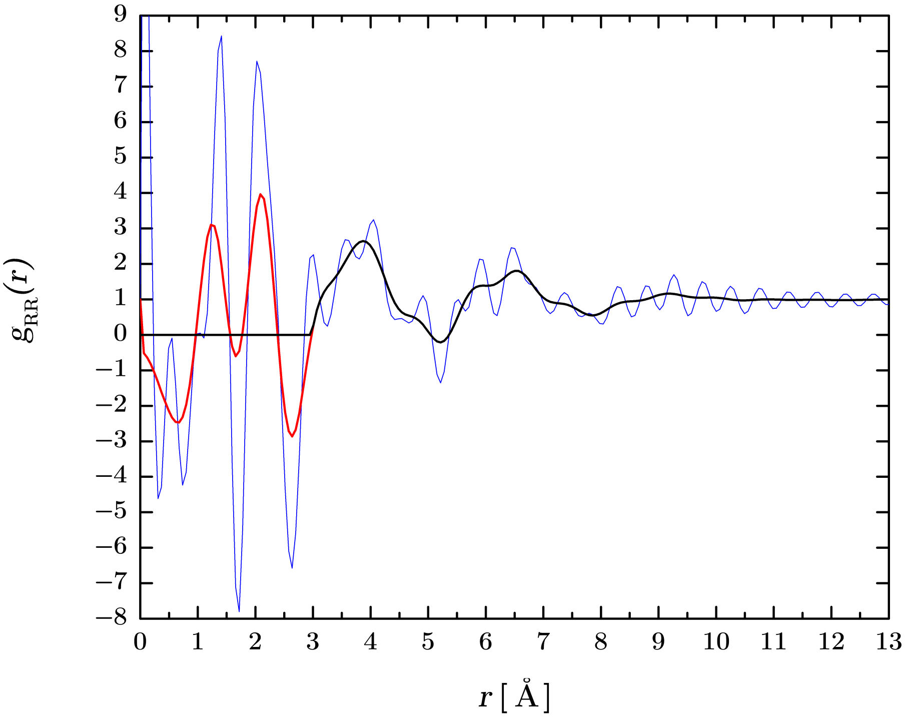

Figure 6-20: Partial pair-distribution function $g_{\mathrm{RR}}(r)$. The solid black line is the Fourier transform of the spline-fitted data set shown in Figure 6-17, after a cosine and a Lorch function were applied to smooth the data sets after $Q_{\max} = 12$ Å^{-1}. The low-r oscillations (solid red lines) are set to the theoretical limit $g_{\mathrm{RR}}(r \to 0)$ limit at r-values smaller than the distance of closest approach between the centres of two atoms. The solid blue line gives the Fourier transform of the spline-fitted data set, with $Q_{\max} = 15$ Å^{-1} and without the application of a cosine or Lorch function.

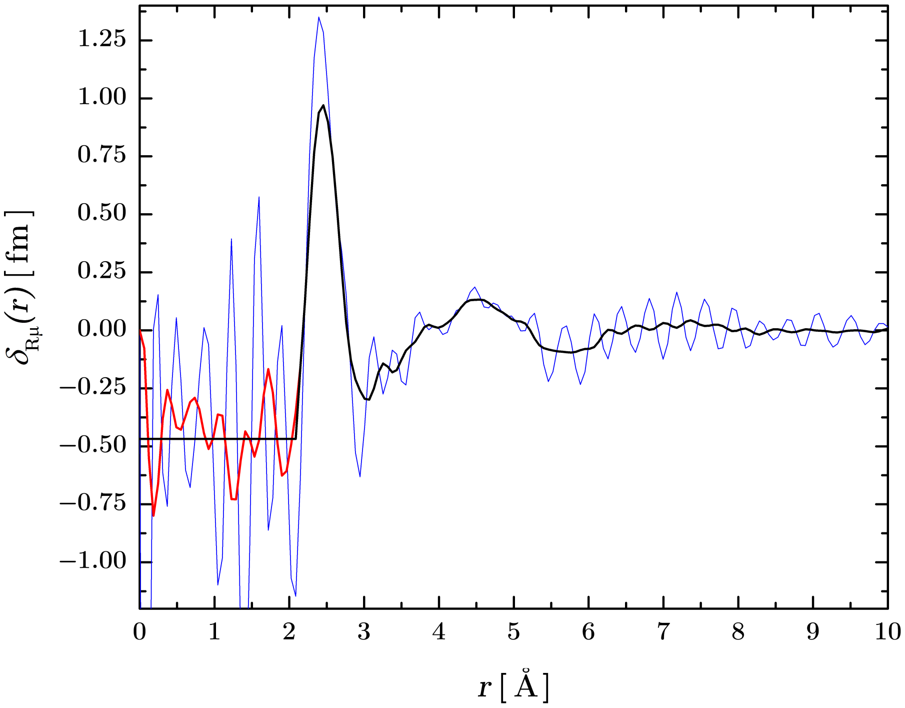

Figure 6-21: Difference function $\delta_{\mathrm{R}\mu}(r)$. The solid black line is the Fourier transform of the spline-fitted data set shown in Figure 6-18, after a Lorch function was applied with $Q_{\max} = 15$ Å^{-1}. The low-r oscillations (solid red lines) are set to their theoretical $\delta_{\mathrm{R}\mu}(r \to 0)$ limit at r-values smaller than the distance of closest approach between the centres of two atoms. The solid blue line gives the Fourier transform of the spline-fitted data set, without the application of a Lorch function.

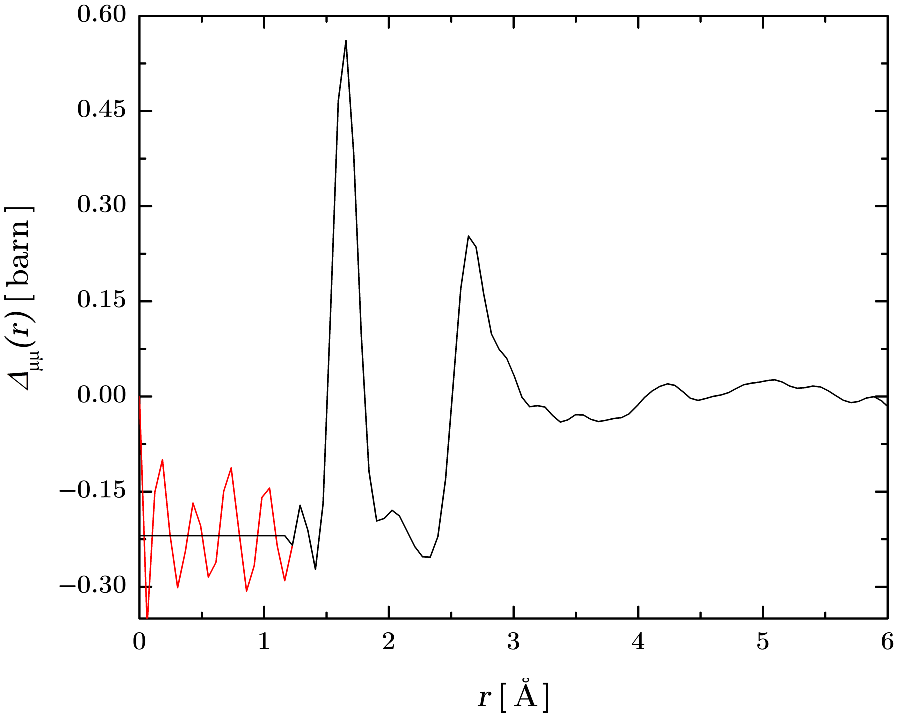

Figure 6-22: Difference function $\Delta_{\mu\mu}(r)$. The solid black line is the Fourier transform of the spline-fitted data set shown in Figure 6-19. The low-r oscillations (solid red lines) are set to their theoretical limit $\Delta_{\mu\mu}(r \rightarrow 0)$ limit at r-values smaller than the distance of closest approach between the centres of two atoms.

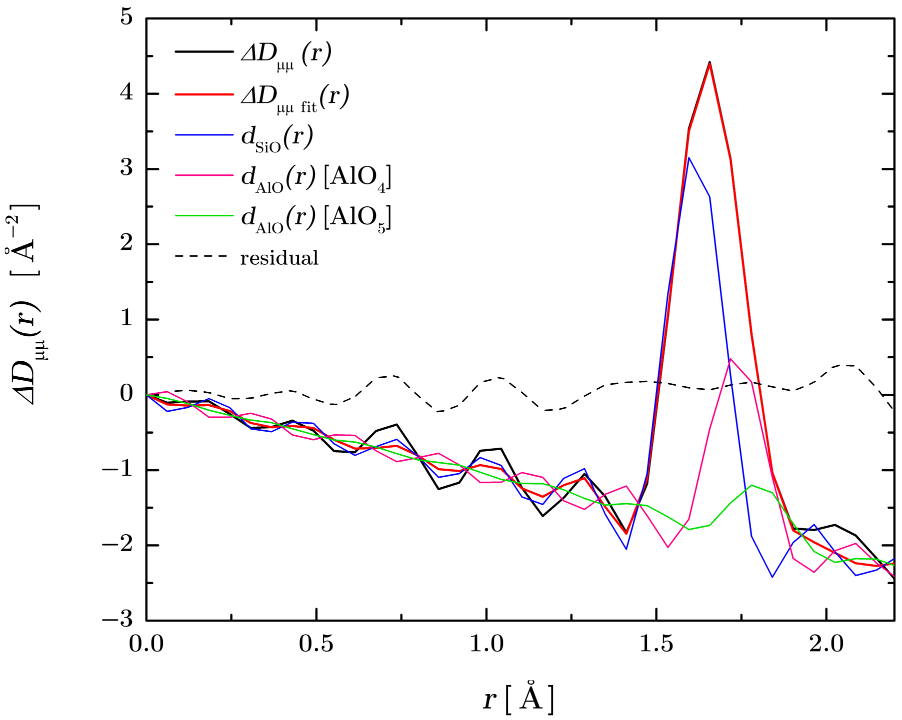

Figure 6-23: The first peak in the $\Delta D_{\mu\mu}(r)$ function. The solid black line is the measured $\Delta D_{\mu\mu}(r)$ function, and is fitted with three Gaussians convoluted with a sinc function using RDFgenie (solid red curve). The solid blue, pink and green curves show the contributions from $d_{\mathrm{SiO}}(r)$, $d_{\mathrm{AlO}}(r)$ for AlO_4 units, and $d_{\mathrm{AlO}}(r)$ for AlO_5 units, respectively. The fit gives a goodness-of-fit parameter of $R_\chi = 0.092$ for the range 0 – 1.9 Å.

6.5 Discussion

A summary of the average coordination numbers and peak positions found in the previous section is given in Table 6.8.

r-space function	Coordination number			Peak position (Å)
	AlO_4, AlO_5	R-O	R-R	
${}^{\mathrm{Nd}}G(r)$	4.0(2), 5.0(1)	-	-	1.75(2), 1.80(2)
${}^{\mathrm{Mix}}G(r)$	4.0(2), 5.0(1)	-	-	1.75(2), 1.82(2)
${}^{\mathrm{Pr}}G(r)$	4.0(2), 5.0(1)	-	-	1.75(2), 1.82(2)
$\Delta G^{(1)}(r)$	4.0(2), 5.0(1)	-	-	1.75(2), 1.82(2)
$\Delta G^{(2)}(r)$	4.0(2), 5.0(1)	-	-	1.75(2), 1.82(2)
$\Delta G^{(3)}(r)$	4.0(2), 5.0(1)	-	-	1.75(2), 1.80(2)
$\Delta_{\mu\mu}(r)$	4.0(2), 5.0(1)	-	-	1.74(2), 1.81(2)
$\Delta G_{\mathrm{R}}^{(1)}(r)$	-	7.3(2)	-	2.43(2)
$\Delta G_{\mathrm{R}}^{(2)}(r)$	-	7.1(2)	-	2.41(2)
$\Delta G_{\mathrm{R}}^{(3)}(r)$	-	7.4(2)	-	2.41(2)
$\delta_{\mathrm{R}\mu}(r)$	-	7.4(2)	-	2.44(4)
$g_{\mathrm{RR}}(r)$	-	-	4.4(2)	3.9(4)

Table 6.8: Summary of the average Al-O, R-O and R-R coordination numbers and peak positions for glassy $(R_2O_3)_{0.2}(Al_2O_3)_{0.2}(SiO_2)_{0.6}$.

The average Al-O coordination numbers and peak positions were obtained from the $G(r)$, $\Delta G^{(i)}(r)$ and $\Delta_{\mu\mu}(r)$ functions by assuming $\bar{n}_{\mathrm{Si}}^{\mathrm{O}} = 4$ and $\bar{r}_{\mathrm{SiO}} = 1.61$ Å. A population of AlO_4 and AlO_5 units, having relative fractions of 80(3)% and 20(3)%, respectively, were found by using the RDFgenie fitting procedure. The bond distances were found to be $\bar{r}_{\mathrm{AlO}} = 1.75(2)$ Å and $\bar{r}_{\mathrm{AlO}} = 1.82(2)$ Å for AlO_4 and AlO_5 units, respectively, and are consistent with those found by Martin *et al.* [127] in Y-aluminophosphate glasses. Chirawatkul [27] performed a ND experiment on $(R_2O_3)_{0.2}(Al_2O_3)_{0.2}(SiO_2)_{0.6}$, where the small rare-earth elements Dy and Ho were selected as an isomorphic pair. She combined her results with RMC modelling and MD simulations, and found an $\bar{n}_{\mathrm{Al}}^{\mathrm{O}}$ value ranging between 4.2(2) and 4.9(2). The value of $\bar{n}_{\mathrm{Al}}^{\mathrm{O}} = 4.2$ that she selected as a constraint for the RMC modelling procedure was estimated by Stebbins [132] for an Y-AS glass having the same chemical formula [125], and is consistent with a population of AlO_4, AlO_5 and AlO_6 units having relative fractions of 78(3)%, 16(3)% and 6(3)%, respectively. In fact, Schaller and Stebbins [125] performed ^{27}Al and ^{17}O Magic Angle Spinning (MAS) NMR experiments on both $(Y_2O_3)_{0.2}(Al_2O_3)_{0.2}(SiO_2)_{0.6}$ and $(La_2O_3)_{0.2}(Al_2O_3)_{0.2}(SiO_2)_{0.6}$ glasses. They found that the La-containing glass has only AlO_4 and AlO_5 units, whilst the Y-containing glass has in addition AlO_6 units. The second peak position in $G(r)$ and $\Delta G^{(i)}(r)$ at ≈ 2.42 Å can be assigned to the R-O correlations. Let's consider the $\Delta G_{\mathrm{R}}^{(i)}(r)$ difference functions and the $\delta_{\mathrm{R}\mu}(r)$ function, where the matrix-matrix correlations are removed. The first peak position $\bar{r}_{\mathrm{RO}}$ varies between 2.41(2) – 2.43(2) Å for $\Delta G^{(i)}(r)$ and is at 2.44(4) Å for $\delta_{\mathrm{R}\mu}(r)$. The coordination number $\bar{n}_{\mathrm{R}}^{\mathrm{O}}$ varies between 7.1(2) and 7.4(2) for the $\Delta G_{\mathrm{R}}^{(\mathrm{i})}(r)$ difference functions and is 7.4(2) for $\delta_{\mathrm{R}\mu}(r)$. For the $(R_2O_3)_{0.2}(Al_2O_3)_{0.2}(SiO_2)_{0.6}$ glass with R = Dy and Ho, Chirawatkul found $\bar{n}_{\mathrm{R}}^{\mathrm{O}} = 7.2(3)$, and $\bar{r}_{\mathrm{RO}}$ values that vary between 2.31(3) - 2.35(3) Å [27]. Hence, in the small RAS glass the $\bar{r}_{\mathrm{RO}}$ bond distance is shorter, as compared to the large RAS glass, but little change is found for $\bar{n}_{\mathrm{R}}^{\mathrm{O}}$, within the experimental error.

Figure 6-20 shows the measured $g_{\mathrm{RR}}(r)$ function. It should be noticed that the unphysical low-r oscillations do not correspond to the first-peak positions associated with the Si-O, Al-O or R-O correlations, *i.e.* the R-μ and μ-μ' correlations appear to have been properly removed. The value $\bar{n}_{\mathrm{R}}^{\mathrm{R}} = 4.4(2)$ found in the present work is comparable to the value $\bar{n}_{\mathrm{R}}^{\mathrm{R}} = 4.6(2)$ found by Chirawatkul [27].

6.6 Conclusion

In this work the structure of the RAS glass $(R_2O_3)_{0.2}(Al_2O_3)_{0.2}(SiO_2)_{0.6}$ was investigated via ND with isomorphic substitution using the large rare-earth elements Nd and Pr as an isomorphic pair. Three isomorphic samples were measured on the D4c diffractometer at the ILL. The results have enabled the R-μ correlations to be separated from the $\mu - \mu'$ and R-R correlations. The results were compared with those obtained by P. Chirawatkul [27], who investigated glassy $(R_2O_3)_{0.2}(Al_2O_3)_{0.2}(SiO_2)_{0.6}$. She used the same diffraction method but with R = Dy and Ho, and interpreted the results using MD simulations and RMC modelling.

The results obtained from the ${}^{\mathrm{R}}G(r)$, $\Delta G^{(i)}(r)$ and $\Delta_{\mu\mu}(r)$ functions of the present work are consistent with a population of AlO_4 and AlO_5 units having relative fractions of 80(3)% and 20(3)%, respectively. In her work, Chirawatkul used a population of AlO_4, AlO_5 and AlO_6 units having relative fractions of 78(3)%, 16(3)% and 6(3)%, respectively, as estimated from the NMR results by Schaller and Stebbins [125], who performed ^{27}Al and ^{17}O MAS NMR experiments on La- and Y-AS glasses having the same $(R_2O_3)_{0.2}(Al_2O_3)_{0.2}(SiO_2)_{0.6}$ composition. They found that the La-containing glass shows the presence of only AlO_4 and AlO_5 units, whilst the Y-containing glass has in addition AlO_6 units.

The comparison between the large-size and small-size rare-earth AS glasses shows that, as the cation field strength increases with decreasing rare-earth radius, the aluminosilicate network is perturbed more strongly. This manifests itself by a reduction in the R-O bond distance from $\bar{r}_{\mathrm{RO}} = 2.43(2)$ Å to $\bar{r}_{\mathrm{RO}} = 2.31(3)$ - $2.35(3)$ Å. As a consequence, $\mathrm{AlO_6}$ units are stabilised for the small RAS system, while only $\mathrm{AlO_4}$ and $\mathrm{AlO_5}$ units are found in the investigated RAS glass. In respect to the R-R nearest-neighbours, a detailed modelling of the present results via MD simulations could help to elucidate more clearly the presence of clustered or dispersed rare-earth species.

7. Overall Conclusions

The method of neutron diffraction with isotopic or isomorphic substitution was used to investigate the atomic-scale structure of three different disordered materials.

In Chapter 4, the structure of a 5 m aqueous solution of NaCl was measured via neutron diffraction with Cl-isotope substitution, for a temperature and pressure range that had not previously been investigated. Two different setups, involving either a Ti-Zr pressure cell or a Paris-Edinburgh press, were employed on the D4c diffractometer at the ILL. In the first case, a substantial improvement in the quality of the data, measured up to 150 °C and 1 kbar, was achieved. In the second case, the boundary of investigated pressures was pushed up to 33.8 kbar at 150 °C [23]. The measured intra-molecular O–D coordination numbers and bond distances for water are $\overline{n}_{\mathrm{O}}^{\mathrm{D}} = 2.00(3)$ and $r_{\mathrm{OD}} = 0.96(1)$ Å over the spanned range of state conditions. The measured total structure factors were combined to give first-order difference functions $\Delta G_{\mathrm{Cl}}(r)$, thus providing new insight into the Cl^{-}ion coordination environment. At a constant pressure of 0.1 kbar and for temperature increasing from 50 °C to 150 °C, the $\Delta G_{\mathrm{Cl}}(r)$ functions show an increase in the weighted peak position $\overline{r}_{\mathrm{ClD}}$ from 2.33(2) to 2.35(2) Å, and a decrease in the $\overline{n}_{\mathrm{Cl}}^{\mathrm{D}}$ coordination number from 5.7(3) to 5.4(3). This effect may be related to the behaviour of the dielectric permittivity of water, which decreases with increasing temperature, thus favouring ion association. At a constant temperature of 150 °C and for pressure increasing from 0.1 to 33.8 kbar, the data sets are affected by low counting statistics and residual background scattering. However, the total structure factors and difference functions show clear pressure-driven changes and indicate that, as for water, the structure becomes more simple-fluid like. The $\overline{r}_{\mathrm{ClD}}$ bond distance drops from 2.35(2) to 2.07(6) Å, and the evolution of the first and second peaks makes it difficult to calculate reliable $\overline{n}_{\mathrm{Cl}}^{\mathrm{D}}$ coordination numbers. The results of this work are being compared with ongoing molecular-dynamics simulations to understand the contributions of the different $g_{\mathrm{Cl}\beta}(r)$ partial pair-distribution functions to $\Delta G_{\mathrm{Cl}}(r)$.

In Chapter 5, the atomic structures of the glasses $As_{0.30}Se_{0.70}$, $As_{0.35}Se_{0.65}$ and $As_{0.40}Se_{0.60}$ were investigated using neutron diffraction with Se-isotope substitution and the GEM diffractometer at ISIS. For the $As_{0.40}Se_{0.60}$ composition, the total structure factors and first-order difference functions were compared with data sets measured on D4c, and show good overall agreement. Comparisons were also made with the RMC results from Hosokawa *et al.* that were obtained using AXS measurements [26], and with the FPMD results from Bauchy *et al.* [25]. The reciprocal-space functions measured by NDIS are better reproduced by RMC as compared to FPMD, especially in the region of the pre-peak at low-Q. In real space, a systematic shift towards smaller r-values is found for the first-peak position in the RMC functions as compared to the NDIS functions. In contrast, the first-peak positions in the FPMD functions are systematically shifted towards larger r-values as compared to the NDIS results. Globally, neither the RMC nor the FPMD results match the NDIS real-space functions, even though the FPMD and RMC partial coordination numbers show the same trend, *i.e.* as the As content increases $\bar{n}_{\mathrm{As}}^{\mathrm{As}}$ increases whereas $\bar{n}_{\mathrm{As}}^{\mathrm{Se}}$ and $\bar{n}_{\mathrm{Se}}^{\mathrm{Se}}$ both decrease. However, the coordination numbers obtained from NDIS are in better overall agreement with the FPMD rather than with the RMC results. A comparison of the coordination numbers obtained from the NDIS, RMC and FPMD methods, with those predicted from the CON and RCN models, reveals that neither of these models describe the investigated glasses in an exhaustive way. However, the CON seems to better describe the network structures for the $As_{0.30}Se_{0.70}$ and $As_{0.35}Se_{0.65}$ compositions, but fails to predict the observed homopolar bonds for the stoichiometric composition. Our NDIS results provide a severe test of the RMC and FPMD models, and reveal discrepancies both in reciprocal and real-space. A comparison between the present results and those obtained from the full set of partial structure factors, measured for $As_{0.40}Se_{0.60}$ on D4c using NDIS [90], will allow for a more complete understanding of the contributions of the different partial pair-distribution functions $g_{\alpha\beta}(r)$ to the various difference functions.

In Chapter 6, the structure of the rare-earth aluminosilicate (RAS) glass $(R_2O_3)_{0.2}(Al_2O_3)_{0.2}(SiO_2)_{0.6}$ was investigated via ND with isomorphic substitution using the large-size rare-earth elements Nd and Pr as an isomorphic pair. The D4c diffractometer at the ILL was employed for these experiments. The results have enabled a separation of the R-R, R-μ and μ-μ' pair-correlation functions, where μ denotes a matrix (Si, Al or O) atom. The results were compared to those obtained by P. Chirawatkul [27], who used ND with isomorphic substitution to investigate the structure of the small-size RAS glass $(R_2O_3)_{0.2}(Al_2O_3)_{0.2}(SiO_2)_{0.6}$, using Dy and Ho as an isomorphic pair. The ND results for both of these materials were complemented by the MAS NMR results of Schaller and Stebbins [125]. The overall picture indicates that the structure of a $(R_2O_3)_{0.2}(Al_2O_3)_{0.2}(SiO_2)_{0.6}$ glass is based on an aluminosilicate network that is perturbed by the presence of the network-modifying rare-earth ions. A comparison between the large-size and small-size RAS glasses shows that as the cation field strength increases with decreasing rare-earth radius, the aluminosilicate network is perturbed more strongly. This manifests itself by a reduction in the R-O bond-distance from $\bar{r}_{\mathrm{RO}} = 2.43(2)$ Å to $\bar{r}_{\mathrm{RO}} = 2.31(3)$ - $2.35(3)$ Å. In consequence, AlO_6 units are stabilised for the small RAS system, while only AlO_4 and AlO_5 units are found in the investigated RAS glass. A detailed modelling of the present results via MD simulations could help to elucidate more clearly the presence of clustered or dispersed rare-earth species.

Looking ahead, it would be interesting to perform an experiment on the structure of subcritical fluids in the water-CO_2 system. Many studies are being made on this geological fluid because CO_2 sequestration in deep aquifers is considered to be a possible solution for the long-term storage of carbon dioxide, in order to mitigate global warming and climate change [14]. Also, the water-CO_2 system is of interest for enhanced geothermal systems that produce electricity using hydrothermal resources [133, 134]. Carbon dioxide could be used as a heat-transmission fluid, combining the generation of renewable energy with the geological storage of CO_2. In the relevant state conditions for this application, the temperature ranges between 100 °C and 300 °C for pressures up to 600 bar. At 300 °C and 520 bar, 15-mole% of CO_2 is dissolved in H_2O, the system is homogeneous, and it is still in a subcritical phase. Under these conditions, there should be enough CO_2 in the system to see structural changes and investigate them via NDIS with H/D isotope substitution. The measured difference functions will contain detailed information on the changes to the structure of water that are induced by the presence of CO_2. Thus, useful information would be provided to understand the microscopic behaviour of this fundamental geological fluid. A high-pressure and temperature setup has been designed to perform a NDIS experiment on D4c at the ILL [135], but the experiment could not be realised within the time scale of this PhD project.

Bibliography

[1] D. Mantegazzi, C. Sanchez-Valle, and T. Driesner. Thermodynamic properties of aqueous NaCl solutions to 1073 K and 4.5 GPa, and implications for dehydration reactions in subducting slabs. *Geochimica et Cosmochimica Acta*, 121:263–290, 2013.

[2] A. R. Hilton. *Chalcogenide Glasses for Infrared Optics*. McGraw-Hill, New York, 2009.

[3] B. J. Eggleton, Luther-Davies B., and K. Richardson. Chalcogenide photonics. *Nature Phot.*, 5:141, 2011.

[4] C. Massobrio, J. Du, M. Bernasconi, and P. S. Salmon. *Molecular Dynamics Simulations of Disordered Materials. From Network Glasses to Phase-Change Memory Alloys*, volume 215 of *Springer Series in Materials Science*. Springer, 2015.

[5] D. L. Price, S. C. Moss, R. Reijers, M. L. Saboungi, and R. Reijers. Intermediate-range order in glasses and liquids. *Journal of Physics C: Solid State Physics*, 21(32):L1069, 1988.

[6] S. R. Elliott. Medium-range structural order in covalent amorphous solids. *Nature*, 354:445–452, 1991.

[7] P. S. Salmon. Real space manifestation of the first sharp diffraction peak in the structure factor of liquid and glassy materials. *Proc. R. Soc. Lond. A.*, 445:351, 1994.

[8] P. A. Madden. A hard look at glass. *Nature*, 435:35–37, 2005.

[9] P. S. Salmon and A. Zeidler. Identifying and characterising the different structural length scales in liquids and glasses: an experimental approach. *Phys. Chem. Chem. Phys.*, 15:15286–15308, 2013.

[10] J. D. Martin. Designing intermediate-range order in amorphous materials. *Nature*, 419:381–384, 2002.

[11] P. S. Salmon, J. W. E. Drewitt, D. A. J. Whittaker, A. Zeidler, K. Wezka, C. L. Bull, M. G. Tucker, M. C. Wilding, M. Guthrie, and D. Marrocchelli. High pressure neutron diffraction study of GeO_2 glass up to 17.5 GPa. *J. Phys.: Condens. Matter*, 24:415102, 2012.

[12] A. Zeidler, J. W. E. Drewitt, P. S. Salmon, A. C. Barnes, W. A. Chrichton, S. Klotz, H. E. Fischer, C. J. Benmore, S. Ramos, and A. C. Hannon. Establishing the structure of GeS_2 at high pressures and temperatures: a combined approach using X-ray and neutron diffraction. *J. Phys.: Condens. Matter*, 21:474217, 2009.

[13] A. Zeidler, P. S. Salmon, and L. B. Skinner. Packing and the structural transformations in liquid and amorphous oxides from ambient to extreme conditions. *Proc. Natl. Acad. Sci. USA*, 111:10045, 2014.

[14] R. J. Bodnar, R. M. Capobianco, J. D. Rimstidt, R. Dilmore, A. Goodman, and G. Guthrie. *Geochemistry of Geologic CO_2 Sequestration - Reviews in Mineralogy & Geochemistry*, volume 77, pp. 123-152. Mineralogical Society of America, 2013.

[15] J. E. Enderby, D. M. North, and P. A. Egelstaff. The partial structure factors of liquid Cu-Sn. *Phil. Mag.*, 14:961, 1966.

[16] G. W. Neilson, A. K. Adya, and S. Ansell. Neutron and X-ray diffraction studies on complex liquids. *Annu. Rep. Prog. Chem., Sect. C: Phys. Chem.*, 98:273–322, 2002.

[17] Y. Waseda. *Anomalous X-Ray Scattering for Materials Characterization. Atomic-Scale Structure Determination.* Springer Berlin / Heidelberg, 2002.

[18] E. A. Stern, S. M. Heald, and E. E. Koch. *Basic Principles and Applications of EXAFS, Handbook of Synchrotron Radiation, Chapter 10.* ESRF, North-Holland edition, 1983.

[19] D. C. Koningsberger and R. Prins. *X-ray absorption: principles, applications, techniques of EXAFS, SEXAFS, and XANES.* New York : Wiley, 1988.

[20] H. E. Fischer, A. C. Barnes, and P. S. Salmon. Neutron and x-ray diffraction studies of liquids and glasses. *Rep. Prog. Phys.*, 69:233, 2006.

[21] R. L. McGreevy and L. Pusztai. Reverse Monte Carlo simulation: a new technique for the determination of disordered structures. *Molec. Simul.*, 1:359– 367, 1988.

[22] A. K. Soper. Tests of the empirical potential structure refinement method and a new method of application to neutron diffraction data on water. *Molecular Physics*, 99(17):1503–1516, 2001.

[23] R. F. Rowlands. *The role of structural disorder in crystalline, glassy and liquid materials*. PhD thesis, University of Bath, 2016.

[24] M. Bauchy, M. Micoulaut, M. Boero, and C. Massobrio. Compositional thresholds and anomalies in connection with stiffness transitions in network glasses. *Phys. Rev. Lett.*, 110:165501, 2013.

[25] M. Bauchy, A. Kachmar, and M. Micoulaut. Structural, dynamic, electronic, and vibrational properties of flexible, intermediate, and stressed rigid As-Se glasses and liquids from first principles molecular dynamics. *The Journal of Chemical Physics*, 141(19):194506, 2014.

[26] S. Hosokawa, W.-C. Pilgrim, J.-F. Bérar, and P. Boolchand. Local- and intermediate-range structures of As-Se glasses from the stoichiometric to the stiffness transition region. *Journal of Non-Crystalline Solids*, 431:31–35, 2016.

[27] P. Chirawatkul. *Structure of liquid and glassy materials from ambient to extreme conditions: a multiprobe approach*. PhD thesis, University of Bath, 2010.

[28] J. Chadwick. Possible existence of a neutron. *Nature*, 129(3252):312, 1932.

[29] E. Fermi and L. Marshall. Interference phenomena of slow neutrons. *Phys. Rev.*, 71(10):666–677, 1947.

[30] L. Meitner and O. R. Frisch. Disintegration of uranium by neutrons: a new type of nuclear reaction. *Nature*, 143(3615):239–240, 1939.

[31] E. Fermi. The development of the first chain reacting pile. *Proc. Am. Phil. Soc.*, 90(1):20–24, 1946.

[32] G. L. Squires. *An Introduction to the Theory of Thermal Neutron Scattering*. Cambridge University Press, Cambridge, 1978.

[33] V. F. Sears. Neutron scattering lengths and cross sections. *Neutron News*, 3:26–37, 1992.

[34] S. M. Bennington. Neutron school: MARI data analysis - multiple scattering and multi-phonon scattering. Unpublished Report, ISIS Pulsed Neutron Source, 2009.

[35] E. Balcar and S. W. Lovesey. *Theory of Magnetic Neutron and Photon Scattering.* Oxford: Clarendon, 1989.

[36] J. C. Wasse and P S Salmon. Structure of molten lanthanum and cerium trihalides by the method of isomorphic substitution in neutron diffraction. *Journal of Physics: Condensed Matter*, 11(6):1381, 1999.

[37] B. I. Bleaney and B. Bleaney. *Electricity and Magnetism.* Oxford: Oxford University Press, 3rd edition, 1989.

[38] A. J. Freeman and J. P. Desclaux. Dirac-Fock studies of some electronic properties of rare-earth ions. *Journal of Magnetism and Magnetic Materials*, 12(1):11 – 21, 1979.

[39] T. E. Faber and J. M. Ziman. A theory of the electrical properties of liquid metals. *Philos. Mag.*, 11:153, 1965.

[40] E. Lorch. Neutron diffraction by germania, silica and radiation-damaged silica glasses. *J. Phys. C*, 2:229, 1969.

[41] R. A. Martin, P. S. Salmon, H. E. Fischer, and G. J. Cuello. Structure of dysprosium and holmium phosphate glasses by the method of isomorphic substitution in neutron diffraction. *J. Phys.: Condens. Matter*, 15:8235, 2003.

[42] D. I. Grimley and A. C. Wright. Neutron scattering from vitreous silica IV. time-of-flight diffraction. *J. Non-Cryst. Solids*, 119:49, 1990.

[43] G. E. Bacon. *Neutron Diffraction.* Oxford: Clarendon, 1975.

[44] J. W. E. Drewitt. *Structure of copper halide melts, rare earth chalcogenide glasses, and glassy germania at high pressure.* PhD thesis, University of Bath, 2009.

[45] H Schober. An introduction to the theory of nuclear neutron scattering in condensed matter. *Journal of Neutron Research*, 17:109–357, 2014.

[46] H. E. Fischer, G. J. Cuello, P. Palleau, D. Feltin, A. C. Barnes, Y. S. Badyal, and J. M. Simonson. D4c: A very high precision diffractometer for disordered materials. *Appl. Phys. A: Mater. Sci. & Proc.*, 74:160, 2002.

[47] A. C. Hannon. Results on disordered materials from the GEneral Materials diffractometer, GEM, at ISIS. *Nuclear Instruments and Methods in Physics Research A*, 551:88–107, October 2005.

[48] D. A. J. Whittaker. *The Structure and Dynamics of Fundemental Glasses by Neutron and X-ray Scattering Techniques.* PhD thesis, University of Bath, 2012.

[49] H. H. Paalman and C. J. Pings. Numerical evaluation of x-ray absorption factors for cylindrical samples and annular sample cells. *J. Appl. Phys.*, 33(8):2635–2639, 1962.

[50] A. K. Soper and P. A. Egelstaff. Multiple scattering and attenuation of neutrons in concentric cylinders. *Nuc. Inst. Meth.*, 178(2-3):415, 1980.

[51] N. I. Dmitrieva, Q. Cai, and M. B. Burg. Cells adapted to high NaCl have many DNA breaks and impaired DNA repair both in cell culture and in vivo. *Proceedings of the National Academy of Sciences of the United States of America*, 101(8):2317–2322, 2004.

[52] E. Dendy Sloan. Fundamental principles and applications of natural gas hydrates. *Nature*, 426:353–363, 2003.

[53] http://worldoceanreview.com/en/wor-1/ocean-chemistry/climate-change-and-methane-hydrates/, March 2016.

[54] http://models.kl-edi.ac.cn/models.html, March 2016.

[55] A. Koschinsky, D. Garbe, S. Sander, and H. Schmidt, K. Straus. Hydrothermal venting at pressure-temperature conditions above the critical point of seawater, 5°S on the Mid-Atlantic Ridge. *Geology*, 36(8):615–618, 2008.

[56] R. J. Bodnar. Synthetic fluid inclusions: XII. The system H_2O-NaCl. Experimental determination of the halite liquidus and isochores for a 40 wt% NaCl solution. *Geochimica et Cosmochimica Acta*, 58(3):1053 – 1063, 1994.

[57] R. J. Bodnar. *Fluid Inclusions: Analysis and Interpretation*, volume 32, 81-99 of *Short Course Series*. A. Samson, A. Anderson and D. Marshall, Mineral. Assoc. Canada edition, 2003.

[58] E. L. Shock and H. C. Helgeson. Calculation of the thermodynamic and transport properties of aqueous species at high pressures and temperatures: Standard partial molal properties of organic species. *Geochimica et Cosmochimica Acta*, 54(4):915 – 945, 1990.

[59] H. C. Hegelson, D. H. Kirkham, and G. C. Flowers. Theoretical prediction of the thermodynamics behavior of aqueous electrolytes at high pressures and temperatures IV. Calculation of activity coefficients, osmotic coefficients, and apparent molal and standard and relative partial molal properties to 600 °C and 5 kbar. *American Journal of Science*, 281:1249–516, 1981.

[60] M. Born. The hydration heat of ions. *Zeitschrift fùr Physik*, 1:45–48, 1920.

[61] D. M. Sherman. Metal complexation and ion association in hydrothermal fluids: insights from quantum chemistry and molecular dynamics. *Geofluids*, 10(1-2):41–57, 2010.

[62] T. Driesner. *Molecular Scale Fundament of Geothermal Fluid Thermodynamics - Reviews in Mineralogy & Geochemistry*, volume 76, pp.5-33. Mineralogical Society of America, 2013.

[63] J. E. Enderby and G. W. Neilson. The structure of electrolyte solutions. *Reports on Progress in Physics*, 44(6):593, 1981.

[64] J. E. Enderby. Ion solvation via neutron scattering. *Chem. Soc. Rev.*, 24:159–168, 1995.

[65] G. Ferlat, J.-C. Soetens, A. San Miguel, and P. A. Bopp. Combining extended x-ray absorption fine structure with numerical simulations for disordered systems. *Journal of Physics: Condensed Matter*, 17(5):S145, 2005.

[66] A. Filipponi, S. De Panfilis, C. Oliva, M. A. Ricci, P. D'Angelo, and D. T. Bowron. Ion hydration under pressure. *Phys. Rev. Lett.*, 91:165505, 2003.

[67] T. Driesner, T. M. Seward, and I. G. Tironi. Molecular dynamics simulation study of ionic hydration and ion association in dilute and 1 molal aqueous sodium chloride solutions from ambient to supercritical conditions. *Geochimica et Cosmochimica Acta*, 62(18):3095 – 3107, 1998.

[68] M. V. Fedotova. Effect of temperature and pressure on structural self-organization of aqueous sodium chloride solutions. *Journal of Molecular Liquids*, 153(1):9 – 14, 2010.

[69] H. Shen, T. Hao, J. Wen, R. R. Tan, and Zhang F. S. Properties of pure water and sodium chloride solutions at high temperatures and pressures: a simulation study. *Molecular Simulation*, 41(18):1488–1494, 2015.

[70] A. K. Soper, G. W. Neilson, J. E. Enderby, and R. A. Howe. A neutron diffraction study of hydration effects in aqueous solutions. *Journal of Physics C: Solid State Physics*, 10(11):1793, 1977.

[71] G.W. Neilson. The effect of pressure on anionic hydration. *Chemical Physics Letters*, 68(2):247 – 250, 1979.

[72] P. H. K. deJong, G. W. Neilson, and M. C. Bellissent-Funel. Hydration of Ni^{2+} and Cl^{-} in a concentrated nickel chloride solution at 100 °C and 300 °C. *The Journal of Chemical Physics*, 105(12):5155–5159, 1996.

[73] P. H. K. deJong and G. W. Neilson. Structural studies of ionic solutions under critical conditions. *Journal of Physics: Condensed Matter*, 8(47):9275, 1996.

[74] P. H. K. deJong and G. W. Neilson. Hydrogen-bond structure in an aqueous solution of sodium chloride at sub- and supercritical conditions. *The Journal of Chemical Physics*, 107(20):8577–8585, 1997.

[75] T. Yamaguchi and A. K. Soper. Observation of chloride-ion hydration in high-temperature liquid and supercritical water by spherical harmonic expansion analysis. *The Journal of Chemical Physics*, 110(7):3529–3535, 1999.

[76] G. Placzek. The scattering of neutrons by systems of heavy nuclei. *Phys. Rev.*, 86(3):377, 1952.

[77] A. C. Barnes, J. E. Enderby, J. Breen, and J. C. Leyte. The water structure around the chloride ion in aqueous polyethylene oxide solutions. *Chemical Physics Letters*, 142(5):405 – 408, 1987.

[78] D. J. Hughs and J. A. Harvey. Neutron cross sections, report: BNL 325. Technical report, Brookhaven National Lab, Brookhaven, USA, 1955.

[79] S. Klotz. *Techniques in high pressure neutron scattering.* CRC Press, Boca Raton, FL, 2013.

[80] A. Zeidler, M. Guthrie, and P. S. Salmon. Pressure-dependent structure of the null-scattering alloy $Ti_{0.676}Zr_{0.324}$. *High Pressure Research*, 35(3):239–246, 2015.

[81] B. Annighöfer. Private communication, 2014.

[82] I. Howell and G. W. Neilson. The coordination of Ni^{2+} in aqueous solution at elevated temperature and pressure. *The Journal of Chemical Physics*, 104(5):2036–2042, 1996.

[83] G. W. Neilson. Private communication, 2013.

[84] H. E. Fischer. Private communication, 2015.

[85] R. W. Potter and D. L. Brown. The volumetric properties of aqueous sodium chloride solutions from 0 °C to 500 °C at pressures up to 2000 bars based on a regression of available data in the literature. *United States Geological Survey Bulletin*, 1421 - C1-36, 1977.

[86] S. Klotz. Private communication, 2014.

[87] Zeidler A. *Ordering in Amorphous Binary Systems.* PhD thesis, University of Bath, 2009.

[88] S. Cummings, J. E. Enderby, G. W. Neilson, J. R. Newsome, R. A. Howe, W. A. Howells, and A. K. Soper. Chloride ions in aqueous solutions. *Nature*, 287:714–715, 1980.

[89] J. E. Enderby, W. S. Howells, and R. A. Howe. The structure of aqueous solutions. *Chemical Physics Letters*, 21:109–112, 1973.

[90] A. Zeidler. Private communication, 2015.

[91] A. Zeidler, P. S. Salmon, H. E. Fischer, C. J. Neuefeind, J. M. Simonson, and T. E. Markland. Isotope effects in water as investigated by neutron diffraction and path integral molecular dynamics. *Journal of Physics: Condensed Matter*, 24(28):284126, 2012.

[92] https://en.wikipedia.org/wiki/Hydrogen-bond, May 2016.

[93] Th. Strässle, A. M. Saitta, Y. Le Godec, G. Hamel, S. Klotz, J. S. Loveday, and R. J. Nelmes. Structure of dense liquid water by neutron scattering to 6.5 GPa and 670 K. *Phys. Rev. Lett.*, 96:067801, 2006.

[94] G. Weck, J. Eggert, P. Loubeyre, N. Desbiens, E. Bourasseau, J.-B. Maillet, M. Mezouar, and M. Hanfland. Phase diagrams and isotopic effects of normal and deuterated water studied via x-ray diffraction up to 4.5 GPa and 500 K. *Phys. Rev. B*, 80:180202, 2009.

[95] Y. Katayama, T. Hattori, H. Saitoh, T. Ikeda, K. Aoki, H. Fukui, and K. Funakoshi. Structure of liquid water under high pressure up to 17 GPa. *Phys. Rev. B*, 81:014109, 2010.

[96] A. M. Saitta and F. Datchi. Structure and phase diagram of high-density water: The role of interstitial molecules. *Phys. Rev. E*, 67:020201, 2003.

[97] S. Bouazizi, F. Hammami, S. Nasr, and M. C. Bellissent-Funel. Neutron scattering experiments on aqueous sodium chloride solutions and heavy water. Comparison to molecular dynamics and X-ray results. *Journal of Molecular Structure*, 892:47–52, 2008.

[98] T. M. Seward. Metal complex formation in aqueous solutions at elevated temperatures and pressures. *Physics and Chemistry of the Earth*, 1314:113 – 132, 1981.

[99] M. Uematsu and E. U. Frank. Static dielectric constant of water and steam. *Journal of Physical and Chemical Reference Data*, 9(4):1291–1306, 1980.

[100] J. C. Phillips. Topology of covalent non-crystalline solids I: Short-range order in chalcogenide alloys. *J. Non-Cryst. Solids*, 34(2):153, 1979.

[101] M. Thorpe. Continuous deformations in random networks. *J. Non-Cryst. Solids*, 57:355, 1983.

[102] M. F. Thorpe, D. J. Jacobs, M. V. Chubynsky, and J. C. Phillips. Self-organization in network glasses. *J. Non-Cryst. Solids*, 266:859, 2000.

[103] P. Boolchand, D. G. Georgiev, and B. Goodman. Discovery of the intermediate phase in chalcogenide glasses. *J. Opto. Adv. Mat,*, 3:703, 2001.

[104] S. R. Elliott. *Physics of Amorphous Materials.* Longman Group UK, Essex, 2nd. edition, 1990.

[105] N. F. Mott. Localized states in a pseudogap and near extremities of conduction and valence band. *Phil. Mag.*, 19(835-852), 1969.

[106] K. S. Liang, A. Bienenstock, and C. W. Bates. Structural studies of glassy $CuAsSe_2$ and Cu-As_2Se_3 alloys. *Phys. Rev. B*, 10:1528–1538, 1974.

[107] R. M. White. Random network model for amorphous alloys. *Journal of Non-Crystalline Solids*, 16(3):387 – 398, 1974.

[108] P. S. Salmon. Structure of liquids and glasses in the Ge-Se binary system. *J. Non-Cryst. Solids*, 353:2959–2974, 2007.

[109] A. C. Stergiou and P. J. Rentzeperis. The crystal structure of arsenic selenide, As_2Se_3. *Zeitschrift fuer Kristallographie*, 173:185, 1985.

[110] A. Zeidler. Private communication, 2014.

[111] P. S. Salmon. The structure of tetrahedral network glass forming systems at intermediate and extended length scales. *J. Phys.: Condens. Matter*, 19:455208, 2007.

[112] S. Hosokawa, A. Goldbach, M. Boll, and F. Hensel. Short- and Intermediate-Range Atomic Structure of Glassy and Liquid As_2Se_3 – An Anomalous X-Ray Scattering Study. *physica status solidi (b)*, 215(1):785–789, 1999.

[113] A. A Vaipolin. Refining the structure of crystalline As_2Se_3 by finding probable correction to the atomic coordinates. *Kristallografiya*, 10:596–600, 1965.

[114] A. L. Renninger and B. L. Averbach. Atomic radial distribution functions of As-Se glasses. *Phys. Rev. B*, 8:1507, 1973.

[115] A. L. Renninger and B. L. Averbach. Crystalline structures of As_2Se_3 and As_4Se_4. *Acta Crystallographica Section B*, 29(8):1583–1589, Aug 1973.

[116] C. J. Benmore and P. S. Salmon. Structure of fast ion conducting and semiconducting glassy chalcogenide alloys. *Phys. Rev. Lett.*, 73:264, 1994.

[117] S. Xin, J. Liu, and P. S. Salmon. Structure of CuAsSe glasses investigated by neutron diffraction with copper isotope substitution. *Phys. Rev. B*, 78:064207, 2008.

[118] F. Y. Hansen, T. S. Knudsen, and K. Carneiro. Structure of amorphous selenium studied by neuron diffraction. *The Journal of Chemical Physics*, 62(4):1556, 1975.

[119] A. Bouzid, K. J. Pizzey, A. Zeidler, G. Ori, M. Boero, C. Massobrio, S. Klotz, H. E. Fischer, C. L. Bull, and P. S. Salmon. Pressure-induced structural changes in the network-forming isostatic glass $GeSe_4$: An investigation by neutron diffraction and first-principles molecular dynamics. *Phys. Rev. B*, 93:014202, Jan 2016.

[120] K. R. Long, B. S. Van Gosen, N. K. Foley, and D. Cordier. The Principal Rare Earth Elements Deposits of the United States. A Summary of Domestic Deposits and a Global Perspective. Technical Report 5220, U. S. Geological Survey, Reston, Viginia., 2010.

[121] http://www.rareearthtechalliance.com/, September 2016.

[122] J. Shen, L.-D. Sun, and C.-H. Yan. Luminescent rare earth nanomaterials for bioprobe applications. *Dalton Trans.*, pages 5687–5697, 2008.

[123] M. J. Weber. *CRC Handbook of Laser Science and Technology. Supplement 2: Optical Materials.* CRC Press, Livermore, 1995.

[124] A. Jaworski, B. Stevensson, and M. Edén. The Bearings from Rare-Earth (RE = La, Lu, Sc, Y) Cations on the Oxygen Environments in Aluminosilicate Glasses: A Study by Solid-State ^{17}O NMR, Molecular Dynamics Simulations, and DFT Calculations. *The Journal of Physical Chemistry C*, 120(24):13181–13198, 2016.

[125] T. Schaller and J. F. Stebbins. The Structural Role of Lanthanum and Yttrium in Aluminosilicate Glasses: A ^{27}Al and ^{17}O MAS NMR Study. *The Journal of Physical Chemistry B*, 102(52):10690–10697, 1998.

[126] R. D. Shannon. Revised effective ionic radii and systematic studies of interatomic distances in halides and chalcogenides. *Acta Crystallographica Section A*, 32(5):751–767, Sep 1976.

[127] R. A. Martin, P. S. Salmon, D. L. Carroll, M. E. Smith, and A. C. Hannon. Structure and thermal properties of yttrium alumino-phosphate glasses. *Journal of Physics: Condensed Matter*, 20(11):115204, 2008.

[128] J. F. Stebbins. Private communication, September 2016.

[129] D. G. Pettifor. The structures of binary compounds. I. Phenomenological structure maps. *Journal of Physics C: Solid State Physics*, 19(3):285, 1986.

[130] E. Leonova, A. S. Hakeem, K. Jansson, B. Stevensson, Z. Shen, J. Grins, S. Esmaeilzadeh, and M. Edén. Nitrogen-rich La-Si-Al-O-N oxynitride glass structures probed by solid state NMR. *Journal of Non-Crystalline Solids*, 354(1):49 – 60, 2008.

[131] M. Faucher, J. Pannetier, Y. Charreire, and P. Caro. Refinement of the Nd_2O_3 and Nd_2O_2S structures at 4 K. *Acta Crystallographica Section B*, 38(1):344–346, 1982.

[132] J. F. Stebbins. Private communication, May 2009.

[133] N. Spycher and K. Pruess. CO_2-H_2O mixtures in the geological sequestration of CO_2. II. Partitioning in chloride brines at 12-100 °C and up to 600 bar. *Geochimica et Cosmochimica Acta*, 69(13):3309 – 3320, 2005.

[134] K. Pruess. Enhanced geothermal systems (EGS) using CO_2 as working fluid - A novel approach for generating renewable energy with simultaneous sequestration of carbon. *Geothermics*, 35(4):351–367, 2006.

[135] A. Polidori, H. E. Fischer, B. Annighöfer, P. S. Salmon, and A. Zeidler. A setup for studying the structure of subcritucal fluids in the water-CO_2 system using NDIS. Technical report, ILL, 2016.